Continuous 3D Printing of Iron and Cobalt Alloys: Heat Treatment and Transformation Mechanisms

by

Jubert M. Pasco

BScE in Metallurgical Engineering, University of the Philippines (Diliman), 2017

A Dissertation Submitted in Partial Fulfillment
of the Requirements for the Degree of

Doctor of Philosophy

in the Graduate Academic Unit of Mechanical Engineering

Supervisor: Clodualdo Aranas, Ph.D., Mechanical Engineering

Examining Board: Rickey Dubay, Ph.D., Mechanical Engineering, Chair
Gobinda Saha, Ph.D., Mechanical Engineering
Olga Palazhchenko, Ph.D., Chemical Engineering

External Examiner: Abu Syed Kabir, Ph.D., Mechanical and Aerospace Engineering, Carleton University

This dissertation is accepted by the Dean of Graduate Studies

THE UNIVERSITY OF NEW BRUNSWICK

August, 2024

© Jubert M. Pasco, 2024

Abstract

The high strength and hardness of maraging steel can be functionally integrated with the thermal stability and toughness of CoCrMo alloy through multi-material additive manufacturing via laser powder bed fusion. To broaden the potential applications of this combination, this work proposes different heat treatment strategies that mutually enhance the mechanical properties of both alloys. Comparative analysis of texture development, precipitation sequence, and mechanical properties of as-built and heat-treated dual structures at different scales has been conducted. The results reveal that discontinuous martensitic transformation occurs in the interface after printing due to the combined effects of solute segregation, local stress distribution, and intermixed cellular growth. Of all the heat treatment attempts, exposure to 1150 °C for 2 hours, 940 °C for 5 hours, and 490 °C for 6 hours achieved the highest tensile strength through cooperative strengthening of intragranular γ-ε transformation in CoCrMo and Ni_3Ti precipitation in maraging steel. Initial evidence of local grain variant selection has been revealed in as-built samples due to thermal cycling, which generates residual stresses, recoil forces, and convective flow. Surprisingly, the missing variants can also be inherited after heat treatment with insufficient solution temperatures. For the CoCrMo alloy, a higher ε-phase fraction is obtained after direct aging compared to solution treatment due to band-like isothermal transformation, coherent grain face massive transformation, and recrystallization. For the maraging steel, over-aging treatment revealed that austenite reversion starts at cellular boundaries that have disintegrated over time due to chemical diffusion. The formation of austenite islands during reversion closely resembles the morphological patterns of prior cellular and melt pool boundaries. Based on overall results, it can be concluded that the

CoCrMo alloy forms a compatible interface with maraging steel, and suitable heat treatment schedules can provide a synergistic balance between strength and ductility for both alloys.

Dedication

Mom, Dad, Bro, Love you 3000.

Acknowledgements

This journey was beautiful. I genuinely cherish all the people that shared this adventure with me. Thank you, Dr. Aranas, for turning my career around. You constantly challenge me to reach my full potential. I express my appreciation to Dr. Youliang He of Natural Resources Canada for all the fruitful discussions that have improved a significant part of this work. I also extend my gratitude towards the examination committee members, Dr. Saha, Dr. Jeans, and Dr. Dubay, who provided insightful questions and suggestions that molded this research work to its current form.

Thank you to everyone at the ADRL team for a treasure chest of memories that will rival the drama in Grey's Anatomy. To my family that has shown their unwavering support everyday, I only hope to see you soon. To my dota friends at ITSL, I thank you for absolutely nothing.

Table of Contents

Abstract ii

Dedication iv

Acknowledgements v

Table of Contents vi

List of Tables xi

List of Figures xii

List of Symbols, Nomenclature, or Abbreviations xxi

Chapter 1: Introduction 1

1.1 Problem Statement 5

1.2 Objectives 6

1.3 Major Contributions of the Work 6

1.4 Thesis Structure 8

1.5 Chapter 1 References 10

Chapter 2: Research Background 14

2.1 Challenges in LPBF multi-material printing 15

2.2 Understanding 3D Printing: melt pool dynamics 17

2.3 Characterization spotlight: Electron Backscatter Diffraction (EBSD) 20

2.4 Texture development during printing: orientation relations 22

2.5 Material candidates for Dual-metal LPBF 27

2.5.1 Alloy Choice 1: Maraging Steels 28

2.5.2 Alloy choice 2: CoCrMo alloy 31

2.6 Chapter 2 References 34

Chapter 3: Combined 3D-printing 41

Background 41

Abstract 43

3.1 Introduction 44

3.2 Materials and Methods 47

3.2.1 Material 47

3.2.2 Heat Treatment 49

3.2.3 Materials Characterization 49

3.3 Results 51

3.3.1 Microstructural investigation 51

3.3.2 Texture Analysis 57

3.3.3 Chemical composition analysis 63

3.3.4 Mechanical Properties 66

3.4 Discussion 71

3.4.1 Interfacial evolution mechanism in the as-printed sample 71

3.4.2 Effect of heat treatment on the dual-alloy interface..... 75

3.4.3 Effect of heat treatment on the mechanical properties..... 76

3.5 Conclusions..... 78

3.6 Chapter 3 References..... 79

Chapter 4: Heat Treatment Optimization..... 85

Background..... 85

Abstract..... 87

4.1 Introduction..... 88

4.2 Materials and Methods..... 91

4.2.1 Alloy preparation..... 91

4.2.2 Heat Treatment..... 92

4.2.3 Material Characterization..... 93

4.3 Results..... 94

4.3.1 Microstructural analysis of as-built samples..... 94

4.3.2 Microstructural analysis of heat-treated samples..... 99

4.3.2.1 Microstructure after HT1 (1150 °C for 6 hrs + 490 °C for 6 hrs)..... 99

4.3.2.2 Microstructure after HT2 (940 °C for 2hrs + 490 °C for 6 hrs)..... 104

4.3.2.3 Microstructure after HT3 (1150 °C for 2 hrs + 940 °C for 5 hrs + 490 °C for 6 hrs)..... 109

4.4 Mechanical Properties..... 116

4.5 Discussion 119
4.5.1 Variant Selection during phase transformation in LPBF maraging steels 120
4.5.2 Comparison of three heat treatment schedules 126
4.6 Conclusions 128
4.7 Chapter 4 References 129
Chapter 5: Microstructural Transformations in CoCrMo Alloy 135
Background 135
Abstract 136
5.1 Introduction 137
5.2 Materials and Methods 139
5.2.1 Material 139
5.2.2 Heat Treatment 140
5.2.3 Materials Characterization 141
5.3 Results 142
5.3.1 Initial microstructures of the as-printed and solution-heat-treated CoCrMo samples 142
5.3.2 Microstructure evolution of CoCrMo alloy upon isothermal aging 147
5.4 Discussion 154
5.4.1 Comparison of the as-printed and solution heat-treated microstructures 154
5.4.2 Effects of isothermal aging at 940 °C to as-printed samples 157

5.4.3 Effects of isothermal aging at 940 °C to solution heat-treated samples 162

5.5 Conclusions 166

5.6 Chapter 5 References 167

Chapter 6: Variant selection in maraging steel 171

Background 171

Abstract 172

6.1 Introduction 172

6.2 Experimental Procedure 174

6.3 Results and Discussion 175

6.4 Conclusions 182

6.5 Chapter 6 References 183

Chapter 7: Conclusions 185

Curriculum Vitae

List of Tables

Table 1.1. Comparison of properties of Dual-metal LPBF candidates. 3

Table 2.1. Well-known orientation relationships between fcc and bcc structures [37]. 25

Table 3.1. Composition analysis of base alloys (in wt. %) 48

Table 3.2. EDS point analysis results for major alloying elements in the CoCrMo region 56

Table 3.3. EDS point analysis results for major alloying elements in maraging steel 56

Table 4.1. Chemical composition of maraging steel and CoCrMo feed powders (in wt %) 91

Table 5.1. Chemical composition of as-built CoCrMo (all values are in wt. %) 139

Table 6.1. Composition of the investigated maraging steel (in wt %). 174

List of Figures

Figure 2.1. General Classification of AM technologies [2]. 14

Figure 2.2. Single layer restriction solutions [12]: a) blade-based powder recoater, b) ultrasonic-based dispenser, c) electrophotographic dispenser, and d) hybrid ultrasonic and blade spreading system. 16

Figure 2.3. Influence of G and R to solidification front size and solidification morphology [27]. 19

Figure 2.4. Typical maps obtained from EBSD analysis: (a) phase map, (b) inverse pole figure map, (c) kernel average misorientation map 21

Figure 2.5. Stereographic projection of well-known fcc-bcc phase transformation ORs projected in the $(111)_{\gamma}$ corresponding to a) {001} bcc poles, b) {011} bcc poles [37]. 26

Figure 3.1. The figure illustrates key phases in the multi-material L-PBF process: (a) Initial stacking of MS1 (maraging steel) powder over MP1 (CoCrMo alloy) powder, (b) Successive layers of MS1 material are solidified under laser interaction, (c) As the procedure progresses, the fused material transitions to MP1, and finally (d) The desired configuration of the dual-metal MP1-MS1 structure is achieved. 48

Figure 3.2. Low (a, b, c) and high (d, e, f) magnification microstructures of the as-built MMAM component: CoCrMo region near the interface (a, d), Interface region (b, e), and maraging steel region near the interface (c, f). 53

Figure 3.3. Low (a, b, c) and high (d, e, f) magnification microstructures of the heat-treated MMAM component: CoCrMo region near the interface (a, d), Interface region (b, e), and maraging steel region near the interface (c, f). 55

Figure 3.4. EDS point analysis of representative samples: As-built (a) CoCrMo and (b) maraging steel, Heat-treated (c) CoCrMo and (d) maraging steel. 57
Figure 3.5. Analysis of as-printed interface region before heat treatment: (a) Inverse pole figure color map, (b) phase map showing fcc, hcp, and bcc structures, (c) Kernel average misorientation maps, (d) corresponding legends for a-c, (e) IPF representation of fcc grains, and (f) IPF representation of bcc grains. 58
Figure 3.6. Comparison of XRD spectra obtained from the (a) CoCrMo region and (b) maraging steel region of the as printed and heat-treated samples. 59
Figure 3.7. BSE images of the CoCrMo region shown in Figure 3.1d. The regions highlighted in red exhibit distinctive parallel bands, which are indicative of the formation of ε-phase. These bands are formed because of the rapid solidification during the LPBF process. 60
Figure 3.8. High resolution EBSD analysis of the CoCrMo region: (a) Phase map showing 100 % FCC phase, (b) band contrast maps that clearly depict the existence of fine parallel bands corresponding to the ε-phase, and (c) KAM maps that highlight localized strain regions formed during the martensitic transformation. 61
Figure 3.9. EBSD Analysis of MMAM component after heat treatment: (a) Inverse pole figure color map, (b) phase map showing fcc, hcp, and bcc structures, (c) Kernel average misorientation maps, (d) corresponding legends for a-c, (e) IPF representation of fcc grains, and (f) IPF representation of bcc grains. 62
Figure 3.10. Comparison of phase map (a) to EDS maps of major alloying elements along the interface after printing: (b) cobalt, (c) chromium, (d) iron, and (e) nickel. 64

Figure 3.11. Comparison of (a) phase map to EDS maps of major alloying elements along the interface after heat treatment: (b) cobalt, (c) chromium, (d) iron, and (e) nickel. 65
Figure 3.12. Contour plots of microhardness values after a) L-PBF printing, and b) solution heat treatment and aging. 67
Figure 3.13. Comparison of engineering stress-strain curves for base alloys and the dual component. Solid lines represent as-built specimens, while dashed lines indicate heat-treated specimens. Maraging steel samples are denoted in blue, CoCrMo samples in red, and dual-component samples are highlighted in black. 69
Figure 3.14. BSEI images illustrating the fracture patterns following tensile testing for (a), (b) as-printed specimens and (c), (d) heat-treated samples. 70
Figure 3.15. Analysis of EBSD results: parent austenite grain reconstruction of martensite regions of the (a) as-printed and (b) heat-treated samples; and phase boundaries that obey the K-S relationship for the (c) as-printed and (d) heat-treated samples. 73
Figure 3.16. Thermodynamic simulation of Martensite start temperature based on alloy distribution along the interface after printing. 74
Figure 4.1. Schematic illustration of three heat treatment schedules (HT1, HT2, and HT3) employed in this work, with the relevant temperatures and holding times considered for both alloys. 93
Figure 4.2. Microstructural features of the as-built MMAM component: (a) transition zone, (b, d) maraging steel cellular structure, and (c, e) CoCrMo cellular structure. 96

Figure 4.3. Texture development in the transition zone of the as-built sample: (a) phase map showing fcc and bcc structures, (b) inverse pole figure color map, (c) kernel average misorientation maps, (d,e,h,i) EDS maps for Co, Cr, Fe, and Ni, respectively, (f) corresponding legends for a-c, (g) IPF representation of fcc grains, and (j) IPF representation of bcc grains. 98

Figure 4.4. Microstructural features after HT1: (a) transition zone, (b, d) maraging steel lath structure, and (c, e) CoCrMo twin structure. 100

Figure 4.5. Texture development in the transition zone of the HT1 sample: (a) phase map showing fcc and bcc structures, (b) inverse pole figure color map, (c) kernel average misorientation maps, (d,e,h,i) EDS maps for Co, Cr, Fe, and Ni, respectively, (f) corresponding legends for a-c, (g) IPF representation of fcc grains, and (j) IPF representation of bcc grains. 102

Figure 4.6. High resolution structures of HT1 sample: (a) TEM-BF images, (b) EDS mapping results, and (c) corresponding selected area diffraction pattern. 103

Figure 4.7. Microstructural features after HT2: (a) transition zone, (b, d) maraging steel lath structure, and (c, e) CoCrMo structure. 105

Figure 4.8. Texture development in the transition zone of the HT2 sample: (a) phase map showing fcc, bcc, and hcp structures, (b) inverse pole figure color map, (c) kernel average misorientation maps, (d,e,h,i) EDS maps for Co, Cr, Fe, and Ni, respectively, (f) corresponding legends for a-c, (g) IPF representation of fcc grains, (j) IPF representation of hcp grains, and (k) IPF representation of bcc grains. 107

Figure 4.9. High resolution structures of HT2 sample: (a) TEM-BF images, (b) EDS mapping results, and (c) corresponding SAED pattern. 108

Figure 4.10. Microstructural features after HT3: (a) transition zone, (b, d) maraging steel lath structure, and (c, e) CoCrMo structure. 110
Figure 4.11. Texture development in the transition zone of the HT3 sample: (a) phase map showing fcc, bcc, and hcp structures, (b) inverse pole figure color map, (c) kernel average misorientation maps, (d,e,h,i) EDS maps for Co, Cr, Fe, and Ni, respectively, (f) corresponding legends for a-c, (g) IPF representation of fcc grains, and (j) IPF representation of bcc grains. 112
Figure 4.12. High resolution structures of HT3 sample: (a) TEM-BF images, (b) EDS mapping results, and (c) corresponding SAED pattern. 114
Figure 4.13. (a) Reconstructed 3D elemental distribution maps combining Ni, Ti, and Mo rich precipitates. Statistical proximity histograms for (b) Ni-Ti-based Ni3Ti precipitates considering the surface value of 4.82 at. % Ti, and (c) Mo-based (Fe,Ni,Co)2(Ti,Mo) con..... 115
Figure 4.14. Hardness variation in the transition zones of as-built and heat-treated specimens. 116
Figure 4.15. Engineering stress-strain curves from uniaxial tests performed on as-built and heat-treated specimens. 119
Figure 4.16. Pole figure analysis of Grain A (a-c) and Grain B (d-f) in as-built samples: (a, d) band contrast with fcc phase IPF color map (left) and corresponding {100}γ pole figures (right), (b, e) band contrast with bcc phase IPF color map (left) and corresponding {100}γ pole figures (right), (c, f) band contrast with phase map (left) and comparison of {100}α to the predicted K-S and N-W variants projected along the {111}γ plane. 124

Figure 4.17. Pole figure analysis of Grain C (a-c) from HT2 and Grain D (d-f) from HT3: (a, d) band contrast with fcc phase IPF color map (left) and corresponding {100}γ pole figures (right), (b, e) band contrast with bcc phase IPF color map (left) and corresponding {100} α' pole figures (right), (c, f) band contrast with phase map (left) and comparison of {100}α' to the predicted K-S and N-W variants projected along the {111}γ plane. 126

Figure 5.1. Initial microstructure of CoCrMo alloys in low (a, b) and high (c) magnification: As-printed microstructure is shown in (a) melt pools, (b) martensitic laths, and (c) precipitation along cell walls. The average composition of precipitates along cells walls (points 001-010) and the cell matrix (points 011-020) are summarized in Table 2. 143

Figure 5.2. Comparison of XRD spectra obtained from the AP, SHT, SAHT and DHT samples. 144

Figure 5.3. EBSD Analysis of an AP sample: (a) Inverse pole figure color map for 100 % fcc structure, (b) band contrast maps with LAGBs and CSL boundaries, (c) Kernel average misorientation map, and (d) corresponding IPF representation and misorientation angle distribution. 145

Figure 5.4. Initial microstructure of CoCrMo alloy in low (a) and high (b) magnification: equiaxed microstructure and annealing twins are shown for the solution heat-treated (SHT) sample. 146

Figure 5.5. EBSD Analysis of an SHT sample: (a) Inverse pole figure color map for 100 % fcc structure, (b) band contrast maps with LAGBs and CSL boundaries, (c) Misorientation distribution along twin boundaries (left) and overall IPF

representation (right), and (d) Kernel average misorientation map with misorientation angle distribution. 147

Figure 5.6. Microstructure of CoCrMo alloy after 5 hr. aging heat treatment at 940 °C: (a) trans-granular laths after direct aging (DHT), (b) ordered carbide precipitates after DHT. 148

Figure 5.7. EBSD Analysis of the DHT sample: (a) Phase maps showing fcc and hcp structures, (b) pattern quality maps with LAGBs and CSL boundaries, (c) Kernel average misorientation maps, and (d) corresponding misorientation angle distribution. 149

Figure 5.8. Microstructure of CoCrMo alloy after 5 hr. aging heat treatment at 940 °C: (a) lath formation after solution and aging heat treatment (SAHT), and (b) GB carbide precipitation after SAHT. 150

Figure 5.9. EBSD Analysis of the SAHT sample: (a) Phase maps showing fcc and hcp structures, (b) pattern quality maps with LAGBs and CSL boundaries, (c) Kernel average misorientation maps, and (d) corresponding misorientation angle distribution. 151

Figure 5.10. Representative engineering stress-strain curves at different conditions..... 152

Figure 5.11. Analysis of ε-phase transformation progression over time for SAHT samples, illustrating 2 hr. aging (11a, 11d, 11g), 3 hr. aging (11b, 11e, and 11h), and 4 hr. aging (11c, 11f, 11i). SEM images highlight carbide precipitation (11a-11c), phase maps showcase the isothermal transformation (11d-11f), band contrast maps with IPF color representation of hcp phases, highlighting ε-γ phase-boundaries that satisfy the Shoji-Nishiyama orientation relationship within 5° (11g-11i). 153

Figure 5.12. Transformation analysis: Figures 12a and 12b show band contrast maps with IPF color representation of hcp phases, highlighting ε-γ phase-boundaries that satisfy the Shoji-Nishiyama orientation relationship within 5° for DHT and SAHT, respectively. Grains that portray the start and end of γ-ε transformation are magnified, along with the growth direction of ε-phase. Pole figure projections of hcp grains for DHT and SAHT are illustrated in Figures 12c and 12d, comparing ε-phase orientations to the projected hcp planes satisfying the Shoji-Nishiyama orientation relationship based on the mean fcc orientation. 161

Figure 5.13. Illustration of transformation mechanisms observed in AM CoCrMo alloy..... 165

Figure 6.1. Inverse pole figure (IPF) color map of maraging steel subjected to various conditions: (a) as-built, (b) direct aging at 490 °C for 3 hours (HT1), (c) annealing above A_f at 940 °C for 2 hours (HT2), and (d) over-aging at 490 °C for 10 hrs (HT3). 176

Figure 6.2. Parent grain reconstruction and analysis of fully martensitic structures: IPF color map of reconstructed prior austenite grains for (a) as-built, (c) HT1, and (e) HT2 conditions. Figure 2b shows the variant distribution color map in the as-built sample, referencing the 24 variants from K-S OR. For HT1 and HT2, representative grain-scale variant distribution maps are showcased in Figures 2d and 2f, respectively, with the variant color map (left) and variant orientation distribution superimposed in the IPF map (right). 177

Figure 6.3. EBSD analysis of HT3: phase map showing fcc and bcc regions, and (b) band contrast map overlain with the reverted austenite (fcc) IPF color map. 180

Figure 6.4. Pole figure analysis of melt pool-shaped and columnar shaped austenite grain: (a-b) band contrast overlaid with IPF color map of fcc phase (left) with pole figures of {100}γ projected along the BD (right), (c-d) band contrast overlaid with IPF color map of bcc phase (left) with pole figures of {100}α projected along the BD (right), (e-f) band contrast overlain with the phase map (left) with comparison of {100}α to the predicted K-S and N-W variants along the {111}γ plane. (a), (c), and (e) refer to the melt pool-shaped austenite grain while (b), (d) and (f) refer to the columnar austenite grain. 181

List of Symbols, Nomenclature, or Abbreviations

AM	Additive Manufacturing
AP	As-Printed structure
APT	Atom Probe Tomography
A_f	Austenite Finish
A_s	Austenite Start
BCC	Body Centered Cubic Phase
BD	Build Direction
λ_1	Cellular Spacing
CAD	Computer-Aided Design
T_c	Critical Temperature
ΔT	Degree Of Undercooling
DHT	Direct Heat-Treated
DED	Directed Energy Deposition
EBSD	Electron Backscatter Diffraction
EDS	Energy Dispersive Spectroscopy
FCC	Face Centered Cubic Phase
γ	Gamma Phase
GBs	Grain Boundaries
G-T	Greninger-Troiano
H-G-J	He-Godet-Jonas
ICP-OES	Inductively Coupled Plasma - Optical Emission Spectroscopy
IMCs	Intermetallic Compounds

IPF	Inverse Pole Figure
KAM	Kernel Average Misorientation
KS	Kurdjumov-Sachs
LPBF	Laser Powder Bed Fusion
LAGBs	Low-Angle Grain Boundaries
M_a	Marangoni Number
ε	Martensitic Epsilon Phase
M_s	Martensitic Transformation Start Temperature
MMAM	Multi-Material Additive Manufacturing
N-W	Nishiyama-Wassermann
OM	Optical Microscope
OR	Orientation Relationship
PQ	Pattern Quality
PAGs	Prior Austenite Grains
SEM	Scanning Electron Microscope
S-N	Shoji-Nishiyama
R	Solidification Growth Rate
SAHT	Solution + Aged Heat-Treated
SHT	Solution Heat-Treated
G	Temperature Gradient
TEM	Transmission Electron Microscopy
vAMC	Voestalpine Additive Manufacturing Center
XRD	X-Ray Diffraction

Chapter 1: Introduction

Additive manufacturing (AM), commonly known as 3D printing, has transformed the landscape of the design sector, making the production of an entire assembly of parts with challenging geometry possible using a single piece produced in one cycle, using a single machine [1–3]. This technology is especially useful in industries like aerospace, automotive, energy, and healthcare, where high-performance parts are crucial. The benefits of AM include being able to use a wide variety of materials, faster production times, less need for repairs or downtime, more control over mechanical properties, and lower overall costs [4–6]. AM builds parts layer by layer from a digital model, which helps to place materials precisely and reduce waste [7,8]. Despite its versatility, a notable limitation has been the restriction to a single material composition per print. The next big step is to develop techniques that allow customization of material composition *within the layers*, an area of research generally referred to as multi-material additive manufacturing (MMAM). Critical materials will be assigned to specific regions only where they are needed, while using lighter or cheaper materials elsewhere.

Numerous examples of industrial applications demonstrate the tremendous potential of exploiting the free form fabrication capability of MMAM. For instance, steel and copper combinations are prevalent in thermal and power generation applications. The huge difference in thermal properties between the two materials can be compensated by utilizing high resolution joints using AM technologies [7,9]. Different titanium alloys with intricate geometries are also being considered for structural components in the aerospace and aviation industries, considering the balance of heat resistance and strength against material expenditure [10]. Adapters in oxygen regenerators can be fabricated using steel-aluminum

alloy combinations where the high surface coating corrosion resistance of alumina is exploited [11]. Metal cutting tools can utilize high hardness and wear resistant components at the cutting tip, while tough and less expensive materials can be assigned to the shank part [9]. MMAM systems can be also used in authenticating other 3D printed materials, such as in adopting unique spectral signatures added on a part using DED [12,13]. Honeywell also has patented an AM technology that fabricates turbine blades using multiple superalloys that are optimized at different regions of the component depending on the service conditions [14]. A nickel-based superalloy with high creep resistance can be assigned to the blade shaft and tip, while a lighter titanium alloy can be assigned in the cooler root regions. [15]. Other examples include conformal cooling channels, thermal insulation coatings, laser telecommunication systems, electrochemical combinations in batteries, and integration of semiconductor components in electronic devices [16].

Laser powder bed fusion (LPBF) stands out as a leading AM method for printing metallic components. The key advantage lies in the near net shape fabrication capabilities, or the ability to produce parts that closely match their final design, eliminating the need for intricate mold designs [3]. The LPBF process applies a laser to selectively melt and bond successive layers of metal powders spread on a build plate based on a sliced model of the desired final product [8,15]. The powder delivery system allows a high printing resolution (20-50 μm, [17]) enhanced by the use of a finer laser spot diameter of 0.08 to 0.1 mm [3], which leads to greater in-plane print resolution and superior surface quality. Accordingly, MMAM applications that require higher precision, accurate spatial distribution control, and finer geometries such as in internal channels, overhanging regions and lattice structures are better accomplished using LPBF [18]. A high relative density in printed metal parts can

also be achieved in LPBF since the high energy from the laser can be focused to achieve a small melt pool size [19]. Aside from evident advantages in geometrical capabilities against conventional manufacturing processes, Damon et al.[20] also pointed out that LPBF is distinctly effective for expensive and resource critical materials because of minimal powder waste and recyclability of unused powder in the process.

The overall focus of this thesis is to demonstrate the capabilities of MMAM by combining an Fe-based alloy in maraging steel and a Co-based alloy in CoCrMo using LPBF. A direct comparison of each material's properties is presented in Table 1.1:

Table 1.1. Comparison of properties of Dual-metal LPBF candidates.

Property	**Maraging Steel** [21]	**CoCrMo Alloy** [22]
Crystal structure	BCC Fe–Ni martensite + intermetallic precipitates (Ni_3Mo & Ni_3Ti)	FCC Co phase + Cr/Mo precipitates
Major alloying elements	Ni, Co, Mo, Ti	Co, Cr, Mo
Carbon content [wt%]	< 0.03	$< .16$
Thermal expansion [µm/m-°C]	8.64	13.6
Thermal conductivity [W/m-C]	19.6	13
Strengthening mechanism	Precipitation strengthening	Precipitation strengthening
Standard heat treatments	Annealing: 815 °C, 1 h Aging: 482, 3-8 h	Stress-relief: 1150 °C, 6h
Magnetism	Ferromagnetic	Non-magnetic
Relevant Temperature transitions	Liquidus (1454 °C), Solidus (1427 °C)	Allotropic transformation (970 °C)
Melting Point [°C]	1413	1350-1430
Density [g/cm^3]	8	8.3

This pairing brings together the best of both worlds: Maraging steels [23–25], known for having superior strength, weldability, and easier serviceability, can be tactically merged with CoCrMo alloys [26,27] which have better thermal stability, higher wear resistance, and inherent biocompatibility. Precipitation strengthening is also improved in both alloys with Mo [24,26]. Initially, this material combination was chosen for improving thermal transport and making injection molding processes better, particularly in simplifying both the cost and design complexity. However, with an appropriate post-processing heat treatment, the possible applications could dramatically expand to high-performance parts that require optimized mechanical properties and demand stricter standards, such as loadbearing structural components [24], heavy tooling and cutting machinery, impact energy absorption assemblies [28], and automotive engine components [29].

For CoCrMo alloys, finding the right balance between the metastable gamma (γ) phase and martensitic epsilon (ε) phase depends on various microstructural factors, including stacking faults [30], recrystallized grains, coherent twins, pinning precipitates [31], and interstitial elements [32]. Depending on the accumulation of Shockley partials and density of dislocations, the γ-ε transformation can take place through strain addition [26], annealing [30], diffusional massive transformation [33], or rapid cooling [34]. The subsequent growth predominantly occurs along parallel striations that extend in $\{111\}_\gamma$ habit planes [35].

On the other hand, for maraging steel, the cyclic heating during AM repeatedly reverts the melt pool back to the parent austenite phase and creates blurred lath transformation morphologies. The orientation relationship (OR) between the original austenite grain and a set of resulting product orientations after solidification, known as variants [36], is influenced by various factors of the transformation process: the local segregation of

alloying elements, the cooling rate of the solidification front, and the accumulated thermal strains. Analyzing the development of transformation textures and corresponding mechanical properties of AM-produced structures is complicated by the columnar dendritic structure and the thermal cycles experienced during printing, which tend to obscure the boundaries of the original austenite grains.

1.1 Problem Statement

This thesis addresses the complex challenges of successfully printing and conducting effective heat treatment for a maraging steel-CoCrMo alloy multi-material component. These challenges are centered around two critical objectives: ensuring that each alloy achieves its optimal internal structure, composition, texture, mechanical properties, and phase transformation, all without compromising the component's overall integrity due to alloy contamination and intermetallic formation at the transition zones. The investigation focuses on three key areas:

- The need to comprehensively characterize the interfacial properties of MMAM components to ensure that the mechanical properties at the interfaces are on par with those of the individual alloys.
- The development of a compatible heat treatment strategy that maximizes the mechanical properties of both alloys, striking a balance that leverages the strengths of each material.
- The inadvertent changes in microstructure and mechanical properties of the individual alloys following non-standard and optimized heat treatments require in-depth analysis and characterization.

1.2 Objectives

The objectives of this work are summarized as follows:

- *Interfacial Characterization*: Identify the interfacial characteristics of a maraging steel-CoCrMo alloy multi-material (MMAM) component, focusing on the mechanisms at play during solidification of the transition zone compared to the base alloys.
- *Heat Treatment Optimization*: Develop a suitable heat treatment strategy to maximize the mechanical properties and microstructural evolution of the entire multi-material component and the individual alloys.
- *CoCrMo Alloy Transformation and Precipitation*: Determine the effects of heat treatment on the transformation behaviors and precipitate formation in CoCrMo alloys outside conventional temperature regimes.
- *Maraging Steel Transformation Behavior*: Determine the effects of heat treatment on transformation behaviors and texture development in maraging steels, with an emphasis on variant selection during austenite reversion.

1.3 Major Contributions of the Work

The major contributions of the research work presented in this thesis are:

- Comprehensive transition zone characterization, mechanical property testing, and analysis of solidification mechanisms for the continuous laser powder bed fusion (L-PBF) of 18Ni(300) maraging steel and CoCrMo alloy, a material pairing that has not been printed before.
- Demonstrated different heat treatment procedures that enable functional synergy between the base alloys, adjusting the individual mechanical properties to suit

specific component applications without compromising the integrity of the transition zones. The observed effect of solute distribution to martensite formation in the interface also aligns well with thermodynamic simulations.

- Introduced a repeatable variant analysis procedure for multi-material components that establishes direct parent-child orientation relationships without the need for parent reconstruction and crystallographic orientation simulation techniques.
- Provided new evidence of grain-scale variant selection unique to AM maraging steel components and proposed the possible mechanism that dictates the missing variants: the distribution of residual stress and recoil forces in the depression region and surface tension in the tail end region of the melt pool. The Marangoni flow driven by surface tension differences also appears to reduce variant selection during solidification, since fewer variants are missing at the edge of the melt pool compared to the center.
- Explained variant selection inheritance mechanism in maraging steels after heat treatment below the solutionizing heat treatment temperature. Similar variants are missing during printing and after aging, which consequently reveals that recrystallization and complete solution treatment above the Ae_3 line is necessary to allow the formation of all possible lath configurations in approximately equal volume fractions.
- In-depth investigation of atomistic behavior and precipitation formation during aging of maraging steels, particularly demonstrating how austenite reversion from alloy depletion during precipitation can be reduced using homogenization and solution heat treatment.

- Compared various phase transformation mechanisms unique to additively manufactured CoCrMo alloys, particularly in preferential carbide formation, coherent grain face massive transformation, annealing twins, and isothermal ε-phase banding.
- Established that the formation of austenite grains during reversion in maraging steels closely resemble the morphological patterns of preceding melt pools and columns. Despite partial disintegration of cellular structures, they critically influence phase and orientation distribution during austenite reversion at long aging times.

1.4 Thesis Structure

The rest of the thesis is organized as follows:

In Chapter 2, the current field of Multi-material additive manufacturing is presented, focusing on the alloys selected for this work. Core concepts relevant to characterization and testing techniques performed in this work are also introduced, including melt pool dynamics, texture analysis via Electron Backscatter Diffraction (EBSD), orientation relationships during phase transformations, stereographic projections, and variant selection mechanisms.

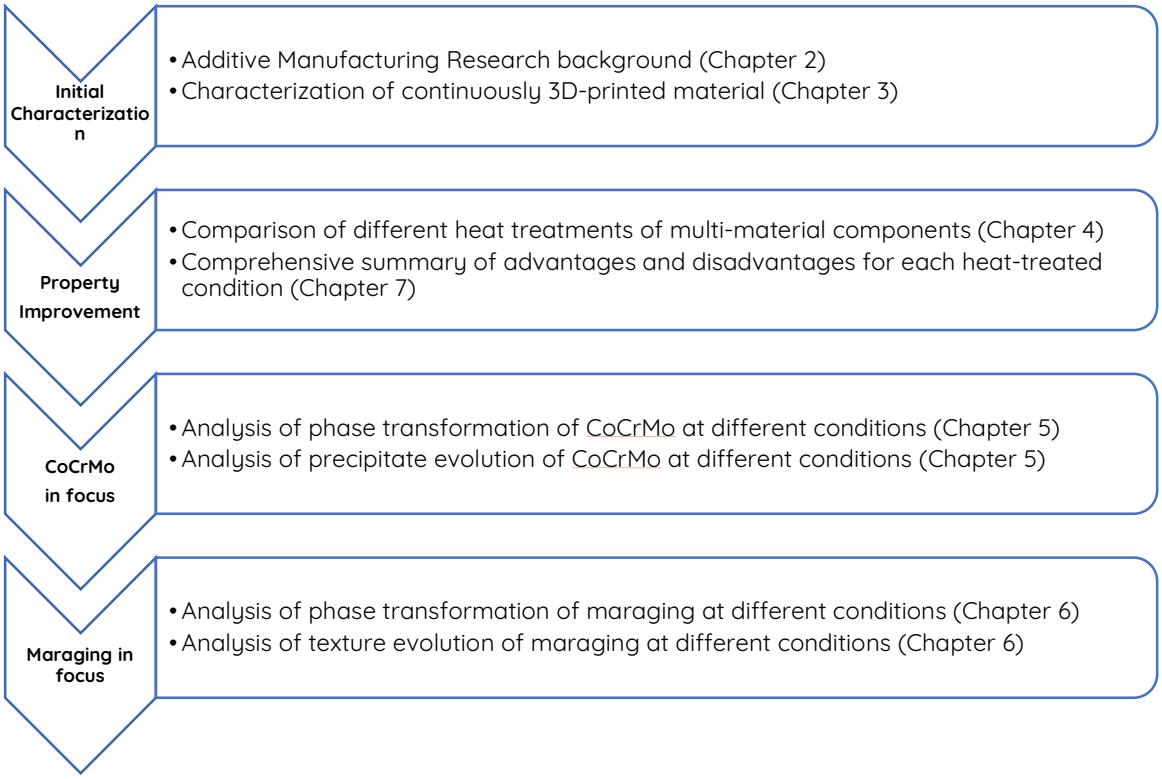
Chapter 3 explores the initial experimentation with continuous 3D-printing and heat treatment of 18Ni(300) maraging steel and CoCrMo alloy using Laser Powder Bed Fusion. While observations revealed the absence of cracks and confirmed compatible interfacial bonding through thermodynamic simulations, intriguing phase transformation mechanisms were detected in the transition zones after printing and after conventional heat treatment.

Chapter 4 broadens the analysis of solidification phenomena during heat treatment of the multi-material component. The objective is to achieve a synergistic balance between the mechanical properties of the overall structure with the internal structure of the base alloys. Optimized heat treatment schedules led to unique interface mechanisms that warranted a deeper phase transformation investigation of the individual alloys. Attention is directed towards the correlation of variant selection to recoil forces, stereographic plotting of austenite-martensite boundaries in the transition zone, and the atomistic behavior of solutes during heat treatment at the interface.

Chapter 5 is dedicated to a detailed examination of phase transformation mechanisms in the CoCrMo alloy. Given that the heat treatment schedules are outside the conventional temperature regimes and exposure durations, this chapter enhances the existing understanding of the transformation phenomena for this alloy. Band-like isothermal transformation, coherent grain face massive transformation, ordered carbide nucleation, twinning and recrystallization phenomena are linked with the observed mechanical properties and microstructures.

Chapter 6 investigates the texture inheritance during the austenite-martensite transformation in maraging steels. Introducing a novel perspective on examining phase transformation phenomena using over-aging, this chapters presents fascinating findings regarding austenite reversion. Although the cell boundaries from printing disintegrate at long aging times, the local element segregation influences austenite reversion in such a way that the location and texture of reverted austenite preferentially traces the prior melt pool boundaries and columns.

Chapter 7 concludes the thesis with a comprehensive summary of the research conducted and the findings obtained. The flowchart below summarizes the workflow for this thesis:



1.5 Chapter 1 References

[1] A. Bandyopadhyay, B. Heer, Additive manufacturing of multi-material structures, Materials Science and Engineering: R: Reports 129 (2018) 1–16. https://doi.org/10.1016/j.mser.2018.04.001.

[2] T. DebRoy, H.L. Wei, J.S. Zuback, T. Mukherjee, J.W. Elmer, J.O. Milewski, A.M. Beese, A. Wilson-Heid, A. De, W. Zhang, Additive manufacturing of metallic components – Process, structure and properties, Progress in Materials Science 92 (2018) 112–224. https://doi.org/10.1016/j.pmatsci.2017.10.001.

[3] S.L. Sing, S. Huang, G.D. Goh, G.L. Goh, C.F. Tey, J.H.K. Tan, W.Y. Yeong, Emerging metallic systems for additive manufacturing: In-situ alloying and multi-metal processing in laser powder bed fusion, Progress in Materials Science 119 (2021) 100795. https://doi.org/10.1016/j.pmatsci.2021.100795.

[4] A. Ben-Artzy, A. Reichardt, J.-P. Borgonia, R.P. Dillon, B. McEnerney, A.A. Shapiro, P. Hosemann, Compositionally graded SS316 to C300 Maraging steel using additive manufacturing, Materials & Design 201 (2021) 109500. https://doi.org/10.1016/j.matdes.2021.109500.

[5] B. Mooney, K.I. Kourousis, R. Raghavendra, Plastic anisotropy of additively manufactured maraging steel: Influence of the build orientation and heat treatments, Additive Manufacturing 25 (2019) 19–31. https://doi.org/10.1016/j.addma.2018.10.032.
[6] Y. Tian, K. Nyamuchiwa, K. Chadha, Y. He, C. Aranas, Laser powder bed fusion of M789 maraging steel on Cr–Mo N709 steel: Microstructure, texture, and mechanical properties, Materials Science and Engineering: A 839 (2022) 142827. https://doi.org/10.1016/j.msea.2022.142827.
[7] C. Tan, K. Zhou, W. Ma, L. Min, Interfacial characteristic and mechanical performance of maraging steel-copper functional bimetal produced by selective laser melting based hybrid manufacture, Materials & Design 155 (2018) 77–85. https://doi.org/10.1016/j.matdes.2018.05.064.
[8] Y. Tian, R. Palad, C. Aranas, Microstructural evolution and mechanical properties of a newly designed steel fabricated by laser powder bed fusion, Additive Manufacturing 36 (2020) 101495. https://doi.org/10.1016/j.addma.2020.101495.
[9] L. Yan, Y. Chen, F. Liou, Additive manufacturing of functionally graded metallic materials using laser metal deposition, Additive Manufacturing 31 (2020) 100901. https://doi.org/10.1016/j.addma.2019.100901.
[10] K. Wei, X. Zeng, F. Li, M. Liu, J. Deng, Microstructure and Mechanical Property of Ti-5Al-2.5Sn/Ti-6Al-4V Dissimilar Titanium Alloys Integrally Fabricated by Selective Laser Melting, JOM 72 (2020) 1031–1038. https://doi.org/10.1007/s11837-019-03988-6.
[11] X. Mei, X. Wang, Y. Peng, H. Gu, G. Zhong, S. Yang, Interfacial characterization and mechanical properties of 316L stainless steel/inconel 718 manufactured by selective laser melting, Materials Science and Engineering: A 758 (2019) 185–191. https://doi.org/10.1016/j.msea.2019.05.011.
[12] S. Flank, A.R. Nassar, T.W. Simpson, N. Valentine, E. Elburn, Fast authentication of metal additive manufacturing, 3D Printing and Additive Manufacturing 4 (2017) 143–147. https://doi.org/10.1089/3dp.2017.0018.
[13] C. Wei, L. Li, X. Zhang, Y.-H. Chueh, 3D printing of multiple metallic materials via modified selective laser melting, CIRP Annals 67 (2018) 245–248. https://doi.org/10.1016/j.cirp.2018.04.096.
[14] D.G. Godfrey, M.C. Morris, M. Menon, Multi-material turbine components, US9266170B2, 2016. https://patents.google.com/patent/US9266170/en (accessed March 17, 2021).
[15] M.G. Scaramuccia, A.G. Demir, L. Caprio, O. Tassa, B. Previtali, Development of processing strategies for multigraded selective laser melting of Ti6Al4V and IN718, Powder Technology 367 (2020) 376–389. https://doi.org/10.1016/j.powtec.2020.04.010.
[16] M. Vaezi, S. Chianrabutra, B. Mellor, S. Yang, Multiple material additive manufacturing – Part 1: a review: This review paper covers a decade of research on multiple material additive manufacturing technologies which can produce complex geometry parts with different materials, Virtual and Physical Prototyping 8 (2013) 19–50. https://doi.org/10.1080/17452759.2013.778175.

[17] A. Khorasani, I. Gibson, J.K. Veetil, A.H. Ghasemi, A review of technological improvements in laser-based powder bed fusion of metal printers, Int J Adv Manuf Technol 108 (2020) 191–209. https://doi.org/10.1007/s00170-020-05361-3.
[18] J. Chen, Y. Yang, C. Song, M. Zhang, S. Wu, D. Wang, Interfacial microstructure and mechanical properties of 316L /CuSn10 multi-material bimetallic structure fabricated by selective laser melting, Materials Science and Engineering: A 752 (2019) 75–85. https://doi.org/10.1016/j.msea.2019.02.097.
[19] Y. Bai, C. Zhao, Y. Zhang, H. Wang, Microstructure and mechanical properties of additively manufactured multi-material component with maraging steel on CrMn steel, Materials Science and Engineering: A 802 (2021) 140630. https://doi.org/10.1016/j.msea.2020.140630.
[20] J. Damon, T. Hanemann, S. Dietrich, G. Graf, K.-H. Lang, V. Schulze, Orientation dependent fatigue performance and mechanisms of selective laser melted maraging steel X3NiCoMoTi18-9-5, International Journal of Fatigue 127 (2019) 395–402. https://doi.org/10.1016/j.ijfatigue.2019.06.025.
[21] A. Ben-Artzy, A. Reichardt, J.-P. Borgonia, R.P. Dillon, B. McEnerney, A.A. Shapiro, P. Hosemann, Compositionally graded SS316 to C300 Maraging steel using additive manufacturing, Materials & Design 201 (2021) 109500. https://doi.org/10.1016/j.matdes.2021.109500.
[22] Y. Kajima, A. Takaichi, N. Kittikundecha, T. Nakamoto, T. Kimura, N. Nomura, A. Kawasaki, T. Hanawa, H. Takahashi, N. Wakabayashi, Effect of heat-treatment temperature on microstructures and mechanical properties of Co–Cr–Mo alloys fabricated by selective laser melting, Materials Science and Engineering: A 726 (2018) 21–31. https://doi.org/10.1016/j.msea.2018.04.048.
[23] R. Han, X. Li, H. Chen, Y. Peng, D. Yan, K. Wang, Microstructure evolution and mechanical properties of TiB2/18Ni300 composite material produced by laser additive manufacturing, Journal of Materials Research and Technology 24 (2023) 4517–4533. https://doi.org/10.1016/j.jmrt.2023.04.043.
[24] M. Niu, G. Zhou, W. Wang, M.B. Shahzad, Y. Shan, K. Yang, Precipitate evolution and strengthening behavior during aging process in a 2.5 GPa grade maraging steel, Acta Materialia 179 (2019) 296–307. https://doi.org/10.1016/j.actamat.2019.08.042.
[25] F. Haftlang, J.B. Seol, A. Zargaran, J. Moon, H.S. Kim, Chemical core-shell metastability-induced large ductility in medium-entropy maraging and reversion alloys, Acta Materialia 256 (2023) 119115. https://doi.org/10.1016/j.actamat.2023.119115.
[26] L.H.M. Antunes, J.J. Hoyos, T.C. Andrade, P.W.C. Sarvezuk, L. Wu, J.A. Ávila, J.P. Oliveira, N. Schell, A.L. Jardini, J. Žilková, P.F. da Silva Farina, H.F.G. Abreu, M. Béreš, Deformation-induced martensitic transformation in Co-28Cr-6Mo alloy produced by laser powder bed fusion: Comparison surface vs. bulk, Additive Manufacturing 46 (2021) 102100. https://doi.org/10.1016/j.addma.2021.102100.
[27] B.R. Coutinho Saraiva, L. Novotný, B. Carpentieri, T.F. Keller, M. Fáberová, R. Bureš, S.F. Rodrigues, J. Rodrigues de Barros Neto, L.H. Martinez Antunes, M. Masoumi, H.F. Gomes de Abreu, M. Béreš, Effect of cyclic loading on microstructure and crack propagation in additively manufactured biomaterial Co–

Cr–Mo alloy, Journal of Materials Research and Technology 26 (2023) 3905–3916. https://doi.org/10.1016/j.jmrt.2023.08.185.
[28] M.C. Niu, L.C. Yin, K. Yang, J.H. Luan, W. Wang, Z.B. Jiao, Synergistic alloying effects on nanoscale precipitation and mechanical properties of ultrahigh-strength steels strengthened by Ni3Ti, Mo-enriched, and Cr-rich co-precipitates, Acta Materialia 209 (2021) 116788. https://doi.org/10.1016/j.actamat.2021.116788.
[29] X. Wang, W. Li, Y. Yao, L. Fan, J. Wang, W. Wang, P. Wen, Z. Yang, H. Chen, In-situ alloyed ultrahigh strength steels via additive manufacturing, Additive Manufacturing 77 (2023) 103825. https://doi.org/10.1016/j.addma.2023.103825.
[30] S. Kurosu, H. Matsumoto, A. Chiba, Isothermal Phase Transformation in Biomedical Co-29Cr-6Mo Alloy without Addition of Carbon or Nitrogen, Metall Mater Trans A 41 (2010) 2613–2625. https://doi.org/10.1007/s11661-010-0273-8.
[31] M. Roudnická, J. Kubásek, L. Pantělejev, O. Molnárová, J. Bigas, J. Drahokoupil, D. Paloušek, D. Vojtěch, Heat treatment of laser powder-bed-fused Co–28Cr–6Mo alloy to remove its microstructural instability by massive FCC→HCP transformation, Additive Manufacturing 47 (2021) 102265. https://doi.org/10.1016/j.addma.2021.102265.
[32] M. Mori, K. Yamanaka, A. Chiba, Phase decomposition in biomedical Co–29Cr–6Mo–0.2N alloy during isothermal heat treatment at 1073K, Journal of Alloys and Compounds 590 (2014) 411–416. https://doi.org/10.1016/j.jallcom.2013.12.126.
[33] B.T. Donkor, J. Song, Y. Fu, M. Kattoura, S.R. Mannava, M.A. Steiner, V.K. Vasudevan, Accelerated γ-face-centered cubic to ε-hexagonal close packed massive transformation in a laser powder bed fusion additively manufactured Co-29Cr-5Mo alloy, Scripta Materialia 179 (2020) 65–69. https://doi.org/10.1016/j.scriptamat.2020.01.012.
[34] S. Kurosu, N. Nomura, A. Chiba, Microstructure and Mechanical Properties of Co-29Cr-6Mo Alloy Aged at 1023 K, Materials Transactions 48 (2007) 1517–1522. https://doi.org/10.2320/matertrans.MRA2007606.
[35] J.-L. Putaux, J.-P. Chevalier, HREM study of self-accommodated thermal ε-martensite in an Fe-Mn-Si-Cr-Ni shape memory alloy, Acta Materialia 44 (1996) 1701–1716. https://doi.org/10.1016/1359-6454(95)00268-5.
[36] F. Niessen, T. Nyyssönen, A.A. Gazder, R. Hielscher, Parent grain reconstruction from partially or fully transformed microstructures in MTEX, J Appl Cryst 55 (2022) 180–194. https://doi.org/10.1107/S1600576721011560.

Chapter 2: Research Background

AM technologies have been classified into seven categories according to raw materials type, power source and processing technique [1]. The classifications of the AM techniques are presented in Figure 2.1[2], categorized as vat photopolymerization, material extrusion, material jetting, binder jetting, sheet lamination, directed energy deposition, and powder bed fusion techniques. Among the wide variety of methods for fabricating metallic materials, Directed Energy Deposition (DED) and Laser Powder Bed Fusion (LPBF) stand out as the most promising and extensively researched techniques for metals.

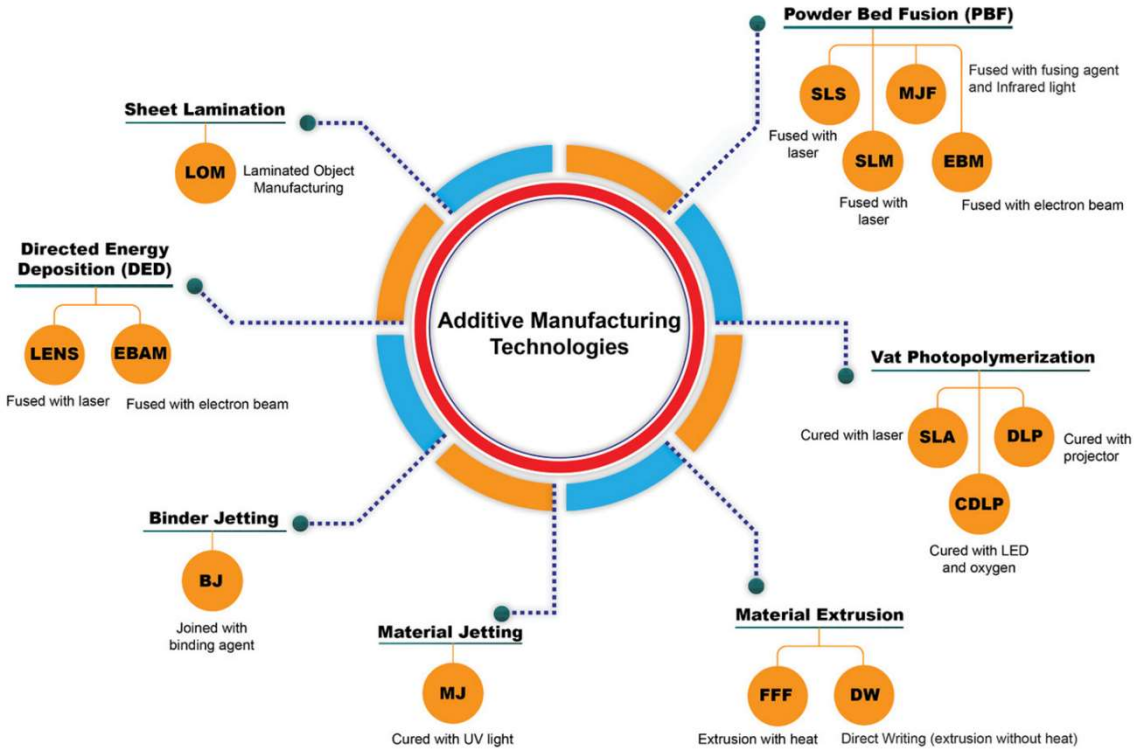


Figure 2.1. General Classification of AM technologies [2].

Multi-material parts are typically assembled using conventional techniques such as laser welding, electron beam welding, friction stir welding, explosive welding, or diffusion bonding [3]. The main issue in conventional techniques relate to the resulting local change

of microstructure in the base metals, which can lead to cracking, distortion, and brittle inter-metallic phase formation. [4]. Although such joining processes will likely remain as the main choice for standard shapes and simple interfaces, certain process conditions and complex material functionalities will necessitate novel techniques that are only attainable using MMAM. Different materials that are separately fabricated and then welded can be integrated in a single process chain [5]. Limitations on tool access, post-processing machining requirements, the need for near planar joining surfaces, and impossibility of joining tight corners and geometries can be eliminated using MMAM [6]. Furthermore, traceability and material part security for existing AM techniques can be improved by adding tracking mechanisms using MMAM [7].

However, MMAM applications can be limited by contamination issues, slow deposition rates (5-20 cm^3/h [8]), and the inherent layer-wise homogenous material limitation. Process conditions cannot be easily adjusted when switching between different materials [9]. Increasing the deposition rates will decrease geometric accuracy. Increasing other printing parameters such as the laser power, scanning speed and hatching space can also improve the production rate, but components will have higher susceptibility to printing defects such as holes and lack of fusion defects [8].

2.1 Challenges in LPBF multi-material printing

As one of the prominent AM techniques, LPBF is under consideration for multi-material AM because it uses base materials in powder form to produce a thin, continuous interface [10]. However, the high heating and cooling rates of laser melting can introduce residual stresses that can be detrimental to interfacial bonding and material compatibility [11]. Despite having geometric flexibility and high resolution, existing LPBF systems are mostly

restricted to a homogenous composition. The particle bed mechanism also hinders customization of powder composition on a specific layer, which can readily be accomplished in the DED process by using multiple powder containers in the feeding system. Nevertheless, several material-spreading techniques have already been proposed to overcome the single layer customization problem [12], and these methods are illustrated in Figure 2.2.

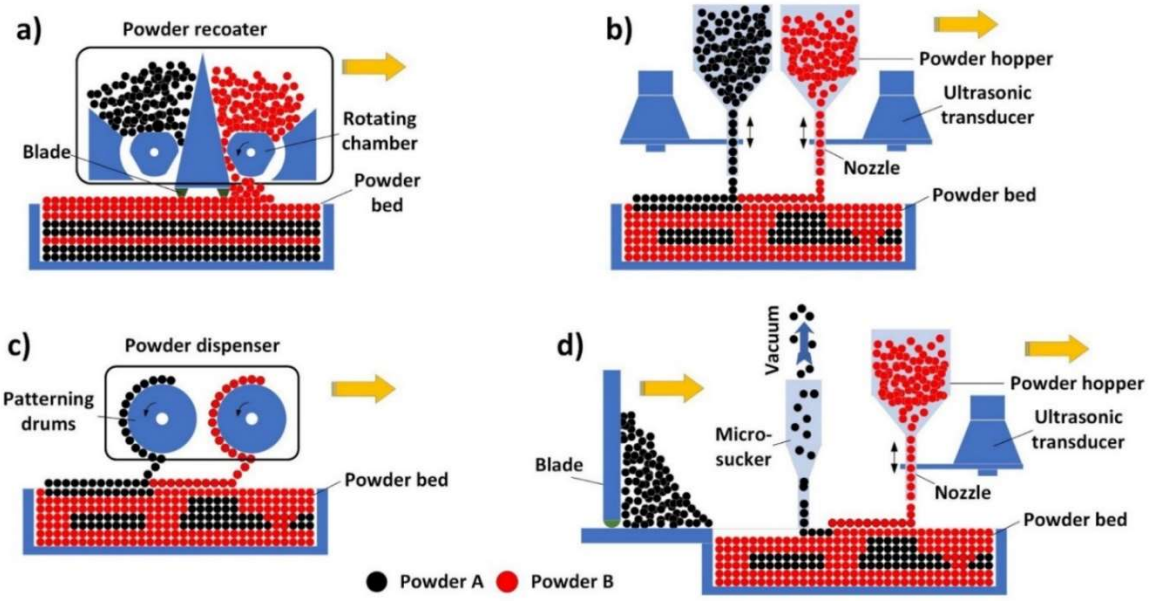


Figure 2.2. Single layer restriction solutions [12]: a) blade-based powder recoater, b) ultrasonic-based dispenser, c) electrophotographic dispenser, and d) hybrid ultrasonic and blade spreading system.

The blade-based powder spreading system in Figure 2.2a has been successfully used in copper-stainless steel bimetallic components using modified powder containers but has only solved the material restriction in the vertical direction [13]. Although the point-to-point processing efficiency of the ultrasonic-based feeding system in Figure 2.2b is still limited, studies have demonstrated the uniform spreading capability of ultrasonic based dispensers [14]. A start-up company named Aerosint invented custom rollers that control powder placement using rotating drums to deposit a specific material at a specific point in

the printing space, as shown in Figure 2.2c [2]. A vacuum cleaning step has also been added in the hybrid-based system in Figure 2.2d, allowing the addition of a second powder type in the same layer once the initial powder type has solidified [15]. Other possible solutions [16] include the use of electrostatic powder deposition [17] and pneumatic pressure-assisted flow [18] although confirming the suitability of the techniques to multi-material printing are yet to be fully explored. Bandyopadhyay & Heer [19] added that high stresses could be induced at the interface if there is a considerable difference in the materials' thermal behavior. However, in some cases, the difference in chemical composition in the interface can also lead to superior mechanical properties by improving the interlocking mechanism between the materials and limiting the formation of possible brittle intermetallic precipitates. For instance, better mechanical properties were observed in an Inconel 718-316 stainless steel bimetallic fabricated using LPBF due to a diffused interface and microstructure in the interfacial region [20]. On the other hand, Binder et al. [21] and Nadimpalli et al. [22] also pointed out the challenge of separating and recycling each material mixed in the powder bed after fabrication. Processing the unused powder feedstock with a mixed material composition introduces a new economical challenge for MMAM using LPBF. In addition, Binder et al. [21] proposed the integration of electronic systems to detect process defects and control the product properties in-situ, but the technique is still a subject for future investigation.

2.2 Understanding 3D Printing: melt pool dynamics

LPBF involves complex interrelated physical phenomena including laser energy absorption and reflection, heat transfer, fluid dynamics, cyclic phase transformation, evaporation, and inherent chemical reactions. Understanding how they interact in the

microsecond and micrometer scales is vital for producing parts without defects and with intended mechanical properties [23]. Only a minor portion of the energy from laser beam is absorbed by the particle surface since photons are constantly being reflected. Therefore, the characteristics of both the laser and the powder significantly influence the formation and the shape of the LPBF melt pool [24].

In LPBF, factors such as surface tension-driven Marangoni convection and vaporization influence the melt dynamics and the formation of pores and spatter [23]. This can be triggered by variations in temperature or composition within the melt pool, leading to a flow that generally moves outward from the center, where temperatures are highest [25]. The Marangoni number (M_a) is a dimensionless measure used to assess the strength of this convective flow, calculated with the formula [24]:

$$M_a = -\frac{d\gamma}{dT}\frac{L\Delta T}{\mu\alpha} \quad [1]$$

where μ represents the dynamic viscosity, α is the thermal conductivity, L is the characteristic length of the melt pool, ΔT constitutes the difference between the maximum temperature with the material's solidus temperature, and $\frac{d\gamma}{dT}$ corresponds to the surface tension sensitivity with temperature. Increasing the melt temperatures can lead to vaporization of volatile elements, the phase transformation of which is accompanied by rapid material movement and expansion which generates recoil pressure. A higher recoil pressure leads to material expulsion and metallic jet formation while a lower recoil pressure leads to a flatter melt pool geometry [26].

After the laser melts the powder layer, the solidification behavior dictates the solute concentration, grain size, and component microstructure. Key factors to consider in the solidification front include the temperature gradient (G), solidification growth rate (R), the degree of undercooling ΔT, and raw material composition. As depicted in Figure 2.3, the solidification morphology is largely influenced by the interaction between G and R. The G/R ratio determines the shape of the solidification, whereas G*R reflects the size of the solidification structure [27]. An increase in the G/R ratio changes the morphology from equiaxed to dendritic, then to cellular, and finally to a planar structure [28]. As additional layers are added, grains grow in an epitaxial manner, adopting the texture of the layer

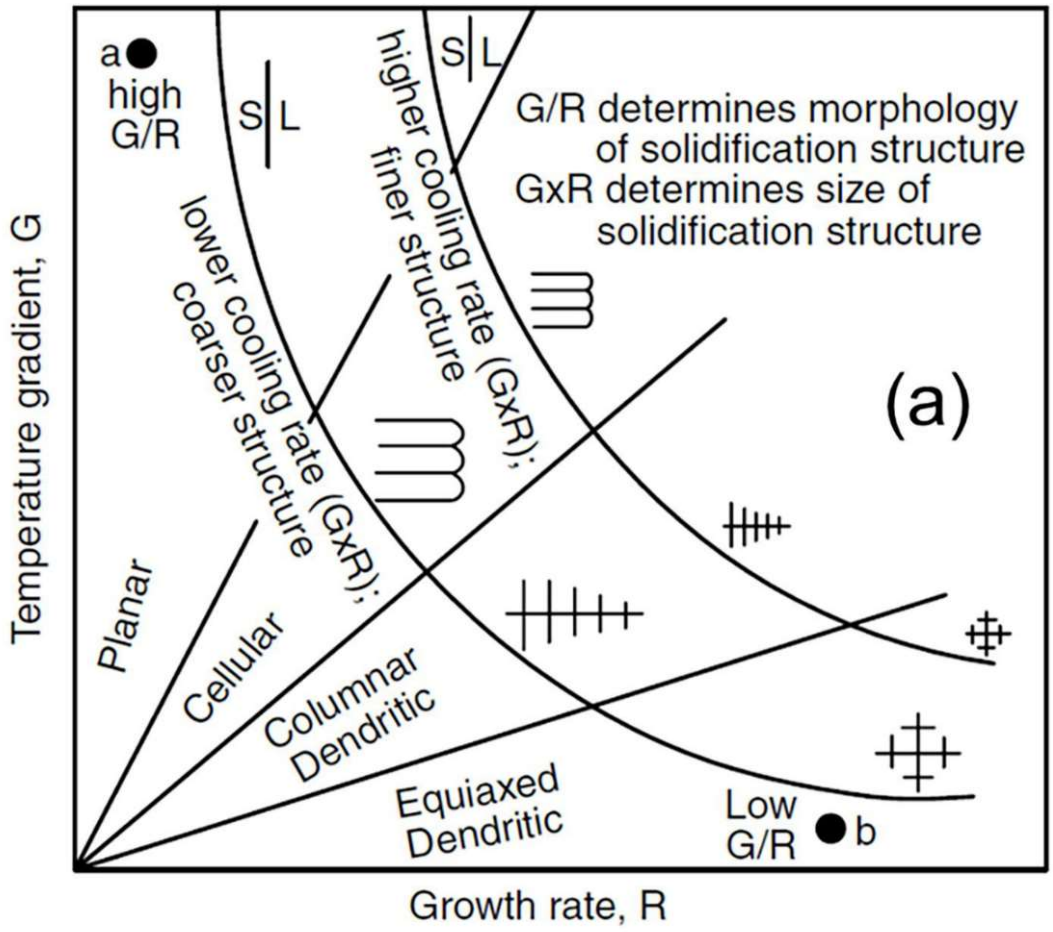


Figure 2.3. Influence of G and R to solidification front size and solidification morphology [27].

below. With changing compositions in multi-material structures, the interplay of textures wherein the characteristics of one alloy affect the next layer's morphology presents a fascinating area for study. Adjustments in the scan strategy, laser power, scan speed, hatch spacing, and layer thickness directly influence the final solidification pattern. Moreover, the unequal distribution of alloying elements, each with distinct liquidus and solidus temperatures, causes segregation within the melting pool, which undergoes repeated heating and cooling cycles.

2.3 Characterization spotlight: Electron Backscatter Diffraction (EBSD)

A significant portion of this thesis involves the analysis of Electron Backscatter Diffraction (EBSD) results. Components created through 3D printing are typically polycrystalline, consisting of grains that exhibit different crystallographic orientations. The process of 3D printing, characterized by directional solidification and the layer-by-layer construction, often results in a preferred orientation, or *texture*, within the material. The observed textures directly correlate with the mechanical properties and performance of the printed component.

Electron backscatter patterns emerge from the interaction between an electron beam and a properly tilted specimen, typically at ~70° from the horizontal. The incident beam, upon hitting the specimen, scatters elastically at large angles, causing electrons to spread out from a point just beneath the specimen's surface to strike the crystal planes from various directions. This scattering process forms patterns of Kikuchi cones whenever the electrons meet the Bragg condition. The generated Kikuchi patterns are distinct for all possible crystal structures and crystal lattice orientations [29].

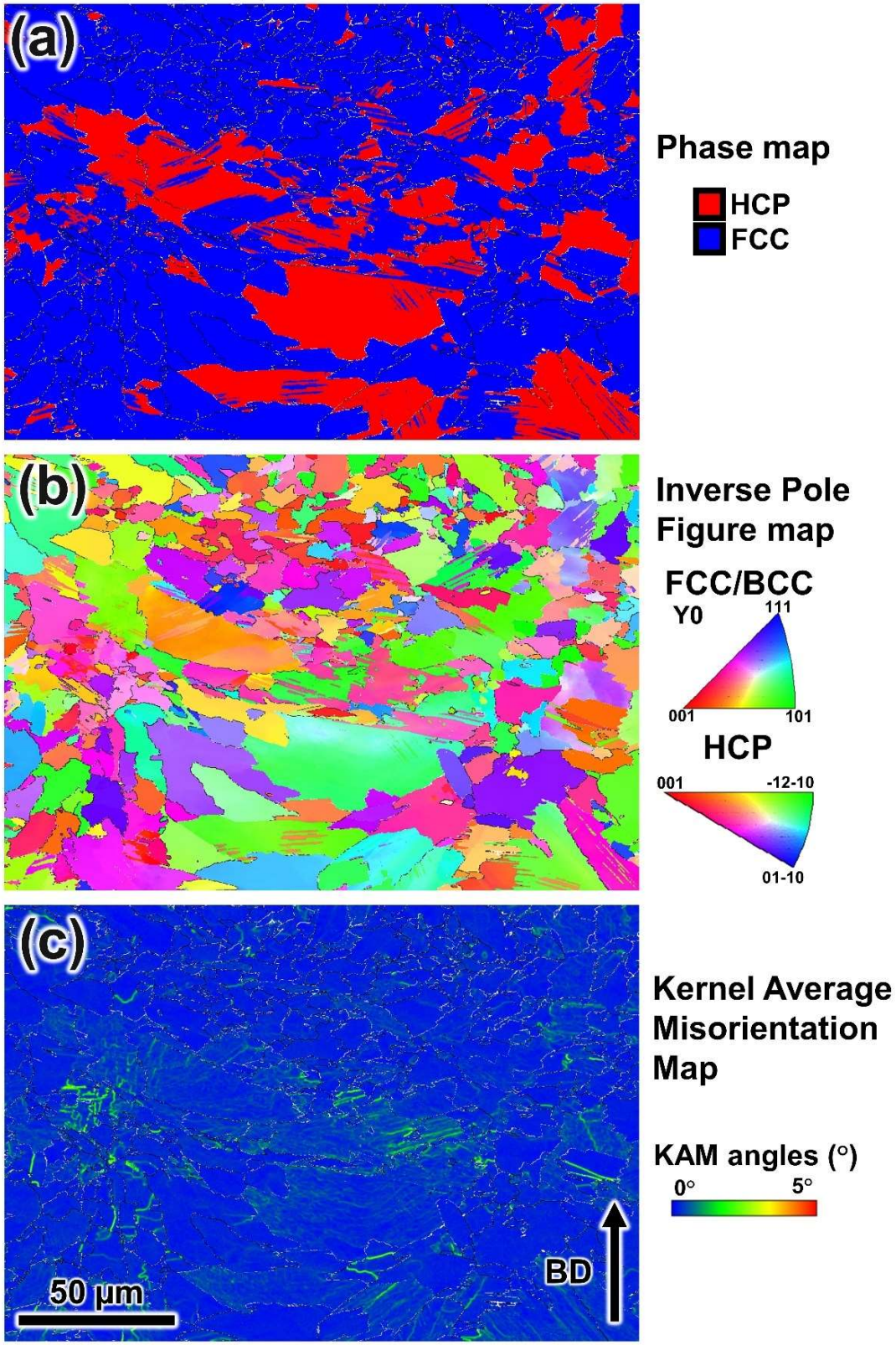


Figure 2.4. Typical maps obtained from EBSD analysis: (a) phase map, (b) inverse pole figure map, (c) kernel average misorientation map

Automated EBSD has revolutionized quantitative texture analysis due to its exceptional

spatial resolution, ability to analyze orientation relationships and stereology, fast processing speeds, and the capacity to visually display local textures and grain boundary characteristics through orientation mapping [30]. The results from EBSD analysis allow the characterization of grain orientations, phase identification, local misorientation, and strain distribution given a two-dimensional section of a material. When paired with microstructural results from Scanning Electron Microscope (SEM) and compositional analysis from Energy Dispersive Spectroscopy (EDS) analysis, a thorough understanding of the component's properties can be confidently obtained. As an example, Figure 2.4 illustrates three fundamental maps generated from EBSD analysis of a heat-treated CoCrMo alloy. Figure 2.4a shows the phase map wherein each phase is distinguished by referencing known lattice geometry of different crystal systems. Figure 2.4b shows the Inverse pole figure (IPF) color maps that colorize the crystallographic orientation of each pixel in every grain based on a reference coordinate system. For AM structures, the building direction is typically assigned as the reference direction. A preferred texture can be intuitively interpreted from the IPF maps when a specific color is more dominant (i.e., mostly green means <110> // BD is preferred). Figure 2.4c represents the Kernel average misorientation maps that emphasize small orientation changes within grains, which can be directly associated with the strain distribution within the microstructure.

2.4 Texture development during printing: orientation relations

Alloys in additive manufacturing experience rapid phase transformation transitions during the cyclic deposition and melting processes. These transitions yield a distinct crystallographic orientation for a 'parent' phase during melting at elevated temperatures and a corresponding 'child' phase after rapid solidification. In most cases, such transformations

are guided by an orientation relationship (OR) established between the parent and child phases. An OR refers to the specific geometric parallelism conditions between lattice planes and directions of parent-child crystal symmetries that are maintained by both phases relative to an invariant boundary [31]. The transformation from the parent to the child structure upon cooling naturally aims to reduce the strain energy in the system. Among various potential lattice changes during this transition, only a select few configurations meet the criteria for minimizing strain energy. This means that two associated phases can have a non-random distribution of orientation relationships [32]. The resulting child orientations, commonly known as *variants*, each possess equal chances of forming from a prior grain. The resulting configuration dilutes the parent texture for energy minimization.

The possible transformation pathways of austenite in steel, influenced by the type and concentration of alloying elements, process cooling rate, and austenite's initial condition (either strain free or deformed), include: (a) diffusion-driven transformation to polygonal ferrite or pearlite, (b) shear-driven transformation to martensite, or (c) a combination of diffusion and shear leading to acicular ferrite or bainite formation [33]. If the austenite displays an initial preferred texture, then the resulting phase (be it ferrite, martensite, acicular ferrite, or bainite) will likely inherit a texture closely related to that of the austenite [34]. In the context of maraging steels, the processing conditions have long been exploited to dictate the martensitic transformation process and define the mechanical attributes of the final product. The enhancement of mechanical strength is partially achieved through a Hall–Petch type effect, where refining the parent grains into smaller martensitic grains reduces the overall grain size of the alloy [35]. To characterize the transformation from the fcc-phase of austenite to its bcc-phase products, three predominant orientation

relationships are commonly employed [36]: The most straightforward relationship is the Bain relationship, which involves a 45° rotation around each of the three <100> austenite axes, resulting in three distinct orientations or variants for the transformed phase:

$$\{001\}_\gamma \parallel \{001\}_\alpha \, , < 100 >_\gamma \parallel < 110 >_\alpha$$

The Kurdjumov-Sachs (KS) relationship, which is characterized by 90° rotations around the 24 <112> austenite axes, yielding 24 potential variants, corresponds to the parallelism conditions:

$$\{111\}_\gamma \parallel \{110\}_\alpha \, , < 1\bar{1}0 >_\gamma \parallel < 1\bar{1}1 >_\alpha$$

Finally, the Nishiyama-Wassermann (N-W) relationship, defined by:

$$\{111\}_\gamma \parallel \{110\}_\alpha \, , < \bar{2}11 >_\gamma \parallel < 1\bar{1}0 >_\alpha$$

Each NW variant is near two K-S variants by only about 5.3° rotation about the [111] austenite direction, with each variant corresponding to 95.2° rotations about $<-1 + 2^{1/2} + 3^{1/2}, 1 + 2^{1/2} + 3^{1/2}, 2^{1/2}>$ axes [34]). The K-S relationship generally provides a closer match to the transformation texture of low-carbon steels compared to the N-W relationship, with the Bain relationship serving as an approximate model [36]. The most common orientation relationships observed in fcc-bcc systems and the corresponding number variants are summarized in Table 2.1[37].

Stereographic projection serves as a classical method to illustrate the angular relationships between different lattice planes and directions. It is particularly useful for mapping arbitrary lattice planes or directions from one crystal to another, especially in the context of illustrating ORs during phase transformation [37]. Using stereographic projection, all the variants of the ORs presented earlier can also be visualized on top of the pole figure of

the parent crystal. Figure 2.5 presents the projection of the {001} and {110} poles of the child bcc (α) phase onto the (111) plane of the parent fcc (γ) phase. As can be observed in Figure 2.5a, eight K-S and four N-W variants cluster around each of the three Bain variants. The Pitsch "spots" are identified by a simple 45º rotation about the <100> axes from the N-W positions, located between pairs of K-S reflections, similar to the N-W reflections. The locations of the Greninger-Troiano (G-T) reflections are particularly noteworthy. Positioned between pairs of K-S and N-W spots, and merely about 2.4º from K-S and 2.9º from N-W, which suggests the correlation of these variants to the other transformation mechanisms [38].

Table 2.1. Well-known orientation relationships between fcc and bcc structures [37].

OR	**Parallelism Conditions**	**No. of Variants**
Bain	$\{001\}_{\text{fcc}} \parallel \{001\}_{\text{bcc}}$ $\langle 100\rangle_{\text{fcc}} \parallel \langle 110\rangle_{\text{bcc}}$	3
Kurdjumov-Sachs (K-S)	$\{111\}_{\text{fcc}} \parallel \{110\}_{\text{bcc}}$ $\langle 110\rangle_{\text{fcc}} \parallel \langle 111\rangle_{\text{bcc}}$	24
Nishiyama-Wassermann (N-W)	$\{111\}_{\text{fcc}} \parallel \{110\}_{\text{bcc}}$ $\langle 112\rangle_{\text{fcc}} \parallel \langle 110\rangle_{\text{bcc}}$	12
Pitsch	$\{100\}_{\text{fcc}} \parallel \{011\}\text{bcc}$ $\langle 011\rangle_{\text{fcc}} \parallel \langle 111\rangle_{\text{bcc}}$	12
Greninger-Trioano (G-T)	$\{111\}_{\text{fcc}} \parallel \{110\}_{\text{bcc}}$ $\langle 5\ 12\ 17\rangle_{\text{fcc}} \parallel \langle 17\ 17\ 7\rangle_{\text{bcc}}$ or $\langle 123\rangle_{\text{fcc}} \parallel \langle 331\rangle_{\text{bcc}}$	24
He-Godet-Jonas (H-G-J)	$\{17\ 17\ 7\}_{\text{fcc}} \parallel \{5\ 12\ 17\}_{\text{bcc}}$ or $\{331\}_{\text{fcc}} \parallel \{123\}_{\text{bcc}}$ $\langle 110\rangle_{\text{fcc}} \parallel \langle 111\rangle_{\text{bcc}}$	24

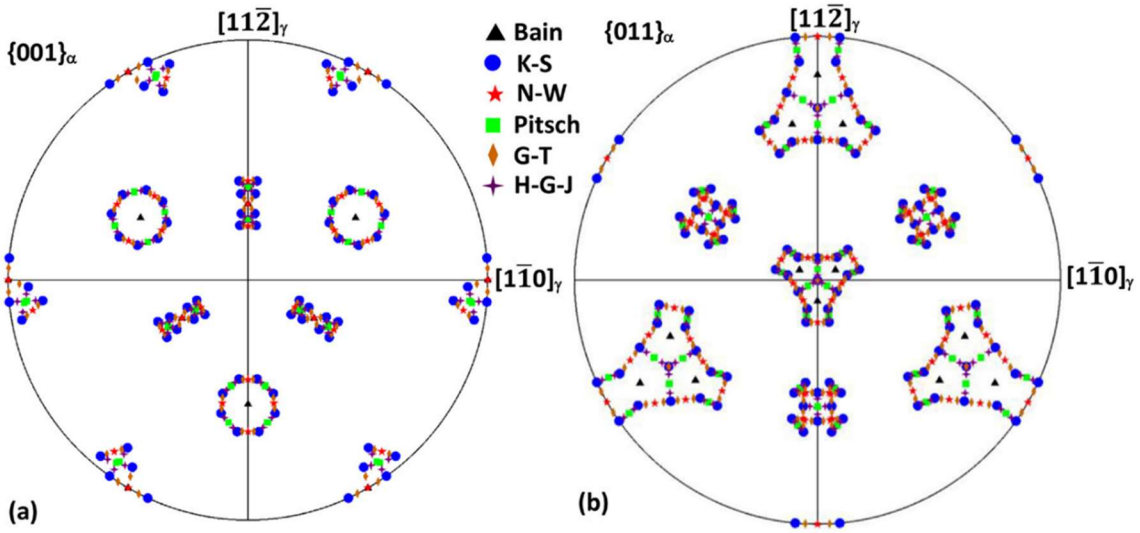


Figure 2.5. Stereographic projection of well-known fcc-bcc phase transformation ORs projected in the $(111)_\gamma$ corresponding to a) {001} bcc poles, b) {011} bcc poles [37].

However, not all variants are present in alloys with unique processing conditions, such as in AM components. A core contribution of this work is in directly providing grain-scale evidence of variant selection mechanisms in austenite-martensite structures from EBSD results without simulation. Various mechanisms have been provided by previous researchers in order to explain the preference of specific variants during unique thermomechanical processing conditions. These explanations can be broadly categorized into three schools of thought:

- The geometric configuration of deformed austenite grains or subgrains tends to promote the growth of variants into particular orientations [39].
- The interplay between transformation-induced strains and existing stresses (whether residual or externally applied) in the austenite grain facilitates the emergence of certain variants [39–41].
- The active slip systems within the austenite, particularly noting that the {111} slip planes and <110> slip directions align with the habit planes and directions

observed in the K-S orientation relationships, encourage the preferential nucleation of the new phase [42].

The study of texture transformation presents two main challenges. Initially, measuring the texture of the parent phase is often problematic due to its instability at room temperature, leading to its complete transformation into product phases. Additionally, accurately determining the orientation relationship between parent and product phases using X-ray techniques is difficult, as pole figures provide only a broad or statistical perspective of the relationship. The complexity of Euler space representation of the angle rotations, being non-linear, further complicates the analysis [36].

However, when both parent and child phases are retained in room temperature, and a sufficient quantitative analysis method such as EBSD can capture the individual orientations of each pixel, an in-depth analysis of the transformation history will be possible. The parent γ-phase retention located in the interface of the MMAM component in this study reveals a new avenue for phase transformation analysis. Variant distribution and local selection in additively manufactured maraging steels have been recently observed by Truong et al [43], but the analysis relied on full parent reconstruction due to the single phase matrix after solidification. Since retained γ-phase exists in the interface of the multi-material component in this study, the orientation of the parent and child grains can be directly correlated.

2.5 Material candidates for Dual-metal LPBF

Several factors should be considered in choosing the materials to be combined in MMAM. Difference in thermal properties will cause uneven melt pool temperature distribution and dissimilar heating and cooling rates, which can lead to defects such as warping,

delamination and cracks due to residual thermal stress accumulation, particularly in the interface. Difference in melting point and laser absorptivity will cause uneven melting and alloying segregation if the laser energy density is inadequate in melting some particles of the higher melting point material or excessive in evaporating some particles of the lower melting point material. The unmelted particles can further be trapped in the molten pool and cause stress concentration or introduce zones of weaknesses in the part. Special conditions such as liquid metal embrittlement should also be taken into consideration. Mixing and diffusion of alloys in the melt pool can cause formation of harmful intermetallic (IMC) compounds that can unpredictably modify the resulting mechanical properties in the interface [16].

2.5.1 Alloy Choice 1: Maraging Steels

One of the most investigated materials for LPBF is a class of iron-based alloys termed maraging (Martensite-aging) steel. Although LPBF employs high cooling rates during processing, maraging steels remain compatible due to its high resistance to cracking [44]. Maraging steels are commonly adopted due to their high strength and high fracture toughness, which originates from the formation of intermetallic compounds (Ni_3Ti, Ni_3Mo, Fe_2Mo, etc.) in a carbon-free martensite matrix during aging treatment [8]. The strengthening mechanism differs from most of the high strength steels that rely on the carbon content, and the lack of interstitial elements also results to excellent weldability of the maraging steel powder. Several aliases are used for the 18Ni(300) grade, such as MS1 by EOS, and X3NiCoMoTi18-9-5. Similar studies [45–48] produced maraging steels by LPBF, which achieved comparable or increased strength in contrast to the wrought counterparts. The main applications of maraging steels include aerospace, defense,

biomedical, and tooling, which further enhance the appeal of LPBF since the reduction in weight and freedom in design are critical parameters to such industries [49].

2.5.1.1 Heat treatment strategies

A standard heat treatment strategy applicable to maraging steels consists of a solution heat treatment followed by an aging heat treatment. Solution heat treatment involves exposure to high temperatures to relieve internal stress, redistribute alloying elements, and achieve a homogenous structure. On the other hand, aging heat treatment allows the reaction of specific alloying elements at a lower temperature to produce precipitates. The specific particles formed can then enhance the material strength by blocking crack movement. A typical heat treatment schedule for maraging steel involves solution treatment at 840 °C for 1 h and aging treatment at 480 °C for 6 h [45,50]. Aging treatment is usually performed between 450-600 °C since ordered and coherent precipitates form at temperatures below 450 °C [51]. Surface techniques such as nitriding, nitrocarburizing, boriding, plasma nitriding and carburizing can also improve the usable duration of maraging steels, especially when applied to plastic injection molds that require wear and corrosion resistance [6].

As-printed maraging steel samples typically exhibit overlapping coarse martensite plates with some retained austenite depending on the printing parameters such as the laser scanning direction, layer thickness, scan speed, hatch space, etc. Sufficient energy should be delivered to fully melt the maraging steel powder and fabricate fully dense parts [51]. On the other hand, samples after solution heat treatment contain a lath martensitic matrix without the solidification melt tracks [45]. Samples after solution and aging treatment also show refined acicular martensite microstructures without the subsequent laser tracks.

Nucleation and growth of precipitates typically occur during aging treatment, including the growth of intrinsically formed precipitates. Intermetallics that can potentially precipitate after age hardening and improve the mechanical properties of maraging steels were enumerated at [50] as η-Ni_3Ti, Fe_2Mo, Ni_3Mo, Ni_3Al, NiAl, Ni_3(Al, Ti), Ni_3(Ti, Mo), and Ni(Al, Fe). Atom Probe Tomography observations in the onset stages of aging show early clustering of Ti atoms [46]. Ni_3Ti is typically the first to nucleate during aging and could also act as nucleation sites for subsequent Ni_3Al and Ni_3Mo precipitation. Further aging can lead to formation of Fe_2Mo precipitates [50]. Significant austenite reversion occurs above 490 °C, where the cellular boundaries start to blur and austenite volume fraction increases.

Normally, the unique microstructure of LPBF fabricated parts allows direct aging without the need for a solution treatment, which is not the case for conventionally produced maraging steel parts [46]. However, the starting microstructure can usually be a non-homogenous martensitic matrix due to significant amount of austenite reversion during printing. Investigations also show additional martensite to austenite formation during aging [51]. Retained austenite forms when fast cooling rates prevent the transformation of solute-rich austenite from the austenite finish to the ambient temperature, while the solute depleted austenite becomes martensite [52]. Accordingly, solution treatment ensures that the resulting microstructure after aging treatment is completely martensitic.

2.5.1.2 Austenite reversion

If the aging treatment is extended beyond the recommended duration, over-aging can cause martensite decomposition and eventual reversion to austenite, resulting to deterioration of strength in the material. Dissolution of the metastable intermetallics that precipitated first

(Ni_3Mo and Ni_3Ti) is expected. Second stage precipitation of primarily Fe_2Mo and Fe_7Mo_6 occurs, which results to iron depletion and eventually Ni concentration [52]. Such solute interaction results to austenite reversion, which when combined with gradual precipitate coarsening or over-aging, results to a reduction of the mechanical strength. Higher temperatures augment the diffusion of solute elements, while lower temperatures allow suppression of austenite reversion and control of precipitate nucleation and growth. However, lowering the temperature can be economically restrictive as a significantly longer aging time is needed to attain peak strength from intermetallic precipitation. Furthermore, the decrease in strength due to austenite reversion is not always detrimental, as a compensation in ductility, toughness, and strain hardening can be achieved by transformation-induced plasticity or TRIP effect [53]. Interestingly, microstructural refinement can be promoted after isothermal treatments between 610-690 °C due to formation of intragranular austenite morphologies that are stable after cooling to room temperature. Austenite reversion can also increase grain boundaries that block movement of dislocations, leading to increased toughness of the heat-treated part.

2.5.2 Alloy choice 2: CoCrMo alloy

The interaction of high-power laser and incremental powder addition during L-PBF AM creates a cellular microstructure that enhances functional performance, which enables its use in a variety of sectors, e.g., biomedical, thermal, automotive, and structural. Examples of common AM materials include corrosion-resistant alloys such as stainless steel, titanium, nickel, and CoCr [54–56]. CoCr alloys, in particular, are commonly employed in mechanical contact applications such as aircraft engines, thermal barrier coatings, artificial joints, and surgical implants, due to their balanced mechanical properties, self-polishing

ability, biocompatibility, and resistance to corrosion and wear [57–59]. However, traditional methods of manufacturing CoCr alloy components, such as casting and powder metallurgy, suffer from the high costs associated with the design and manufacturing of the dies and the difficulties to rapidly change the designs. Additionally, the high hardness and wear resistance of these alloys make machining very challenging. CoCr alloys have also conventionally relied on long aging conditions of up to 10 hours to achieve phase transformation and discontinuous precipitation [58,60]. In contrast, the transformation mechanism of AM structures features solute segregation along cellular boundaries, enabling fast saturation and linear interface-controlled growth through thermally activated jumps across incoherent interphase interfaces with very short incubation times of approximately 0.25-0.5 hours [61].

The mechanical properties of Co-based alloys are largely influenced by the interaction of the microstructural elements, including twin structures, stacking faults, lattice dislocations, precipitates, and multi-phase boundaries. With the addition of a hierarchical structure and segregated alloying elements, the heat treatment of AM alloys triggers intricate transformation phenomena that require detailed study. The metastable γ-fcc phase of this alloy can be converted into a harder, more wear-resistant ε-phase (hcp) through a number of ways: athermal transformation by rapid quenching [62], low-temperature isothermal annealing [60], deformation-induced displacive mechanism [63], or short-range diffusion via massive transformation [64]. A solution heat treatment step above the fcc-hcp transformation temperature is usually first performed to recover the ductility, release the internal stresses, redistribute the alloying elements, dissolve the precipitates, and achieve a homogenous structure. A prolonged exposure to 1150 °C for 6 hours has been proven

successful in reducing residual stresses and eliminating anisotropic behavior for CoCrMo alloys produced using L-PBF, resulting in a fully recrystallized structure with equiaxed grains [65]. Various microstructural features, including low-energy coherent twins, solute clusters, grain boundaries, and ultrafine dendrites, can then serve as ε-phase embryos under specific heat treatment conditions. The subsequent growth is controlled by the local dislocations and the systematic arrangement of Shockley partials, as the transformation takes place by faulting along the fcc's most densely packed planes [66,67]. The nucleated ε-phase also displays the Shoji-Nishiyama orientation relationship [68] with the surrounding γ-phase grains and manifests as dense parallel bands that can eventually thicken and form complete grains.

The initial composition of the alloy also significantly influences the formation of the precipitates, their morphology, and the transformation kinetics under various heat treatment conditions. Carbon as a γ-phase stabilizing element, determines the presence of carbides, mitigates the precipitation of the σ-phase, and controls the extent of massive transformation [61]. The addition of Mo inhibits the precipitation of Cr-rich carbides and preserves the alloy's corrosion resistance [69]. Nitrogen inhibits the athermal martensitic transformation, and favors the creation of nanoscale Cr_2N precipitates within the γ matrix [70]. In traditional CoCrMo alloys, carbides tend to nucleate along intrinsic stacking faults and grain boundaries, increasing in percentage during aging conditions through growth along dislocations and forming lamellar structures [71]. However, in AM structures, cell boundaries have been observed as potential nucleation sites for carbides [72], Some researchers even reported needle-like morphologies [65] due to solute segregation along the heavily dislocated cell walls. Past studies have also reported the formation of σ-phase

in similar alloys with low carbon [73], embrittlement caused by M_6C and σ-phase [74], presence of low Cr laves phase [75], Si-enriched precipitates [76] and discontinuous precipitation of σ and $M_{23}C_6$ [77].

2.6 Chapter 2 References

[1] ISO/ASTM 52900, Standard Terminology for Additive Manufacturing – General Principles –Terminology, ASTM International, 2015.

[2] M. Rafiee, R.D. Farahani, D. Therriault, Multi-Material 3D and 4D Printing: A Survey, Advanced Science 7 (2020) 1902307. https://doi.org/10.1002/advs.201902307.

[3] C.F. Tey, X. Tan, S.L. Sing, W.Y. Yeong, Additive manufacturing of multiple materials by selective laser melting: Ti-alloy to stainless steel via a Cu-alloy interlayer, Additive Manufacturing 31 (2020) 100970. https://doi.org/10.1016/j.addma.2019.100970.

[4] Md.R.U. Ahsan, X. Fan, G.-J. Seo, C. Ji, M. Noakes, A. Nycz, P.K. Liaw, D.B. Kim, Microstructures and mechanical behavior of the bimetallic additively-manufactured structure (BAMS) of austenitic stainless steel and Inconel 625, Journal of Materials Science & Technology 74 (2021) 176–188. https://doi.org/10.1016/j.jmst.2020.10.001.

[5] J. Chen, Y. Yang, C. Song, M. Zhang, S. Wu, D. Wang, Interfacial microstructure and mechanical properties of 316L /CuSn10 multi-material bimetallic structure fabricated by selective laser melting, Materials Science and Engineering: A 752 (2019) 75–85. https://doi.org/10.1016/j.msea.2019.02.097.

[6] I. Hatos, I. Fekete, T. Ibriksz, J.G. Kovács, M.B. Maros, H. Hargitai, Surface modification and wear properties of direct metal laser sintered hybrid tools used in moulds, Journal of Mechanical Engineering 64 (2018) 121–129. https://doi.org/10.5545/sv-jme.2017.4942.

[7] M. Vaezi, S. Chianrabutra, B. Mellor, S. Yang, Multiple material additive manufacturing – Part 1: a review: This review paper covers a decade of research on multiple material additive manufacturing technologies which can produce complex geometry parts with different materials, Virtual and Physical Prototyping 8 (2013) 19–50. https://doi.org/10.1080/17452759.2013.778175.

[8] Y. Bai, C. Zhao, Y. Zhang, H. Wang, Microstructure and mechanical properties of additively manufactured multi-material component with maraging steel on CrMn steel, Materials Science and Engineering: A 802 (2021) 140630. https://doi.org/10.1016/j.msea.2020.140630.

[9] S.C. Ligon, R. Liska, J. Stampfl, M. Gurr, R. Mülhaupt, Polymers for 3D Printing and Customized Additive Manufacturing, Chem. Rev. 117 (2017) 10212–10290. https://doi.org/10.1021/acs.chemrev.7b00074.

[10] M. Zhang, Y. Yang, D. Wang, C. Song, J. Chen, Microstructure and mechanical properties of CuSn/18Ni300 bimetallic porous structures manufactured by selective laser melting, Materials & Design 165 (2019) 107583. https://doi.org/10.1016/j.matdes.2019.107583.

[11] Y. Kajima, A. Takaichi, N. Kittikundecha, T. Nakamoto, T. Kimura, N. Nomura, A. Kawasaki, T. Hanawa, H. Takahashi, N. Wakabayashi, Effect of heat-treatment temperature on microstructures and mechanical properties of Co–Cr–Mo alloys fabricated by selective laser melting, Materials Science and Engineering: A 726 (2018) 21–31. https://doi.org/10.1016/j.msea.2018.04.048.
[12] C. Wei, L. Li, Recent progress and scientific challenges in multi-material additive manufacturing via laser-based powder bed fusion, Virtual and Physical Prototyping 16 (2021) 347–371. https://doi.org/10.1080/17452759.2021.1928520.
[13] D.B. Pedersen, Additive Manufacturing: Multi Material Processing and Part Quality Control, Technical University of Denmark, Kgs. Lyngby, 2013.
[14] O.M. Al-Jamal, S. Hinduja, L. Li, Characteristics of the bond in Cu–H13 tool steel parts fabricated using SLM, CIRP Annals 57 (2008) 239–242. https://doi.org/10.1016/j.cirp.2008.03.010.
[15] K. Lappo, B. Jackson, K. Wood, D. Bourell, J. Beaman, Discrete multiple material selective laser sintering (M2SLS): Experimental study of part processing, 2003.
[16] C. Wei, Z. Zhang, D. Cheng, Z. Sun, M. Zhu, L. Li, An overview of laser-based multiple metallic material additive manufacturing: from macro- to micro-scales, Int. J. Extrem. Manuf. 3 (2020) 012003. https://doi.org/10.1088/2631-7990/abce04.
[17] M.J. Benning, K. Dalgarno, Proof of concept of a novel combined consolidation and transfer mechanism for electrophotographic 3D printing, Rapid Prototyping Journal 24 (2018) 1040–1048. https://doi.org/10.1108/RPJ-04-2018-0111.
[18] P. Kumar, J.K. Santosa, E. Beck, S. Das, Direct-write deposition of fine powders through miniature hopper-nozzles for multi-material solid freeform fabrication, Rapid Prototyping Journal 10 (2004) 14–23. https://doi.org/10.1108/13552540410512499.
[19] A. Bandyopadhyay, B. Heer, Additive manufacturing of multi-material structures, Materials Science and Engineering: R: Reports 129 (2018) 1–16. https://doi.org/10.1016/j.mser.2018.04.001.
[20] W.-Y. Chen, X. Zhang, M. Li, R. Xu, C. Zhao, T. Sun, Laser powder bed fusion of Inconel 718 on 316 stainless steel, Additive Manufacturing 36 (2020) 101500. https://doi.org/10.1016/j.addma.2020.101500.
[21] M. Binder, C. Anstaett, M. Horn, F. Herzer, G. Schlick, C. Seidel, J. Schilp, G. Reinhart, Potentials and challenges of multi-material processing by laser-based powder bed fusion, in: 2020: pp. 376–387.
[22] V.K. Nadimpalli, T. Dahmen, E.H. Valente, S. Mohanty, D.B. Pedersen, Multi-material additive manufacturing of steels using laser powder bed fusion, in: 2019: pp. 240–243.
[23] H. Gu, C. Wei, L. Li, Q. Han, R. Setchi, M. Ryan, Q. Li, Multi-physics modelling of molten pool development and track formation in multi-track, multi-layer and multi-material selective laser melting, International Journal of Heat and Mass Transfer 151 (2020). https://doi.org/10.1016/j.ijheatmasstransfer.2020.119458.
[24] S.L. Sing, S. Huang, G.D. Goh, G.L. Goh, C.F. Tey, J.H.K. Tan, W.Y. Yeong, Emerging metallic systems for additive manufacturing: *In-situ* alloying and multi-metal processing in laser powder bed fusion, Progress in Materials Science 119 (2021) 100795. https://doi.org/10.1016/j.pmatsci.2021.100795.

[25] L. Rongy, A. De Wit, Steady Marangoni flow traveling with chemical fronts, Journal of Chemical Physics 124 (2006). https://doi.org/10.1063/1.2186313.
[26] Y. Liu, Y. Yang, S. Mai, D. Wang, C. Song, Investigation into spatter behavior during selective laser melting of AISI 316L stainless steel powder, Materials & Design 87 (2015) 797–806. https://doi.org/10.1016/j.matdes.2015.08.086.
[27] T. DebRoy, H.L. Wei, J.S. Zuback, T. Mukherjee, J.W. Elmer, J.O. Milewski, A.M. Beese, A. Wilson-Heid, A. De, W. Zhang, Additive manufacturing of metallic components – Process, structure and properties, Progress in Materials Science 92 (2018) 112–224. https://doi.org/10.1016/j.pmatsci.2017.10.001.
[28] A. Basak, S. Das, Epitaxy and Microstructure Evolution in Metal Additive Manufacturing, Annual Review of Materials Research 46 (2016) 125–149. https://doi.org/10.1146/annurev-matsci-070115-031728.
[29] D.J. Dingley, V. Randle, Microtexture determination by electron back-scatter diffraction, J Mater Sci 27 (1992) 4545–4566. https://doi.org/10.1007/BF01165988.
[30] R.A. Schwarzer, D.P. Field, B.L. Adams, M. Kumar, A.J. Schwartz, Present State of Electron Backscatter Diffraction and Prospective Developments, in: A.J. Schwartz, M. Kumar, B.L. Adams, D.P. Field (Eds.), Electron Backscatter Diffraction in Materials Science, Springer US, Boston, MA, 2009: pp. 1–20. https://doi.org/10.1007/978-0-387-88136-2_1.
[31] H.K.D.H. Bhadeshia, Worked examples in the geometry of crystals / H.K.D.H. Bhadeshia., Institute of Metals, 1987.
[32] K.D. Zilnyk, D.R. Almeida Junior, H.R.Z. Sandim, P.R. Rios, D. Raabe, Misorientation distribution between martensite and austenite in Fe-31 wt%Ni-0.01 wt%C, Acta Materialia 143 (2018) 227–236. https://doi.org/10.1016/j.actamat.2017.10.026.
[33] C.J. Aranas, Dynamic transformation of austenite to ferrite above the Ae^3 temperature, (n.d.). https://escholarship.mcgill.ca/concern/theses/tx31qm527 (accessed March 30, 2024).
[34] R.K. Ray, J.J. Jonas, Transformation textures in steels, International Materials Reviews 35 (1990) 1–36. https://doi.org/10.1179/095066090790324046.
[35] F. Niessen, T. Nyyssönen, A.A. Gazder, R. Hielscher, Parent grain reconstruction from partially or fully transformed microstructures in MTEX, J Appl Cryst 55 (2022) 180–194. https://doi.org/10.1107/S1600576721011560.
[36] S. Godet, J.C. Glez, Y. He, J.J. Jonas, P.J. Jacques, Grain-scale characterization of transformation textures, J Appl Cryst 37 (2004) 417–425. https://doi.org/10.1107/S0021889804007320.
[37] Y. He, Stereographic Projection of Theoretical Orientation Relationships Between Crystals of Any Types in Phase Transformation and Precipitation, Crystal Research and Technology 59 (2024) 2300242. https://doi.org/10.1002/crat.202300242.
[38] J.J. Jonas, Y. He, S. Godet, Representation of misorientations in Rodrigues-Frank space: Application to the bain, Kurdjumov-Sachs, Nishiyama-Wassermann, Pitsch and Greninger-Troiano orientation relationships, Materials Science Forum 495–497 (2005) 1177–1182. https://doi.org/10.4028/0-87849-975-x.1177.
[39] M.P. Butrón-Guillén, C.S. Da Costa Viana, J.J. Jonas, A variant selection model for predicting the transformation texture of deformed austenite, Metall Mater Trans A 28 (1997) 1755–1768. https://doi.org/10.1007/s11661-997-0107-5.

[40] M. Humbert, F. Wagner, C. Esling, Numbering the crystallographic variants in phase transformation, J Appl Cryst 25 (1992) 724–730. https://doi.org/10.1107/S0021889892005375.
[41] P. Bate, B. Hutchinson, The effect of elastic interactions between displacive transformations on textures in steels, Acta Materialia 48 (2000) 3183–3192. https://doi.org/10.1016/S1359-6454(00)00106-3.
[42] Y.L. He, S. Godet, P.J. Jacques, J.J. Jonas, Crystallographic Relationships between FCC and BCC Crystals: A Study Using EBSD Techniques, Solid State Phenomena 105 (2005) 121–126. https://doi.org/10.4028/www.scientific.net/SSP.105.121.
[43] T.D. Truong, G. Asala, O.T. Ola, O.A. Ojo, A.G. Odeshi, Effects of process parameters and loading direction on the impact strength of additively manufactured 18%Ni-M350 maraging steel under dynamic impact loading, Materials Science and Engineering: A 874 (2023) 145074. https://doi.org/10.1016/j.msea.2023.145074.
[44] Y. Tian, R. Palad, C. Aranas, Microstructural evolution and mechanical properties of a newly designed steel fabricated by laser powder bed fusion, Additive Manufacturing 36 (2020) 101495. https://doi.org/10.1016/j.addma.2020.101495.
[45] Y. Bai, Y. Yang, D. Wang, M. Zhang, Influence mechanism of parameters process and mechanical properties evolution mechanism of maraging steel 300 by selective laser melting, Materials Science and Engineering: A 703 (2017) 116–123. https://doi.org/10.1016/j.msea.2017.06.033.
[46] E. Jägle, Z. Sheng, P. Kürnsteiner, S. Ocylok, A. Weisheit, D. Raabe, Comparison of Maraging Steel Micro- and Nanostructure Produced Conventionally and by Laser Additive Manufacturing, Materials 10 (2016) 8. https://doi.org/10.3390/ma10010008.
[47] C. Tan, K. Zhou, W. Ma, L. Min, Interfacial characteristic and mechanical performance of maraging steel-copper functional bimetal produced by selective laser melting based hybrid manufacture, Materials & Design 155 (2018) 77–85. https://doi.org/10.1016/j.matdes.2018.05.064.
[48] S. Yin, C. Chen, X. Yan, X. Feng, R. Jenkins, P. O'Reilly, M. Liu, H. Li, R. Lupoi, The influence of aging temperature and aging time on the mechanical and tribological properties of selective laser melted maraging 18Ni-300 steel, Additive Manufacturing 22 (2018) 592–600. https://doi.org/10.1016/j.addma.2018.06.005.
[49] T.C. Henry, F.R. Phillips, D.P. Cole, E. Garboczi, R.A. Haynes, T. Johnson, In situ fatigue monitoring investigation of additively manufactured maraging steel, International Journal of Advanced Manufacturing Technology 107 (2020) 3499–3510. https://doi.org/10.1007/s00170-020-05255-4.
[50] C. Tan, K. Zhou, W. Ma, P. Zhang, M. Liu, T. Kuang, Microstructural evolution, nanoprecipitation behavior and mechanical properties of selective laser melted high-performance grade 300 maraging steel, Materials & Design 134 (2017) 23–34. https://doi.org/10.1016/j.matdes.2017.08.026.
[51] J. Mutua, S. Nakata, T. Onda, Z.-C. Chen, Optimization of selective laser melting parameters and influence of post heat treatment on microstructure and mechanical properties of maraging steel, Materials & Design 139 (2018) 486–497. https://doi.org/10.1016/j.matdes.2017.11.042.
[52] B. Mooney, K.I. Kourousis, R. Raghavendra, Plastic anisotropy of additively manufactured maraging steel: Influence of the build orientation and heat treatments,

Additive Manufacturing 25 (2019) 19–31. https://doi.org/10.1016/j.addma.2018.10.032.
[53] F.F. Conde, J.D. Escobar, J.P. Oliveira, A.L. Jardini, W.W. Bose Filho, J.A. Avila, Austenite reversion kinetics and stability during tempering of an additively manufactured maraging 300 steel, Additive Manufacturing 29 (2019) 100804. https://doi.org/10.1016/j.addma.2019.100804.
[54] A. du Plessis, S.M.J. Razavi, M. Benedetti, S. Murchio, M. Leary, M. Watson, D. Bhate, F. Berto, Properties and applications of additively manufactured metallic cellular materials: A review, Progress in Materials Science 125 (2022) 100918. https://doi.org/10.1016/j.pmatsci.2021.100918.
[55] M. Godec, S. Zaefferer, B. Podgornik, M. Šinko, E. Tchernychova, Quantitative multiscale correlative microstructure analysis of additive manufacturing of stainless steel 316L processed by selective laser melting, Materials Characterization 160 (2020) 110074. https://doi.org/10.1016/j.matchar.2019.110074.
[56] S. Gribbin, S. Ghorbanpour, N.C. Ferreri, J. Bicknell, I. Tsukrov, M. Knezevic, Role of grain structure, grain boundaries, crystallographic texture, precipitates, and porosity on fatigue behavior of Inconel 718 at room and elevated temperatures, Materials Characterization 149 (2019) 184–197. https://doi.org/10.1016/j.matchar.2019.01.028.
[57] B. Konieczny, A. Szczesio-Wlodarczyk, J. Sokolowski, K. Bociong, Challenges of Co–Cr Alloy Additive Manufacturing Methods in Dentistry—The Current State of Knowledge (Systematic Review), Materials 13 (2020) 3524. https://doi.org/10.3390/ma13163524.
[58] S. Kurosu, H. Matsumoto, A. Chiba, Isothermal Phase Transformation in Biomedical Co-29Cr-6Mo Alloy without Addition of Carbon or Nitrogen, Metall Mater Trans A 41 (2010) 2613–2625. https://doi.org/10.1007/s11661-010-0273-8.
[59] X. Dong, Y. Zhou, Y. Qu, M. Wu, Q. Sun, H. Shi, H. Peng, Y. Zhang, S. Xu, N. Li, J. Yan, Recrystallization behavior and grain boundary character evolution in Co-Cr alloy from selective laser melting to heat treatment, Materials Characterization 185 (2022) 111716. https://doi.org/10.1016/j.matchar.2021.111716.
[60] M. Mori, K. Yamanaka, A. Chiba, Phase decomposition in biomedical Co–29Cr–6Mo–0.2N alloy during isothermal heat treatment at 1073K, Journal of Alloys and Compounds 590 (2014) 411–416. https://doi.org/10.1016/j.jallcom.2013.12.126.
[61] B.T. Donkor, J. Song, Y. Fu, M. Kattoura, S.R. Mannava, M.A. Steiner, V.K. Vasudevan, Accelerated γ-face-centered cubic to ε-hexagonal close packed massive transformation in a laser powder bed fusion additively manufactured Co-29Cr-5Mo alloy, Scripta Materialia 179 (2020) 65–69. https://doi.org/10.1016/j.scriptamat.2020.01.012.
[62] K. Yamanaka, M. Mori, Y. Koizumi, A. Chiba, Local strain evolution due to athermal γ→ε martensitic transformation in biomedical CoCrMo alloys, Journal of the Mechanical Behavior of Biomedical Materials 32 (2014) 52–61. https://doi.org/10.1016/j.jmbbm.2013.12.019.
[63] L.H.M. Antunes, M. Béreš, J.J. Hoyos, L. Novotný, H.F.G. de Abreu, P.F. da Silva Farina, Kinetics of FCC to HCP Transformation During Aging Heat Treatment of Co–28Cr–6Mo Alloy Fabricated by Laser-Powder Bed Fusion, Metall Mater Trans A (2023). https://doi.org/10.1007/s11661-023-07016-w.

[64] M. Roudnická, J. Kubásek, L. Pantělejev, O. Molnárová, J. Bigas, J. Drahokoupil, D. Paloušek, D. Vojtěch, Heat treatment of laser powder-bed-fused Co–28Cr–6Mo alloy to remove its microstructural instability by massive FCC→HCP transformation, Additive Manufacturing 47 (2021) 102265. https://doi.org/10.1016/j.addma.2021.102265.
[65] A. Takaichi, Y. Kajima, N. Kittikundecha, H.L. Htat, H.H. Wai Cho, T. Hanawa, T. Yoneyama, N. Wakabayashi, Effect of heat treatment on the anisotropic microstructural and mechanical properties of Co–Cr–Mo alloys produced by selective laser melting, Journal of the Mechanical Behavior of Biomedical Materials 102 (2020) 103496. https://doi.org/10.1016/j.jmbbm.2019.103496.
[66] N.C. Dahn, D. Morphy, K. Rajan, Kinetics of the martensitic f.c.c.→ h.c.p. transformation in CoCrMo alloy powders, Acta Metallurgica 32 (1984) 1317–1322. https://doi.org/10.1016/0001-6160(84)90077-4.
[67] G.B. Olson, M. Cohen, A general mechanism of martensitic nucleation: Part I. General concepts and the FCC → HCP transformation, Metall Mater Trans A 7 (1976) 1897–1904. https://doi.org/10.1007/BF02659822.
[68] M.E. Fine, M. Meshii, C.M. Wayman, Z. Nishiyama, eds., MATERIALS SCIENCE AND TECHNOLOGY, in: Martensitic Transformation, Academic Press, 1978: p. ii. https://doi.org/10.1016/B978-0-12-519850-9.50001-6.
[69] W.Q. Toh, X. Tan, A. Bhowmik, E. Liu, S.B. Tor, Tribochemical Characterization and Tribocorrosive Behavior of CoCrMo Alloys: A Review, Materials 11 (2018) 30. https://doi.org/10.3390/ma11010030.
[70] K. Yamanaka, M. Mori, A. Chiba, Nanoarchitectured Co–Cr–Mo orthopedic implant alloys: Nitrogen-enhanced nanostructural evolution and its effect on phase stability, Acta Biomaterialia 9 (2013) 6259–6267. https://doi.org/10.1016/j.actbio.2012.12.013.
[71] R.N.J. Taylor, R.B. Waterhouse, A study of the ageing behaviour of a cobalt based implant alloy, J Mater Sci 18 (1983) 3265–3280. https://doi.org/10.1007/BF00544151.
[72] M. Zhang, Y. Yang, C. Song, Y. Bai, Z. Xiao, An investigation into the aging behavior of CoCrMo alloys fabricated by selective laser melting, Journal of Alloys and Compounds 750 (2018) 878–886. https://doi.org/10.1016/j.jallcom.2018.04.054.
[73] M. Roudnická, O. Molnárová, J. Drahokoupil, J. Kubásek, J. Bigas, V. Šreibr, D. Paloušek, D. Vojtěch, Microstructural instability of L-PBF Co-28Cr-6Mo alloy at elevated temperatures, Additive Manufacturing 44 (2021) 102025. https://doi.org/10.1016/j.addma.2021.102025.
[74] K. Yamanaka, M. Mori, Y. Torita, A. Chiba, Impact of minor alloying with C and Si on the precipitation behavior and mechanical properties of N-doped Co–Cr alloy dental castings, Materials Science and Engineering: C 92 (2018) 112–120. https://doi.org/10.1016/j.msec.2018.06.035.
[75] H. Li, M. Wang, D. Lou, W. Xia, X. Fang, Microstructural features of biomedical cobalt–chromium–molybdenum (CoCrMo) alloy from powder bed fusion to aging heat treatment, Journal of Materials Science & Technology 45 (2020) 146–156. https://doi.org/10.1016/j.jmst.2019.11.031.
[76] K.K. Bawane, D. Srinivasan, D. Banerjee, Microstructural Evolution and Mechanical Properties of Direct Metal Laser-Sintered (DMLS) CoCrMo After Heat Treatment,

Metallurgical and Materials Transactions A: Physical Metallurgy and Materials Science 49 (2018) 3793–3811. https://doi.org/10.1007/s11661-018-4771-4.
[77] L.E. Ramírez, M. Castro, M. Méndez, J. Lacaze, M. Herrera, G. Lesoult, Precipitation path of secondary phases during solidification of the Co–25.5%Cr–5.5%Mo–0.26%C alloy, Scripta Materialia 47 (2002) 811–816. https://doi.org/10.1016/S1359-6462(02)00305-6.

Chapter 3: Combined 3D-printing

Background

The rise of additive manufacturing is taking a fascinating turn with the exploration of multi-material structures, particularly on how these materials blend at thin boundaries. The unique ways in which elements from different powders distribute and segregate themselves during 3D printing mean that when combining two different, but complementary, alloys, the process of how they solidify together at their joining points will be remarkably complex. This complexity allows the creation of new kinds of components that not only fit together surprisingly well but also exhibit desirable characteristics for end-products with multiple applications.

Moreover, after these multi-material components are printed, there's a crucial step of heat treatment to ensure the interfaces between different phases remain stable, thereby achieving the desired characteristics across the entire structure. This chapter investigates the effects of applying combined heat treatments—namely solution treatment and aging—in a newly made combination of 18Ni(300) maraging steel and CoCrMo alloy, all through laser powder bed fusion. Some of the novel concepts presented in this chapter are:

- No previous studies have utilized a single printing strategy to fabricate a maraging steel and CoCrMo alloy combination, and there have only been a few works exploring multi-material printing using laser powder bed fusion.
- Even less is known about how heat treatment influences the overall properties of additively manufactured multi-material components, particularly one with alloys that require different temperatures for phase transformation.

- Following the printing of these composite components, an uncommon pattern of martensitic transformation for maraging steel occurs at the interface. This chapter presents thermodynamic simulations that aim to explain the transformation history of the observed interfacial microstructure.
- This chapter reveals how to achieve microstructural stability with a targeted solution and aging heat treatment, interpreting the changes based on microstructure, phase boundary orientation relationships, composition distribution and material properties obtained along the interface.

This section has been published: J. Pasco, Y. Tian, K. Chadha, L. Jiang, T. Dorin, C. Aranas Jr, Unusual interface phase transformation during continuous additive manufacturing of maraging steel and Co–30Cr–7Mo alloy, Mater. Sci. Eng. A 881 (2023) 145336.

Abstract

The high strength and hardness of maraging steel can be functionally integrated with the thermal stability and toughness of CoCrMo alloy through multi-material additive manufacturing via laser powder bed fusion. However, appropriate heat treatment is necessary to stabilize the multi-phase interface after printing and achieve desired material properties. In the present study, we investigate the effects of solution and aging heat treatment on the interface characteristics and mechanical properties of maraging steel-CoCrMo multi-material components. The results reveal that a discontinuous martensitic transformation occurs in the interface after printing due to the combined effects of solute segregation, local stress distribution, and intermixed cellular growth. In contrast, consistent parallel martensite laths were observed after heat treatment due to the homogenized alloying element distribution, extensive residual stress relief and stable interface structure. Furthermore, the mechanical testing results revealed that the tensile strength of the maraging steel-CoCrMo alloy was maintained at about 1185 ± 18 MPa before and after heat treatment, complemented by an increase in elongation from 14.7 ± 1.3 % to 27.1 ± 2.1 %. The microstructure and mechanical properties obtained are then correlated based on phase boundary orientation relationships and simulated martensite start temperatures in different regions along the interface. Based on overall results, it can be concluded that the CoCrMo alloy forms a compatible interface with maraging steel. Heat treatment can still be performed to improve the strength of maraging steel by precipitation strengthening without compromising the strength of CoCrMo alloy and the interface.

3.1 Introduction

Designing hybrid components with spatially varying compositions and distributed functional properties is now possible through multi-material additive manufacturing (AM). Innovative techniques such as layer path planning [1], brittle phase prevention through machine learning [2], and molten pool multi-physics modelling [3] can lead to efficient and cost-effective end-use parts. Laser-based powder bed fusion (L-PBF) is one of the metal AM technologies that applies a laser system to selectively melt and bond successive layers of feed powder based on a sliced computer-aided design (CAD) model of the desired final product [4]. Process modifications on feed delivery systems [5] and recycling mechanisms [6] are being developed to utilize L-PBF in the fabrication of multi-material parts.

The current study is focused on incorporating the material combination of iron-based maraging steel and cobalt-based CoCrMo alloy to provide an optimal balance of resistance to deformation, fracture, and heat, which are critical properties in many engineering applications. Maraging steels (MS1 in powder form) are a class of precipitation-strengthened steels with considerable nickel alloying in a carbon-free martensite matrix. By selectively using the more expensive CoCrMo alloy only where its unique properties (e.g., thermal stability) are needed, and using the generally cheaper maraging steel elsewhere, it could be possible to optimize cost efficiency in production. Maraging steels are commonly adopted due to their high strength, high fracture toughness, sound dimensional stability, and good resistance to cracking during AM [7]. The strengthening mechanism relies on the formation of Fe, Ti, Ni, Al, and Mo intermetallic compounds after aging heat treatment [8], and the lack of interstitial elements also results in excellent

weldability of the maraging steel powder [9]. Maraging steels are extensively used in specialty vehicles, military, aerospace, and tooling applications which further enhance the appeal of L-PBF since the reduction in weight and freedom in design are critical parameters to such industries [10]. In the same way, CoCrMo alloys also offer a good combination of mechanical properties, wear resistance, and biocompatibility that is useful in the medical, aerospace, and gas turbine hardware industries [11]. Common components manufactured using CoCrMo alloys include orthopedic implants, prostheses, fuel nozzles, and aircraft engines [12,13]. Several studies have also explored the feasibility of using CoCrMo alloys as a functionally-graded surface coating for a Ti–6Al–4V substrate [14], an Inconel 718 substrate [5], and a 316L stainless steel laser-clad joint [15] using other deposition methods.

After the fabrication of MMAM structures, these final components generally undergo heat treatment procedures. The post-processing stage is crucial for modulating specific characteristics such as homogenization of the microstructure, relief of internal stresses, enhancement of mechanical properties, reduction of porosity, and control of phase distribution. However, implementing conventional heat treatment strategies will not necessarily translate to identical mechanical properties in MMAM components due to the inherent heterogeneous structure developed by the solidification process. Furthermore, managing the final property of each alloy in a multi-material component after heat treatment introduces another strategic obstacle since each composition can react differently to every processing step applied. For maraging steels, the influence of multiple factors such as printing parameters [16], build orientation [17], solution heat treatment [9], age-hardening precipitates [18], and reverted austenite transformation [19] to the resulting

mechanical properties have been investigated. Similarly, Roudnicka et al. [20] identified that current research in CoCrMo alloys has primarily focused on either optimizing the print settings [21], determining the mechanical properties [22], or examining the effects of heat treatment [23].

Due to the need to explore the potential applications of multi-material additive manufacturing, the present work employs two different powders (maraging steel and CoCrMo alloy) to fabricate a multi-material component through the L-PBF process. The primary goal of combining the desirable mechanical attributes of these materials is for applications in tooling and mold-making. Dies, cutting tools, and mold machinery undergo heavy usage and must endure high temperatures while maintaining toughness. Following successful heat treatment, these materials can further meet specific mechanical standards, extending their potential use. They can be utilized in the automotive sector for crafting high-performance transmission and engine components which require durability and stress-resistance, or defense components such as artillery systems that can benefit from increased resilience and longevity under harsh operational conditions. The continuous printing of this material combination using L-PBF has not been explored by other researchers, but the two alloys exhibit similar properties and good mutual solubility. A preliminary study was also performed by the present authors [24]; however, the integrity of the interface and the effect of heat treatment are not yet established. Studies that explore the overall effect of heat treatment on multi-material AM structures are also limited. Therefore, due to the shortcomings of the available literature, the scope of the current work is to establish the characteristic microstructure, microhardness, chemical distribution, mechanical properties, and fracture surfaces of the interface section of the multi-material

system. The underlying mechanism during solidification will then be investigated and compared to the features observed after heat treatment. The overall compatibility of the heat-treatment strategy to the multi-material combination is assessed.

3.2 Materials and Methods

3.2.1 Material

The multi-material AM structure under investigation was procured from voestalpine Additive Manufacturing Center Ltd. (vAMC) based in Mississauga, Ontario, Canada. The AM structure was derived from gas atomized MS1 (maraging steel) and MP1 (CoCrMo alloy) powders, each having a particle size ranging from 15 to 70 μm. The L-PBF process was performed with an EOS M290 machine. The powders' chemical composition was verified through Inductively Coupled Plasma - Optical Emission Spectroscopy (ICP-OES) for bulk analysis of the major and minor alloying elements, and the results are presented in Table 3.1. The fabrication process for the multi-material component, as depicted in Figure 3.1. a, involves initially loading equal volumes of MS1 and MP1 into the feed delivery system. As the powder recoater dispenses the first layers, the MP1 powder is deposited and subsequently melted. Once the predetermined volume for MP1 is reached, the feed powder is switched to MS1, maintaining consistent printing conditions throughout. This procedure results in the final component consisting of equal volumes of both alloys. The laser power was consistently held between 280-300 W, and the laser speed was fixed at 1100 mm/s. The chosen hatching style was a zigzag stripe pattern with a 50° rotation in each subsequent layer, with the target layer thickness set to 50 μm. The hatch distance was sustained between 0.09 and 0.11 mm. These conditions were preserved as the feed powder was switched from MP1 to MS1 (see Figure 3.1. b and Figure 3.1. c). To mitigate oxidation,

the entire manufacturing process was conducted under an argon atmosphere. High precision cutting techniques were employed to generate representative cubic specimens with 10 mm sides and cylindrical specimens with diameters and lengths of 4 mm and 16 mm, respectively. All specimens should contain the MS1-MP1 interface in the middle.

Table 3.1. Composition analysis of base alloys (in wt. %)

Powder	Fe	Ni	Co	Cr	Mo	C	Si	Mn	Ti
MS1	66.27	17.9	9.4	-	4.8	0.03	0.15	0.15	1.3
MP1	0.6	0.1	60.44	29.7	7.2	0.16	0.7	1.1	-

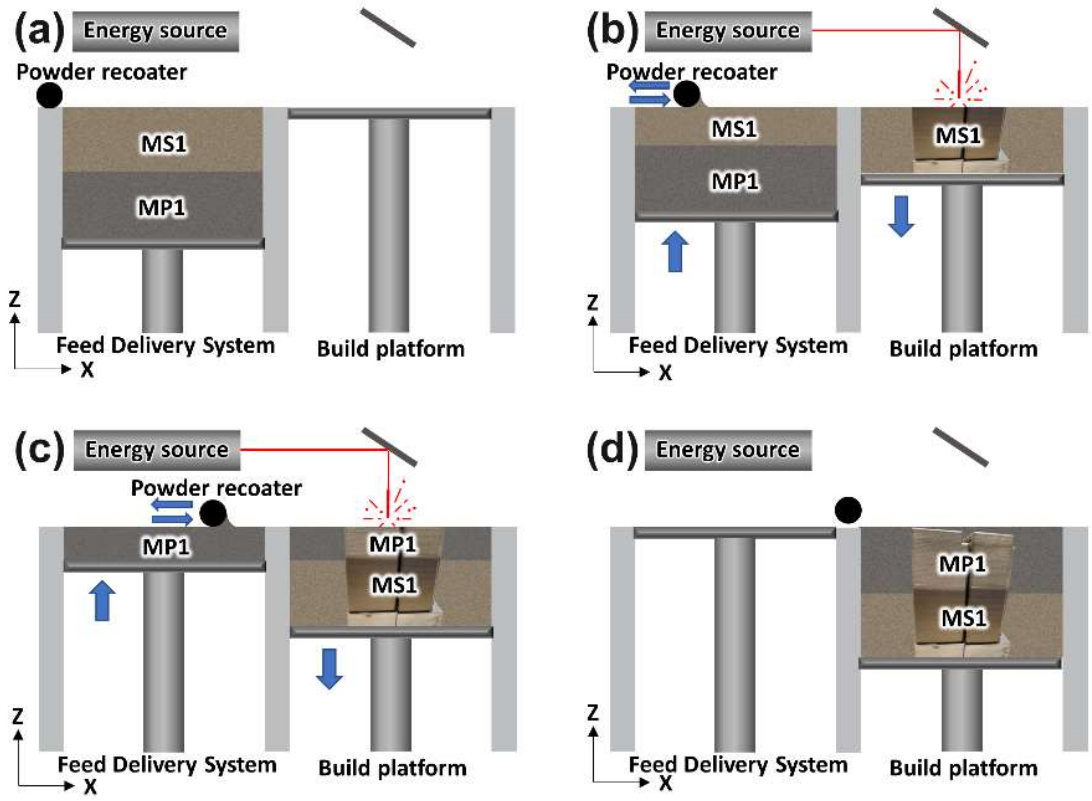


Figure 3.1. The figure illustrates key phases in the multi-material L-PBF process: (a) Initial stacking of MS1 (maraging steel) powder over MP1 (CoCrMo alloy) powder, (b) Successive layers of MS1 material are solidified under laser interaction, (c) As the procedure progresses, the fused material transitions to MP1, and finally (d) The desired configuration of the dual-metal MP1-MS1 structure is achieved.

3.2.2 Heat Treatment

The dual-metal component underwent combined solution and aging heat treatments in a vacuum tube furnace, maintaining a pressure of 10^{-5} bar. Drawing on differential scanning calorimetry results from [25], an endothermic peak at 1139 °C linked to precipitate dissolution was identified for the CoCrMo alloy. Consequently, the samples were subjected to solution annealing at 1147 °C for 6 hours, with a heating rate of 2 °C/s. The step was designed for an overall reduction of residual stresses present after printing and a slight recovery of ductility in CoCrMo, while also acting as a solution heat treatment at a slightly higher temperature for maraging steel. Following this, the samples undergo an aging heat treatment, which involves subjecting them to a temperature of 490 °C for a duration of 6 hours at an equivalent rate of heating and cooling. According to supplier specifications and other studies [26,27], a 6-hour duration suffices for maraging steel precipitate formation. This treatment is likely to have a minimal impact on the CoCrMo region since the γ- ε phase transformation typically occurs post-isothermal heat treatment at 700 – 950 °C [28]. The samples were then quenched using compressed nitrogen gas with 5-6 bar to room temperature after each condition.

3.2.3 Materials Characterization

To examine the effects of heat treatment on the L-PBF samples, microstructural changes were observed using optical (OM) and scanning electron (SEM) microscopes. Samples that include the interface were sectioned parallel to the building direction and processed through a series of mechanical grinding and polishing operations. The relative density of the dual-metal component was measured from 10 micrographs across the interface using a Zeta Instruments optical microscope. This analysis included 4 images captured at a lower

magnification of 50x, covering an observation area of 1.2 x 0.9 mm, and 6 images obtained at a higher magnification of 200x, covering an observation area of 0.3 x 0.25 mm. The selected sections were randomly chosen and spaced at least 1 mm apart. Afterwards, the ImageJ software was employed, utilizing the threshold function to measure the percentage area of porosity in the micrographs.

To reveal the microstructure in the maraging steel region, as-built and heat-treated samples were electrochemically etched using an ammonium persulfate solution at 6 V for 10 s. For the CoCrMo region, as-built samples were electrochemically etched in a 10% H_2SO_4 and CH_3OH solution at 6V for 25 s at room temperature. For heat-treated samples, electrochemical etching in 9% HCl was applied at 4 V for 10 s [29]. Cellular and martensitic structures were captured using a JEOL JSM-6010/LA SEM equipped with an energy dispersive spectrometer analyzer. To determine the distribution of phases and the crystallographic orientation, EBSD samples were further prepared using a 0.02 μm silica solution in a Buehler vibratory polisher for a day. Electron Backscatter Diffraction (EBSD) analysis was implemented using a ThermoFisher Scios 2 SEM equipped with an EBSD detector. To establish the relationship between texture information and the dispersion of alloying elements in both base alloys along the interface, diffraction data was collected, and an energy dispersive spectrometer analyzer was used simultaneously. This analysis was conducted for both as-printed and heat-treated samples. Primary EBSD maps were processed using HKL Channel5 software, while additional images associated with the EDS maps, Kernel Average Misorientation (KAM) maps of non-fcc grains, and parent grain reconstruction maps were generated using Aztec Crystal software. The XRD spectra from both as-printed and heat-treated samples in the CoCrMo region were also characterized and

obtained using a Bruker D8 advance spectrometer with Cu Kα radiation. Results were obtained perpendicular to the building direction, applying 40 kV at 30 mA with a step size of 0.02° and scanning time of 1s. The proportions of γ and ε phases were calculated based on the $\{10\bar{1}1\}_{\varepsilon}$ and $\{200\}_{\gamma}$ XRD peaks, located in 46-48° and 51-53°, respectively, following the methodology suggested by Sage and Guillaud [30]:

$$\%_{hcp} = \frac{I_{hcp}^{10\bar{1}1}}{1.5 * I_{fcc}^{200} + I_{hcp}^{10\bar{1}1}} \quad [1]$$

Where $\%_{hcp}$ represents the percentage of the ε-phase and *I* denote the integrated intensities under the relevant XRD peaks. To depict the changes in mechanical properties with focus on the strength of interface, uniaxial tensile tests and microhardness measurements were performed on as-built and heat-treated samples. Nanoindentation measurements were taken using an iMicro KLA nano-indenter with a target load of 1 N and depth of 5000 nm. Microhardness line profiles were repeated at least 3 times for both conditions following a 50 μm indent spacing (d/h = 10). Cylindrical tensile coupons with a 16 mm gauge length and 4 mm diameter were also prepared, ensuring that the interface was in the middle. Tensile testing was performed according to ASTM-E8 specifications using an Instron 1332 machine with a 50 kN load cell. Three tensile coupons were tested for both conditions at a strain rate of 0.005 s^{-1}.

3.3 Results

3.3.1 Microstructural investigation

The representative microstructure for each section of the MS1/MP1 (maraging steel-CoCrMo alloy) dual-metal structure is presented in Figure 3.2. The interface displayed strong metallurgical bonding across multiple layers by having a consistent relative density

of 99.88 ± .04 %, compared to 99.87 ± .03 % in the maraging steel region and 99.7 ± .05 % in the CoCrMo region. Although the arranged parameters are primarily optimized for printing MS1 powder, process defects were minimal throughout the material due to the remarkable similarity between the alloy properties (such as melting point, density, and thermal coefficient [11,31]). Adequate melt pool penetration and layer overlap combined with good virgin feedstock flowability also helped in avoiding key-hole defects and lack-of-fusion defects.

Metallographic sections were taken parallel to the building direction for all relevant regions. A similar melt pool size can be observed for both alloy regions since deposition was continuously performed with the arranged printing conditions. The high energy input (300 W) generated melt tracks that have comparable widths of 145-190 μm for CoCrMo and 150-200 μm for maraging steel. The average melt pool depth is 54 ± 3 μm in the CoCrMo region and 52 ± 5 μm in the maraging steel region. The melt pool characteristics remain consistent in the interface, as shown in Figure 3.2b. Since a maraging steel etchant is used in Figure 3.2b and CoCrMo has a higher corrosion resistance, some of the melt pools in the CoCrMo region and in the interface appear hazy. Nevertheless, adjacent melt tracks of CoCrMo and maraging steel exhibit good melt pool overlap and bonding.

At higher magnifications, the formation of well-known cellular structures can be observed in all regions, as shown in Figure 3.2d-f and the EDS analysis in Figure 3.4a-4b. The CoCrMo alloy section exhibited a mixture of column and cell boundaries with an average cell size of ~ 0.7 ± 0.2 μm shown in Figure 3.2d and Figure 3.4a. The melt pool cores exhibit fine honeycombed-shaped cells that propagate in different directions, generating competitive growth which is influenced by the melt environment [9,25]. On the other hand,

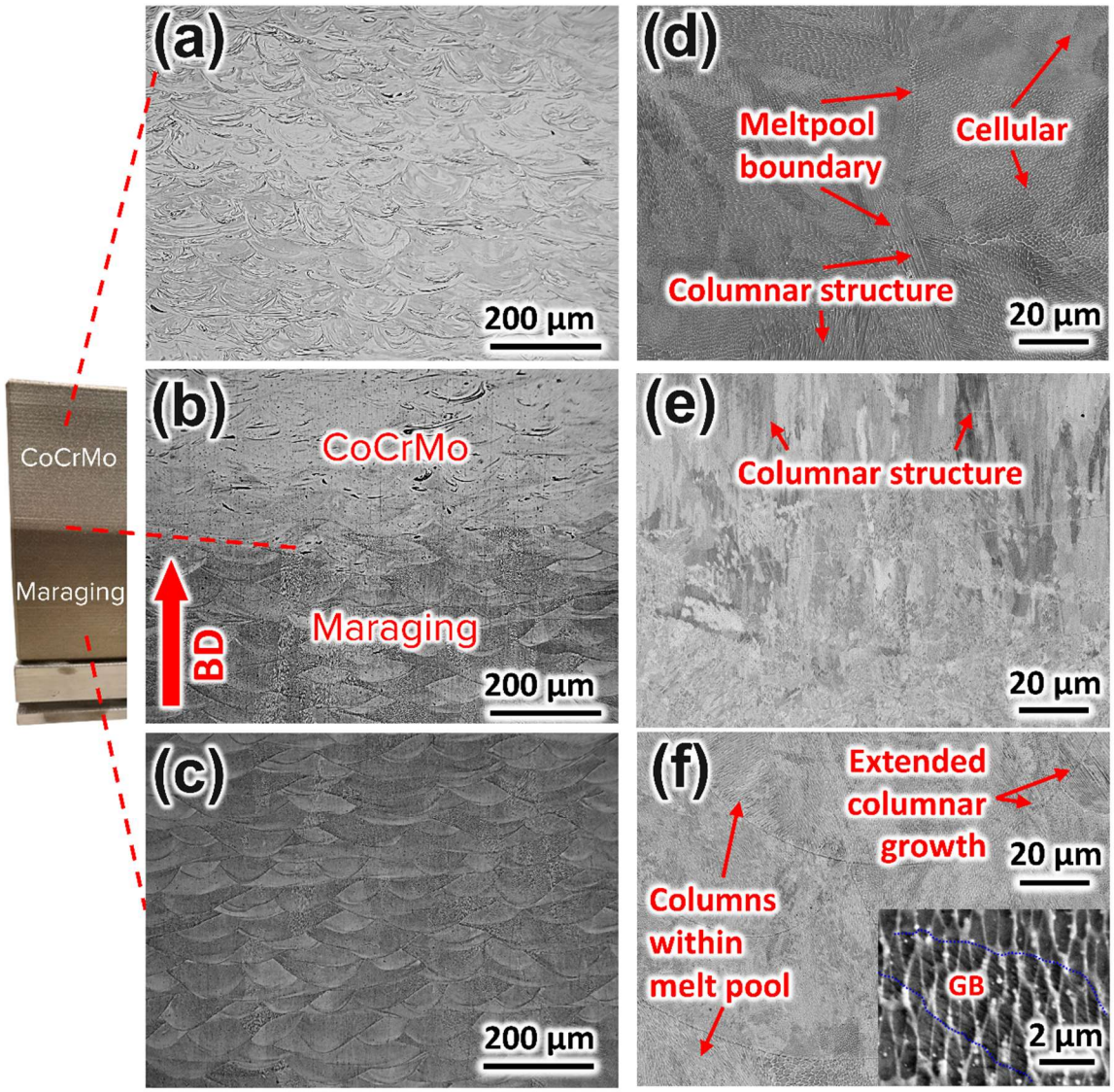


Figure 3.2. Low (a, b, c) and high (d, e, f) magnification microstructures of the as-built MMAM component: CoCrMo region near the interface (a, d), Interface region (b, e), and maraging steel region near the interface (c, f).

the maraging steel region in Figure 3.2f and Figure 3.4a exhibits a slightly finer cell structure having diameters of ~ 0.5 ± 0.1 µm, but the presence of an intermixed elongated columnar microstructure can also be observed. A closer look reveals the independence of the cellular structure to the boundaries of the grains of maraging steel, shown as blue dash lines. Due to the heat flux direction generated by the scanning pattern, columnar cells are primarily formed near the melt pool boundaries. The columns can either abruptly terminate

within the melt pool boundaries or extend their growth across the melt tracks. Based on the interface microstructure shown in Figure 3.2e, the fine maraging steel cellular structure remains intact as the epitaxial growth of the bigger CoCrMo grains is initiated. The solidification of CoCrMo generates columns that follow the building direction and appear to be immiscible to maraging steel, resulting in the independent formation of the grain boundaries and cell structures as the melt pool solidifies.

The applied heat treatment generated distinct microstructural changes to each region of the dual-metal structure, as presented in Figure 3.3. In the CoCrMo region shown in Figure 3.3a, traces of previous melt tracks and the associated cellular microstructure cannot be detected. Elongated columnar structures were replaced with larger, equiaxed grains that contain annealing twins. Changes can also be observed in the maraging steel region shown in Figure 3.3c, which contains a fully block martensitic microstructure devoid of any previous cellular structures and melt pool boundaries. Multiple packet-block-lath regions that span across random directions shown in Figure 3.3f emulate the hierarchical martensite microstructure typically present in conventionally-produced maraging steels [32]. However, the martensite laths situated near the interface seem to arrange themselves either parallel or at a 45° angle with respect to the build direction, as shown in Figure 3.3b, and Figure 3.3e, respectively. Further validation of the lath orientation will be provided through EBSD results. Similarly, the columnar regions within the material have aligned with the build direction and have remained intact even after the homogenization process, showing the influence of epitaxial growth to the resulting interface phase transformation.

EDS analysis was also performed in both alloys before and after heat treatment, and the results are shown in Table 3.2 for CoCrMo and Table 3.3 for maraging steel. SEM images

showing the location of each point measurement taken for EDS analysis are also presented in Figure 3.4. A minimum of 4 measurements were taken, and the results were grouped according to the distinct feature of the region where the data point was evaluated.

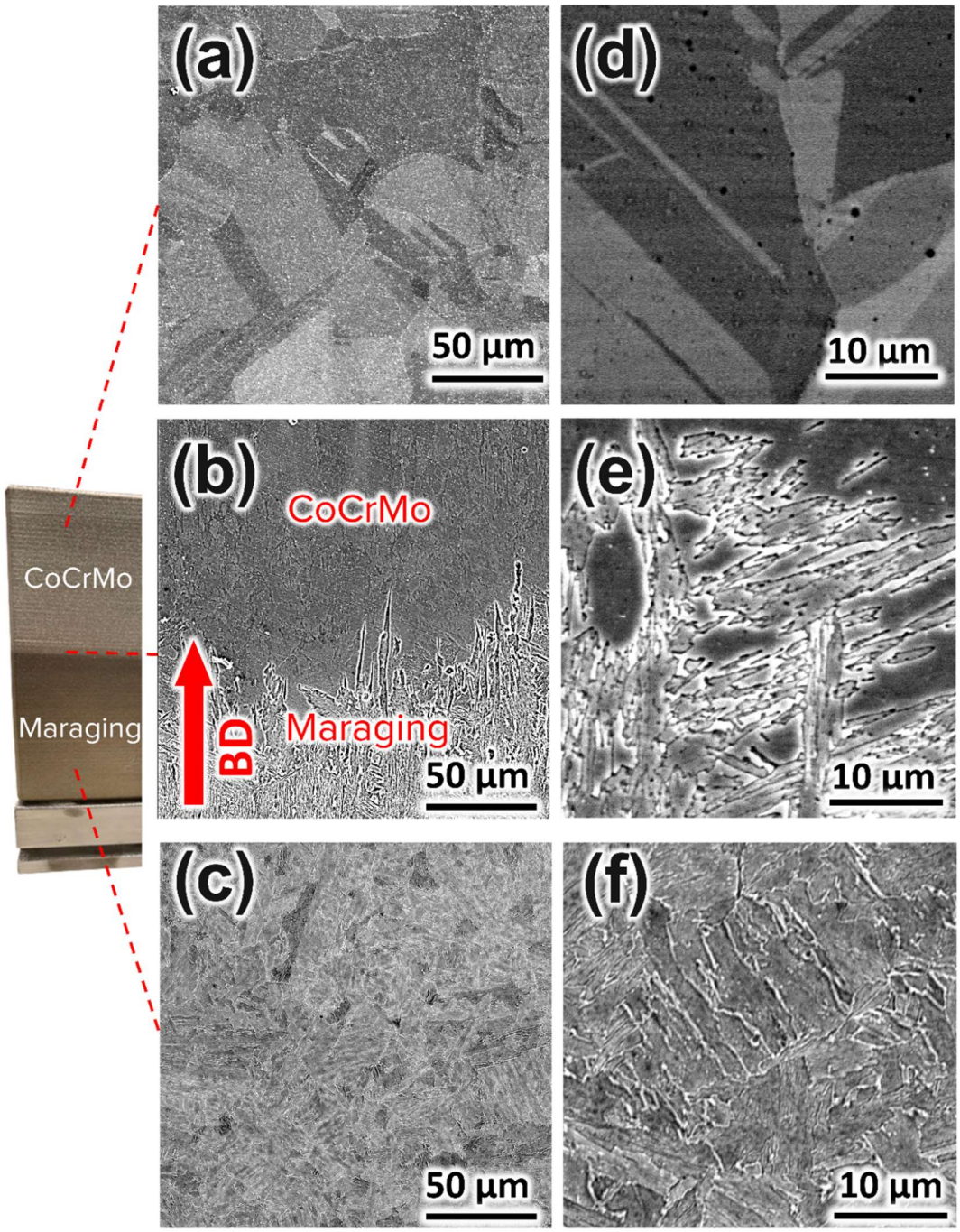


Figure 3.3. Low (a, b, c) and high (d, e, f) magnification microstructures of the heat-treated MMAM component: CoCrMo region near the interface (a, d), Interface region (b, e), and maraging steel region near the interface (c, f).

Table 3.2. EDS point analysis results for major alloying elements in the CoCrMo region

	Chemical Composition (in wt. %)			
	Co	**Cr**	**Mo**	**Trace (Fe, Ni, C, Si, Mn)**
CoCrMo As-built (a)				
Cell Matrix (A1-A7)	61.1 ± .3	30.4 ± .1	6.4 ± .3	2.1 ± .4
Cell boundary (A8-A14)	60.7 ± .6	29.5 ± .4	7.3 ± .3	2.5 ± .5
Heat-treated (c)				
Twin regions (C1-C4)	58.7 ± .5	30.4 ± .4	8.3 ± .5	2.6 ± .3
Matrix (C5-C8)	59.8 ± .1	29.9 ± .3	8.3 ± .4	2.0 ± .3

Table 3.3. EDS point analysis results for major alloying elements in maraging steel

	Chemical Composition (in wt. %)					
	Fe	**Ni**	**Co**	**Mo**	**Ti**	**Trace (C, Si, Mn)**
Maraging As-built (c)						
Cell boundary (B1-B7)	62.8 ± .2	17.6 ± .3	9.1 ± .1	6.5 ± .1	1.6 ± .3	2.4 ± .2
Cell Matrix (B8-B14)	65.8 ± .2	17.9 ± .1	9.4 ± .1	5.2 ± .1	1.1 ± .2	0.6 ± .1
Heat-treated (d)						
lath boundary (D1-D4)	62.1 ± .1	17.1 ± .1	8.7 ± .1	5.2 ± .3	1.1 ± .1	5.8 ± .2
Matrix (D5-D8)	61.9 ± .3	17.2 ± .1	8.7 ± .2	5.3 ± .1	1.2 ± .2	5.7 ± .2

After printing, the CoCrMo matrix is saturated by Co and Cr, while other alloying elements such as Mo have a slightly higher concentration in the cell boundaries. There is little chemical compositional difference detected between the twinning regions and the matrix of the heat-treated samples, which is the goal when applying solution heat treatment. Cellular boundaries dissolved and caused overall chemical homogenization in the cobalt matrix. Similarly, the maraging steel region exhibits a slightly higher concentration of Mo and Ti in the cell boundaries compared to the matrix, which is also attributed to the thermal conditions during printing. The subsequent solution heat treatment temperature removed the elemental segregation and produced a homogenous matrix. The aging step is expected to only modify the martensite morphology along with the formation of fine precipitates,

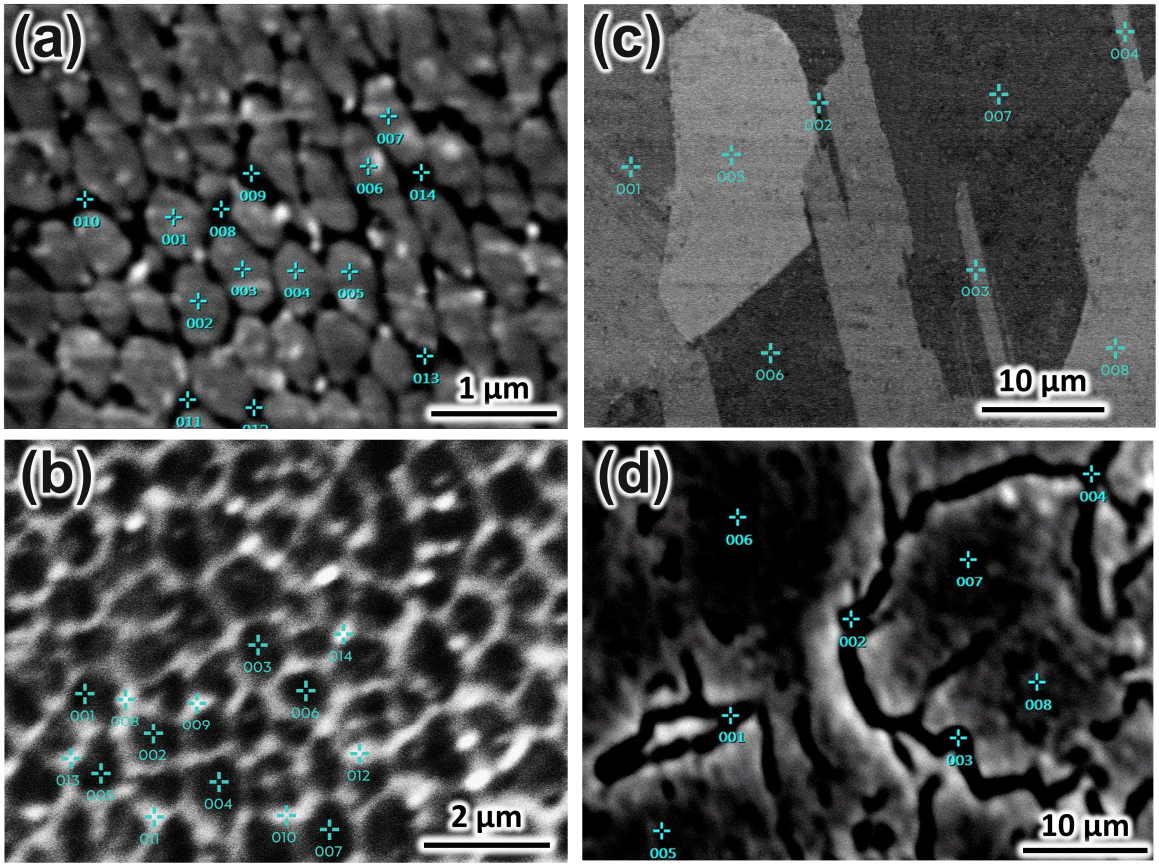


Figure 3.4. EDS point analysis of representative samples: As-built (a) CoCrMo and (b) maraging steel, Heat-treated (c) CoCrMo and (d) maraging steel.

but the magnifications necessary to examine such particles were unattainable using SEM or EBSD [9,33].

3.3.2 Texture Analysis

The orientation of grains, distribution of phases, and kernel average misorientation (KAM) map along the interface of the as-printed sample are presented in Figure 3.5. Based on the order of printing, the upper region represents the CoCrMo region, while the lower side represents the maraging steel region. Starting with the maraging steel region at the bottom, the IPF color map in Figure 3.5a shows fine, inconsistent, martensitic subgrains with an average size of 9.9 ± 5.1 µm. The phase map in Figure 3.5b shows a dominant bcc (martensite) phase, oriented primarily along the <111> // BD, with only ~1.5% austenite

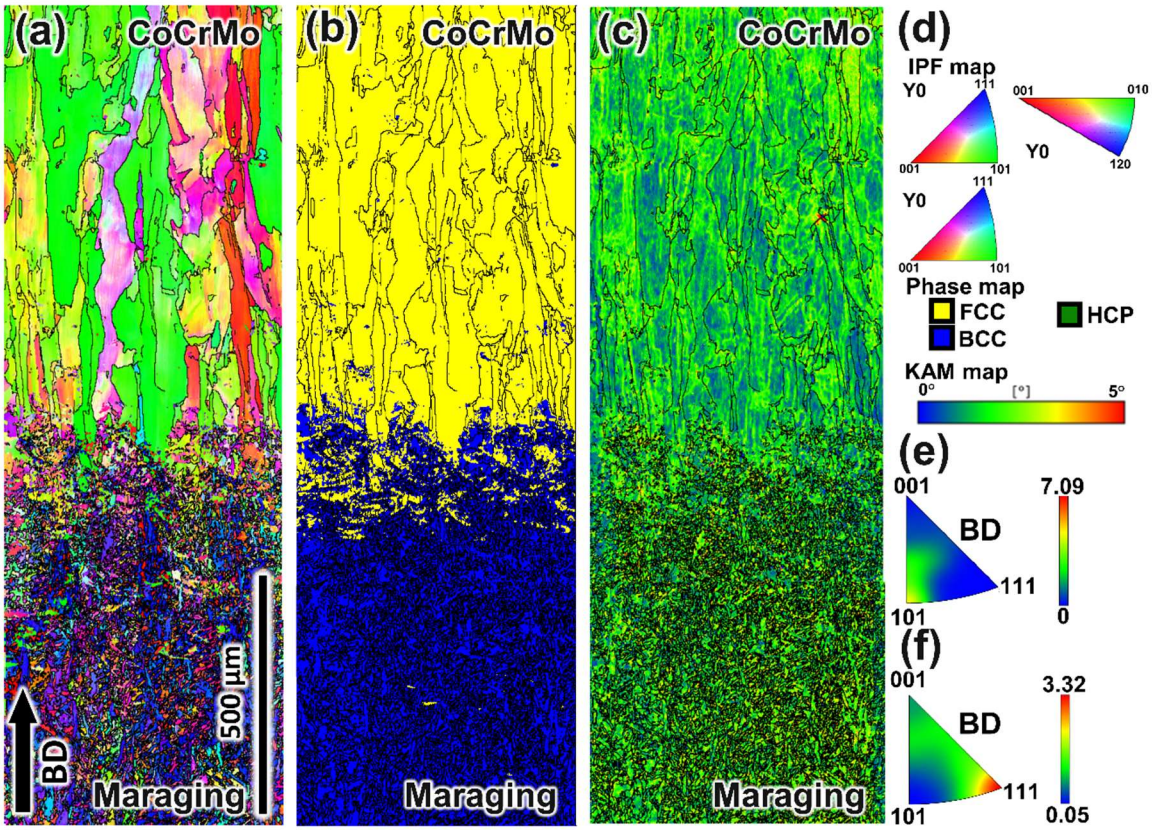


Figure 3.5. Analysis of as-printed interface region before heat treatment: (a) Inverse pole figure color map, (b) phase map showing fcc, hcp, and bcc structures, (c) Kernel average misorientation maps, (d) corresponding legends for a-c, (e) IPF representation of fcc grains, and (f) IPF representation of bcc grains.

that appears to be finer than the chosen step size (1.5 µm). The KAM map in Figure 3.5c also shows that most bcc subgrains exhibit high KAM values (KAM > 3°) that indicate the presence of strain accumulation and formation of dislocation walls [34]. As the powder was switched to the CoCrMo alloy, the disordered effects of the maraging steel texture and cellular microstructure on the melt solidification can be observed. Due to the combined effects of solute segregation, the stirring effect of Bénard-Marangoni convection [35], and accumulated strain, a diverse interface can be observed. Martensite forms after solidification of a uniform fcc matrix (fcc γ-cobalt and fcc austenite), but the transformation is non-uniform. Some fcc phase islands remain in the same phase and follow the curved shape of the melt pool. The complex phenomena that govern the interface

based on boundary orientation and alloying element distribution will be discussed later in detail.

As more layers of CoCrMo are introduced, the dilution of maraging steel becomes negligible, and the melt pool solidifies to a homogenous fcc γ-cobalt phase. The change in texture is evident from the maraging steel to CoCrMo region in the IPF map. However, instead of a strong columnar fiber texture primarily along the <100> // BD, which is aligned with the thermal gradient direction during printing, some columnar grains exhibit an orientation along the <110> // BD. This appears to be the influence of the previous fcc fibers that followed growth along the austenite grains. The epitaxial growth that occurred in the previous layers allowed heterogeneous nucleation of columnar grains in different orientations. The results also show that the average grain size in the CoCrMo region is 98 ± 7.1 μm with a high-aspect ratio of 6.9. Although the phase map shows 99.9 % fcc structure, XRD measurements shown in Figure 3.6 confirmed the presence of ~4 % hcp ε-phase within the fcc fibers. BSE images in Figure 3.7 also show multiple groups of parallel bands that exist in the cellular microstructure of the CoCrMo region. Previous studies

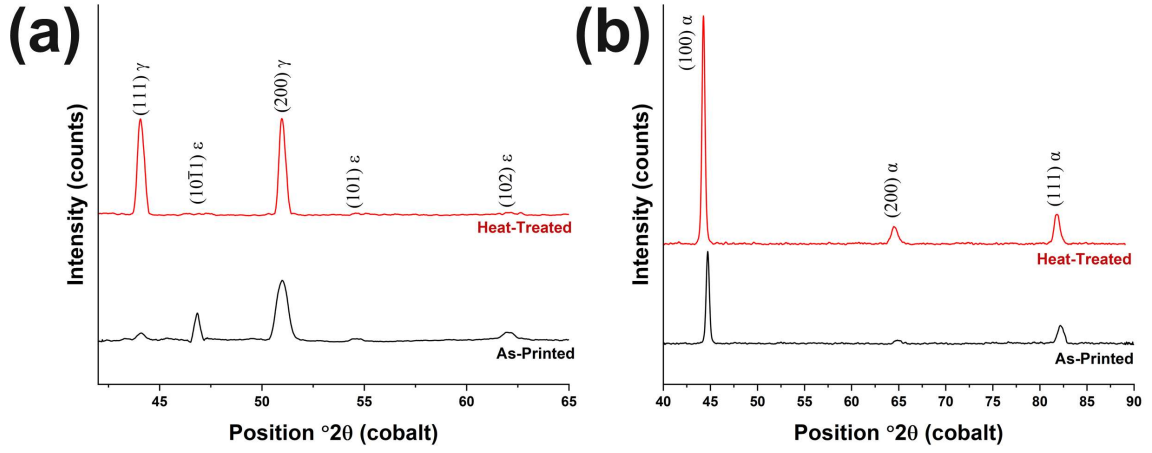


Figure 3.6. Comparison of XRD spectra obtained from the (a) CoCrMo region and (b) maraging steel region of the as printed and heat-treated samples.

[36,37] have shown that these bands are ε-phase striations that manifest at high quench rates (such as in 3D printing) since the transition from γ to ε can be readily achieved through the displacement of a/6 <112> Shockley partial dislocations along alternate {111} densely packed planes [38,39]. The KAM map also illustrates a lamellar distribution of the misorientations within the fcc grains, which is associated with the stresses experienced during repeated heating and cooling cycles throughout fabrication. Higher resolution EBSD analysis was performed in the CoCrMo region, as shown in Figure 3.8, with a step size of 0.2 μm. The band contrast map in Figure 3.8b also confirms the presence of ε-phase bands. In addition, the KAM map in Figure 3.8c shows the formation of lamellar strain regions around ε-phase bands which is a characteristic feature of the martensitic γ-ε transformation resulting from the rapid solidification rates involved in AM [28,37]. Other studies have compared this result to TEM observations and confirmed the presence of fine hcp needles for up to about 30 % of the total phase content [20,40,41].

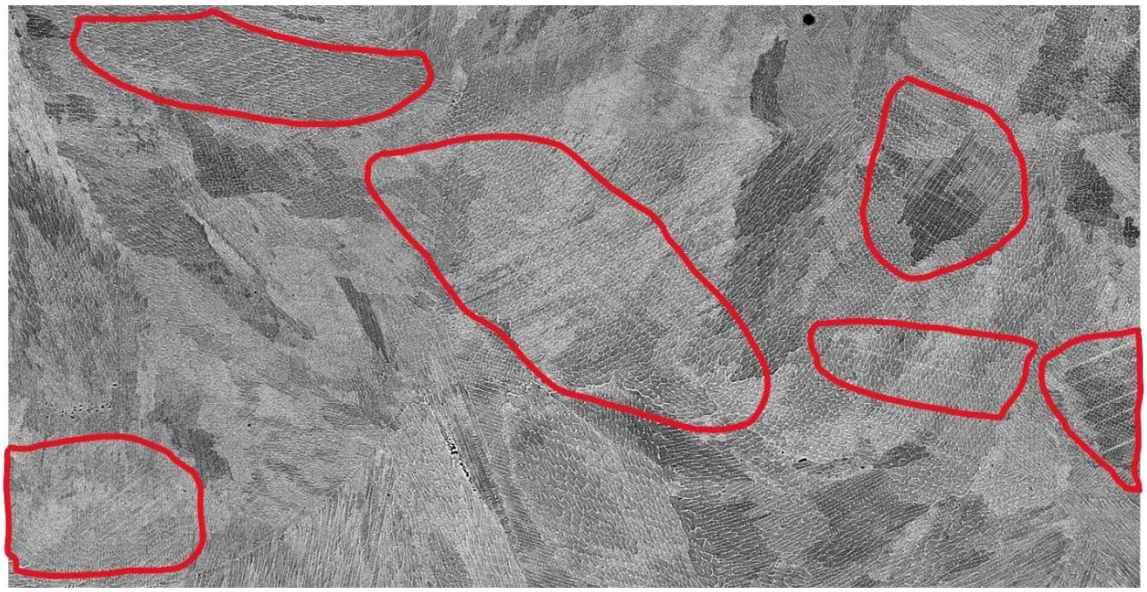


Figure 3.7. BSE images of the CoCrMo region shown in Figure 3.1d. The regions highlighted in red exhibit distinctive parallel bands, which are indicative of the formation of ε-phase. These bands are formed because of the rapid solidification during the LPBF process.

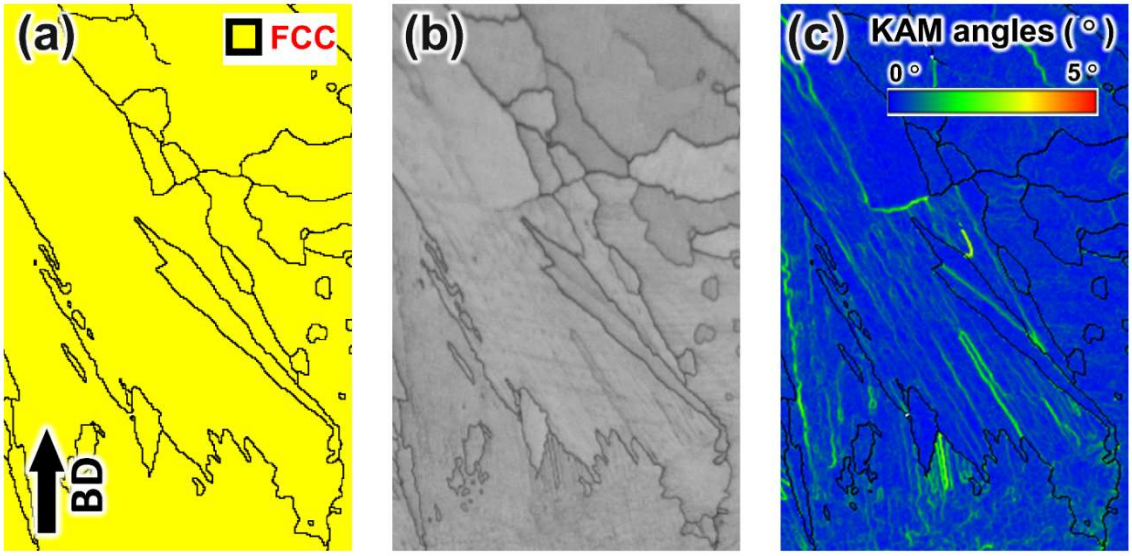


Figure 3.8. High resolution EBSD analysis of the CoCrMo region: (a) Phase map showing 100 % FCC phase, (b) band contrast maps that clearly depict the existence of fine parallel bands corresponding to the ε-phase, and (c) KAM maps that highlight localized strain regions formed during the martensitic transformation.

The EBSD analysis results after the applied solution and aging heat treatment are presented in Figure 3.9. The maraging steel region exhibited significant growth of martensite laths because of the prolonged solution heat treatment. This growth resulted in a larger block size compared to the as-built structures, measuring approximately 17 ± 8 microns. The hierarchical structure attributed to conventional maraging steels can be observed, and the consistency of the block sizes between packets can be readily observed. A longer solution heat treatment duration was used to accommodate the CoCrMo alloy. Although groups of blocks oriented in the <100> // BD and <111> // BD can be observed, the martensite regions appear to be equiaxed and have no preferred orientation. Virtually no traces of retained austenite remained after heat treatment since alloying elements were evenly distributed [33]. The KAM map in Figure 3.9c also shows that most of the boundaries have low KAM values, indicating sufficient stress relief that accumulated during printing and after the aging heat treatment.

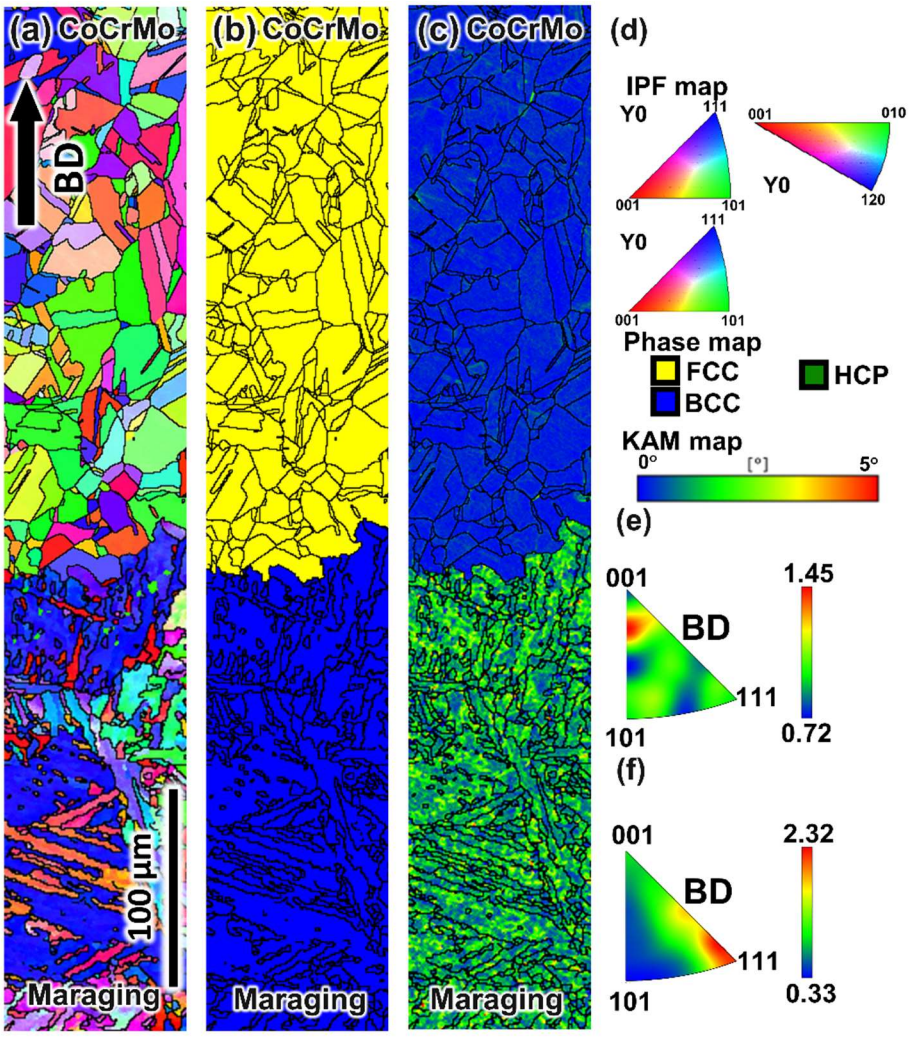


Figure 3.9. EBSD Analysis of MMAM component after heat treatment: (a) Inverse pole figure color map, (b) phase map showing fcc, hcp, and bcc structures, (c) Kernel average misorientation maps, (d) corresponding legends for a-c, (e) IPF representation of fcc grains, and (f) IPF representation of bcc grains.

The change in texture along the interface region after heat treatment can further be analyzed from the EBSD maps, and the results agree with the microstructural investigation. Closer to the maraging steel region, directional growth of martensite resulted in parallel laths that are oriented along the <111> // BD. On the other hand, the martensite grains closer to the CoCrMo region appear as extremely fine subgrains that are exclusively in the <100> // BD. Both regions still exhibit a homogenous bcc phase, but the extent of martensite lath growth differs. This will be related to the solute distribution, to be discussed later in detail.

The effect of heat treatment is also evident in the CoCrMo region, showing the disappearance of highly textured fiber structures into massive equiaxed γ-phase grains. A complete fcc phase was also obtained from the XRD spectra. The relief of residual stresses can be assumed based on the very low internal misorientation values depicted in the corresponding KAM map. No preferential texture was observed. The extended solution heat treatment duration also resulted in uniform grains, since the average grain size changed to ~35.2 ± 2.7 μm, and the aspect ratio decreased to 2.8. This suggests that static recrystallization occurred using the driving force of residual stresses present in the fibers [21,23].

3.3.3 Chemical composition analysis

To understand the effects of solute distribution on the microstructure and texture observations along the interface, the concentration profiles of major alloying elements (Co, Cr, Fe and Ni) after printing and after heat treatment are presented in Figure 3.10 and Figure 3.11, respectively. For reference, the corresponding phase maps are included in each condition alongside the EDS maps.

The upper region represents the CoCrMo region that has a high concentration of Co and Cr, while the lower side represents the maraging steel region with a high concentration of Fe and Ni. The EDS maps of the as-printed sample (shown in Figure 3.10) show extensive solute segregation in all regions, which agrees with the formation of cellular structures on both alloys. Both Fe and Co share a similar degree of inhomogeneity, but Cr and Ni still exhibit uneven distribution after printing. Nevertheless, a significant portion of the base alloys retained the same phase despite segregation of major alloying elements before

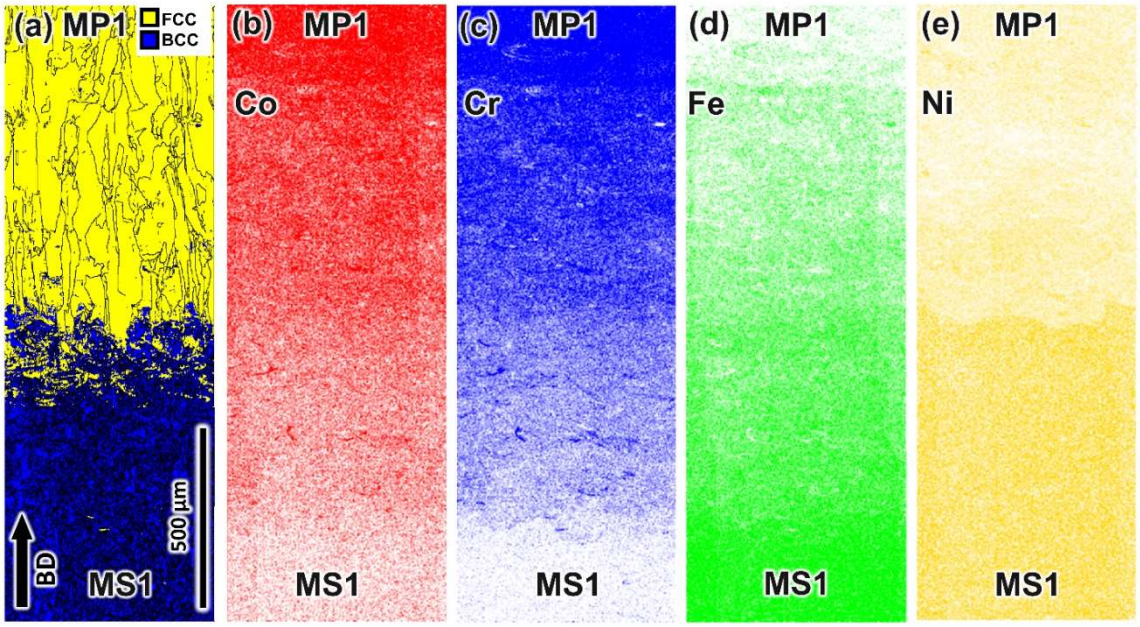


Figure 3.10. Comparison of phase map (a) to EDS maps of major alloying elements along the interface after printing: (b) cobalt, (c) chromium, (d) iron, and (e) nickel.

solidification. However, the same tendency cannot be said about the interface, which exhibited a mixed phase distribution upon solidification. A high segregation of Co and Cr solutes develops in the maraging steel region, and a corresponding reduction of Fe and Ni concentration can be seen in specific areas in the interface. Consequently, a fluctuating bcc martensite transformation occurs after the melt pool solidifies to a fully fcc phase region. The areas rich in Co and Cr prevent the growth of martensite subgrains, resulting in fcc phase islands that resemble the shape of the melt pool. As more CoCrMo layers are introduced and epitaxial growth continues, the melt pool then remains in fcc and the complex transformation terminates.

In contrast, the subsequent heat treatment had a significant impact on the chemical composition distribution along the interface shown in Figure 3.11. The regions in the maraging steel and CoCrMo base alloys exhibit an even spread of the respective main

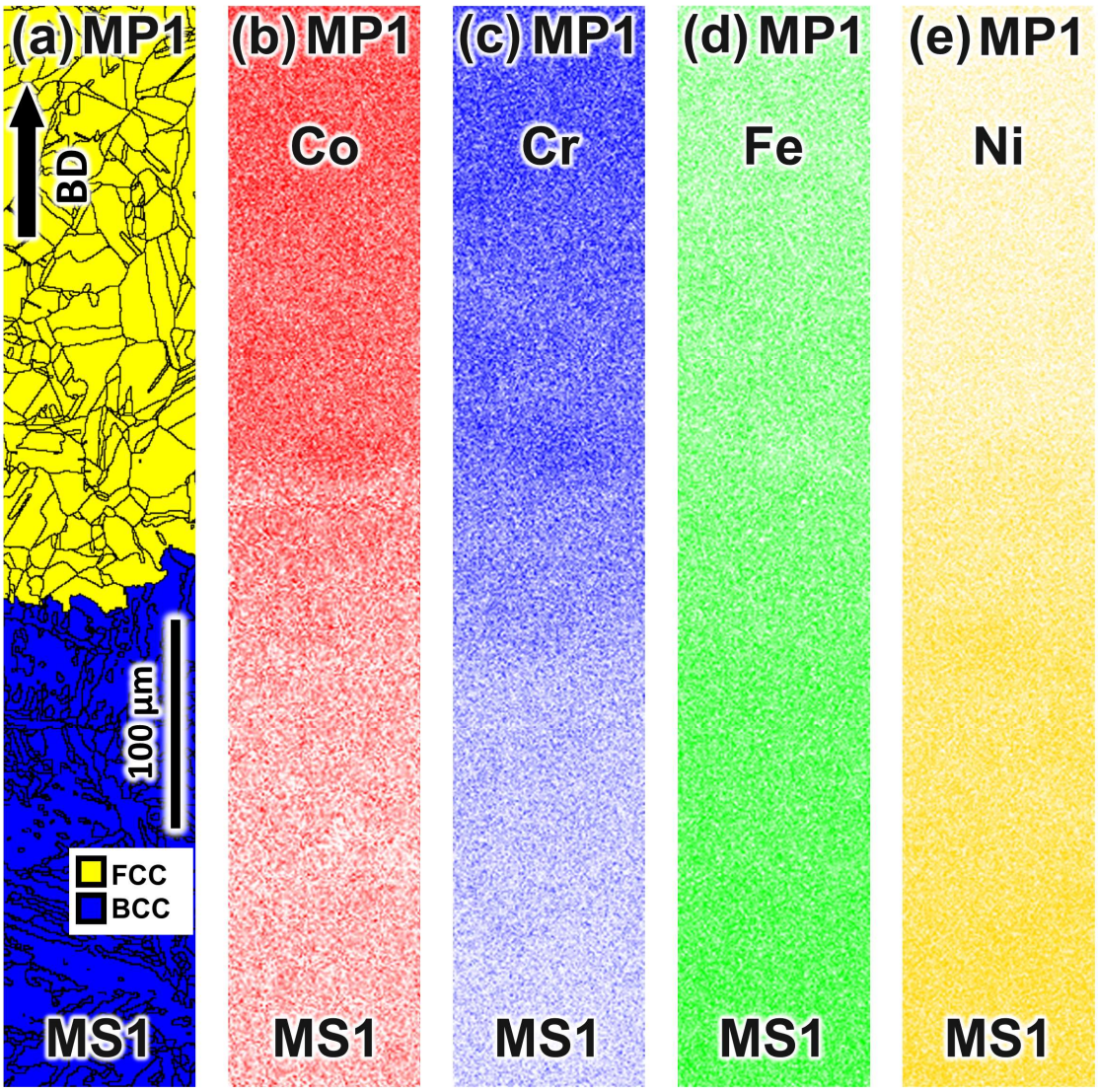


Figure 3.11. Comparison of (a) phase map to EDS maps of major alloying elements along the interface after heat treatment: (b) cobalt, (c) chromium, (d) iron, and (e) nickel.

alloying elements, which reflects the decomposition of cellular boundaries. Both regions also exhibit a more consistent microstructure and texture. A steep concentration gradient of around 300 µm is observed in the interface, and the corresponding grain size and orientation differences observed in Figure 3.9 can now be interpreted based on the element distribution. Closer to the maraging steel region, a slight dilution of the MP1 powder composition impedes the formation of nucleation sites for martensite transformation and promotes epitaxial growth. This resulted in directional growth and parallel laths that are

oriented along the <111> // BD direction. On the other hand, the CoCrMo region with scarce Fe and Ni concentrations resulted in an environment with insufficient tendency for martensite growth, which results in extremely fine subgrains that are exclusively in the <100> // BD direction. Due to the homogenous alloying distribution, a sharp bcc-fcc phase boundary is formed in the interface. As more layers of CoCrMo are introduced, the dilution of maraging steel becomes negligible, and the concentration measurements become equivalent to the CoCrMo powder composition. Finally, the solution heat treatment resulted in the formation of large fcc grains with even solute distribution in the CoCrMo region.

3.3.4 Mechanical Properties

The change in microhardness of cross-sections across the interface was obtained under both conditions, and the results are presented as contour plots in Figure 3.12a for the as-built sample, and Figure 3.12b for the heat-treated sample. The CoCrMo and maraging steel regions are designated to the left and to the right of the interface, respectively. The hardness points are presented relative to their distance from the perceived interface, which was identified based on the microstructure and hardness variation. The average hardness in the maraging steel region for the as-built sample is 402 ± 9 HV, which agrees with most of the results from other as-built maraging steel studies [9,42,43]. On the other hand, the CoCrMo region had slightly lower hardness of 348 ± 7 HV, which was also reported in other as-built CoCrMo studies [13,29]. In general, the as-built contour plot reveals highly varied microhardness values, and the regions of the base materials are hard to distinguish. The presence of a hierarchical microstructure in both regions, combined with the accumulation of local thermal strains during the printing process, contributes to the diverse

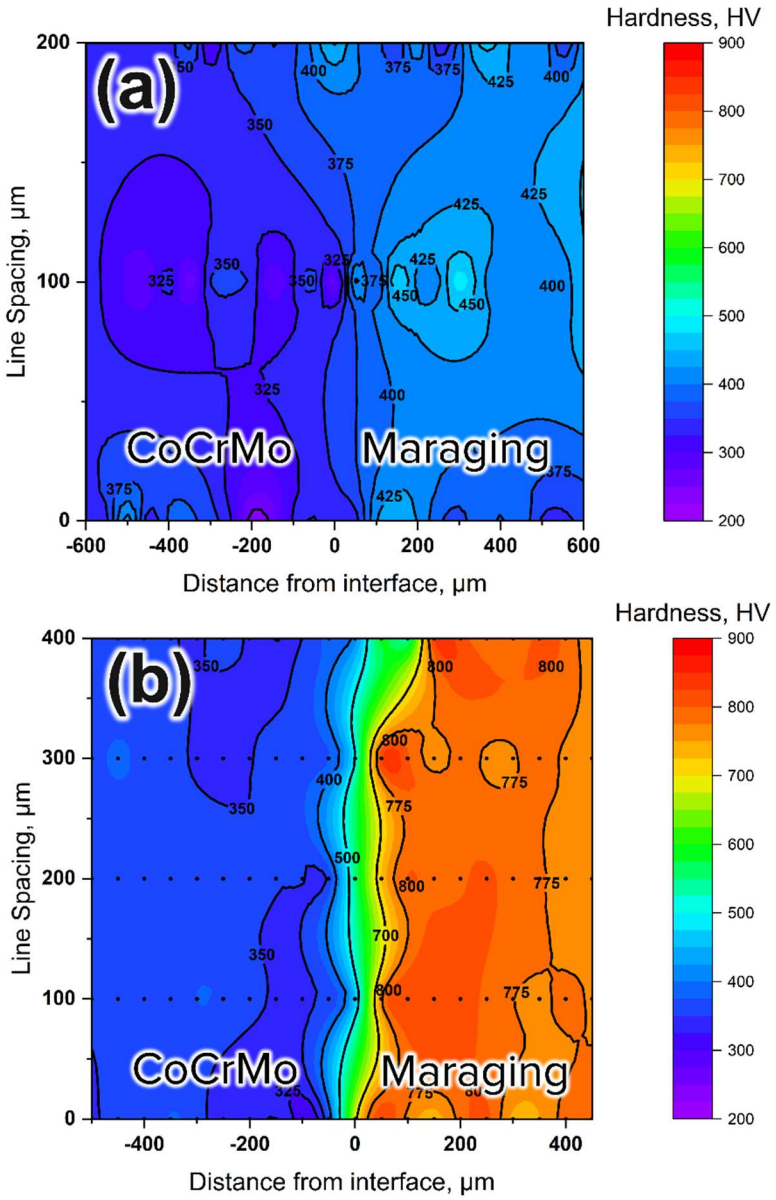


Figure 3.12. Contour plots of microhardness values after a) L-PBF printing, and b) solution heat treatment and aging.

microhardness distribution throughout the material. A transition region of 400 µm was detected with an average hardness of 370.8 ± 7 HV. Interestingly, despite the base alloys sharing a small difference in microhardness values, the microhardness measurements along the interface exhibited a smooth and gradual transition without any sudden peaks or unusually low hardness regions. This observation indirectly suggests the absence of precipitates or phases that significantly influence the microhardness values.

In contrast to the as-built results, distinct regions of the base alloys can be recognized in the microhardness contour plot of the heat-treated sample in Figure 3.12b. A significant increase in the average microhardness of the maraging steel region to 645 ± 3 HV suggests the occurrence of precipitation strengthening. The most notable feature in the hardness profiles is the sharp drop in hardness that occurs in the interface region, which has an average hardness value of 413 ± 18 HV. Unlike the as-built sample, indents that are closer to the maraging steel region have a higher average hardness than indents closer to the CoCrMo region. A sharp transition in the interface is observed and the CoCrMo region retained a slightly lower microhardness average of 340 ± 3 HV following the associated stress relief. Consistent with the contrast in microstructure and phase distribution after heat treatment, the boundaries of microhardness between both base alloys become more evident. Notably, regions near the interface exhibit a consistent and uniform distribution of hardness with minimal standard deviation. It's worth mentioning that the spatial precision of the Vickers tests may not be adequate to decisively discern if the decrease in hardness takes place abruptly at a layer or if it transpires more progressively across the area. Furthermore, the interfaces will not be linear due to the laser melt pool tracks during printing that produces scalloped edge shapes [44]. The steep interface region where the microhardness value changes also demonstrate the high-resolution printing capability of L-PBF.

Figure 3.13 depicts the representative engineering stress-strain curves for the as-built and heat-treated dual-alloy samples, with a comparison to the tensile data of the base alloys (selected from 3 tests for each condition). The combined AM structure obtained a tensile strength of 1185 ± 18 MPa, which is between the observed tensile strengths for the individual maraging steel and CoCrMo alloys (1238 ± 15 MPa and 1162 ± 21,

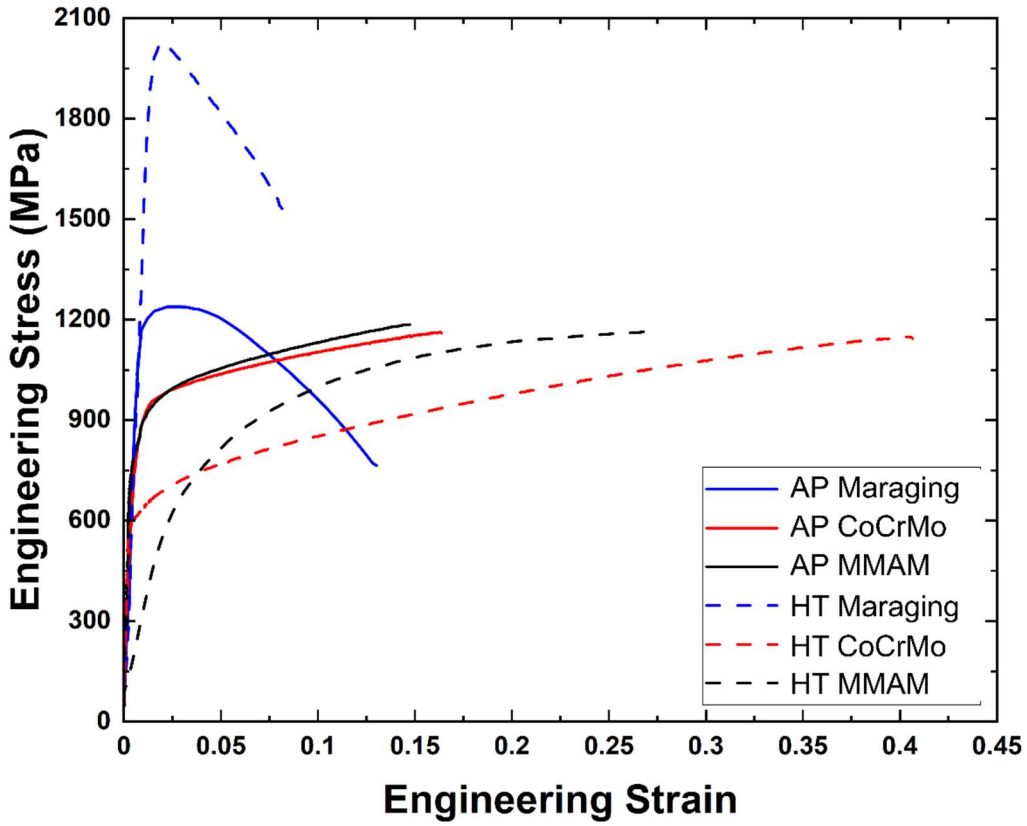


Figure 3.13. Comparison of engineering stress-strain curves for base alloys and the dual component. Solid lines represent as-built specimens, while dashed lines indicate heat-treated specimens. Maraging steel samples are denoted in blue, CoCrMo samples in red, and dual-component samples are highlighted in black.

respectively). The 0.2% offset yield strength of 973 ± 23 MPa leaned closer to the yield strength of CoCrMo (966 ± 17 MPa) rather than maraging steel (1198 ± 21 MPa), and the trend persisted in the observed elongation values (14.7 ± 1.3 % compared to 16.3 ± 1.1 % for CoCrMo and 13.03 ± 1.7 % for maraging steel).

After heat treatment, the combined AM structure exhibited a slight decrease in yield strength to 704 ± 16 MPa but maintained the tensile strength to 1164 ± 18 MPa. While the CoCrMo sample also maintained the tensile strength to 1148 ± 13 MPa, a considerable increase to the tensile strength of maraging steel was observed (2019 ± 15 MPa). The sustained UTS values indicates that the joining properties remained intact, despite the

precipitation strengthening in maraging steel (decreasing ductility) and stress relief in CoCrMo (slightly lowers strength). The heat-treated dual-alloy sample also showcased an improved elongation of 27.1 ± 2.1 %, mirroring the dramatic increase in ductility of the CoCrMo sample to 40.7 ± 2.6 %. Despite its increased tensile strength, the maraging steel sample experienced a notable decrease in ductility to 8.3 ± 1.4 %.

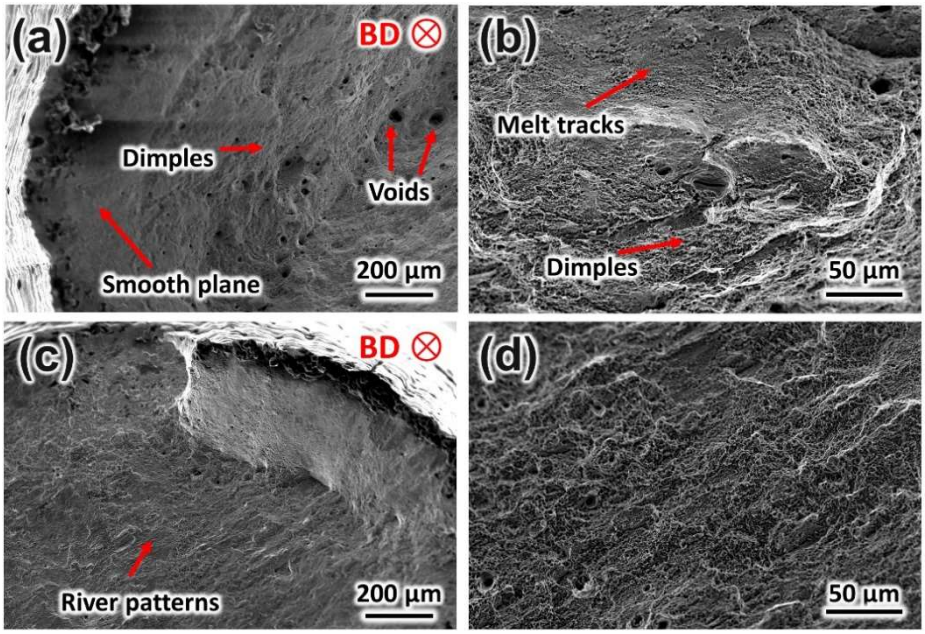


Figure 3.14. BSEI images illustrating the fracture patterns following tensile testing for (a), (b) as-printed specimens and (c), (d) heat-treated samples.

The fractured surfaces of the as-built and heat-treated specimens observed via SEM are displayed in Figure 3.14. All micrographs were captured parallel to the building direction, focusing on the CoCrMo section. Figure 3.14a-b display the fracture surface of the as-built sample, marked by a mix of morphologies that include dimples, voids, and cleavage facets. With the hierarchical structure post-printing and the ductility disparity between CoCrMo and maraging steel, the resultant MMAM structure revealed an irregular failure mode. Scattered pores and river-like patterns point towards ductile fracture, while abrupt and ragged tears are reminiscent of brittle failure. Nonetheless, the mechanical properties of the combined AM structure stayed within the range of the base alloys. In contrast, the heat-

treated specimen revealed a river-like dimple morphology consistent with increased elongation observed after tensile testing, as shown in Figure 3.14c-d. Following ductile failure, micro-dimples are evenly dispersed across the fracture surface, creating a homogenous appearance. The uniformly sized grains found in both regions eliminated any geometrical irregularities that could act as stress concentration points, thereby mitigating the risk of early fracture.

3.4 Discussion

3.4.1 Interfacial evolution mechanism in the as-printed sample

The distinct characteristics in different regions of the as-printed samples will first be correlated to understand the underlying mechanism during solidification of the mixed maraging steel-CoCrMo interface. Both base alloys exhibit a heterogenous cellular structure after printing. Although cell boundaries form chemical inhomogeneities during printing, they do not generate sharp boundaries that coincide with the grains for both CoCrMo and maraging steel alloys. The segregation of solutes along the boundaries is attributed to a particle accumulated structure formation mechanism driven by surface tension [45]. In addition, the saturation of alloying elements in both alloys does not necessarily lead to secondary precipitate phase formation or inclusions observed in other AM alloys such as IN718 and SS316L [46], which can have detrimental effects on mechanical properties. Instead, other studies have observed the relationship between cell wall formation and the dislocation substructures in maraging steel [32] and CoCrMo alloy [47] after LPBF fabrication, associating it with the cyclic thermal stresses experienced during printing. Due to such unique conditions, printing maraging steel achieves martensite subgrains that do not resemble the hierarchical structure in conventional maraging steels

and printing CoCrMo achieves fine dendritic fcc-hcp structures that do not resemble conventional CoCrMo alloys. Consequently, a complex composite environment is formed upon solidification after the first layers of MP1 powder are mixed with the re-melted MS1 molten pool. Additional analysis has been applied to the IPF map of the as-printed sample shown in Figure 3.5, and the results of parent austenite grain reconstruction applied on the martensite region based on the protocol developed by Huang et al. [48] are presented in Figure 3.15a**.** Although other studies have identified the low susceptibility of maraging steel to a dominant texture after printing [7,17,49], the fine martensite subgrains observed in this study appear to originate from columnar austenite grains. This signifies a preferred orientation for epitaxial growth of the austenite structure during solidification. Furthermore, the orientation of some columnar grains detected in the CoCrMo regions can also be related to the prior austenite grains. Instead of a dominant <100> // BD columnar structure that is expected if CoCrMo is to be printed separately, continuous FCC growth in the interface resulted in some grains that have a preferred orientation in <110> // BD. Therefore, these observations suggest that during the solidification of the interface, columnar grains that are exclusively fcc phase and experience solute segregation are formed.

The occurrence of martensite transformation during further rapid cooling in the interface should then be investigated. To demonstrate the effect of solute distribution to the formation of martensite, the average composition of alloying elements obtained from the EDS maps presented in Figure 3.10 was used as input to calculate the starting temperature of martensitic transformation (M_s), based on a commercially available software that can generate kinetic and thermodynamic models for steel and cobalt alloys [32,50]. The results

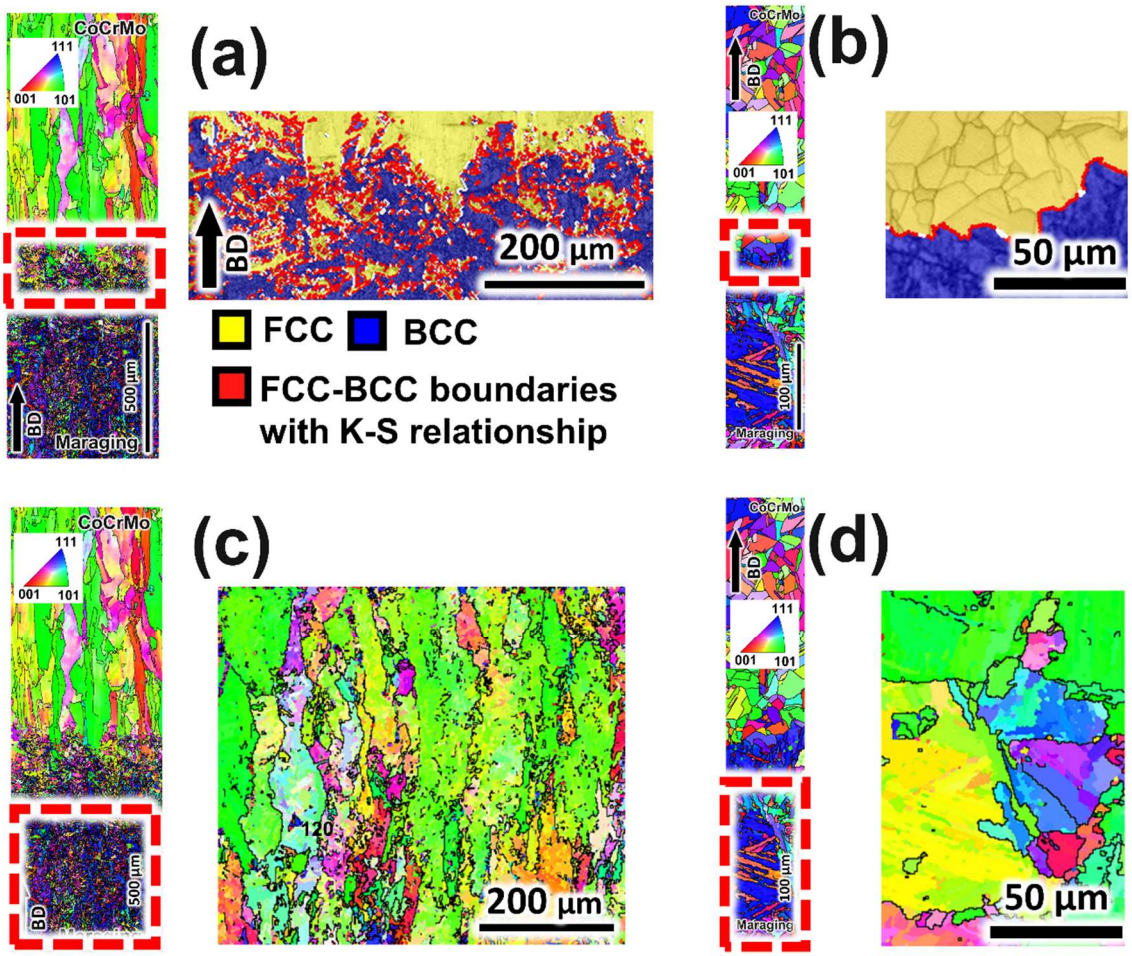


Figure 3.15. Analysis of EBSD results: parent austenite grain reconstruction of martensite regions of the (a) as-printed and (b) heat-treated samples; and phase boundaries that obey the K-S relationship for the (c) as-printed and (d) heat-treated samples.

are presented in Figure 3.16. Evidently, as more CoCrMo layers are introduced, the addition of Co and Cr impedes the transformation of austenite grains during rapid cooling. Since the alloying element distribution is also heterogenous, specific regions exhibit different tendencies in nucleation and subsequent growth of martensite subgrains. In the cellular level, the slight differences of major alloying elements along the cell walls observed in the EDS point analysis in Figure 3.4 can also cause uneven martensite transformation. The excess Mo and Ti concentration in maraging steel cell walls can promote austenite retention in the cell boundaries, while the reduction of Cr and Co concentration inside the CoCrMo cells can also promote martensite formation in the cell

matrix. Furthermore, heterogenous martensite nucleation corresponds to a volume expansion that can induce localized stresses which could then obstruct and even prevent further transformation of neighboring austenite regions [32,51].

To confirm that discontinuous martensite transformation occurred in the interface, fcc-bcc phase boundaries that obey the Kudjumov-Sachs (K-S) orientation relationships within 5° are also identified in Figure 3.15c. The K-S relationships [52] are established lattice orientation relationships originally observed between transformed martensite and parent austenite in low and ultra-low carbon steels defined as:

$$(1\ 1\ 1)_{\gamma} \,||\, (0\ 1\ 1)_{\alpha'}\ ,\ [\bar{1}\ 0\ 1]_{\gamma} \,||\, [\bar{1}\ \bar{1}\ 1]_{\alpha'} \qquad [2]$$

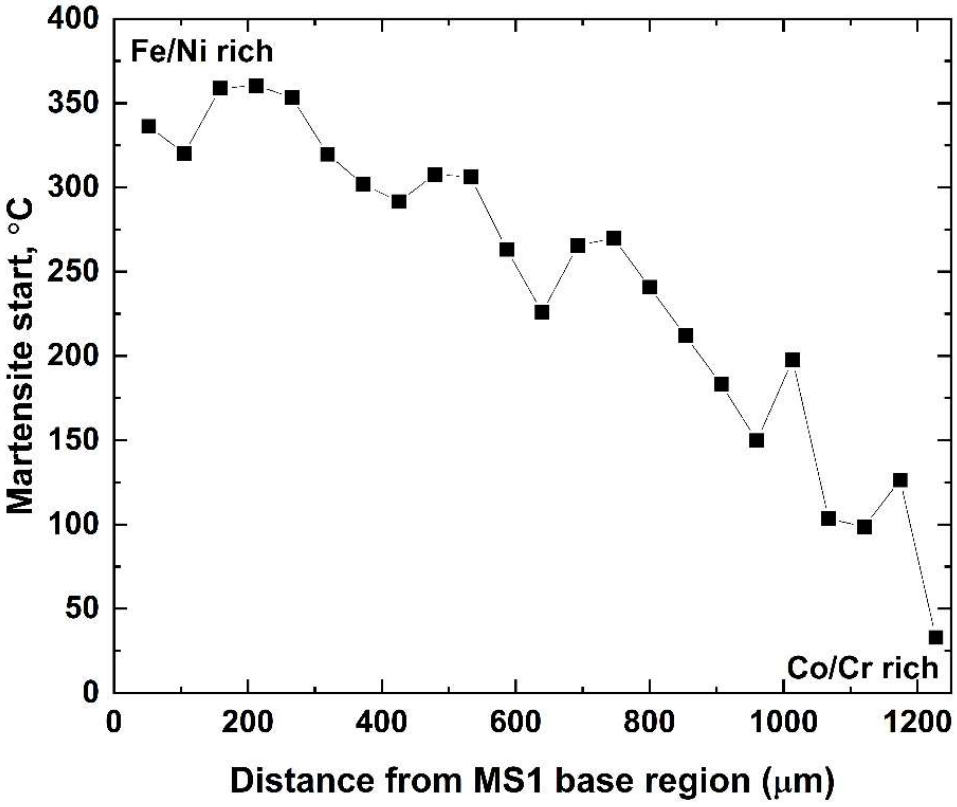


Figure 3.16. Thermodynamic simulation of Martensite start temperature based on alloy distribution along the interface after printing.

with γ and α' representing austenite and martensite, respectively. A majority (81.3 %) of the identified fcc-bcc boundaries in the as-printed interface shown in Figure 3.5 and Figure 3.15c satisfies the defined relationship and outlined regions wherein austenite has been retained. Segregated fcc phase islands that resemble the shape and stirring effect of Bénard-Marangoni convection [35] are formed due to the differences in solute concentration and propensity to martensite nucleation. In summary, the interface formed by continuous printing of is dictated by the growth orientation before solidification, negligible presence of secondary phases, local alloying element distribution, local stresses due to martensite volume expansion, and intermixed grain and cellular growth.

3.4.2 Effect of heat treatment on the dual-alloy interface

Heat treatment schedules applied to multi-material structures deviate from the standard temperature combinations to satisfy the mechanical requirements of all the components involved. Although the solution heat treatment provided sufficient stress relief and complete dissolution of the cellular structures to both alloys, the duration is longer than necessary for the maraging steel region, leading to some level of grain coarsening observed in Figure 3.9. The aging step is also unnecessary for the CoCrMo region but can lead to some level of material hardening with no changes in the cellular structure [20]. More importantly, a unique interface morphology was detected after the combined effects of heat treatment. The contrast in martensite formation mechanism is then analyzed based on the results of parent austenite grain reconstruction of the heat-treated maraging steel region in Figure 3.15b and investigation of fcc-bcc boundary orientation relationships along the interface after heat treatment presented in Figure 3.15d. Since a uniform compositional gradient is formed, the discontinuous fcc phase islands and martensite subgrains are

replaced with consistent parallel laths that are oriented along the <111> // BD. While a hierarchical equiaxed packet-block-lath martensite structure is formed in the maraging steel region, the presence of Co and Cr near the interface limits nucleation sites and promotes directional lath growth. Based on the phase map in Figure 3.9, austenite retention is suppressed due to the applied solution heat treatment. Consequently, solute homogenization resulted in a decrease in local strains due to uniform transformation between austenite grains. Previous studies have reported that skipping the solution heat treatment step results in the formation of more austenite after direct aging [9,19]. Precise control of the printing parameters can also dictate the amount of retained austenite after printing [17]. Finally, the martensite grains become finer closer to the CoCrMo region, as there is limited driving force for growth beyond the Fe- and Ni-rich maraging steel regions.

3.4.3 Effect of heat treatment on the mechanical properties

The overall change in hardness shows early evidence of the successful application of the heat treatment strategy to both base alloys. For the maraging steel region, the significant increase in hardness indicates precipitation strengthening after heat treatment, since solution-treated and aged maraging steel samples typically exhibit hardness values greater than 600 HV [42,53,54]. Bai et al. [9] also observed that the abrupt increase in hardness depends more on the abundance of martensite formed after aging and is not heavily affected by the solution heat treatment process. For the CoCrMo region, the reduction in hardness implies enhanced ductility, as was similarly observed in [13]. Tensile testing of the as-built samples caused premature fracture close to the interface, which can be attributed to strain mismatch between maraging steel and CoCrMo during loading. Despite having similar tensile properties, the maraging steel section's marginally superior hardness and tensile

strength lead to more noticeable contraction near the failure surface in the CoCrMo section. The appearance of scattered irregular dimples is indicative of a ductile intragranular fracture in the as-printed surface [55], and the observed initial ductility (14.7 ± 1.3 % εf) of the combined AM structure facilitated the nucleation and growth of pores throughout the fracture surface. However, due to the heterogeneous microstructure and the presence of localized thermal strain post-printing, a brittle mode of failure was accelerated, evident from the formation of planes that cracked smoothly and interspersed with coalescing voids. As-built samples typically exhibit anisotropy due to the nature of the fabrication process [17]. Furthermore, the scattered pores observed on the fracture surface can function as nucleation sites for micro-void accumulation, which can initiate crack growth due to stress concentration.

After heat treatment, distinct mechanical properties emerged for each alloy, and the resulting failure surface is also closer to the CoCrMo section. Volume shrinkage happened primarily on the CoCrMo side, and the precipitation strengthening allowed the maraging steel section to resist plastic deformation while absorbing the energy during the stretching process. Although the maraging steel region possesses low ductility, the overall ductility of the dual-alloy structure is enhanced following heat treatment. Based on the reduced number of dislocations and chemical homogenization after heat treatment, the overall toughness of the material increased. A ductile fracture surface was also observed in the heat-treated samples. Notably, no local inclusions or voids were detected, reinforcing the effectiveness of the applied solution heat treatment. The failure occurred preferentially in the CoCrMo region, and the extended deformation occurs primarily through strain-induced γ-fcc → ε-hcp martensite transformation [21,56,57]. Antunes et al. [22] also identified

through in-situ XRD investigation of tensile-loaded CoCrMo specimens that solution heat treatment prolongs the γ-fcc → ε-hcp transformation and results in lesser ε-hcp phase transformation at lower lattice micro-strain values compared to as-built samples. As stretching continues, ε-hcp phase transformation steadily increases in solution-treated samples and reaches peak transformation at high strain values.

3.5 Conclusions

The interface characteristics of a dual-metal CoCrMo alloy-maraging steel component fabricated by laser powder bed fusion in the as-built and solution heat treated and aged conditions were investigated in this study. Based on the results, the following conclusions were established:

- The microstructures obtained from optical microscopy, SEM imaging, EBSD technique and XRD analysis suggest that the application of solution heat treatment benefits both maraging steel and CoCrMo alloys by improving ductility, relieving residual stresses, and promoting structural homogeneity along the interface.
- The hardness measurement from nano-indentation implies that a successful precipitation strengthening and stress relief occurred in the multi-material alloy. The mechanical testing results revealed that the tensile strength was maintained at 1185 ± 18 MPa before and after heat treatment, complemented with an increase in elongation from 14.7 ± 1.3 % % to 27.1 ± 2.1 %. Based on the fracture point after tensile testing and the individual mechanical properties of the base alloys, the strength and ductility measured can be associated with the strength of the bond between CoCrMo and maraging steel.

- The mixed structure observed in the interface of the as-printed samples is a result of discontinuous martensite transformation of fully fcc phase columnar grains experiencing solute segregation. The untransformed fcc islands are a product of the combined effects of growth orientation before solidification, negligible presence of secondary phases, local alloying element distribution, local stresses due to martensite volume expansion, and intermixed grain and cellular growth.

- Heat treatment results to the decomposition of cellular boundaries and converts the diverse as-printed interface into homogenous parallel martensite laths which nucleates and grows depending on the solute distribution.

- The successful combination of maraging steel and CoCrMo alloy as an MMAM structure provides a variety of potential applications and benefits, particularly in fields requiring high performance and durability. Supplemental heat treatment can be employed to enhance maraging steel's strength by precipitation strengthening without compromising the strength of CoCrMo alloy and the interface.

3.6 Chapter 3 References

[1] A. Vassilakos, J. Giannatsis, V. Dedoussis, Fabrication of parts with heterogeneous structure using material extrusion additive manufacturing, Virtual Phys. Prototyp. 16 (2021) 267–290. https://doi.org/10.1080/17452759.2021.1919154.

[2] O.V. Eliseeva, T. Kirk, P. Samimi, R. Malak, R. Arróyave, A. Elwany, I. Karaman, Functionally Graded Materials through robotics-inspired path planning, Mater. Des. 182 (2019). https://doi.org/10.1016/j.matdes.2019.107975.

[3] H. Gu, C. Wei, L. Li, Q. Han, R. Setchi, M. Ryan, Q. Li, Multi-physics modelling of molten pool development and track formation in multi-track, multi-layer and multi-material selective laser melting, Int. J. Heat Mass Transf. 151 (2020). https://doi.org/10.1016/j.ijheatmasstransfer.2020.119458.

[4] Y. Tian, R. Palad, C. Aranas, Microstructural evolution and mechanical properties of a newly designed steel fabricated by laser powder bed fusion, Addit. Manuf. 36 (2020) 101495. https://doi.org/10.1016/j.addma.2020.101495.

[5] Y. Wen, B. Zhang, R.L. Narayan, P. Wang, X. Song, H. Zhao, U. Ramamurty, X. Qu, Laser powder bed fusion of compositionally graded CoCrMo-Inconel 718, Addit. Manuf. 40 (2021) 101926. https://doi.org/10.1016/j.addma.2021.101926.
[6] C. Wei, L. Li, Recent progress and scientific challenges in multi-material additive manufacturing via laser-based powder bed fusion, Virtual Phys. Prototyp. 16 (2021) 347–371. https://doi.org/10.1080/17452759.2021.1928520.
[7] F.F. Conde, J.A. Avila, J.P. Oliveira, N. Schell, M.F. Oliveira, J.D. Escobar, Effect of the as-built microstructure on the martensite to austenite transformation in a 18Ni maraging steel after laser-based powder bed fusion, Addit. Manuf. 46 (2021) 102122. https://doi.org/10.1016/j.addma.2021.102122.
[8] S. Dehgahi, R. Alaghmandfard, J. Tallon, A. Odeshi, M. Mohammadi, Microstructural evolution and high strain rate compressive behavior of as-built and heat-treated additively manufactured maraging steels, Mater. Sci. Eng. A 815 (2021) 141183. https://doi.org/10.1016/j.msea.2021.141183.
[9] Y. Bai, C. Zhao, Y. Zhang, H. Wang, Microstructure and mechanical properties of additively manufactured multi-material component with maraging steel on CrMn steel, Mater. Sci. Eng. A 802 (2021) 140630. https://doi.org/10.1016/j.msea.2020.140630.
[10] T.C. Henry, F.R. Phillips, D.P. Cole, E. Garboczi, R.A. Haynes, T. Johnson, In situ fatigue monitoring investigation of additively manufactured maraging steel, Int. J. Adv. Manuf. Technol. 107 (2020) 3499–3510. https://doi.org/10.1007/s00170-020-05255-4.
[11] Y. Kajima, A. Takaichi, N. Kittikundecha, T. Nakamoto, T. Kimura, N. Nomura, A. Kawasaki, T. Hanawa, H. Takahashi, N. Wakabayashi, Effect of heat-treatment temperature on microstructures and mechanical properties of Co–Cr–Mo alloys fabricated by selective laser melting, Mater. Sci. Eng. A 726 (2018) 21–31. https://doi.org/10.1016/j.msea.2018.04.048.
[12] D.T. De Macedo, L.B. Cruvinel, A.L. Neto, G.E. Totten, L.C. Casteletti, Thermal spray coatings on an aged 7475 aluminum alloy substrate, in: 2007: pp. 346–350.
[13] Y. Kajima, A. Takaichi, N. Kittikundecha, T. Nakamoto, T. Kimura, N. Nomura, A. Kawasaki, T. Hanawa, H. Takahashi, N. Wakabayashi, Effect of heat-treatment temperature on microstructures and mechanical properties of Co–Cr–Mo alloys fabricated by selective laser melting, Mater. Sci. Eng. A 726 (2018) 21–31. https://doi.org/10.1016/j.msea.2018.04.048.
[14] B. Vamsi Krishna, W. Xue, S. Bose, A. Bandyopadhyay, Functionally graded Co–Cr–Mo coating on Ti–6Al–4V alloy structures, Acta Biomater. 4 (2008) 697–706. https://doi.org/10.1016/j.actbio.2007.10.005.
[15] P. Ganesh, A. Moitra, P. Tiwari, S. Sathyanarayanan, H. Kumar, S.K. Rai, R. Kaul, C.P. Paul, R.C. Prasad, L.M. Kukreja, Fracture behavior of laser-clad joint of Stellite 21 on AISI 316L stainless steel, Mater. Sci. Eng. A 527 (2010) 3748–3756. https://doi.org/10.1016/j.msea.2010.03.017.
[16] J. Mutua, S. Nakata, T. Onda, Z.-C. Chen, Optimization of selective laser melting parameters and influence of post heat treatment on microstructure and mechanical properties of maraging steel, Mater. Des. 139 (2018) 486–497. https://doi.org/10.1016/j.matdes.2017.11.042.

[17] B. Mooney, K.I. Kourousis, R. Raghavendra, Plastic anisotropy of additively manufactured maraging steel: Influence of the build orientation and heat treatments, Addit. Manuf. 25 (2019) 19–31. https://doi.org/10.1016/j.addma.2018.10.032.
[18] E.A. Jägle, P.-P. Choi, J. Van Humbeeck, D. Raabe, Precipitation and austenite reversion behavior of a maraging steel produced by selective laser melting, J. Mater. Res. 29 (2014) 2072–2079. https://doi.org/10.1557/jmr.2014.204.
[19] F.F. Conde, J.D. Escobar, J.P. Oliveira, A.L. Jardini, W.W. Bose Filho, J.A. Avila, Austenite reversion kinetics and stability during tempering of an additively manufactured maraging 300 steel, Addit. Manuf. 29 (2019) 100804. https://doi.org/10.1016/j.addma.2019.100804.
[20] M. Roudnická, O. Molnárová, J. Drahokoupil, J. Kubásek, J. Bigas, V. Šreibr, D. Paloušek, D. Vojtěch, Microstructural instability of L-PBF Co-28Cr-6Mo alloy at elevated temperatures, Addit. Manuf. 44 (2021) 102025. https://doi.org/10.1016/j.addma.2021.102025.
[21] A. Takaichi, Y. Kajima, N. Kittikundecha, H.L. Htat, H.H. Wai Cho, T. Hanawa, T. Yoneyama, N. Wakabayashi, Effect of heat treatment on the anisotropic microstructural and mechanical properties of Co–Cr–Mo alloys produced by selective laser melting, J. Mech. Behav. Biomed. Mater. 102 (2020) 103496. https://doi.org/10.1016/j.jmbbm.2019.103496.
[22] L.H.M. Antunes, J.J. Hoyos, T.C. Andrade, P.W.C. Sarvezuk, L. Wu, J.A. Ávila, J.P. Oliveira, N. Schell, A.L. Jardini, J. Žilková, P.F. da Silva Farina, H.F.G. Abreu, M. Béreš, Deformation-induced martensitic transformation in Co-28Cr-6Mo alloy produced by laser powder bed fusion: Comparison surface vs. bulk, Addit. Manuf. 46 (2021) 102100. https://doi.org/10.1016/j.addma.2021.102100.
[23] K.K. Bawane, D. Srinivasan, D. Banerjee, Microstructural Evolution and Mechanical Properties of Direct Metal Laser-Sintered (DMLS) CoCrMo After Heat Treatment, Metall. Mater. Trans. A 49 (2018) 3793–3811. https://doi.org/10.1007/s11661-018-4771-4.
[24] K. Chadha, Y. Tian, J. Pasco, C. Aranas, Dual-metal laser powder bed fusion of iron- and cobalt-based alloys, Mater. Charact. 178 (2021) 111285. https://doi.org/10.1016/j.matchar.2021.111285.
[25] M. Zhang, Y. Yang, C. Song, Y. Bai, Z. Xiao, An investigation into the aging behavior of CoCrMo alloys fabricated by selective laser melting, J. Alloys Compd. 750 (2018) 878–886. https://doi.org/10.1016/j.jallcom.2018.04.054.
[26] G. Özer, A. Karaaslan, A Study on the Effects of Different Heat-Treatment Parameters on Microstructure–Mechanical Properties and Corrosion Behavior of Maraging Steel Produced by Direct Metal Laser Sintering, Steel Res. Int. 91 (2020). https://doi.org/10.1002/srin.202000195.
[27] G.B. Bang, J.H. Park, W.R. Kim, S.-K. Hyun, H.-K. Park, T.W. Lee, H.G. Kim, Study on the effect of preheating temperature of SLM process on characteristics of CoCrMo alloy, Mater. Sci. Eng. A 841 (2022) 143020. https://doi.org/10.1016/j.msea.2022.143020.
[28] H.F. López, A.J. Saldivar-Garcia, Martensitic Transformation in a Cast CoCrMo-C Alloy, Metall. Mater. Trans. A 39 (2008) 8–18. https://doi.org/10.1007/s11661-007-9370-8.

[29] M. Roudnická, J. Kubásek, L. Pantělejev, O. Molnárová, J. Bigas, J. Drahokoupil, D. Paloušek, D. Vojtěch, Heat treatment of laser powder-bed-fused Co–28Cr–6Mo alloy to remove its microstructural instability by massive FCC→HCP transformation, Addit. Manuf. 47 (2021) 102265. https://doi.org/10.1016/j.addma.2021.102265.
[30] M. Sage, C. Guillaud, Méthode d'analyse quantitative des variétés allotropiques du cobalt par les rayons X, Rev. Métallurgie 47 (1950) 139–145. https://doi.org/10.1051/metal/195047020139.
[31] A. Ben-Artzy, A. Reichardt, J.-P. Borgonia, R.P. Dillon, B. McEnerney, A.A. Shapiro, P. Hosemann, Compositionally graded SS316 to C300 Maraging steel using additive manufacturing, Mater. Des. 201 (2021) 109500. https://doi.org/10.1016/j.matdes.2021.109500.
[32] S. Wei, P. Kumar, K.B. Lau, D. Wuu, L.-L. Liew, F. Wei, S.L. Teo, A. Cheong, C.K. Ng, B. Zhang, C.C. Tan, P. Wang, U. Ramamurty, Effect of heat treatment on the microstructure and mechanical properties of 2.4 GPa grade maraging steel fabricated by laser powder bed fusion, Addit. Manuf. 59 (2022) 103190. https://doi.org/10.1016/j.addma.2022.103190.
[33] L. Kučerová, K. Burdová, Š. Jeníček, I. Chena, Effect of solution annealing and precipitation hardening at 250 °C–550 °C on microstructure and mechanical properties of additively manufactured 1.2709 maraging steel, Mater. Sci. Eng. A 814 (2021) 141195. https://doi.org/10.1016/j.msea.2021.141195.
[34] S. Dehgahi, M. Sanjari, M.H. Ghoncheh, B.S. Amirkhiz, M. Mohammadi, Concurrent improvement of strength and ductility in heat-treated C300 maraging steels produced by laser powder bed fusion technique, Addit. Manuf. 39 (2021) 101847. https://doi.org/10.1016/j.addma.2021.101847.
[35] X. Liu, X. Zhou, B. Xu, J. Ma, C. Zhao, Z. Shen, W. Liu, Morphological Development of Sub-Grain Cellular/Bands Microstructures in Selective Laser Melting, Materials 12 (2019) 1204. https://doi.org/10.3390/ma12081204.
[36] L.H.M. Antunes, J.J. Hoyos, T.C. Andrade, P.W.C. Sarvezuk, L. Wu, J.A. Ávila, J.P. Oliveira, N. Schell, A.L. Jardini, J. Žilková, P.F. da Silva Farina, H.F.G. Abreu, M. Béreš, Deformation-induced martensitic transformation in Co-28Cr-6Mo alloy produced by laser powder bed fusion: Comparison surface vs. bulk, Addit. Manuf. 46 (2021) 102100. https://doi.org/10.1016/j.addma.2021.102100.
[37] S. Kurosu, H. Matsumoto, A. Chiba, Isothermal Phase Transformation in Biomedical Co-29Cr-6Mo Alloy without Addition of Carbon or Nitrogen, Metall. Mater. Trans. A 41 (2010) 2613–2625. https://doi.org/10.1007/s11661-010-0273-8.
[38] S. Mahajan, M.L. Green, D. Brasen, A model for the FCC→HCP transformation, its applications, and experimental evidence, Metall. Trans. A 8 (1977) 283–293. https://doi.org/10.1007/BF02661642.
[39] G. Barucca, E. Santecchia, G. Majni, E. Girardin, E. Bassoli, L. Denti, A. Gatto, L. Iuliano, T. Moskalewicz, P. Mengucci, Structural characterization of biomedical Co–Cr–Mo components produced by direct metal laser sintering, Mater. Sci. Eng. C 48 (2015) 263–269. https://doi.org/10.1016/j.msec.2014.12.009.
[40] S.M.J. Razavi, A. Avanzini, G. Cornacchia, L. Giorleo, F. Berto, Effect of heat treatment on fatigue behavior of as-built notched CoCrMo parts produced by Selective Laser Melting, Int. J. Fatigue 142 (2021). https://doi.org/10.1016/j.ijfatigue.2020.105926.

[41] H. Li, M. Wang, D. Lou, W. Xia, X. Fang, Microstructural features of biomedical cobalt–chromium–molybdenum (CoCrMo) alloy from powder bed fusion to aging heat treatment, J. Mater. Sci. Technol. 45 (2020) 146–156. https://doi.org/10.1016/j.jmst.2019.11.031.
[42] S. Yin, C. Chen, X. Yan, X. Feng, R. Jenkins, P. O'Reilly, M. Liu, H. Li, R. Lupoi, The influence of aging temperature and aging time on the mechanical and tribological properties of selective laser melted maraging 18Ni-300 steel, Addit. Manuf. 22 (2018) 592–600. https://doi.org/10.1016/j.addma.2018.06.005.
[43] L. Kučerová, I. Zetková, Š. Jeníček, K. Burdová, Hybrid parts produced by deposition of 18Ni300 maraging steel via selective laser melting on forged and heat treated advanced high strength steel, Addit. Manuf. 32 (2020) 101108. https://doi.org/10.1016/j.addma.2020.101108.
[44] A. Ben-Artzy, A. Reichardt, J.-P. Borgonia, R.P. Dillon, B. McEnerney, A.A. Shapiro, P. Hosemann, Compositionally graded SS316 to C300 Maraging steel using additive manufacturing, Mater. Des. 201 (2021) 109500. https://doi.org/10.1016/j.matdes.2021.109500.
[45] K.G. Prashanth, J. Eckert, Formation of metastable cellular microstructures in selective laser melted alloys, J. Alloys Compd. 707 (2017) 27–34. https://doi.org/10.1016/j.jallcom.2016.12.209.
[46] R. Ghanavati, H. Naffakh-Moosavy, M. Moradi, Additive manufacturing of thin-walled SS316L-IN718 functionally graded materials by direct laser metal deposition, J. Mater. Res. Technol. 15 (2021) 2673–2685. https://doi.org/10.1016/j.jmrt.2021.09.061.
[47] Z. Wang, S.Y. Tang, S. Scudino, Yu.P. Ivanov, R.T. Qu, D. Wang, C. Yang, W.W. Zhang, A.L. Greer, J. Eckert, K.G. Prashanth, Additive manufacturing of a martensitic Co–Cr–Mo alloy: Towards circumventing the strength–ductility trade-off, Addit. Manuf. 37 (2021) 101725. https://doi.org/10.1016/j.addma.2020.101725.
[48] C.-Y. Huang, H.-C. Ni, H.-W. Yen, New protocol for orientation reconstruction from martensite to austenite in steels, Materialia 9 (2020) 100554. https://doi.org/10.1016/j.mtla.2019.100554.
[49] K. Chadha, Y. Tian, P. Bocher, J.G. Spray, C. Aranas Jr., Microstructure evolution, mechanical properties and deformation behavior of an additively manufactured maraging steel, Materials 13 (2020). https://doi.org/10.3390/ma13102380.
[50] N. Saunders, Z. Guo, X. Li, A.P. Miodownik, J.P. Schillé, The calculation of TTT and CCT diagrams for general steels, Calc. TTT CCT Diagr. Gen. Steels (2004) 1–12.
[51] J.M. Moyer, G.S. Ansell, The volume expansion accompanying the martensite transformation in iron-carbon alloys, Metall. Trans. A 6 (1975) 1785–1791. https://doi.org/10.1007/BF02642308.
[52] M.E. Fine, M. Meshii, C.M. Wayman, Z. Nishiyama, eds., MATERIALS SCIENCE AND TECHNOLOGY, in: Martensitic Transform., Academic Press, 1978: p. ii. https://doi.org/10.1016/B978-0-12-519850-9.50001-6.
[53] Y. Bai, Y. Yang, D. Wang, M. Zhang, Influence mechanism of parameters process and mechanical properties evolution mechanism of maraging steel 300 by selective laser melting, Mater. Sci. Eng. A 703 (2017) 116–123. https://doi.org/10.1016/j.msea.2017.06.033.

[54] C. Tan, K. Zhou, W. Ma, P. Zhang, M. Liu, T. Kuang, Microstructural evolution, nanoprecipitation behavior and mechanical properties of selective laser melted high-performance grade 300 maraging steel, Mater. Des. 134 (2017) 23–34. https://doi.org/10.1016/j.matdes.2017.08.026.
[55] S.L. Sing, S. Huang, W.Y. Yeong, Effect of solution heat treatment on microstructure and mechanical properties of laser powder bed fusion produced cobalt-28chromium-6molybdenum, Mater. Sci. Eng. A 769 (2020) 138511. https://doi.org/10.1016/j.msea.2019.138511.
[56] D. de Castro Girão, M. Béreš, A.L. Jardini, R.M. Filho, C.C. Silva, A. de Siervo, H.F. Gomes de Abreu, W.S. Araújo, An assessment of biomedical CoCrMo alloy fabricated by direct metal laser sintering technique for implant applications, Mater. Sci. Eng. C 107 (2020) 110305. https://doi.org/10.1016/j.msec.2019.110305.
[57] M. Roudnická, J. Kubásek, L. Pantělejev, O. Molnárová, J. Bigas, J. Drahokoupil, D. Paloušek, D. Vojtěch, Heat treatment of laser powder-bed-fused Co–28Cr–6Mo alloy to remove its microstructural instability by massive FCC→HCP transformation, Addit. Manuf. 47 (2021) 102265. https://doi.org/10.1016/j.addma.2021.102265.

Chapter 4: Heat Treatment Optimization

Background

In the previous chapter, the successful continuous laser powder bed fusion (L-PBF) of 18Ni(300) maraging steel and CoCrMo alloy was presented in detail. An initial conventional heat treatment step was also applied, and the resulting mechanical properties were compared to the original component. The next challenge is to fine-tune the material properties through heat treatment to meet the specific demands of the potential applications of this alloy combination, such as in injection molding, cutting machinery, and engine assemblies. An optimized heat treatment process after printing is crucial, but this step faces an obvious constraint: finding the right balance of temperature and exposure duration is tricky because each alloy responds differently to heat, undergoing unique transformations at various cycles. The main objectives in this chapter are twofold: achieving the best possible microstructure and mechanical strength for each alloy while making sure that the transition zones where the materials meet are compatible and strong.

Comprehensive analysis and characterization of mechanical properties and microstructural evolution has been performed through scanning electron microscopy (SEM), transmission electron microscopy (TEM), electron backscatter diffraction (EBSD), atom probe tomography (APT), microhardness tests, and uniaxial tensile tests. This investigation has led to some exciting discoveries with a number of useful and novel findings, given the limited research on how heat treatment impacts the fusion zones of these materials:

- The first-time observation of grain-scale variant selection during the martensitic solidification of L-PBF structures, influenced by recoil pressure from thermal cycling.
- The inherited absence of missing variants even after heat treatment when solution treatment is not applied.
- The potential for reducing austenite reversion caused by alloy depletion during precipitation through the application of homogenization and solution heat treatments.

These results open new research pathways in the analysis of combined structures and texture inheritance of printable alloys undergoing phase transformation during solidification and heat treatment.

This section is recently submitted to the journal Virtual and Physical Prototyping (after revision following the feedback of reviewers) as a research article entitled 'Evidence of grain-scale variant selection in multi-material laser powder bed fusion of FeNi- and CoCr-based alloys.'

Abstract

This study demonstrates the successful fabrication of a multi-material 18Ni(300) maraging steel - CoCrMo alloy using laser powder bed fusion (L-PBF), which in its as-built state, displays suboptimal mechanical performance. Addressing this, we propose different heat treatment strategies that mutually enhance the mechanical properties of both alloys. The intricate chemical diffusion and phase distribution mechanisms in the multi-material transition zones are also investigated. Comparative analysis of texture development, precipitation sequence, and mechanical properties of as-built and heat-treated maraging steel-CoCrMo dual structures at different scales has been conducted. The results indicate that post-processing at 1150 °C for 2 hours, 940 °C for 5 hours, and 490 °C for 6 hours achieved the highest tensile strength through cooperative strengthening of intragranular γ-ε transformation in CoCrMo, and Ni_3Ti precipitation in maraging steel. Adding the solution treatment at 1150 °C also balanced the formation of acicular Ni_3Ti clusters with Mo-rich clusters corresponding to $(Fe,Ni,Co)_2(Ti,Mo)$ precipitates, and revealed that chemical segregation and element depletion influence austenite reversion. Initial evidence of local grain variant selection has been revealed in as-built samples due to thermal cycling and repeated austenite reversion, which generates residual stresses, recoil forces, and convective flow. Surprisingly, the missing variants can also be inherited after heat treatment with insufficient solution temperatures.

4.1 Introduction

Multi-material additive manufacturing (MMAM) introduces a new design degree of freedom through strategic placement of compatible alloys within a heterogenous component. This approach results in multi-functional, cost-effective parts with tunable local characteristics, reduced reliance on vulnerable joint systems, and adaptability to combined environmental constraints [1,2]. With the fabrication goal of increasing the length-scale resolution of geometrical sophistication, the incremental deposition in Laser-based powder bed fusion (L-PBF) allows the formation of thin layer boundaries that promote raw material efficiency and limit alloy migration through interdiffusion [3,4]. The choice between a sharp, gradual, or intermediate material transition [5] should consider the solidification dynamics and compositional fit of the individual feed materials to be fused.

In this work, the combination of maraging steel and CoCrMo alloy was extensively investigated for MMAM, followed by post-processing. The directionality of the mechanical properties in the final product can be controlled according to the individual merits of both alloys: Maraging steels [6–8], known for having superior strength, weldability, and easier serviceability, can be tactically merged with CoCrMo alloys [9,10] which have better thermal stability, higher wear resistance, and inherent biocompatibility. The initial motivation for this material combination is for thermal transport and injection molding applications, wherein local material choice heavily depends on cost and complexity considerations [11]. However, successful post-processing and heat treatment will dramatically broaden its application to components requiring more comprehensive mechanical performance and standard certification, such as loadbearing structural

components [7], heavy tooling and cutting machinery, impact energy absorption assemblies [12], and automotive engine components [13].

Two main challenges emerge when designing a suitable heat treatment schedule for a MMAM component: first, the desired internal structure, dislocation distribution, texture, mechanical properties, and phase transformations should be achieved in each alloy; and second, the resulting alloy migration, intermetallic precipitation, and phase distribution along the transition zones should not introduce points of weaknesses and compromise the integrity of the entire structure. For CoCrMo alloys, the balance between the metastable γ-phase and martensitic ε-phase hinges on the interactions between several microstructural elements including stacking faults [14], recrystallized grains, coherent twins, pinning precipitates [15], and interstitial elements [16]. A prolonged exposure to 1150 °C for 6 hours has been proven successful in reducing residual stresses and eliminating anisotropic behavior for CoCrMo alloys produced using L-PBF, resulting in a stress-free structure with equiaxed grains [17]. Depending on the accumulation of Shockley partials and density of dislocations, the γ-ε transformation can take place through strain addition [9], annealing [14], diffusional massive transformation [18], or rapid cooling [19]. The subsequent growth predominantly occurs along parallel striations that extend in $\{111\}_\gamma$ habit planes [20].

For martensitic transformation in maraging steels, which will be the focus in this study, the crystal symmetry of the parent austenite (γ) grain often dictates a predetermined set of martensite child (α') orientations or 'variants' that minimizes the lattice mismatch during phase change [21]. Several orientation relationships have been used to define texture transfer after steel transformations, the simplest being the Bain relationship described as $\{001\}_\gamma \parallel \{001\}_\alpha$ and $<100>_\gamma \parallel <110>_\alpha$ [22]. This equates to a 45° rotation in each of the

three <100> axes. The Kurdjumov-Sachs (KS) relationship represents 24 possible variants through 90° rotations along the 24 <112> axes with the parallelism condition $\{111\}_\gamma \parallel \{110\}_\alpha$ and $<1\bar{1}0>_\gamma \parallel <1\bar{1}1>_\alpha$. On the other hand, the Nishiyama-Wassermann (NW) relationship corresponds to 12 potential variants through 95.2° rotations about the $<-1 + 2^{1/2} + 3^{1/2}, 1 + 2^{1/2} + 3^{1/2}, 2^{1/2}>$ axes [23] specified by the $\{111\}_\gamma \parallel \{110\}_\alpha$ and $<\bar{2}11>_\gamma \parallel <1\bar{1}0>_\alpha$ condition. Surrounding each Bain variant are four NW variants, each in between two of eight total KS variants that are clustered into relevant Bain Circles [24]. Other mutual orientation relations have been comprehensively investigated in Refs. [25,26].

The direct analysis of transformation texture development in AM structures becomes challenging due to the columnar dendritic morphology and accumulated thermal cycling during printing, which blurs the original γ grain boundaries. However, the parent γ-phase retention occuring in the interface of the MMAM component in this study reveals a new avenue for phase transformation analysis. Variant distribution and local selection in additively manufactured maraging steels have been recently observed by Truong et al [27], but the analysis relied on full parent reconstruction due to the single phase matrix after solidification. Since retained γ-phase exists in the interface of the multi-material component in this study, the orientation of the parent and child grains can be directly correlated. Recognizing the other processing considerations explained above, the primary objective of this study is to systematically investigate the effects of continuous LPBF and heat treatments to the mechanical properties and microstructural evolution in CoCrMo alloy-maraging steel dual structure. Main concepts of phase transformation, texture development, strain distribution, and precipitate nucleation were correlated to the resulting hardness and tensile properties. This work also proposes new perspectives on solidification

and variant selection during AM and provides guidance in post-processing analysis for MMAM components.

4.2 Materials and Methods

4.2.1 Alloy preparation

The fabricated MMAM component was produced from voestalpine Additive Manufacturing Center Ltd. (vAMC) in Mississauga, Ontario, Canada, using gas atomized powders of maraging steels and CoCrMo alloys with particle diameter ranges of 15-70 μm and 15-50 μm, respectively. The continuous L-PBF process has been discussed in detail on the previous work presented in Ref. [11], utilizing an EOS M290 machine under Ar gas atmosphere equipped with the following set parameters for both powders: 1100 mm/s laser speed, zigzag stripe hatching style with 50° alternating rotation, 50 μm target layer thickness, hatch distance of 0.1 mm, and laser power of 280-300 W. The maraging steel layers are loaded and melted first, syncing the switch in the powder recoater to CoCrMo alloy powders once the target volume is reached. No cracks were observed in the component after printing. The chemical composition of the powders was validated through Inductively Coupled Plasma - Optical Emission Spectroscopy (ICP-OES) tests, and the elemental constituents are shown in Table 4.1. Representative samples and tensile coupons incorporating the material transition zone in the middle were prepared for separate analysis and heat treatment.

Table 4.1. Chemical composition of maraging steel and CoCrMo feed powders (in wt %)

Material	Fe	Co	Cr	Ni	Mo	Ti	Mn	Si	C
Maraging	balance	9.30	-	18.00	4.90	1.10	0.15	0.10	0.03
CoCrMo	0.75	balance	30.00	0.10	7.00	-	1.00	1.00	0.16

4.2.2 Heat Treatment

As-built samples were subjected to three heat treatment conditions detailed in Figure 4.1 using a quartz tube furnace in an Ar gas atmosphere. Differential scanning calorimetry investigations on CoCrMo fabricated using L-PBF [28] identified two distinct endothermic peaks at 965 °C and 1139 °C, which are associated with the γ-ε phase transition and precipitate dissolution temperatures, respectively. On the other hand, dilatometry tests on maraging steel samples in this study using a 1 °C/s heating rate determined the precipitation range of 450-550 °C, the austenite start (A_s) at 660 °C, and the austenite finish (A_f) at 950 °C, while the solutionizing temperature is expected above 1100 °C [29]. The temperature and exposure durations were strategically chosen based on the desired mechanical properties and internal structures for both alloys. For HT1, exposure at 1150 °C for 6 hours followed by 490 °C for 6 hours were employed. The first step is to trigger complete solution treatment, stress relief and high ductility recovery in the CoCrMo at the expense of coarser prior austenite grain size in maraging steel, while the second step is for aging treatment of maraging steel below the γ-ε transformation region of CoCrMo. For HT2, soaking at 940 °C for 2 hours followed by 490 °C for 6 hours were chosen. This focuses on achieving high strength in maraging steel at the expense of some ductility in CoCrMo. The first step acts as an austenitizing treatment for maraging steel and short aging for CoCrMo alloy, while the second step acts as an aging treatment for maraging steel similar to HT1. The final treatment condition in HT3 is performed in three steps: 1150 °C for 2 hours + 940 °C for 5 hours + 490 °C for 6 hours. With the aim of balancing the strength achieved from both alloys, the first step is a shortened solution treatment to recover some ductility in CoCrMo, followed by considerable γ-ε phase massive transformation in the second step. For the maraging steel, the three steps represent a solution-austenitizing-aging treatment that

incorporates the CoCrMo exposure durations. Heating rates for all temperatures were set at 5 °C/min and samples were water quenched after the set duration.

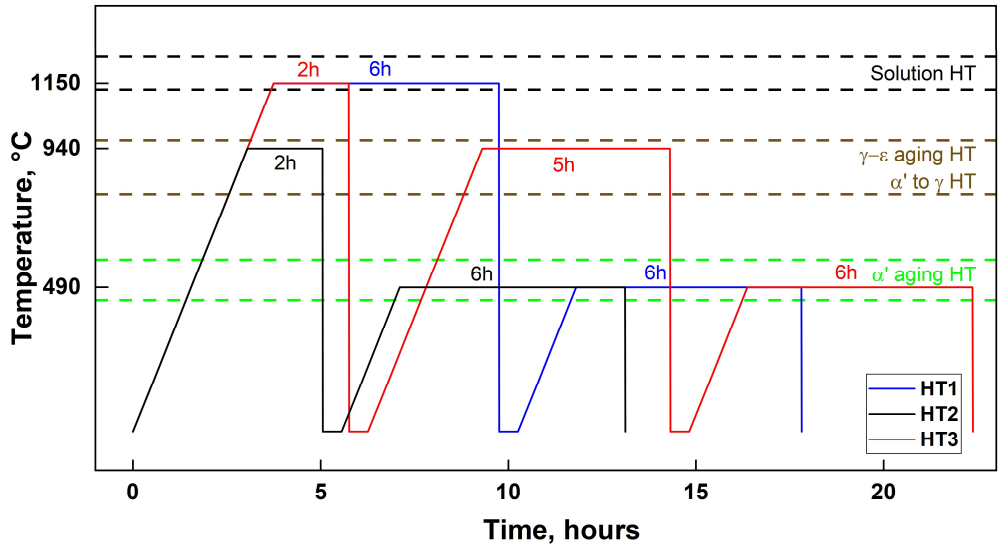


Figure 4.1. Schematic illustration of three heat treatment schedules (HT1, HT2, and HT3) employed in this work, with the relevant temperatures and holding times considered for both alloys.

4.2.3 Material Characterization

Microscopic analysis was performed using a JEOL JSM 6010 SEM on mirror polished samples obtained parallel to the build direction (BD) to investigate the as-built and heat-treated microstructures. Electrochemical etching with an ammonium persulfate solution for 10 s at 6 V was applied to the maraging steel region, while a mixture of 10% H_2SO_4 and CH_3OH solution for 25 s at 6V was applied to the CoCrMo region. Heat-treated CoCrMo specimens were electrochemically etched in a 9% HCl solution at 4V for 10 s. To correlate the chemical distribution and texture development along the transition zones of all conditions, energy-dispersive spectroscopy (EDS) and electron backscatter diffraction (EBSD) was simultaneously performed using a Scios 2 DualBeam SEM system equipped with an EBSD detector and EDS analyzer. All inverse pole figure (IPF), kernel average misorientation (KAM), EDS, and phase maps were generated using the Aztec Crystal

software. In-depth pole figure and variant analysis was performed using a custom MATLAB code utilizing the MTEX software [30] and previous works from Ref [26]. Transmission electron microscopy (TEM) foils were electropolished in a twin-jet Tenupol apparatus in 5% perchloric acid in methanol at -20°C at a voltage of 15V. TEM was performed on a JEOL 2100F FEG-TEM at 200 kV acceleration voltage. Atom probe tomography (APT) samples were prepared by the standard two-step electropolishing [31]. APT data was collected on a CAMECA Local Electrode Atom Probe LEAP 5000XR instrument, at 25 K with a pulse fraction of 20%, a pulse repetition rate of 200 kHz and a detection rate of 0.5%. APT data were reconstructed and analyzed with the IVAS embedded in CAMECA AP suite 6 software.

To examine the influence of the internal structure on mechanical properties, uniaxial tensile tests and microhardness measurements were conducted on as-built and heat-treated specimens. Hardness tests were carried out using the iMicro KLA nano-indenter with a set load of 1 N and indentation depth of 5000 nm, repeating each measurement five times in 17 locations across the transition zones while maintaining a 50 μm indent spacing (total length of ~850 μm). In accordance with ASTM-E8 standards, tensile testing of cylindrical MMAM coupons featuring a 16 mm gauge length and 4 mm diameter were implemented at a nominal strain rate of 0.005 s^{-1} using an Instron 1332 machine equipped with a 50 kN load cell.

4.3 Results

4.3.1 Microstructural analysis of as-built samples

Figure 4.2a illustrates the volatile as-built interface structure which exhibits a blend of fine martensitic maraging steel cells and large columnar CoCrMo grains. The addition of the

initial CoCrMo layers leads to non-uniform martensitic solidification in the exposed maraging steel layers, which creates a unique cellular and melt pool configuration due to the phase resemblance of the two alloys before solidification. The slightly lower thermal conductivity of CoCrMo also results in a coarser sub-grain structure. The acicular structure of martensite is influenced by the local composition and temperature gradient that evolves along the building direction, which leads to the penetration of laths into CoCrMo. This structure reinforces the interfacial bonding along the immiscible interface and leads to a compatible transition as the new material solidifies.

The first material to be deposited is maraging steel, and a closer look at the microstructures in Figure 4.2b and Figure 4.2d obtained along the building direction (BD) show familiar AM structures with melt pool boundaries that have an average width of ~165 ± 17 μm and depth of ~55 ± 13 μm surrounded by unevenly sized cells with an average diameter of 0.45 ± 0.1 μm and thickness of ~75 nm. The primary cellular spacing (λ_1) corresponds to an approximate cooling rate of 6.2 $\times 10^6$ based on the equation CR $=\left(\frac{\lambda_1}{80}\right)^{-\frac{1}{0.33}}$ [32,33]. Due to the heat flow generated during printing, most columnar structures marked by red arrows in Figure 4.2b preferentially expand perpendicular to the melt tracks and blend with the finer cells developed in the melt cores. The typical heterogenous cellular microstructure can also be recognized in the CoCrMo alloy region shown in Figure 4.2c and Figure 4.2e. The observed melt tracks have an average width of ~165 ± 15 μm and melt pool depth of ~54 ± 11 μm. The cellular spacing (λ_1) of 0.51 ± 0.09 μm corresponds to a cooling rate of 4.5 $\times 10^6$, which is very similar with maraging steel due to the small difference in thermal conductivity (13 W/m-K for CoCrMo compared to 15 W/m-K for maraging steel). Multiple groups of elongated cells that stretch along the melt tracks are mixed with spherical cells

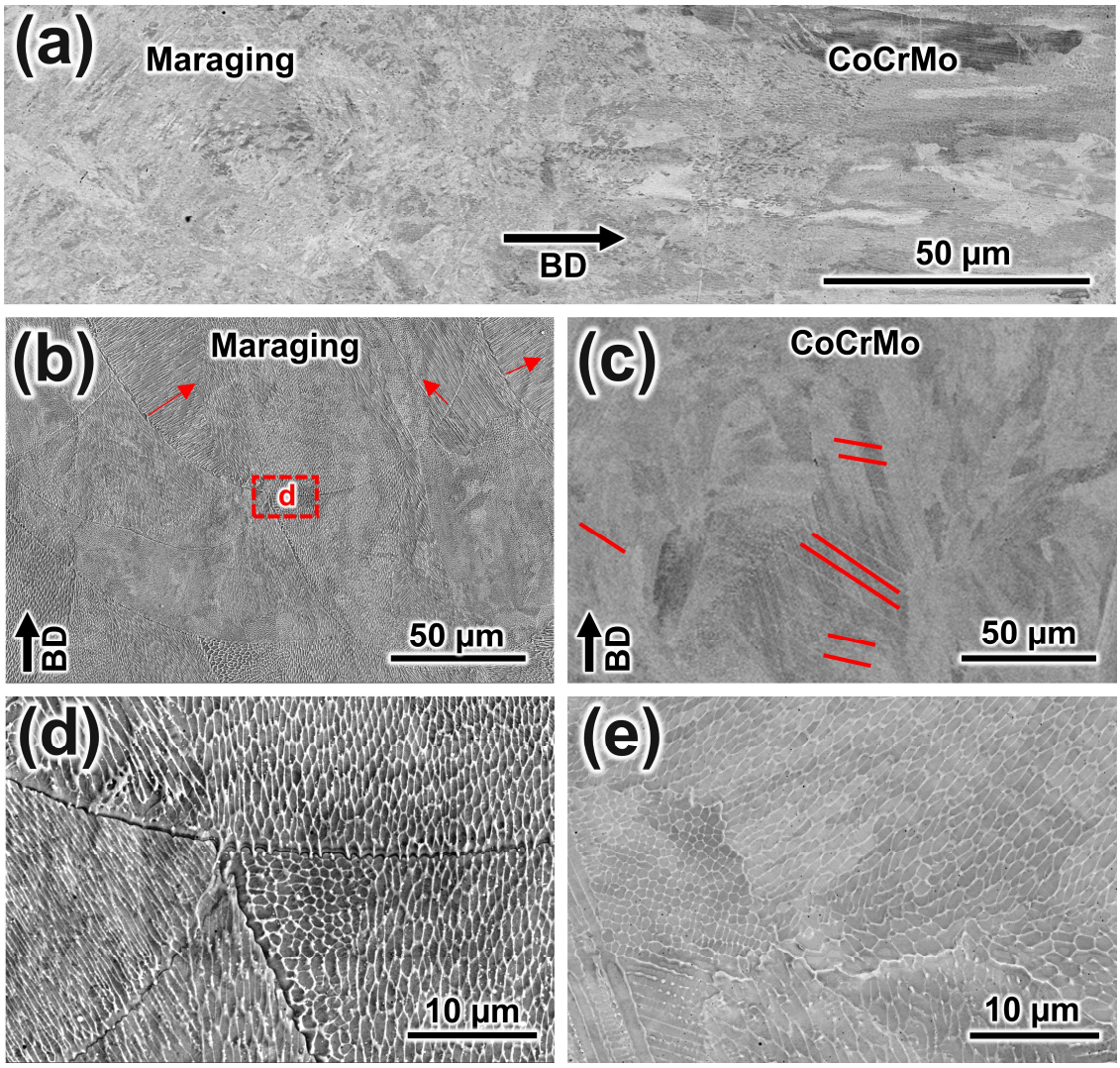


Figure 4.2. Microstructural features of the as-built MMAM component: (a) transition zone, (b, d) maraging steel cellular structure, and (c, e) CoCrMo cellular structure.

that are primarily observed inside the track cores, and the cell boundaries have a thickness of ~80 nm. The underlying grains are predominantly columnar and exhibit epitaxial growth across multiple layers of the melted powder. Groups of parallel bands identified as ε-phase striations [15,34] and marked by red lines in Figure 4.2c result in a striated structure that generally extends across melt tracks but mostly terminate along grain boundaries (some transgranular bands still exist).

Figure 4.3 presents the phase distribution, orientation properties, and kernel average misorientation (KAM) map at the interface of the freshly printed sample. A fragmented martensitic structure is observed in the maraging steel region, consisting exclusively of bcc phase with an average crystallographic lath thickness of 2.3 ± 0.7 μm. Multiple laths show a similar alignment to both the <100>//BD and <111>//BD, but the growth of continuous blocks has been interrupted by the variable solidification conditions during printing. This results in diverse lath sizes and detached strips (marked in black in Figure 4.3b) that could have fully formed under consistent thermal conditions but are instead contributing to a more refined microstructure. The underlying matrix that is influenced by the melt pool morphology still shows alignment between <100>//BD and <111>//BD, forming columnar boundaries over several layers growing epitaxially.

During initial deposition of the CoCrMo layers, the liquefied region contains a mixed composition distribution from both alloys. Even though both powders dissolve to fcc phase after melting, only the maraging steel composition undergoes a bcc phase transformation during solidification. Co- and Cr-rich regions shown in EDS maps in Figure 4.3d and Figure 4.3e (taken from the area highlighted in Figure 4.3a) had a higher tendency of retaining large grain fcc regions upon cooling, while Fe-rich regions experience isolated martensitic transformation that usually results to finer laths. Segregation of Co and Cr minimizes the expected martensite start temperature, leading to untransformed fcc islands in the center of the melt. The generated circular flow also migrates Fe-rich alloying elements and allows fragmented lath solidification above the melt. The columnar structure with alloy segregation provides unique transformation conditions which form limited martensite variant types that will be identified in the discussion section. In particular,

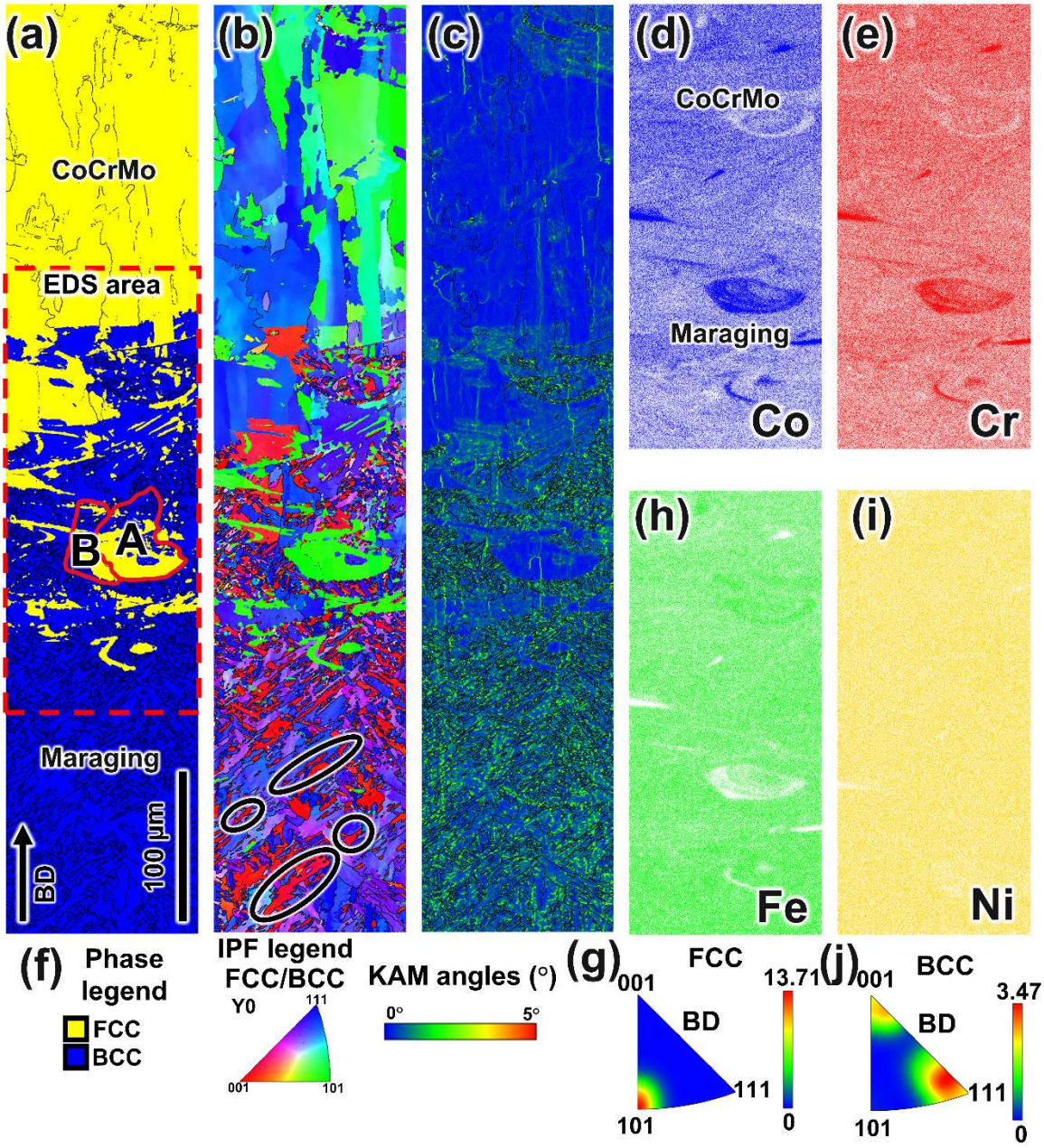


Figure 4.3. Texture development in the transition zone of the as-built sample: (a) phase map showing fcc and bcc structures, (b) inverse pole figure color map, (c) kernel average misorientation maps, (d,e,h,i) EDS maps for Co, Cr, Fe, and Ni, respectively, (f) corresponding legends for a-c, (g) IPF representation of fcc grains, and (j) IPF representation of bcc grains.

regions A and B in Figure 4.3a will be analyzed later for grain-scale variant distribution. Other factors, such as accumulated thermal strain, partitioning of alloying elements with differing melting temperatures, and the turbulent mixing effects of Bénard-Marangoni flow

[35], result in residual fcc regions in the interface that resemble the prior melt pool boundaries. In addition, the KAM maps in Figure 4.3c show that the associated strain with the martensite transformation leads to areas with high concentration of low angle KAM values, enveloping untransformed fcc regions that are essentially strain-free. This is evident in some regions without isolated strips that have a reduced distribution of low misorientation values. After the ~240 μm mixed-phase interface takes shape, the successive layers resemble the original CoCrMo composition. Although melt pool sizes for both materials were similar, the grains for CoCrMo are larger and columnar, averaging 92 ± 11 μm in size. A strong texture along <110>//BD and <110>//BD can be observed, which notably resembles the texture preference observed in the fcc islands along the interface.

4.3.2 Microstructural analysis of heat-treated samples

The applied heat treatments generated the target microstructural changes at both alloys, but unique transformation mechanisms have been observed close to the interface of the dual-metal structures. The occurence of intermetallic precipitation is also investigated within the maraging steel region, especially since all conditions involved a 6-hour aging treatment at 490 °C. Sub-sections below will present the observations from HT1, HT2 and HT3.

4.3.2.1 Microstructure after HT1 (1150 °C for 6 hrs + 490 °C for 6 hrs)

Figure 4.4 shows microstructural features within key regions of the dual-alloy specimen following HT1. Dissolution of alloying elements in both base alloys occurred at the expense of the preexisting cellular structures. In the CoCrMo region, equiaxed polygonal grains are predominant, while the maraging steel region is characterized by a hierarchical packet-block-lath structure. The major axis of martensite laths that evolved near the

interface in Figure 4.4a aligns with the composition gradient (parallel to the BD) and terminates at the CoCrMo grains while preserving epitaxial growth. Significant lath size evolution is evident in the maraging microstructure in Figure 4.4b and Figure 4.4d. High-temperature conditions facilitated stress relief and uniform solute distribution, thereby promoting continuous nucleation and extension across all directions. On the other hand, huge grains that are devoid of ε-hcp bands but contain annealing twins (i.e., not present in the as-printed state in Fig. 2) formed in the CoCrMo region in Figure 4.4c and Figure 4.4e.

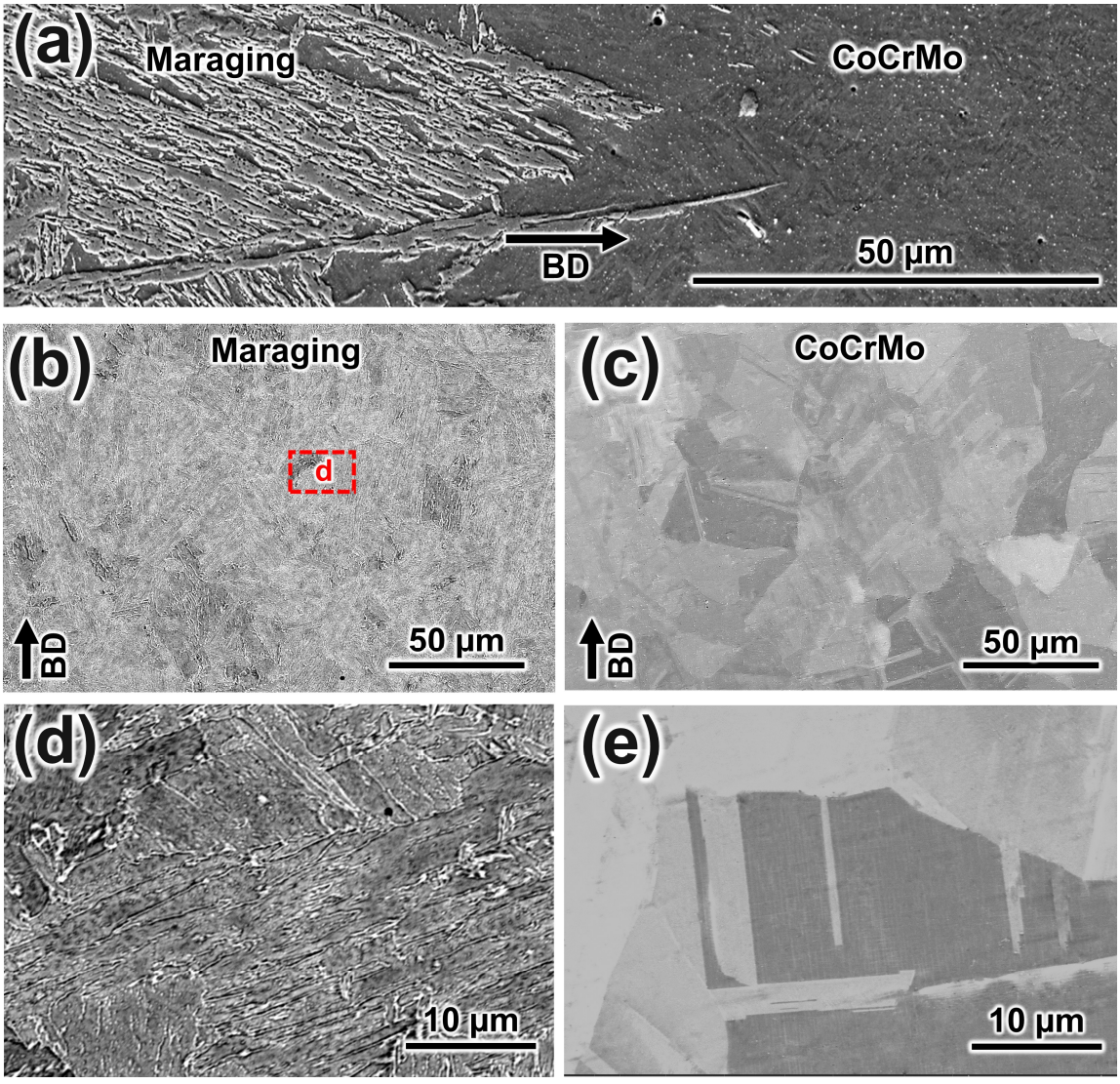


Figure 4.4. Microstructural features after HT1: (a) transition zone, (b, d) maraging steel lath structure, and (c, e) CoCrMo twin structure.

Crystallographic analysis of samples subjected to HT1 in Figure 5 further reveals that a well-defined phase boundary emerged at the interface, separating the bcc-phase martensite from the fcc-phase CoCrMo. Within the maraging steel region, large martensite blocks having widths averaging 6.4 ± 2.6 μm in thickness are evident. The previously observed texture and isolated martensite packets after printing have vanished, resulting in a randomized orientation distribution. Closer to the interface in Figure 4.5a, the fcc islands that formerly mirrored the shape of the melt pool are no longer visible, replaced by thick martensite laths aligned along <111>//BD and extending perpendicular to the interface. Martensite packets in Figure 4.5b that are far from the interface show cooperative growth and energy minimization in all directions, but the scarcity of nucleation sites near the interface results in directional growth along the composition gradient (parallel to BD) shown in Figure 4.5d-4.5i. The martensite laths formed a pronounced border with the CoCrMo grains, which have transformed into equiaxed grains averaging 36.7 ± 15.1 μm in size with distributed annealing twins. The twin boundaries observed in the CoCrMo region satisfy the misorientation conditions for Σ3 special grain boundaries (GBs) of <111> 60°. The KAM maps in Figure 4.5c also indicate an abrupt transition from an even spread of low angle misorientation boundaries in the maraging steel regions, a product of the lattice distortion from martensitic transformation, to equiaxed grains devoid of local strains or low KAM values, signifying successful stress relief in the CoCrMo region. Overall, no traces of the melt pool morphology can be observed from the texture distribution in both regions, and a sharp phase transition has developed in the interface. A more comprehensive discussion of texture development after this heat treatment can be found in Ref. [11].

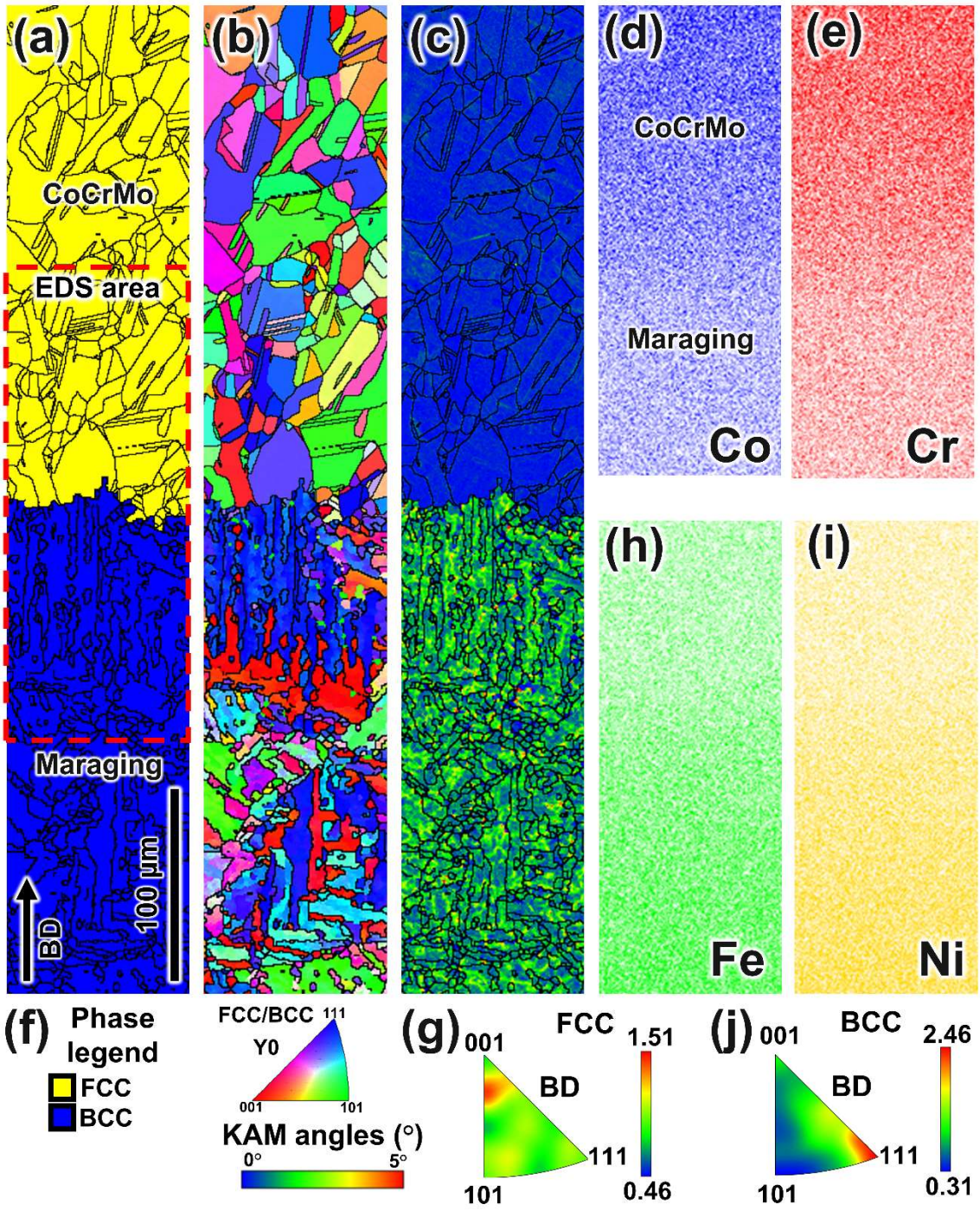


Figure 4.5. Texture development in the transition zone of the HT1 sample: (a) phase map showing fcc and bcc structures, (b) inverse pole figure color map, (c) kernel average misorientation maps, (d,e,h,i) EDS maps for Co, Cr, Fe, and Ni, respectively, (f) corresponding legends for a-c, (g) IPF representation of fcc grains, and (j) IPF representation of bcc grains.

TEM characterization results in Figure 4.6 provide additional insight into the morphology

and distribution of precipitates within the maraging steel region. The disappearance of cellular walls is associated with the annihilation of entangled dislocations and redistribution of alloying elements. Overgrown lath structures in Figure 4.6a exhibit a thickness of 496.2 ± 28.1 nm, which is ~6x the size observed in other conditions. Uniform lath growth is also accompanied by dense acicular precipitates embedded throughout the matrix, with an average length of 33.9 ± 3.9 nm. EDS results in Figure 4.6b confirm that the precipitates coincide with Mo-enriched clusters, which is indicative of Fe_7Mo_6 or Fe_2Mo formation. Unlike the observations made by Mei [36], who linked austenite reversion to Mo-enriched precipitates after over-aging at 540°C, the preliminary solution heat treatment employed in the current study preserves a single-phase matrix after aging.

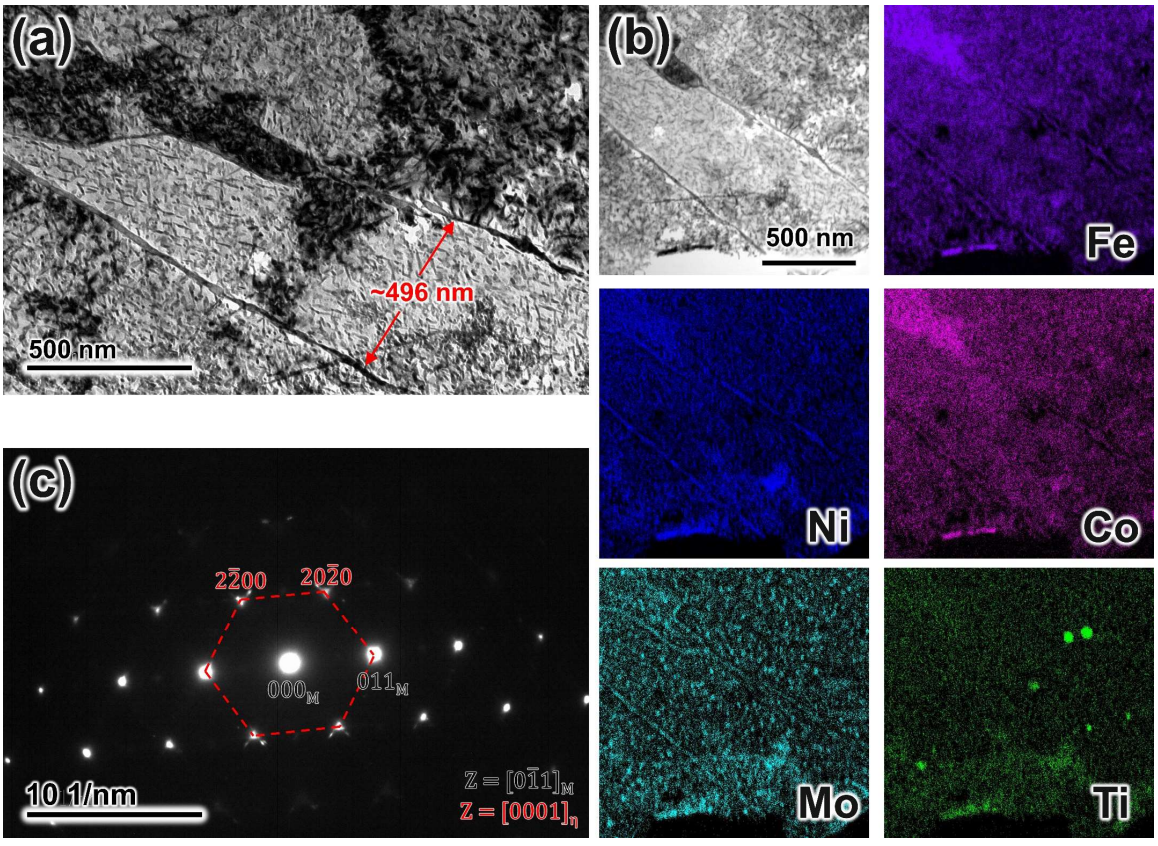


Figure 4.6. High resolution structures of HT1 sample: (a) TEM-BF images, (b) EDS mapping results, and (c) corresponding selected area diffraction pattern.

Additionally, the absence of Ni segregation implies that Ni either remains unconsumed during the precipitation process or reverts back into the matrix following over-aging. Given that Ni acts as a principal austenite stabilizer capable of inducing austenite reversion in maraging steels, the suppression of the bcc-fcc phase transition is evident.

4.3.2.2 Microstructure after HT2 (940 °C for 2hrs + 490 °C for 6 hrs)

The emphasis with HT2 is to achieve high strength in maraging steel at the expense of ductility and stress relief in CoCrMo. Skipping the solution treatment step resulted in inconsistent microstructures on both regions and the interface. The microstructure morphology after HT2 is displayed in Figure 4.7, highlighting the discontinuous martensite lath distribution in the interface. The brief exposure to 940 °C gave sufficient driving force to dissolve cellular boundaries and develop lath structures in the maraging steel region, as depicted in Figure 4.7b and Figure 4.7d. However, the cellular structure was partially retained in the CoCrMo region, as shown in Figure 4.7c and Figure 4.7e. Additionally, this region manifested significant ε-hcp bands—indicated by red lines in Figure 4.7c—with varying lengths and with multiple bands intersecting in highly striated regions. Some bands are transgranular and some groups of parallel bands criss-cross on top of each other. Although sharp boundaries have formed, multiple elongated grains still resembled the melt pool structure after printing. A closer look in Figure 4.7e reveals the partial disintegration of the cell walls into finely dispersed and elongated boundaries. Coarse, irregularly shaped precipitates marked by blue arrows also preferentially formed along grain boundaries, which are identified as carbide precipitates through EDS.

The HT2 interface features four distinct phases, two of which (fcc-Co and fcc-austenite) are indistinguishable in the phase map (see Figure 4.8). The non-uniform chemical

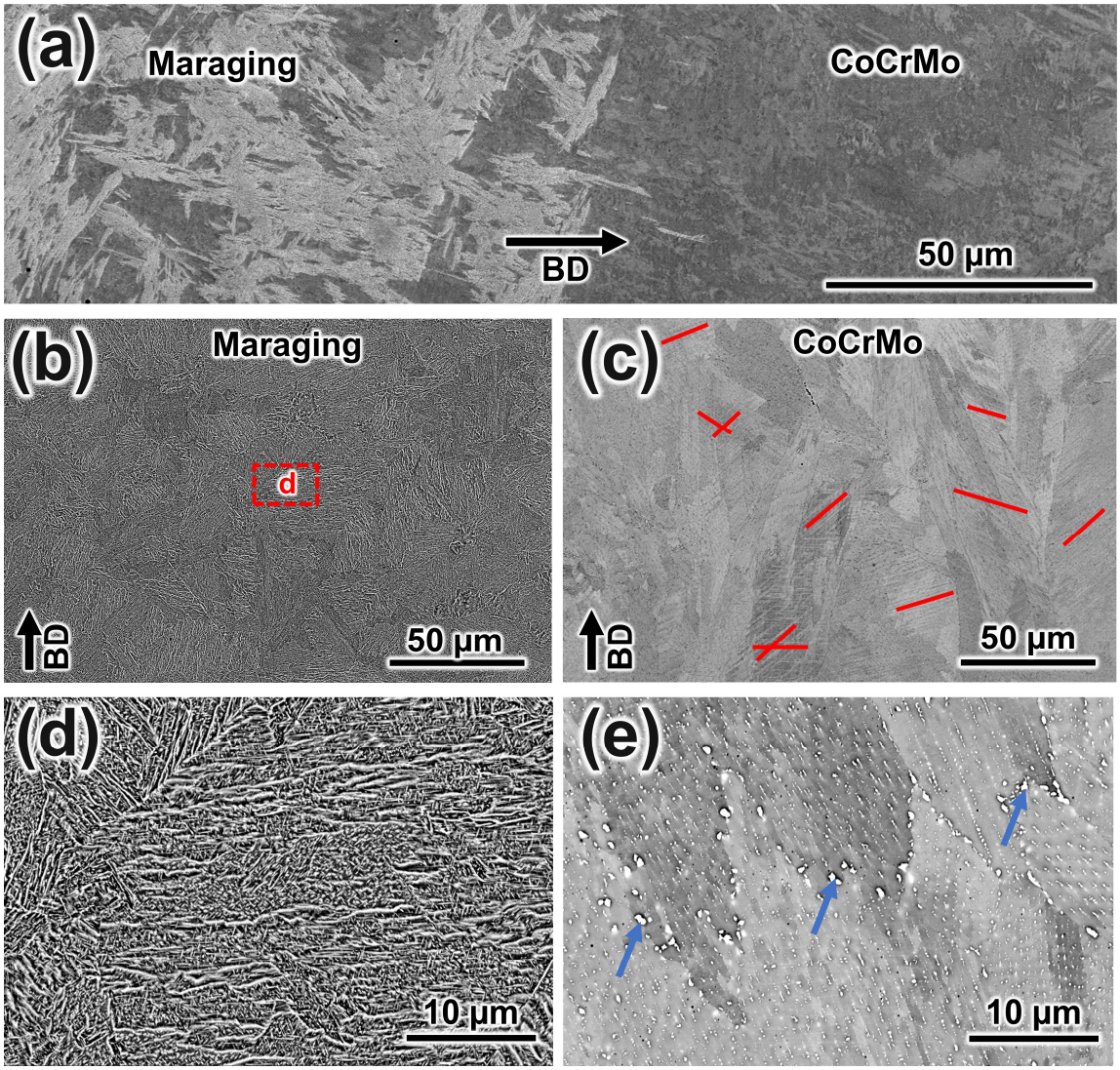


Figure 4.7. Microstructural features after HT2: (a) transition zone, (b, d) maraging steel lath structure, and (c, e) CoCrMo structure.

distribution is reflected on the discontinuous arrangement of phases, with boundaries that resemble the original melt pool shape prior to heat treatment. For instance, the center of the melt-shaped intermixture in Figure 4.8a, which preserved the fcc phase after solidification, shows Fe-depletion with Co- and Cr-enrichment based on the EDS maps in Figure 4.8d and Figure 4.8e. Region C traced in Figure 4.8a will be analyzed later for grain-scale variant distribution. The predominantly fcc interface featured large columnar grains oriented along <110>//BD overlain by transformed bcc laths with a strong texture along

<111>//BD and <100>//BD, tracing nucleation sites without Co and Cr segregation. Unlike the large, untransformed islands in the as-built sample, alloying element diffusion led to the formation of isolated laths inside the melt pool-shaped interface. The laths that formed at the edge of the melt also appear similarly oriented and more continuous in Figure 4.8b. However, the redistribution of Co and Cr led to retention of fine fcc regions dispersed within the laths. Closer to the interface, fcc retention is more severe, with the fcc phase percentage rising to 34.3 %, compared to 7.7 % near the maraging steel region. Sufficient nucleation sites are available for formation of full packets, but the inconsistent martensite structure after printing was still inherited. Avoiding solution HT also produced the thinnest block width average of 2.6 ± 1.9 μm. Large, segregated phases after printing were diffused as transformation from γ-ε for CoCrMo and γ-α' for maraging steel occurred simultaneously. Furthermore, the CoCrMo region showed considerable transformation to ε-phase despite only 2 hours of aging, showing the onset of massive transformation in unevenly sized grains that retained the original AM grain morphology. Massive transformation is an interface-controlled growth [14,18] that results in ε-hcp grains with different grain sizes and no crystallographic coherency with the previous γ grains. This agrees with the transgranular and overlapping striations observed in the microstructure. None of the grains underwent complete transformation due to the short aging duration, resulting in a non-uniform microstructure with 16.3 % ε-phase. The KAM maps in Figure 4.8c display the disparity in strain distribution between regions with successful bcc/hcp conversion and those that retained the fcc phase. While the post-heat treatment interface likely exhibited limited strain initially, subsequent transformation in the maraging steel region generated strain-concentrated regions, marked by pronounced low-angle

misorientations. Meanwhile, γ-ε phase transformation occurs through slip and features negligible misorientation with the surrounding fcc matrix.

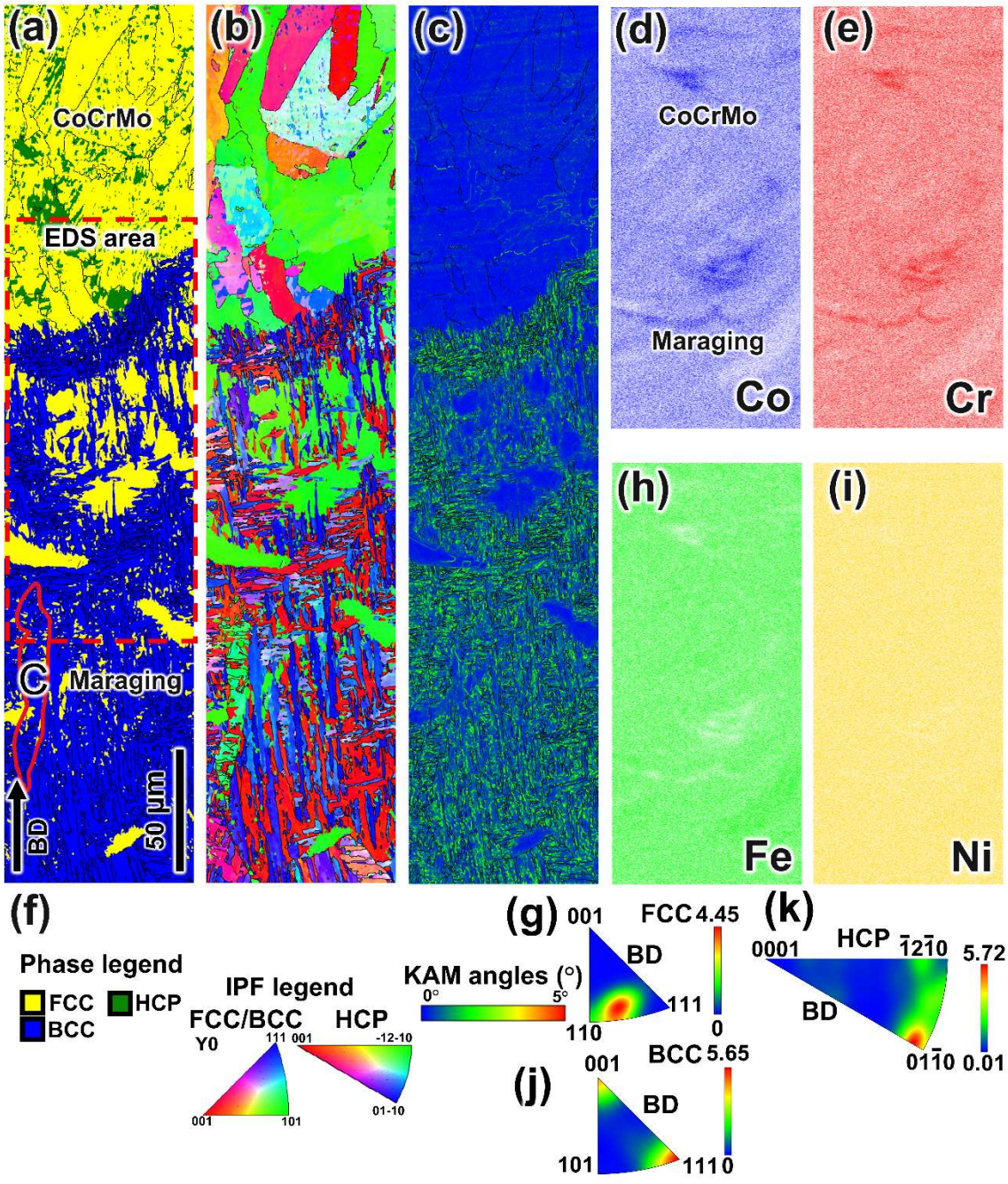


Figure 4.8. Texture development in the transition zone of the HT2 sample: (a) phase map showing fcc, bcc, and hcp structures, (b) inverse pole figure color map, (c) kernel average misorientation maps, (d,e,h,i) EDS maps for Co, Cr, Fe, and Ni, respectively, (f) corresponding legends for a-c, (g) IPF representation of fcc grains, (j) IPF representation of hcp grains, and (k) IPF representation of bcc grains.

Figure 4.9 provides a closer look of the lath structure within the maraging steel region. HT2 triggers full austenitization at 940 °C but only partial disintegration of cell walls and annihilation of dislocations. As a result, lath formation is fragmented with localized strains and non-uniform composition upon quenching. Subsequent aging yields a blurred structure containing dense precipitates and dislocations forests which can be seen in Figure 4.9a. Laths with well-defined parallel boundaries displayed a reduced average thickness of 74.7 ± 15.8 nm, which is considerably thinner than HT1. Unlike the Mo-rich precipitates evident in HT1, EDS analysis of the HT2 specimen, shown in Figure 4.9b, exhibited Ni- and Ti-rich acicular precipitates with an average size of 55.2 ± 8.5 nm. The accelerated formation of Ni-Ti precipitates can be attributed to their low nucleation energy and high lattice coherency, and it is generally observed at the initial stages of aging [37–39]. Preferential

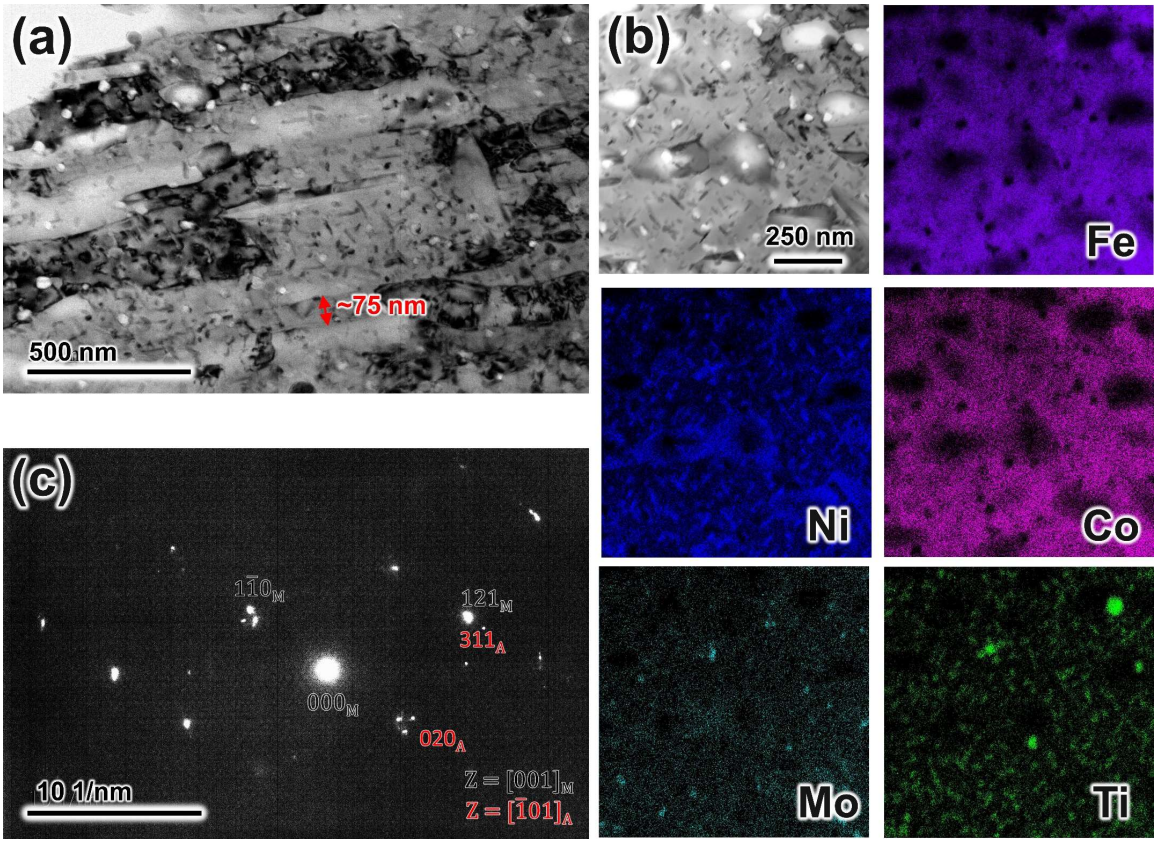


Figure 4.9. High resolution structures of HT2 sample: (a) TEM-BF images, (b) EDS mapping results, and (c) corresponding SAED pattern.

precipitation consumed Ni from the matrix and left islands that favor austenite nucleation, since Ni is enriched while Fe and Co remain depleted in these regions. There is a slight indication of Mo segregation but at a lesser extent compared to the ellipsoidal clusters formed in HT1. Prolonged aging could allow Fe and Mo to serve as substitutional lattice elements; however, the insufficient homogenization likely suppressed this behavior within the dual-phase matrix.

4.3.2.3 Microstructure after HT3 (1150 °C for 2 hrs + 940 °C for 5 hrs + 490 °C for 6 hrs)

A synergistic balance between strength and ductility for both regions is desired in HT3, where CoCrMo experiences solution heat treatment and extended aging at the expense of some grain coarsening in the maraging steel region. The microstructure in Figure 4.10 shows a continuous interface in HT3, avoiding the inconsistent lath formation in HT2 and the prominent lath growth in HT1. The maraging steel region in Figure 4.10b and Figure 4.10d lost cellular features and traces of epitaxial growth since the initial heat treatment stages induced extensive homogenization. Considering that the ε-phase transition and precipitate dissolution temperatures for CoCrMo were found at ~970 °C and ~1140 °C, respectively [34], all treatment combinations effectively removed the melt tracks within the maraging steel region.

The focus of HT3, however, is in altering the ε-phase transformation mechanism in CoCrMo. Regions highlighted in red in Figure 4.10c showcase consistent, parallel ε-phase bands that are constrained within grains and previous melt pool boundaries. Unlike the dense striations in HT2, these bands mostly terminated at grain boundaries and displayed no overlap. The added solution treatment step preserves the previous γ grain boundaries in

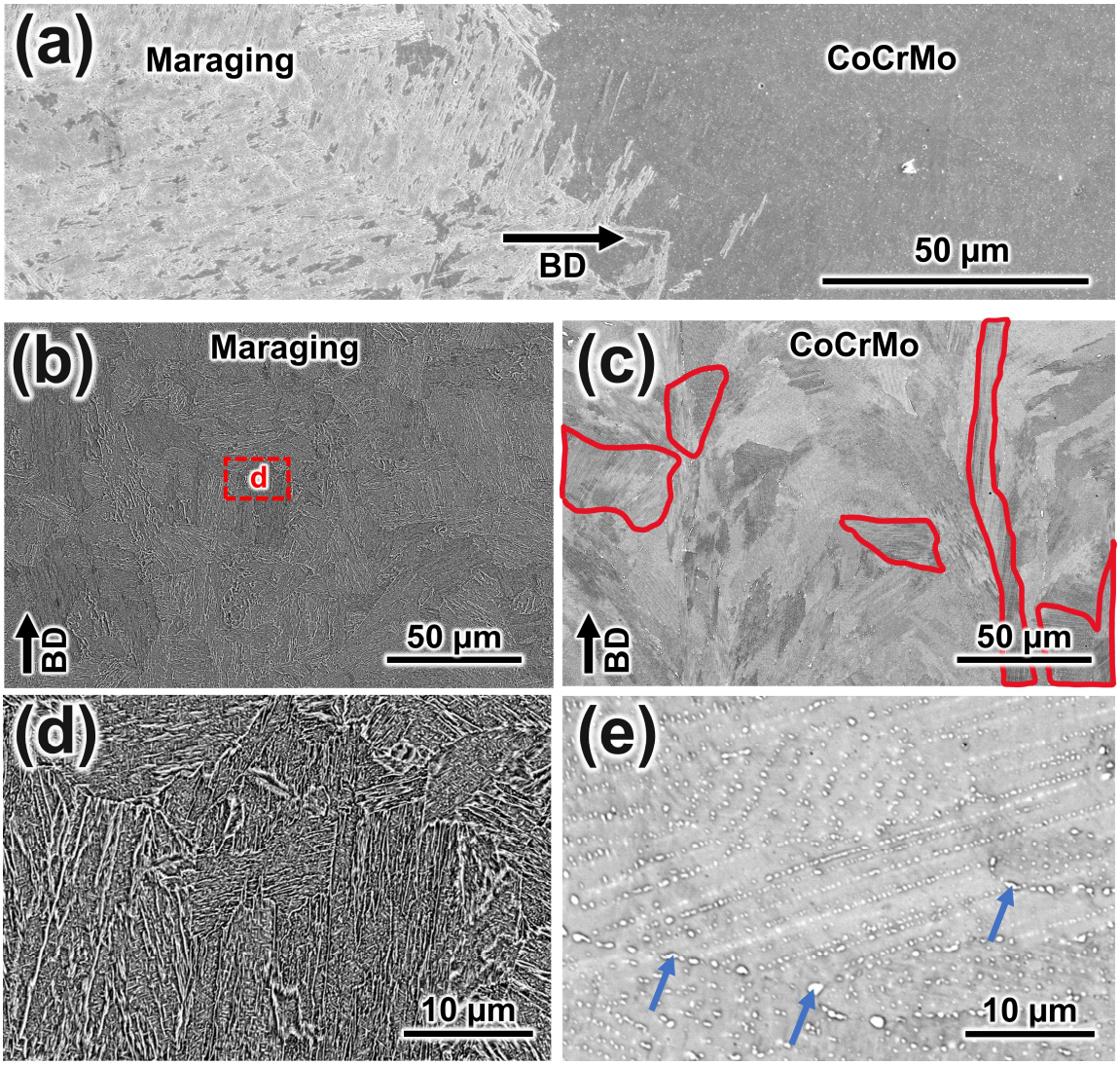


Figure 4.10. Microstructural features after HT3: (a) transition zone, (b, d) maraging steel lath structure, and (c, e) CoCrMo structure.

the succeeding γ-ε transformation. The presence of some equiaxed regions that include grains free of striations and containing sharp edges can also be observed. Figure 4.10e displays coarse precipitates that are exclusively formed in grain boundaries, which are identified as carbide precipitates through EDS. Unlike HT2, the matrix now contains round and elongated precipitates aligned in a parallel manner. These precipitates trace the observed ε-hcp bands, implying that rearrangement occurred after a longer aging time.

The EBSD analysis of the HT3 specimen presented in Figure 4.11 also revealed a sophisticated multi-phase interface which reflects the targeted phase transformation in both alloys. In the maraging steel region, the two-stage solution HT led to formation of martensite blocks that are continuous and randomly oriented, with block widths averaging 2.8 ± 0.8 μm. The melt pool morphology and refined microstructure in the as-built samples disappeared. The redistribution of interface alloying elements also formed residual austenite islands scattered along bcc boundaries, shown in Figure 4.11a. However, austenite retention occurred to a lesser extent compared to HT2 due to the extended homogenization observed in Figure 4.11d-4.11i. Region D traced in Figure 4.11a will be analyzed later for grain-scale variant distribution. Closer to the interface, fcc retention is more severe, with the fcc phase percentage rising to 28.1 %, compared to 2.7 % near the maraging steel region. However, as seen in Figure 4.11b, lath growth persisted omni-directionally and results in a random interface texture despite the presence of four different phases. Of all the heat treatment conditions, HT3 showed the smoothest end-to-end composition and texture variation. Lath formation ceased in the interface, and large bcc martensite grains solidified in contact with both hcp and fcc-Co grains.

In the CoCrMo region, exposure to 940 °C for 5 hours caused phase transformation of γ-fcc to up to 73.6% ε-hcp. Nucleation starts at the grain boundaries and along parallel striations wherein carbide precipitates were observed in the microstructure. This suggests that local carbon depletion due to precipitation creates favorable sites for transformation. While carbon segregation at partially dissolved cell walls promoted massive transformation in HT2, the added solution treatment step in HT3 shifts the nucleation sites towards grain boundaries and parallel ε-hcp bands. Additionally, carbide precipitates located at these

interfaces can exert a solute drag effect by impeding the migration of boundaries during the transformation process. This enables the preservation of prior γ boundaries after aging,

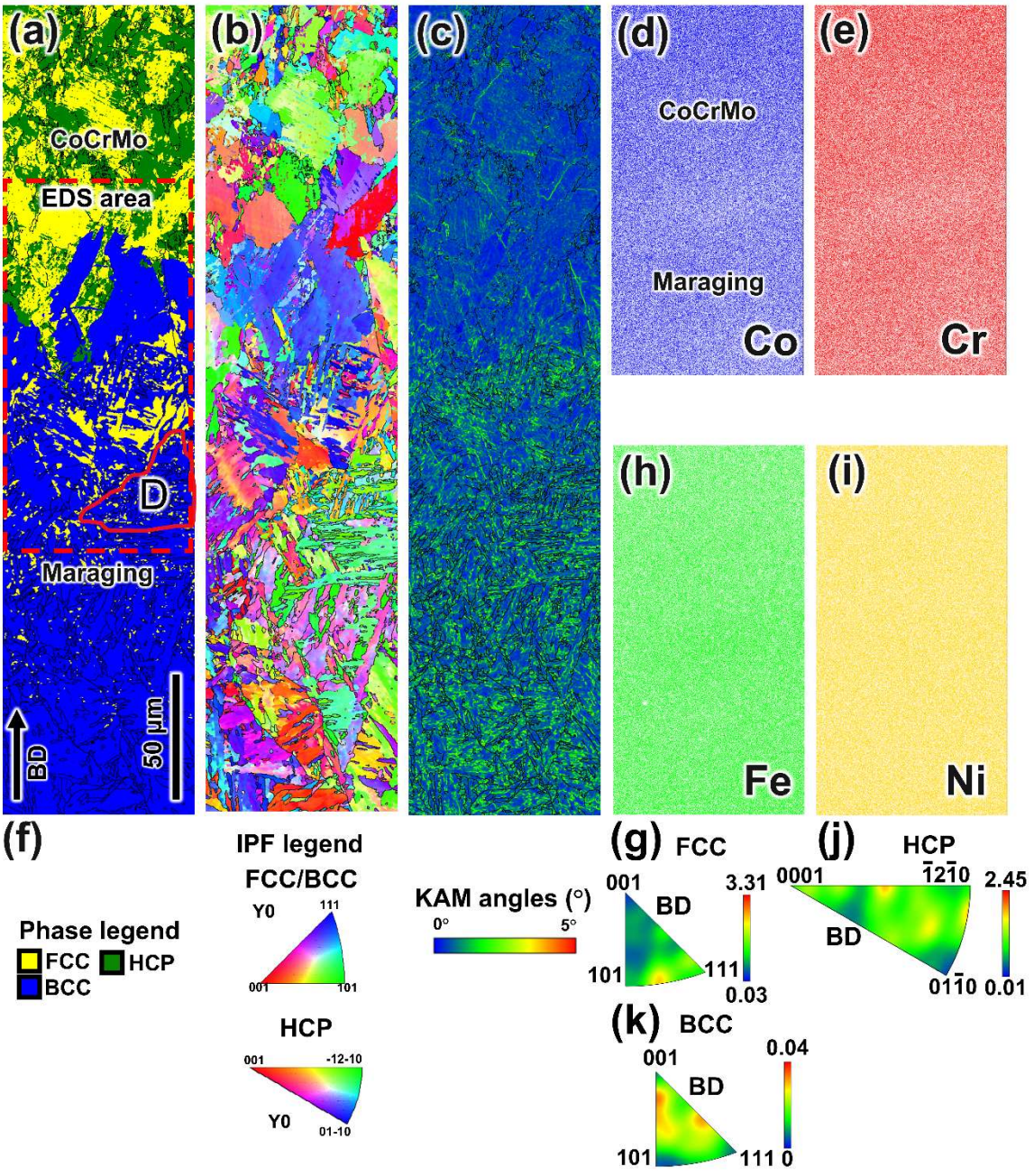


Figure 4.11. Texture development in the transition zone of the HT3 sample: (a) phase map showing fcc, bcc, and hcp structures, (b) inverse pole figure color map, (c) kernel average misorientation maps, (d,e,h,i) EDS maps for Co, Cr, Fe, and Ni, respectively, (f) corresponding legends for a-c, (g) IPF representation of fcc grains, and (j) IPF representation of bcc grains.

effectively confining the expansion of ε-phase within individual grains. As with the other conditions, the KAM map in Figure 4.11c depicts strain related to martensitic transformation in the maraging steel region. However, regions close to the fine austenite islands and large bcc grains exhibited a diminished intensity of low angle misorientations. In the CoCrMo region, local strains between ε-phase bands and surrounding γ-phase grains were identified, but the hcp grains from massive transformation did not manifest any low angle misorientations.

Figure 4.12 presents detailed TEM analysis for the HT3 specimen. Lath boundaries are difficult to distinguish as they overlap with densely scattered dislocations and ultrafine precipitates. Moreover, these laths exhibit random orientations and are rarely adjacent or parallel. The prominent elongated structures enriched in Fe, Ni, and Co were identified as laths, distinguished by their substantial thickness of 103.4 ± 16.7 nm—dimensions and alloy enrichment that are not typically associated with Ni-based precipitates. Additionally, they do not match the position of neither the Mo-enriched ellipsoidal precipitation clusters nor the finer acicular Ni-Ti segregation which have an average thickness of 47.6 ± 7.4 nm. During HT2, precipitation triggered Ni-enriched areas that reverted to austenite. But in the case of HT3, the depletion associated with precipitation resulted in random lath configurations that have no tendency to transform, thereby maintaining a single-phase matrix. The added benefit of the extended solution treatment is the stability of Ni_3Ti nucleation despite Mo clustering and substitution. Given that the evenly distributed alloying elements counteract the depletion associated with precipitation, the results underscore the crucial role of preexisting local chemical segregation in influencing

austenite reversion. HT1 and HT3 indicate that having a homogenous matrix overshadows the reversion effects of precipitate formation and subsequent Ni-depletion.

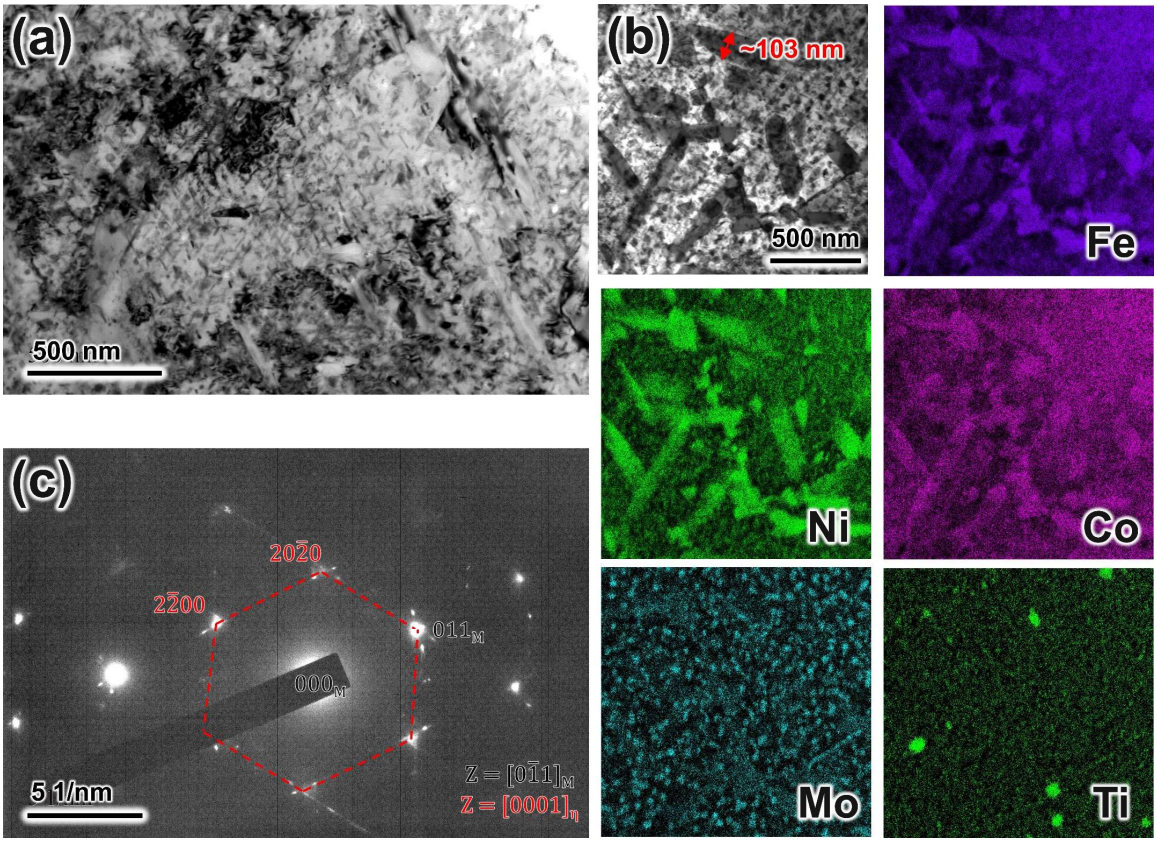


Figure 4.12. High resolution structures of HT3 sample: (a) TEM-BF images, (b) EDS mapping results, and (c) corresponding SAED pattern.

Atom probe tomography (APT) was used to further examine the formation of intermetallic precipitates that have formed during aging within the maraging steel matrix. Figure 4.13a displays the 3D reconstructed volumes of solutes, featuring Ti clusters in green and Mo clusters in red, situated near a lath boundary in the HT3 sample. The corresponding iso-concentration surfaces emphasize enriched regions and corresponding proximity histograms for both precipitate types, depicted in Figure 4.13b and Figure 4.13c for Ti and Mo, respectively. The elongated Ti-rich precipitates show alignment in two distinct directions and can be differentiated from the blocky morphology of the Mo-rich

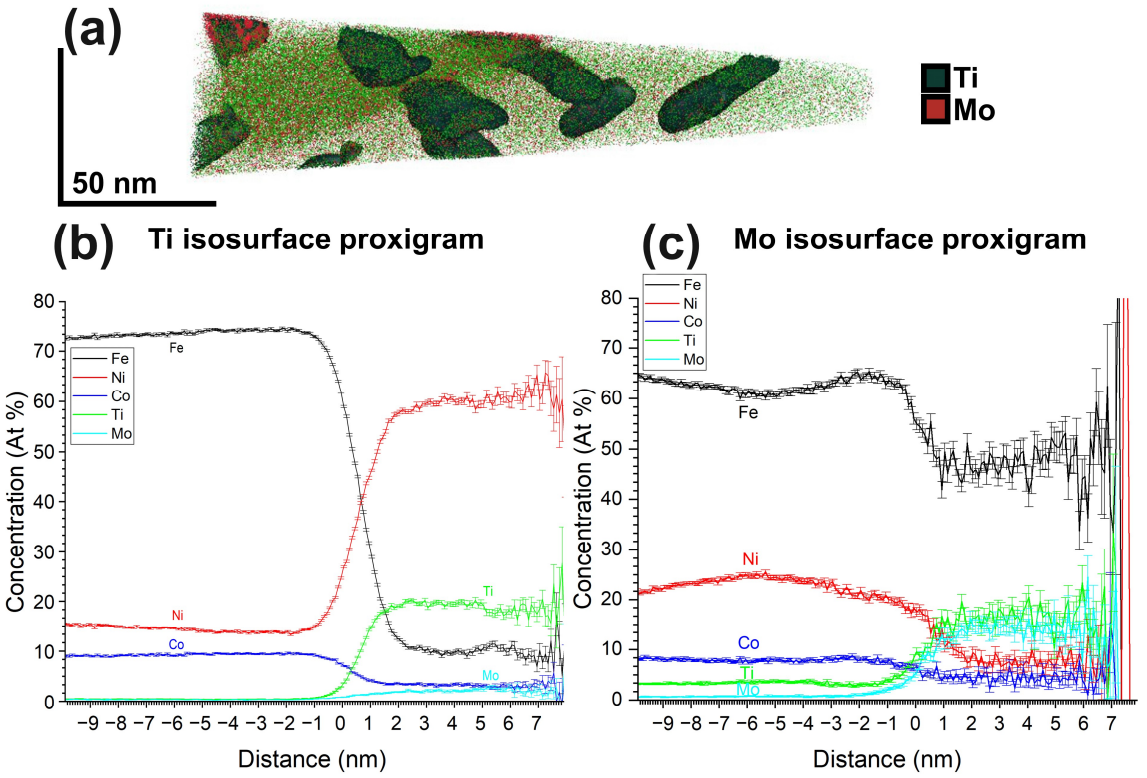


Figure 4.13. (a) Reconstructed 3D elemental distribution maps combining Ni, Ti, and Mo rich precipitates. Statistical proximity histograms for (b) Ni-Ti-based Ni3Ti precipitates considering the surface value of 4.82 at. % Ti, and (c) Mo-based (Fe,Ni,Co)2(Ti,Mo) con

precipitates. This observation aligns with the TEM-EDS data shown in Figures 4.5, 4.8 and 4.11. Upon examining the Ti clusters, which are expected to emerge at the initial stages of aging, a Ni to Ti ratio of nearly 3:1 indicative of Ni_3Ti precipitation is observed. At the same time, a rise in Mo concentration within these precipitates is seen, while regions rich in Mo precipitates show a noticeable depletion of Ni instead. As can be further seen in Figure 4.13c, the Mo-rich clusters showed a compositional ratio between Fe+Ni+Co to Ti+Mo of approximately 2:1, hinting at a substitutional process during the formation of $(Fe,Ni,Co)_2(Ti,Mo)$. Both Ti and Mo show identical elemental percentages in this stage of aging, which suggests that the eventual Ni and Ti rejection during the formation of ellipsoidal Mo precipitates is delayed by the addition of a solution heat treatment step in

HT3. This agrees with the lack of Mo-rich clusters and major precipitation of Ni_3Ti in HT2, consequently leading to austenite reversion.

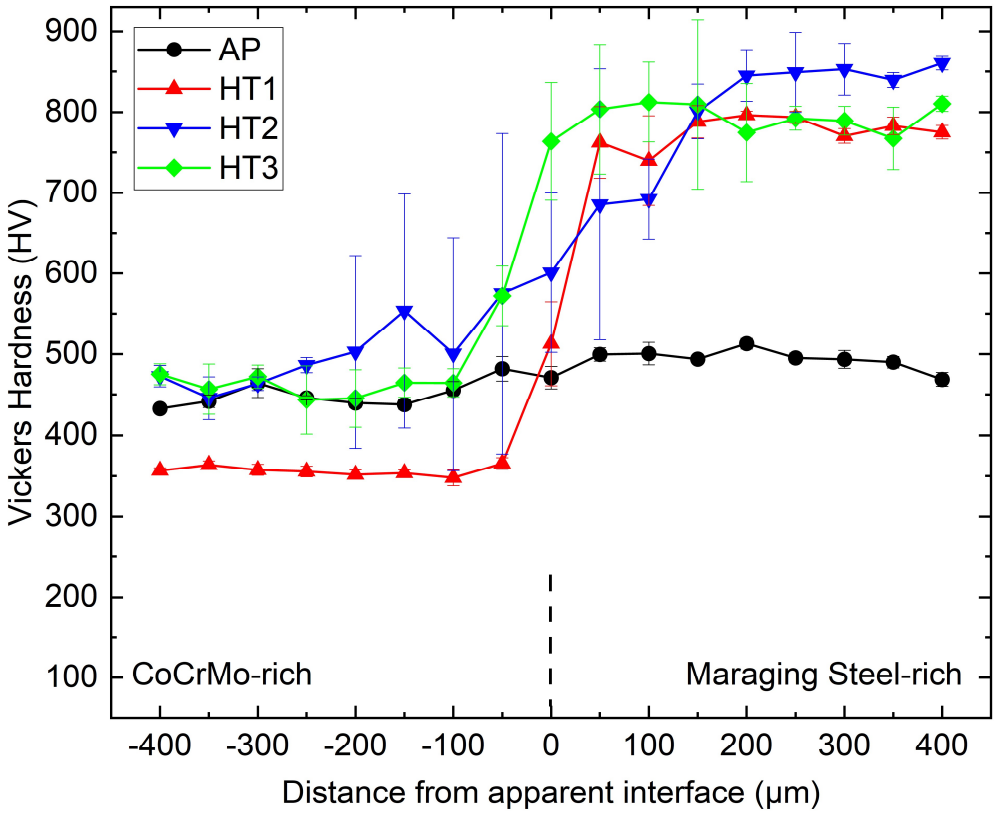


Figure 4.14. Hardness variation in the transition zones of as-built and heat-treated specimens.

4.4 Mechanical Properties

Figure 4.14 depicts the nanoindentation results across the interfaces of the as-built and heat-treated conditions. The initial cross-section after LPBF shows a continuous microhardness transition, with an average of 445 ± 8 HV and 493 ± 8 HV for the CoCrMo alloy and maraging steel regions, respectively. The formation of a single-phase fcc solid solution at the interface enhances the compatibility of the two alloys, eliminating the need for a gradual composition transition. The absence of unusual hardness spikes or soft regions indirectly invalidate brittle intermetallic precipitation or formation of unwanted phases which can arise from compositional blending. Despite the inherent transient heating

periods and the presence of vigorous Marangoni convection at the interface, the fusion region only spans ~250 μm (around 5 layers) and agrees with the EBSD results in Figure 4.2 .

After HT1, stress-relief is attained in CoCrMo and led to a decreased average hardness of 355 ± 6 HV while maraging steel undergoes strengthening precipitation that considerably increased the average hardness to 778 ± 8 HV. The joint tensile specimen had a marked increase in elongation to 40.7 %, while the ultimate tensile strength is sustained at 1149 MPa. The overall chemical and microstructural consistency in both alloys created a pronounced hardness difference across the α-γ phase boundary. The suppression of austenite reversion also contributed to minimal hardness deviation throughout the specimen. The observed hardness increase in the maraging steel region correlates with the Mo-rich clusters in Figure 4.5, and the values remained comparable to the 820 ± 48 HV in HT2 that contains Ni,Ti-rich precipitates instead. HT2 also had a slightly elevated hardness of 474 ± 35 HV in CoCrMo due to the emergence of ε-hcp bands. Considerable microhardness fluctuations were recorded across ~400 μm in the HT2 interface, which reveals the complex interplay of discontinuous lath formation, austenite reversion and retention in the maraging steel region against the partial cell disintegration, non-uniform grain morphology, and massive transformation in the CoCrMo region. Although this condition attained the highest microhardness average in the maraging steel region, some level of solution treatment will be mandatory if a more stable or an isotropic component is desired.

In an attempt to improve mechanical properties for both alloys in HT3, a moderate average microhardness increase to 460 ± 24 HV and 794 ± 28 HV was detected in the CoCrMo and

maraging steel regions, respectively. Reasonable deviations were observed away from the interface, which is attributed to suppression of austenite reversion and cellular dissolution in maraging steel and evenly sized grains and ordered precipitation in CoCrMo.

Representative engineering stress-strain curves of dual-component tensile coupons for all conditions are also presented in Figure 4.15. The combined as-built tensile specimen revealed an ultimate tensile strength of 1162 MPa and elongation of 16.4 %, which are intermediate values that lie between the strength and ductility of the base alloys [11]. A marked increase in ductility to 40.7 % was acquired in HT1 since the effects of segregation and residual thermal stresses have been mitigated. The tensile strength is also sustained at 1149 MPa despite the distinct phase boundary produced in the interface. For applications where a high ductility is unnecessary, both HT2 and HT3 demonstrated enhanced mechanical properties compared to the as-built specimen. Specifically, the tensile strength for HT2 was recorded at 1489 MPa with a ductility of 17.8%, while HT3 showed the highest strength of 1511 MPa and a better ductility of 21.2 %. Although HT2 manifested the highest hardness values and confirmed dominant Ni_3Ti precipitation in the maraging steel area, as evidenced by TEM and APT analysis, HT3 still had the superior overall properties. This is attributed to the additional strength provided by the considerable ε-hcp transformation in CoCrMo which influenced the subsequent void nucleation and coalescence. By cooperatively exploiting transformation and precipitation mechanisms in both regions, better overall strength and ductility was attained. It is important to recognize that the primary objective of the applied treatments is not to modify the tensile properties of the combined material but to introduce beneficial improvements in the distinct mechanical properties of the base alloys. While it is still vital that the joining properties

remain intact for all treatment conditions, there exists a narrow scope of potential applications for the combined component where the most critical mechanical property will be the overall tensile characteristics.

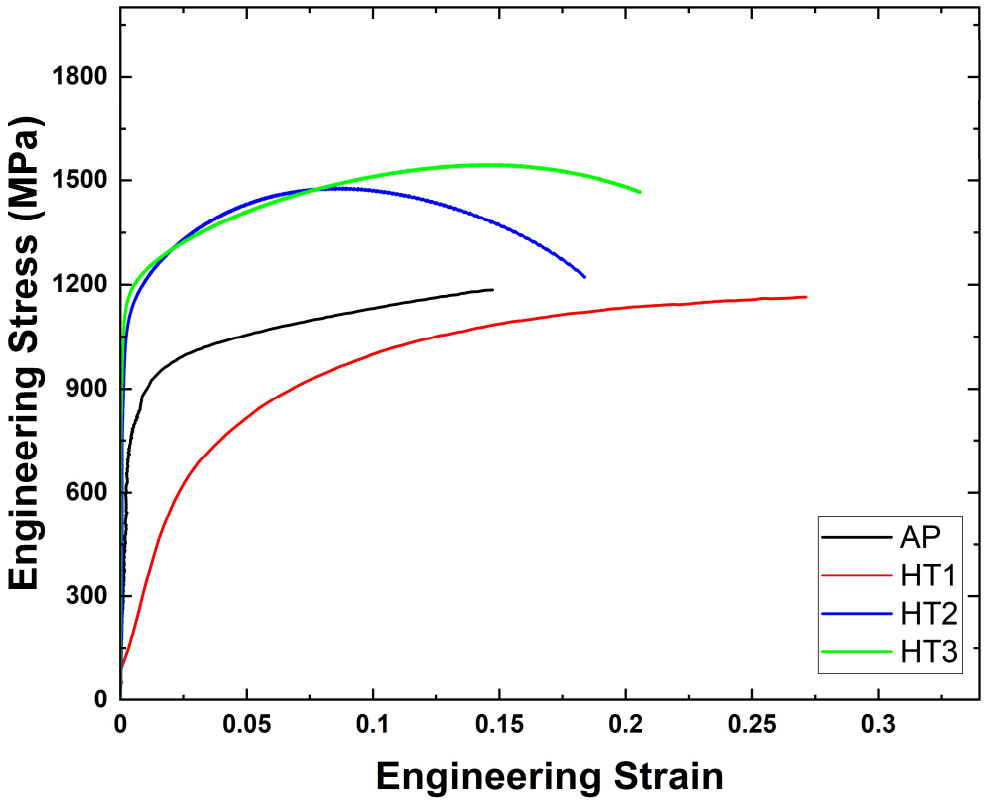


Figure 4.15. Engineering stress-strain curves from uniaxial tests performed on as-built and heat-treated specimens.

4.5 Discussion

In previous works on multi-material AM components, the compatibility of CoCrMo alloy with a wide range of alloys like Ti6Al4V [40], IN718 [41], 410 SS [42], and others has been demonstrated. In this study, continuous printing with maraging steels showcased that thermal property and phase resemblance during melting (i.e. both fcc) led to consistent melt pool characteristics despite the use of a sharp chemical composition transition and continuous processing parameters. Focusing on the transition zone reveals the influence of

chemical diffusion, vigorous convective flow, and mutual redeposition to subsequent heat treatment.

One limitation in maraging steel phase transformation investigation is that it solidifies to single phase bcc after printing. However, local strain and alloy inhomogenities hindered complete transformation near the interface, allowing the retention of some information about the parent morphology. While HT2 and HT3 employ combined solution and aging temperatures, the phase distribution in the transition zone allows a new perspective on martensitic variant formation in AM components, as discussed below.

4.5.1 Variant Selection during phase transformation in LPBF maraging steels

During martensite nucleation in low-carbon maraging steels, laths that originate from the same austenite grain will seek a final orientation that accomodates the overall minimum energy after transformation [43]. This results to a random configuration of product orientations that have identical odds of aligning with any 12 or 24 possible variants when either the NW or KS OR is satisfied. Normally, groups of laths with similar orientation make up blocks, while blocks with the same habit plane arrange into packets, forming the hierarchical packet-block-lath structure originally identified by Krauss [44]. Rapid cooling rates during LPBF also convert the melt pool to a fully martensitic matrix after solidification. However, packet and block boundaries are difficult to distinguish from the cellular structure. This prevents the straightforward identification of prior austenite morphology and texture information during EBSD analysis, prompting the need for parent reconstruction algorithms. Although the currently available pixel and grain-based reconstruction methods have improved in computational efficiency [30,45] and demonstrates good applicability to AM structures (most of which show the columnar nature

of melt pools prior to solidification [29,46]), the following limitations are still a point of contention:

- Every captured pixel orientation can be linked with any of the 12/24 possible variants and reconstruction can't fully predict the preferred austenite texture prior to transformation.
- Crucial insights from KAM distribution and special boundaries will not be available from parent reconstruction, rendering the investigation of dislocation density generated during printing difficult. It is also impossible to distinguish the influence of residual strains from cyclic heating to the lattice distortion associated with martensitic transformation from the original KAM maps. In particular, the lattice invariant shear generates an array of screw dislocations while entangled dislocations are inherited from the austenite matrix prior to transformation [47].
- The certainty that the theoretical orientation relationship holds despite the repeated phase reversion of the matrix to austenite due to iterative laser melting and solidication can not be guaranteed.

However, the retention of melt-pool-shaped austenite islands at the interface in this study provides a rare opportunity to perform a deeper investigation on the governing phase transformation mechanisms during printing *without using reconstruction*. The single parent orientation observed from the austenite island restricts the possible orientations of surrounding products to 12/24. Since the phase boundaries found in the interface in this study also satisfy the KS and NW relations within a 5° deviation, grain-scale variant analysis can be performed to relate the retained austenite orientation with the surrounding martensite. The observed texture inheritance can then be related to other parameters that

influenced the transformation dynamics, such as variable heating gradient in the melt, compositional variation, and segregation of austenite stabilizing elements along cell walls.

Figure 4.16 presents the variant analysis of representative grains A and B in the as-built sample highlighted in Figure 4.2, featuring columnar grains in the interface that contain austenite islands. The fcc-phase regions have a preferred texture along <110> // BD, while the transformed bcc-phase regions were aligned along the <111> // BD and <100> // BD. The columnar sections were grouped based on orientation spread, and the average fcc orientation was used as basis in categorizing bcc laths to include in variant analysis and in predicting all theoretical variant orientations. Grain A near the melt track has an average austenite Euler orientation of $\varphi_1 = 117°$, $\phi_2 = 46°$, and $\varphi_3 = 55°$, with a mean deviation of 3° while grain B near the center of the melt pool has an average austenite orientation of $\varphi_1 = 89°$, $\phi_2 = 43°$, and $\varphi_3 = 1°$, with a mean deviation of 4°. Figure 4.16a and 4.16d depict the pole figure representation of the $\{100\}_\gamma$ orientations in the respective grains, revealing a low deviation. The corresponding martensite $\{100\}_\alpha$ orientations within each austenite grain were also projected and colored in gray in pole figures in Figure 4.16b and 4.16e. A comparison with the previous $\{100\}_\gamma$ pole figures reveal that the $\{100\}_\alpha$ projections surround the $\{100\}_\gamma$ positions and form localized orientation clusters, indicating that a transformation relationship is preserved within the grain. To investigate the orientation distribution between the two phases, Figure 4.16e and Figure 4.16f compare the positions of predicted variants (governed by the aforementioned ORs) against the experimental martensite orientations. Also included are the KS and NW variants represented by blue circles and red triangles, respectively. The Bishop-Hill nomenclature [48,49] was used to label the KS variants, wherein each variant is classified based on the densely-packed

$\{111\}_\gamma$ plane parallellism condition. The letters a, b, c, and d are designated to the (111), $(\bar{1}\,\bar{1}\,1)$, $(\bar{1}11)$, and $(1\bar{1}1)$ planes, respectively while the subscripts I, II, and III denote the Burgers vectors corresponding to type $<01\bar{1}>$, <101>, and $<1\bar{1}0>$ directions, respectively [48,49] . The $\{100\}_\alpha$ in gray are then superimposed on the predicted variants. The entire pole figure was rotated so that the $[1\bar{1}0]$ and $[\bar{1}\bar{1}2]$ planes of the γ projections are oriented along the x- and y-axes, respectively. This arrangement provides a clear illustration of the variant distribution using the three Bain circles surrounding the γ projections [43].

Grain-scale variant selection is already evident near the melt track in Section A (Figure 4.16a), where none of the $\{100\}_\alpha$ projections coincided with six KS variants (-aII, -dII, aII, dII, -dI, -aI) and two NW variants (1 & 12). Closer to the center of the melt pool in Section B (Figure 4.16d), fewer KS variants (aI, -aII, aII, -aI) and only the NW variant 1 are missing. Previous studies have linked variant selection to plastic deformation substructures and slip activity [50]. However, the preliminary findings in this study show that residual stress and recoil pressure from thermal cycling can also contribute to this phenomenon. The Marangoni flow driven by surface tension differences also appears to alleviate variant selection during solidification, since *fewer* variants are missing at the edge of the melt pool compared to the center, and a more vigorous convective flow and high thermal gradient is expected at the edges. Studies in melt flow physics [51] have subdivided the melt track according to the predominant forces acting in various regions, namely the `depression region` set at the laser spot (Grain A) and the `tail end` region located at the end of the melt track (Grain B). This classification can be relevant to the variant selection observed in this study, since recoil forces are more dominant in the depression region corresponding to

grain A (where variant selection is more severe) compared to the tail end region where surface tension is more dominant, corresponding to grain B.

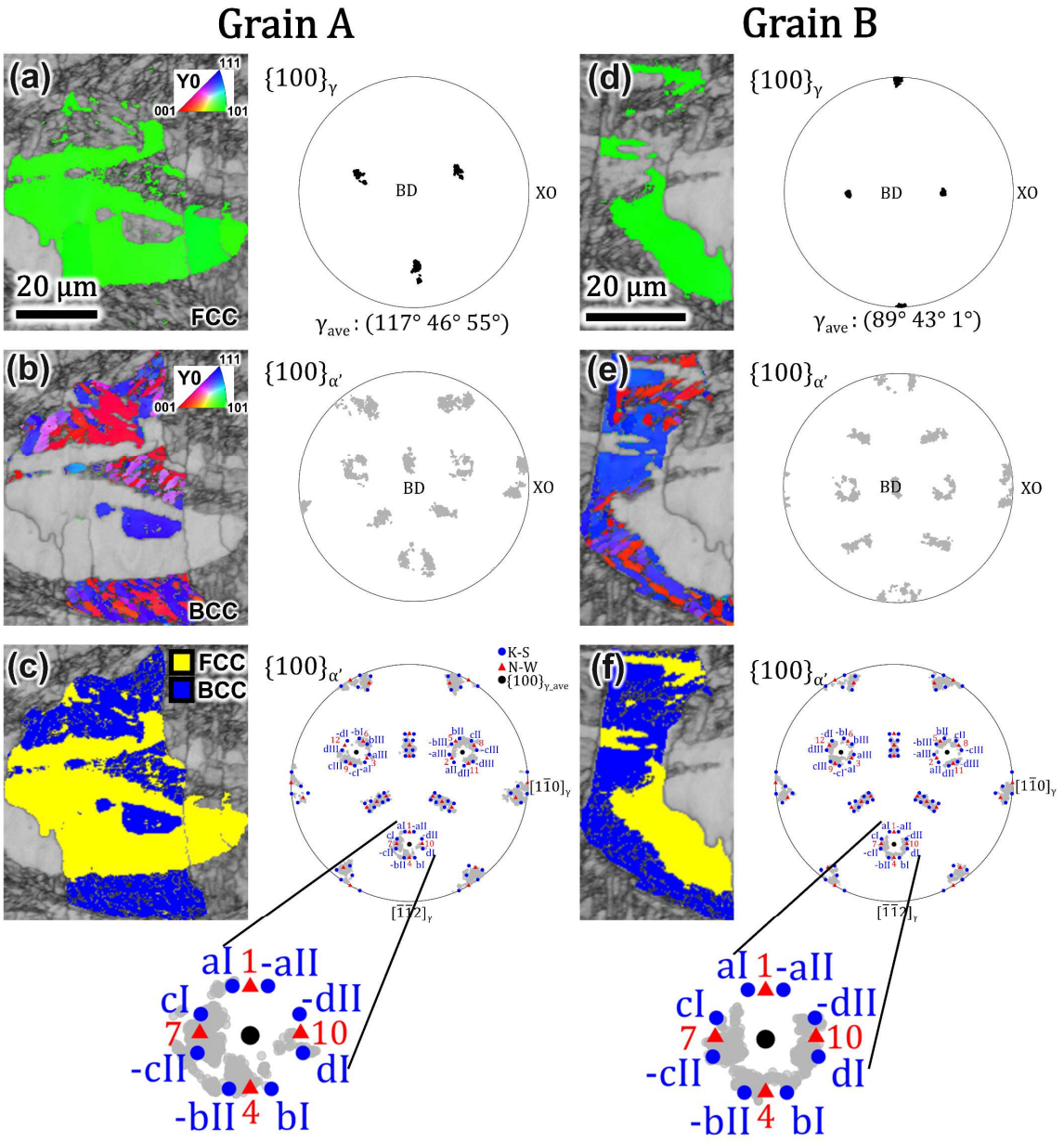


Figure 4.16. Pole figure analysis of Grain A (a-c) and Grain B (d-f) in as-built samples: (a, d) band contrast with fcc phase IPF color map (left) and corresponding {100}γ pole figures (right), (b, e) band contrast with bcc phase IPF color map (left) and corresponding {100}γ pole figures (right), (c, f) band contrast with phase map (left) and comparison of {100}α to the predicted K-S and N-W variants projected along the {111}γ plane.

Additionally, some $\{100\}_{\alpha}$ projections preferentially aligned with specific variants in both A and B, with certain measurements spread considerably far from the Bain Circle

predictions. Previous welding simulations have reported no variant selection despite a high cooling rate [52]. However, this study shows that if the solidification involves repeated reversion and limited transgranular transformation, which is the case for LPBF, the laths can assume final orientations that have considerable discrepancy from the expected plane and direction parallelism conditions.

Only HT2 and HT3 exhibited the presence of retained/reverted austenite within martensitic grains, which is necessary for variant analysis without reconstruction. Accordingly, Figure 4.17 showcases the variant analysis of two representative grains: Grain C from the HT2 interface in Figure 4.8 and Grain D from the HT3 interface in Figure 4.12. The austenite regions within grain C had an average orientation of $\varphi_1 = 1°$, $\phi_2 = 42°$, and $\varphi_3 = 6°$, with an average spread of 5°. The columnar morphology from AM is retained in HT2 since the solution treatment step is skipped. Interestingly, not only did the cell structure in HT2 persisted but they also *inherited* some of the missing variants from the as-built samples. Similar to grain A, four KS variants (a1, -aII, aII, dII) and NW variant 1 did not coincide with any of the $\{100\}_\alpha$ projections. On the other hand, the austenite regions in grain D had an average orientation of $\varphi_1 = 320°$, $\phi_2 = 35°$, and $\varphi_3 = 80°$ with an average spread of 4°. The surrounding martensitic laths in HT3 did not resemble the prior cellular structures and exhibited a random orientation configuration despite the presence of retained austenite. Moreover, the $\{100\}_\alpha$ projections are evenly distributed among all 24 KS variants and 12 NW variants, eliminating any hints of variant selection. The analysis reveals that recrystallization and complete solution treatment above the Ae_3 line is necessary to allow the formation of all possible lath configurations in approximately equal volume fractions.

Austenitizing beyond the Ae_1 boundary in HT2 is inadequate in preserving all potential martensitic variants.

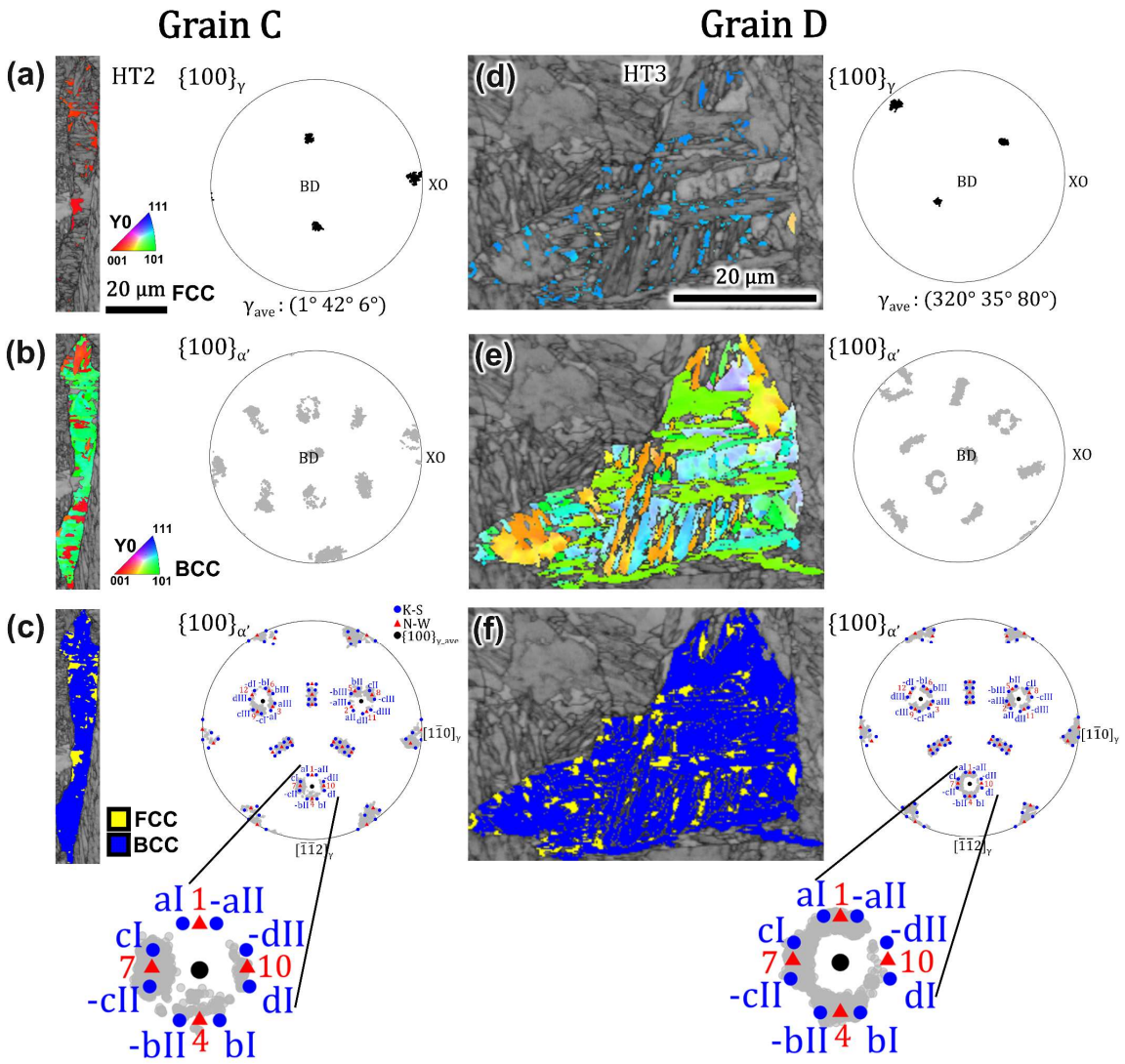


Figure 4.17. Pole figure analysis of Grain C (a-c) from HT2 and Grain D (d-f) from HT3: (a, d) band contrast with fcc phase IPF color map (left) and corresponding {100}γ pole figures (right), (b, e) band contrast with bcc phase IPF color map (left) and corresponding {100} α' pole figures (right), (c, f) band contrast with phase map (left) and comparison of {100}α' to the predicted K-S and N-W variants projected along the {111}γ plane.

4.5.2 Comparison of three heat treatment schedules

While HT1 is a solution treatment previously applied to CoCrMo alloys, the impact of prolonged exposure at elevated temperatures has relatively been unexplored for maraging steels made with L-PBF. Previous studies have identified the considerable influence of increasing the austenitizing temperature to grain size [53], which was also confirmed through morphological and crystallographic comparison in this study. The continuous phase boundary in HT1 also suggests that achieving a consistent interface in a multi-material structure requires both adequate exposure times and sufficiently high temperatures to counteract the segregation effects prompted by the solidification conditions. The influence of solution treatment to the nucleation of intermetallic precipitates in maraging steel was also revealed, showing a single phase matrix with Mo-enriched clusters.

In HT2, enhanced mechanical properties and a marked increase in hardness were observed due to a combination of dispersed acicular precipitates that trigger secondary hardening and the presence of thermally stable reverted austenite that contributes to enhanced toughness and strain induced hardening [54]. The emergence of Ni- and Ti-rich precipitates is coherent with the bcc phase and provides additional energy in impeding dislocation movement [7], which in turn facilitates preferential nucleation and subsequent alloy depletion upon continued aging. Chemical segregation remains evident close to the interface, promoting preferred austenite growth in regions with Co and Cr amounts above the bulk composition. Although other reports on cell wall segregation did not necessarily convert to fcc phase after solidification [55], the rearrangement of dislocation forests further led to fragmented lath formation. Investigations on austenite reversion at elevated temperatures differentiated the role of substitutional elements to the rate of austenite

stabilization with the role of interstitial movement with intermetallic precipitation and dislocation distribution [56,57].

HT3 principally employed a dual-stage solution treatment to maraging steel with the objective of optimizing the properties of the CoCrMo region. The unintended benefit of extending the solution treatment is the stabilization of Ni_3Ti precipitates, which coexisted with Mo-rich precipitates. A better overall strength and ductility is achieved by maximizing strengthening mechanisms from both alloys. The examination of the maraging steel region also revealed acicular and ellipsoidal precipitates within a single-phase matrix.

4.6 Conclusions

This work analyzed the impacts of continuous LPBF and heat treatments on the mechanical behavior and microstructural characteristics of a CoCrMo alloy-maraging steel dual structure. The main conclusions are summarized as follows:

- The transition zone of as-built specimens exhibited phase compatibility, fragmented lath formation and austenite retention in Co and Cr rich regions, creating the ideal environment for γ-α' phase transformation investigation. Thermal cycling triggers grain-scale martensite variant selection and considerable deviation from the Bain Circle predictions, attributed to residual stress and recoil pressure that is aggravated in the center of the melt. This phenomenon is alleviated close to the melt pool boundaries due to vigorous convective flow.
- Prolonged solution treatment and aging in HT1 (1150 °C for 6 hrs + 490 °C for 6 hrs) generated coherent twins and enhanced ductility in CoCrMo. Ellipsoidal Mo-rich precipitates and substantial lath size evolution are also observed within

maraging steel. A distinct fcc-bcc phase boundary emerged in the transition zone due to chemical homogenization.

- Peak strength in the maraging steel region is achieved during HT2 (940 °C for 2hrs + 490 °C for 6 hrs), primarily due to Ni_3Ti precipitation. However, Ni depletion and non-uniform chemical distribution leads to austenite reversion and disappearance of the same variants that are absent in the as-built sample. A two-hour aging treatment at 940 °C is sufficient for γ-ε massive transformation to occur within CoCrMo.

- HT3 (1150 °C for 2 hrs + 940 °C for 5 hrs + 490 °C for 6 hrs) generated the smoothest end-to-end composition, texture, and hardness variation among all heat treatment schedules, which is correlated with the dissolution of cellular structures and complete martensite variant evolution. Achieving the highest tensile strength is attributed to cooperative strengthening from intermetallic precipitation in maraging steel and significant γ-ε transformation in CoCrMo.

- A uniform chemical distribution in the matrix mitigates the occurrence of austenite reversion and overshadows the influence of precipitation-induced alloy depletion on austenite transformation.

4.7 Chapter 4 References

[1] K.C. Cheung, N. Gershenfeld, Reversibly Assembled Cellular Composite Materials, Science 341 (2013) 1219–1221. https://doi.org/10.1126/science.1240889.

[2] M. Vaezi, S. Chianrabutra, B. Mellor, S. Yang, Multiple material additive manufacturing – Part 1: a review: This review paper covers a decade of research on multiple material additive manufacturing technologies which can produce complex geometry parts with different materials, Virtual Phys. Prototyp. 8 (2013) 19–50. https://doi.org/10.1080/17452759.2013.778175.

[3] D. Wang, L. Liu, G. Deng, C. Deng, Y. Bai, Y. Yang, W. Wu, J. Chen, Y. Liu, Y. Wang, X. Lin, C. Han, Recent progress on additive manufacturing of multi-material structures with laser powder bed fusion, Virtual Phys. Prototyp. 17 (2022) 329–365. https://doi.org/10.1080/17452759.2022.2028343.
[4] C. Wei, L. Li, Recent progress and scientific challenges in multi-material additive manufacturing via laser-based powder bed fusion, Virtual Phys. Prototyp. 16 (2021) 347–371. https://doi.org/10.1080/17452759.2021.1928520.
[5] K. Nyamuchiwa, R. Palad, J. Panlican, Y. Tian, C. Aranas, Recent Progress in Hybrid Additive Manufacturing of Metallic Materials, Appl. Sci. 13 (2023) 8383. https://doi.org/10.3390/app13148383.
[6] R. Han, X. Li, H. Chen, Y. Peng, D. Yan, K. Wang, Microstructure evolution and mechanical properties of TiB2/18Ni300 composite material produced by laser additive manufacturing, J. Mater. Res. Technol. 24 (2023) 4517–4533. https://doi.org/10.1016/j.jmrt.2023.04.043.
[7] M. Niu, G. Zhou, W. Wang, M.B. Shahzad, Y. Shan, K. Yang, Precipitate evolution and strengthening behavior during aging process in a 2.5 GPa grade maraging steel, Acta Mater. 179 (2019) 296–307. https://doi.org/10.1016/j.actamat.2019.08.042.
[8] F. Haftlang, J.B. Seol, A. Zargaran, J. Moon, H.S. Kim, Chemical core-shell metastability-induced large ductility in medium-entropy maraging and reversion alloys, Acta Mater. 256 (2023) 119115. https://doi.org/10.1016/j.actamat.2023.119115.
[9] L.H.M. Antunes, J.J. Hoyos, T.C. Andrade, P.W.C. Sarvezuk, L. Wu, J.A. Ávila, J.P. Oliveira, N. Schell, A.L. Jardini, J. Žilková, P.F. da Silva Farina, H.F.G. Abreu, M. Béreš, Deformation-induced martensitic transformation in Co-28Cr-6Mo alloy produced by laser powder bed fusion: Comparison surface vs. bulk, Addit. Manuf. 46 (2021) 102100. https://doi.org/10.1016/j.addma.2021.102100.
[10] B.R. Coutinho Saraiva, L. Novotný, B. Carpentieri, T.F. Keller, M. Fáberová, R. Bureš, S.F. Rodrigues, J. Rodrigues de Barros Neto, L.H. Martinez Antunes, M. Masoumi, H.F. Gomes de Abreu, M. Béreš, Effect of cyclic loading on microstructure and crack propagation in additively manufactured biomaterial Co–Cr–Mo alloy, J. Mater. Res. Technol. 26 (2023) 3905–3916. https://doi.org/10.1016/j.jmrt.2023.08.185.
[11] J. Pasco, Y. Tian, K. Chadha, L. Jiang, T. Dorin, C. Aranas Jr, Unusual interface phase transformation during continuous additive manufacturing of maraging steel and Co–30Cr–7Mo alloy, Mater. Sci. Eng. A 881 (2023) 145336. https://doi.org/10.1016/j.msea.2023.145336.
[12] M.C. Niu, L.C. Yin, K. Yang, J.H. Luan, W. Wang, Z.B. Jiao, Synergistic alloying effects on nanoscale precipitation and mechanical properties of ultrahigh-strength steels strengthened by Ni3Ti, Mo-enriched, and Cr-rich co-precipitates, Acta Mater. 209 (2021) 116788. https://doi.org/10.1016/j.actamat.2021.116788.
[13] X. Wang, W. Li, Y. Yao, L. Fan, J. Wang, W. Wang, P. Wen, Z. Yang, H. Chen, In-situ alloyed ultrahigh strength steels via additive manufacturing, Addit. Manuf. 77 (2023) 103825. https://doi.org/10.1016/j.addma.2023.103825.
[14] S. Kurosu, H. Matsumoto, A. Chiba, Isothermal Phase Transformation in Biomedical Co-29Cr-6Mo Alloy without Addition of Carbon or Nitrogen, Metall. Mater. Trans. A 41 (2010) 2613–2625. https://doi.org/10.1007/s11661-010-0273-8.

[15] M. Roudnická, J. Kubásek, L. Pantělejev, O. Molnárová, J. Bigas, J. Drahokoupil, D. Paloušek, D. Vojtěch, Heat treatment of laser powder-bed-fused Co–28Cr–6Mo alloy to remove its microstructural instability by massive FCC→HCP transformation, Addit. Manuf. 47 (2021) 102265. https://doi.org/10.1016/j.addma.2021.102265.
[16] M. Mori, K. Yamanaka, A. Chiba, Phase decomposition in biomedical Co–29Cr–6Mo–0.2N alloy during isothermal heat treatment at 1073K, J. Alloys Compd. 590 (2014) 411–416. https://doi.org/10.1016/j.jallcom.2013.12.126.
[17] A. Takaichi, Y. Kajima, N. Kittikundecha, H.L. Htat, H.H. Wai Cho, T. Hanawa, T. Yoneyama, N. Wakabayashi, Effect of heat treatment on the anisotropic microstructural and mechanical properties of Co–Cr–Mo alloys produced by selective laser melting, J. Mech. Behav. Biomed. Mater. 102 (2020) 103496. https://doi.org/10.1016/j.jmbbm.2019.103496.
[18] B.T. Donkor, J. Song, Y. Fu, M. Kattoura, S.R. Mannava, M.A. Steiner, V.K. Vasudevan, Accelerated γ-face-centered cubic to ε-hexagonal close packed massive transformation in a laser powder bed fusion additively manufactured Co-29Cr-5Mo alloy, Scr. Mater. 179 (2020) 65–69. https://doi.org/10.1016/j.scriptamat.2020.01.012.
[19] S. Kurosu, N. Nomura, A. Chiba, Microstructure and Mechanical Properties of Co-29Cr-6Mo Alloy Aged at 1023 K, Mater. Trans. 48 (2007) 1517–1522. https://doi.org/10.2320/matertrans.MRA2007606.
[20] J.-L. Putaux, J.-P. Chevalier, HREM study of self-accommodated thermal ε-martensite in an Fe-Mn-Si-Cr-Ni shape memory alloy, Acta Mater. 44 (1996) 1701–1716. https://doi.org/10.1016/1359-6454(95)00268-5.
[21] T. Nyyssönen, A.A. Gazder, R. Hielscher, F. Niessen, Habit plane determination from reconstructed parent phase orientation maps, Acta Mater. 255 (2023) 119035. https://doi.org/10.1016/j.actamat.2023.119035.
[22] E.C. Bain, N.Y. Dunkirk, The nature of martensite, Trans AIME 70 (1924) 25–47.
[23] R.K. Ray, J.J. Jonas, Transformation textures in steels, Int. Mater. Rev. 35 (1990) 1–36. https://doi.org/10.1179/095066090790324046.
[24] J.J. Jonas, Y. He, S. Godet, Representation of misorientations in Rodrigues-Frank space: Application to the bain, Kurdjumov-Sachs, Nishiyama-Wassermann, Pitsch and Greninger-Troiano orientation relationships, Mater. Sci. Forum 495–497 (2005) 1177–1182. https://doi.org/10.4028/0-87849-975-x.1177.
[25] S. Godet, J.C. Glez, Y. He, J.J. Jonas, P.J. Jacques, Grain-scale characterization of transformation textures, J. Appl. Crystallogr. 37 (2004) 417–425. https://doi.org/10.1107/S0021889804007320.
[26] Y. He, S. Godet, P.J. Jacques, J.J. Jonas, Crystallographic relations between face- and body-centred cubic crystals formed under near-equilibrium conditions: Observations from the Gibeon meteorite, Acta Mater. 54 (2006) 1323–1334. https://doi.org/10.1016/j.actamat.2005.11.008.
[27] T.D. Truong, G. Asala, O.T. Ola, O.A. Ojo, A.G. Odeshi, Effects of additive manufacturing process parameters and heat treatment on texture evolution and variant selection during austenite-martensite transformation in 18%Ni-M350 maraging steel, Mater. Charact. 204 (2023) 113190. https://doi.org/10.1016/j.matchar.2023.113190.

[28] M. Zhang, Y. Yang, C. Song, Y. Bai, Z. Xiao, An investigation into the aging behavior of CoCrMo alloys fabricated by selective laser melting, J. Alloys Compd. 750 (2018) 878–886. https://doi.org/10.1016/j.jallcom.2018.04.054.
[29] S. Wei, P. Kumar, K.B. Lau, D. Wuu, L.-L. Liew, F. Wei, S.L. Teo, A. Cheong, C.K. Ng, B. Zhang, C.C. Tan, P. Wang, U. Ramamurty, Effect of heat treatment on the microstructure and mechanical properties of 2.4 GPa grade maraging steel fabricated by laser powder bed fusion, Addit. Manuf. 59 (2022) 103190. https://doi.org/10.1016/j.addma.2022.103190.
[30] F. Niessen, T. Nyyssönen, A.A. Gazder, R. Hielscher, Parent grain reconstruction from partially or fully transformed microstructures in MTEX, J. Appl. Crystallogr. 55 (2022) 180–194. https://doi.org/10.1107/S1600576721011560.
[31] M.K. Miller, R.G. Forbes, Atom-Probe Tomography: The Local Electrode Atom Probe, Springer US, Boston, MA, 2014. https://doi.org/10.1007/978-1-4899-7430-3.
[32] C. Tan, K. Zhou, W. Ma, L. Min, Interfacial characteristic and mechanical performance of maraging steel-copper functional bimetal produced by selective laser melting based hybrid manufacture, Mater. Des. 155 (2018) 77–85. https://doi.org/10.1016/j.matdes.2018.05.064.
[33] Th. Schubert, W. Löser, S. Schinnerling, I. Bächer, Alternative phase formation in thin strip casting of stainless steels, Mater. Sci. Technol. 11 (1995) 181–185. https://doi.org/10.1179/mst.1995.11.2.181.
[34] H.F. López, A.J. Saldivar-Garcia, Martensitic Transformation in a Cast CoCrMo-C Alloy, Metall. Mater. Trans. A 39 (2008) 8–18. https://doi.org/10.1007/s11661-007-9370-8.
[35] X. Liu, X. Zhou, B. Xu, J. Ma, C. Zhao, Z. Shen, W. Liu, Morphological Development of Sub-Grain Cellular/Bands Microstructures in Selective Laser Melting, Materials 12 (2019) 1204. https://doi.org/10.3390/ma12081204.
[36] X. Mei, Y. Yan, H. Fu, X. Gao, S. Huang, L. Qiao, Effect of aging temperature on microstructure evolution and strengthening behavior of L-PBF 18Ni(300) maraging steel, Addit. Manuf. 58 (2022) 103071. https://doi.org/10.1016/j.addma.2022.103071.
[37] T. Allam, K.G. Pradeep, P. Köhnen, A. Marshal, J.H. Schleifenbaum, C. Haase, Tailoring the nanostructure of laser powder bed fusion additively manufactured maraging steel, Addit. Manuf. 36 (2020) 101561. https://doi.org/10.1016/j.addma.2020.101561.
[38] E.A. Jägle, P.-P. Choi, J. Van Humbeeck, D. Raabe, Precipitation and austenite reversion behavior of a maraging steel produced by selective laser melting, J. Mater. Res. 29 (2014) 2072–2079. https://doi.org/10.1557/jmr.2014.204.
[39] C. Tan, K. Zhou, W. Ma, P. Zhang, M. Liu, T. Kuang, Microstructural evolution, nanoprecipitation behavior and mechanical properties of selective laser melted high-performance grade 300 maraging steel, Mater. Des. 134 (2017) 23–34. https://doi.org/10.1016/j.matdes.2017.08.026.
[40] F. Bartolomeu, O. Carvalho, M. Gasik, F.S. Silva, Multi-functional Ti6Al4V-CoCrMo implants fabricated by multi-material laser powder bed fusion technology: A disruptive material's design and manufacturing philosophy, J. Mech. Behav. Biomed. Mater. 138 (2023) 105583. https://doi.org/10.1016/j.jmbbm.2022.105583.

[41] Y. Wen, B. Zhang, R.L. Narayan, P. Wang, X. Song, H. Zhao, U. Ramamurty, X. Qu, Laser powder bed fusion of compositionally graded CoCrMo-Inconel 718, Addit. Manuf. 40 (2021) 101926. https://doi.org/10.1016/j.addma.2021.101926.
[42] K.D. Traxel, A. Bandyopadhyay, First Demonstration of Additive Manufacturing of Cutting Tools using Directed Energy Deposition System: Stellite^{TM}-Based Cutting Tools, Addit. Manuf. 25 (2019) 460–468. https://doi.org/10.1016/j.addma.2018.11.019.
[43] Y. He, J.J. Jonas, S. Godet, P.J. Jacques, Crystallographic features of theγ-to-α transformation in a Nb-added transformation-induced plasticity steel, Metall. Mater. Trans. A 37 (2006) 2641–2653. https://doi.org/10.1007/BF02586099.
[44] G. Krauss, Steels: heat treatment and processing principles, ASM International, Materials Park, OH, 1989. https://cir.nii.ac.jp/crid/1130000798012046336 (accessed October 9, 2023).
[45] M. Kubota, K. Ushioda, G. Miyamoto, T. Furuhara, Analysis of recrystallization behavior of hot-deformed austenite reconstructed from electron backscattering diffraction orientation maps of lath martensite, Scr. Mater. 112 (2016) 92–95. https://doi.org/10.1016/j.scriptamat.2015.09.020.
[46] A.I. Saville, S.C. Vogel, A. Creuziger, J.T. Benzing, A.L. Pilchak, P. Nandwana, J. Klemm-Toole, K.D. Clarke, S.L. Semiatin, A.J. Clarke, Texture evolution as a function of scan strategy and build height in electron beam melted Ti-6Al-4V, Addit. Manuf. 46 (2021) 102118. https://doi.org/10.1016/j.addma.2021.102118.
[47] T. Maki, 2 - Morphology and substructure of martensite in steels, in: E. Pereloma, D.V. Edmonds (Eds.), Phase Transform. Steels, Woodhead Publishing, 2012: pp. 34–58. https://doi.org/10.1533/9780857096111.1.34.
[48] J.F.W. Bishop, R. Hill, XLVI. A theory of the plastic distortion of a polycrystalline aggregate under combined stresses., Lond. Edinb. Dublin Philos. Mag. J. Sci. 42 (1951) 414–427. https://doi.org/10.1080/14786445108561065.
[49] J.F.W. Bishop, R. Hill, CXXVIII. A theoretical derivation of the plastic properties of a polycrystalline face-centred metal, Lond. Edinb. Dublin Philos. Mag. J. Sci. 42 (1951) 1298–1307. https://doi.org/10.1080/14786444108561385.
[50] M. Sum, J.J. Jonas, A Dislocation Reaction Model for Variant Selection During the Austenite-to-Martensite Transformation, Texture Stress Microstruct. 31 (1998) 187–215. https://doi.org/10.1155/TSM.31.187.
[51] S.A. Khairallah, A.T. Anderson, A. Rubenchik, W.E. King, Laser powder-bed fusion additive manufacturing: Physics of complex melt flow and formation mechanisms of pores, spatter, and denudation zones, Acta Mater. 108 (2016) 36–45. https://doi.org/10.1016/j.actamat.2016.02.014.
[52] Y.L. He, S. Godet, P.J. Jacques, J.J. Jonas, Crystallographic Relationships between FCC and BCC Crystals: A Study Using EBSD Techniques, Solid State Phenom. 105 (2005) 121–126. https://doi.org/10.4028/www.scientific.net/SSP.105.121.
[53] G.B. Olson, M. Cohen, A general mechanism of martensitic nucleation: Part I. General concepts and the FCC → HCP transformation, Metall. Trans. A 7 (1976) 1897–1904. https://doi.org/10.1007/BF02659822.
[54] F.F. Conde, J.D. Escobar, J.P. Oliveira, A.L. Jardini, W.W. Bose Filho, J.A. Avila, Austenite reversion kinetics and stability during tempering of an additively

manufactured maraging 300 steel, Addit. Manuf. 29 (2019) 100804. https://doi.org/10.1016/j.addma.2019.100804.
[55] P. Kürnsteiner, M.B. Wilms, A. Weisheit, P. Barriobero-Vila, E.A. Jägle, D. Raabe, Massive nanoprecipitation in an Fe-19Ni-xAl maraging steel triggered by the intrinsic heat treatment during laser metal deposition, Acta Mater. 129 (2017) 52–60. https://doi.org/10.1016/j.actamat.2017.02.069.
[56] F.F. Conde, J.A. Avila, J.P. Oliveira, N. Schell, M.F. Oliveira, J.D. Escobar, Effect of the as-built microstructure on the martensite to austenite transformation in a 18Ni maraging steel after laser-based powder bed fusion, Addit. Manuf. 46 (2021) 102122. https://doi.org/10.1016/j.addma.2021.102122.
[57] L.P.M. dos Santos, M. Béreš, M.O. de Castro, P.W.C. Sarvezuk, L. Wu, L.F.G. Herculano, A. Paesano, C.C. Silva, M. Masoumi, H.F.G. de Abreu, Kinetics of Reverted Austenite in 18 wt.% Ni Grade 300 Maraging Steel: An In-Situ Synchrotron X-Ray Diffraction and Texture Study, JOM 72 (2020) 3502–3512. https://doi.org/10.1007/s11837-020-04254-w.

Chapter 5: Microstructural Transformations in CoCrMo Alloy

Background

Optimizing the heat treatment schedule for the multi-material component revealed microstructural changes and interface dynamics that were not expected from the individual alloys. The heat treatment schedules applied have shown both advantages and disadvantages when focusing on the target properties for each alloy. Moreover, the printing process causes solute segregation and the rapid solidification of thin layers which result in intriguing properties. The initial microstructure's significance becomes more pronounced following heat treatment, during which unforeseen phase transformation mechanisms can occur at various temperatures or exposure times.

Considering the current gaps in knowledge regarding the effects of aging temperature on the properties of additively manufactured structures, this chapter is focused on investigating the transformation behavior and precipitate formation for one of the powder components: the Co-30Cr-7Mo alloy. This chapter provides an in-depth examination of texture evolution, twin formation, strain distribution, and grain boundary migration under varying heat treatment conditions. Unique to this work, the simultaneous occurrence of two types of phase transformation mechanisms have been verified through carbide precipitation, thin-band formation and pole figure representation of multi-phase orientation relationships.

This section has been published: J. Pasco, L. Jiang, T. Dorin, A. Keshavarzkermani, Y. He, C. Aranas, Phase transformation in additively manufactured CoCrMo alloy after solution and aging heat treatment, Mater. Charact. 207 (2024) 113467.

Abstract

The unique structure and solute distribution of CoCrMo alloys produced using Laser Powder Bed Fusion (L-PBF) technique require custom heat-treating processes to achieve the targeted phase distribution and mechanical properties. The rise of multi-material additively manufactured structures also prompts further study at temperatures beyond standard aging and solution treatment conditions. In the present study, the phase transformation behavior, precipitate distribution, and γ-ε phase boundary orientation relationships of as-printed and solution heat-treated CoCrMo samples after aging heat treatment at 940 °C were investigated. The results show a higher ε-phase fraction of 71.2% in directly aged samples compared to 49.2% in solution heat-treated samples. This discrepancy is attributed to band-like isothermal transformation, coherent grain face massive transformation, and recrystallization. Carbide nucleation sites shifted from disintegrated cellular structures in directly aged samples to grain boundaries and twin interfaces in solution-treated samples. The presence of transgranular ε-phase bands and adjacent grains with analogous orientations observed after direct aging were linked to the weak <110> // BD and <111> // BD texture after printing. Tensile tests demonstrated an increase in tensile strength from 1162 MPa to 1261 MPa after direct aging, while significant enhancement in ductility from 16.4% to 26.1% was attained after solution heat treatment. While direct aging is more suitable for applications requiring high strength and wear resistance, solution heat treatment is advantageous when a consistent morphology and stress-free isotropic structures are desired.

5.1 Introduction

The technological maturation in additive manufacturing (AM) and the adoption of metallic components made by AM have gained significant momentum recently, due to its advantages such as near-net-shape, rapid prototyping, intelligent manufacturing, low energy and environmental costs, etc. [1]. Examples of common AM materials include corrosion-resistant alloys such as stainless steel, titanium, nickel, and CoCr [2–4]. CoCr alloys, in particular, are commonly employed in mechanical contact applications such as aircraft engines, thermal barrier coatings, artificial joints, and surgical implants, due to their balanced mechanical properties, self-polishing ability, biocompatibility, and resistance to corrosion and wear [5–7]. However, traditional methods of manufacturing CoCr alloy components, such as casting and powder metallurgy, suffer from the high costs associated with the design and manufacturing of the dies and the difficulties to rapidly change the designs. Additionally, the high hardness and wear resistance of these alloys make machining very challenging.

The metastable γ-fcc phase of Co-based alloys can be converted into a harder, more wear-resistant ε-phase (hcp) through a number of ways: athermal transformation by rapid quenching [8], low-temperature isothermal annealing [9], deformation-induced displacive mechanism [10,11], or short-range diffusion via massive transformation [12]. Considerable ε-phase formation in wrought and cast CoCrMo-C alloys has been documented only after long aging conditions, with complete transformation after 15-25 hours [13]. It should be noted that not all CoCr alloys are subjected to such heat treatments, particularly when high strength is a primary consideration. Nevertheless, the transformation mechanism of AM structures features solute segregation along cellular boundaries, enabling fast saturation

and linear interface-controlled growth through thermally activated jumps across incoherent interphase interfaces with very short incubation times of approximately 0.25-0.5 hours [14].

The concept of hybrid material processing, which merges multiple materials to satisfy various environmental conditions within a unified structure, has recently sparked interest in the research of AM components [15–17]. While these multi-material structures feature a synergistic combination of alloy properties, a strategic dilemma should not be overlooked in the post-processing heat treatment of these components. For instance, a CoCrMo alloy has been utilized as a wear-resistant, functionally graded coating on a Ti6Al4V base using Laser Engineering Net Shaping, creating metal-on-metal prosthetic devices [18]. However, the aging treatment for CoCrMo has similar temperature conditions for solution treatment of Ti6Al4V (40-100 °C below the β transus temperature of ~ 980 °C) [19]. This means that the proportion between the α+β phases in Ti6Al4V should be balanced with the γ-ε transformation in CoCrMo during treatment. The researchers in this study also investigated the feasibility of continuous printing of two distinct alloys, maraging steel and CoCrMo alloy, through the L-PBF process [20]. The conditions in the current study will be at the upper range of what is typically used in isothermal ε-phase transformation for CoCrMo (750-950 °C). Although favorable interfacial properties have been demonstrated, the precise transformation mechanism and the precipitation phenomenon have not been studied, which warrants further investigation.

Given the limited understanding of how the aging temperature impacts the material properties of AM structures, this study aims at exploring the transformation behavior and precipitate formation in both as-printed and solution-treated CoCrMo alloy samples

produced using L-PBF. The investigation includes a comparison of characteristic microstructure, phase formation, grain morphology, strain distribution, precipitate distribution, and ε-phase orientation during aging under different initial microstructural conditions. The phase morphology and preferred nucleation sites for ε-phase structures are revealed using electron backscatter diffraction (EBSD) and scanning electron microscopy (SEM). The transformation mechanism is then elaborated based on orientation analysis and precipitate distribution.

5.2 Materials and Methods

5.2.1 Material

The CoCrMo alloy investigated in this research was manufactured by voestalpine Additive Manufacturing Center Ltd. in Mississauga, Ontario, Canada, utilizing gas-atomized powders with particle sizes between 15 and 45 μm. The flow rate of the feed powder was determined to be 3.4 s/50 g, in accordance with the ASTM B964-16 standard, while the apparent density was measured at 3.68 mg/mm^3, following the ASTM B417-18 standard. The component was produced using L-PBF on an EOS M290 device equipped with a 400 W laser system with a layer thickness of 50 μm and energy density of ~ 55 J/mm^3. The chemical composition of the as-built specimen was measured through inductively coupled plasma (ICP) analysis with combustion methods and is listed in Table 5.1.

Table 5.1. Chemical composition of as-built CoCrMo (all values are in wt. %)

Material	C	Cr	Si	Mn	Mo	Ni	Fe	N	Co
CoCrMo	0.11	28.01	0.73	0.44	5.64	0.10	0.43	0.22	Balance

5.2.2 Heat Treatment

Three different heat treatment conditions were applied to the as-printed (AP) samples using a tube furnace with ±5 °C accuracy. Single differential scanning calorimetry studies of CoCrMo AM samples in [21] have observed two endothermic sharp peaks at 965 °C and 1139 °C, which are related to the ε-phase transition and dissolution of precipitates, respectively. Further, isothermal testing has shown remarkably faster transformation rates at 900°C (75% after 0.5 hr, 87% after 4 hr) when compared to 750°C (59% after 0.5 hr, 64% after 4 hr) for SLM samples. Previous isothermal tests were performed close to 800-850 °C as this is where the nose of transformation curves for as-cast and wrought alloys lies [13]. To investigate the accelerated transformation rates observed in AM samples, this study was conducted at a slightly elevated temperature.

Additionally, solution treatment typically increases the number of possible nucleation sites in forged alloys through incoherent twin boundaries and twin-twin intersections [22]. However, it's unclear how this translates to AM samples, given that such treatments could counter the alloy segregation driving massive transformation. A secondary objective of this study, therefore, was to analyze the interplay between isothermal and massive transformations. The hourly progression of these transformation types in solution treated samples were studied using EBSD.

Representative as-printed CoCrMo samples underwent a combination of solution and aging heat treatment. The heat treatments were carried out in a vacuum of 10^{-5} bar pressure in a tube furnace. For the solution heat treatment, the samples were heated to 1150 °C for 2 hours with a heating rate of 5 °C/s (since the solution temperature for CoCrMo is above 1100 °C) and quenched with water, which was labeled as SHT. Subsequently, both the as

printed and SHT samples were subjected to an aging heat treatment at 940 °C for 5 hours, with the same heating rate of 5 °C/s and quenched with water. The aged samples directly from L-PBF and from initially solution heat-treated are referred to as DHT and SAHT, respectively. In summary, there are four different conditions for the samples: as-printed (AP), solution heat-treated (SHT), aged (DHT) and solution + aged (SAHT).

5.2.3 Materials Characterization

The phase morphology and distribution of precipitates in the CoCrMo samples fabricated using L-PBF were characterized using optical microscopy (OM), SEM, and EBSD. Samples were machined parallel to the building direction and underwent mechanical grinding and polishing for metallographic preparation. The as-printed samples were electrochemically etched in a 10% H_2SO_4 and CH_3OH solution under 6V for 25 s at ambient temperature. For the rest of the heat-treated samples, electrochemical etching was performed using a HCl acid and H_2O_2 solution (20:1) under 4V for 5–10 s [23]. To obtain phase distribution, crystallographic orientation, and solute distribution, EBSD and energy dispersive spectroscopy (EDS) were conducted. These samples underwent an additional stage of polishing using a 0.02 μm silica suspension in a Buehler VibroMet 2 polisher for 2 days. EBSD scans were performed with a ThermoFisher Scios 2 SEM equipped with an EBSD detector. Kernel average misorientation (KAM) maps were used to characterize the distribution of internal strains, considering misorientation angle averages below 5°. A custom Matlab code incorporating the MTEX software was developed to predict the ideal orientations of ε-phase necessary to exhibit the Shoji-Nishiyama orientation relationship with the mean γ-phase orientation. Pole figures were also presented to compare the orientations observed during fcc-hcp transformation under all conditions.

Examination of X-ray diffraction (XRD) spectra was also conducted on all samples using a Bruker D8 Advance spectrometer, employing Cu-Kα radiation aligned perpendicular to the building direction. A scan range of 30-60˚ (2θ) was used while operating at 40 kV and 30 mA at a step size of 0.02˚ and dwell time of 1 second. The volume fractions of the γ and ε phases were estimated from the $\{10\bar{1}1\}_{\varepsilon}$ (46-48°) and $\{200\}_{\gamma}$ (51-53°) XRD peaks using the proposed procedure by Sage and Guillaud [24]:

$$\%_{hcp} = \frac{I_{hcp}^{10\bar{1}1}}{1.5 * I_{fcc}^{200} + I_{hcp}^{10\bar{1}1}} \quad [1]$$

where f_{hc} is the fraction of ε-phase, and I are the integrated intensities under the associated XRD peaks.

To investigate the changes in mechanical properties after printing and after heat treatment, uniaxial tensile tests were conducted for each condition. Tensile tests were carried out in compliance with ASTM-E8 guidelines, utilizing an Instron 1332 machine equipped with a 50 kN load cell. All uniaxial tests were performed at a uniform strain rate of 0.005 s^{-1}.

5.3 Results

5.3.1 Initial microstructures of the as-printed and solution-heat-treated CoCrMo samples

The microstructures of the AP and SHT samples are shown in Figure 5.1. The AP samples displayed characteristic L-PBF structures with continuous melt tracks. The average width and depth of the tracks are 151 ± 19 μm and 101 ± 16 μm, respectively (Figure 5.1a). As more layers were melted, the fast solidification rate and steep thermal gradient facilitate the epitaxial formation of columnar structure. The blue lines in Figure 5.1b, similar to what was observed in [25], exhibit multiple parallel bands of ε-phase that terminate mostly inside

grain boundaries but can also extend across cell walls and melt tracks. This periodic lath structure induces gradient strains within grains and may maintain a specific orientation relationship with the surrounding matrix. The structure's identification as ε-phase is later confirmed by KAM maps and agrees with the 15.6 % ε-phase percentage calculated from the $\{10\bar{1}1\}_{\varepsilon}$ and $\{200\}_{\gamma}$ XRD peaks in Figure 5.2 using the Sage-Guillaud's method [24]. At high magnifications, the microstructure also shows a combination of fine spherical cells with an average diameter of ~0.9 ± 0.2 μm and wall thickness of ~.08 ± .02 μm mixed with elongated structures that trace the radial heat profile. Fine precipitates that show as bright spots are marked by red circles in Figure 5.1c and are exclusively distributed in the cellular boundaries. The EDS data, along with the average composition of the precipitates situated along the cell walls (points 001-010) compared to the matrix (points 011-020) are

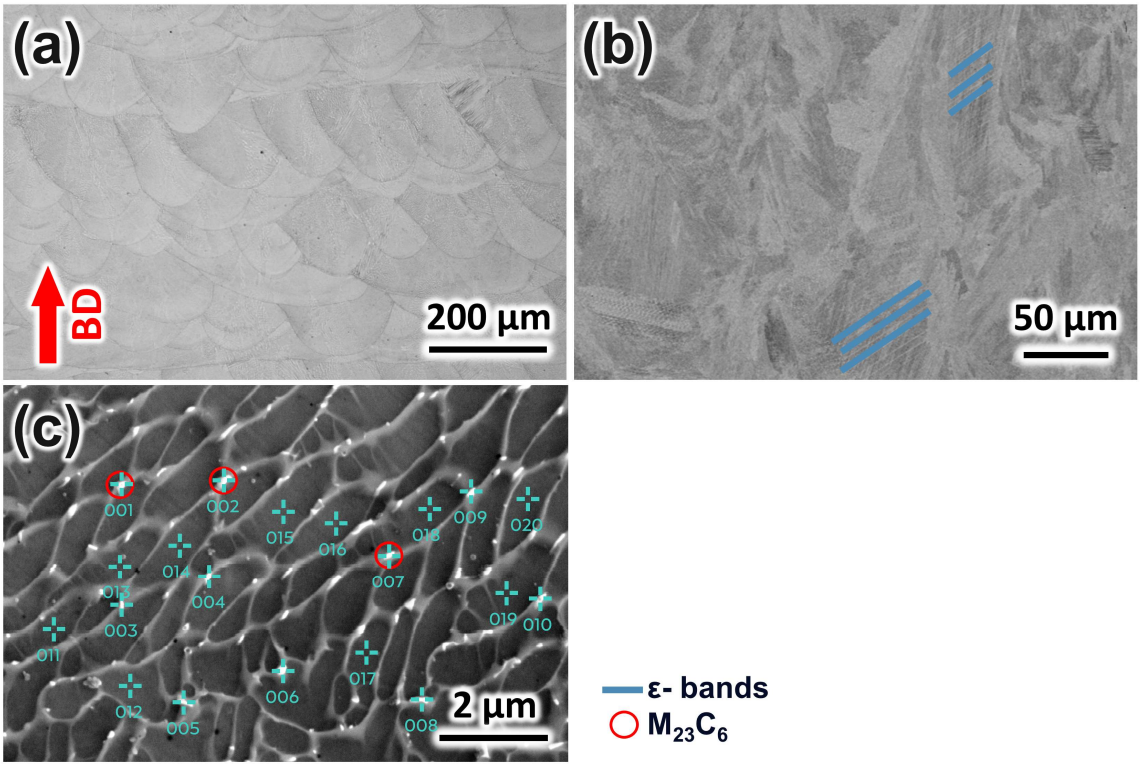


Figure 5.1. Initial microstructure of CoCrMo alloys in low (a, b) and high (c) magnification: As-printed microstructure is shown in (a) melt pools, (b) martensitic laths, and (c) precipitation along cell walls. The average composition of precipitates along cells walls (points 001-010) and the cell matrix (points 011-020) are summarized in Table 2.

shown in Table 5.. A high content of Mo, Si and C is noticed, which is indicative of $M_{23}C_6$ carbides.

Table 5.2. EDS point analyses showing solute segregation in at. % (min. 10 points)

		Co	Cr	Mo	C	Si	Mn
AP	cell walls	57.0 ± .8	28.9 ± .7	5.2 ± .3	4.4 ± .2	3.2 ± .3	0.8 ± .2
	cell interior	58.3 ± .9	33.0 ± .5	4.1 ± .4	1.0 ± .1	2.4 ± .1	0.8 ± .1
DHT	precipitates	52.8 ± .8	28.2 ± .6	7.9 ± .6	5.7 ± .4	4.5 ± .1	0.5 ± .2
	matrix	58.9 ± .7	32.1 ± .8	4.2 ± .5	1.4 ± .2	2.6 ± .2	0.4 ± .1
SAHT	precipitates	55.6 ± .6	29.7 ± .4	5.9 ± .4	5.4 ± .2	2.3 ± .3	0.8 ± .1
	matrix	59.8 ± .4	32.0 ± .3	4.2 ± .3	1.0 ± .1	2.3 ± .1	0.5 ± .1

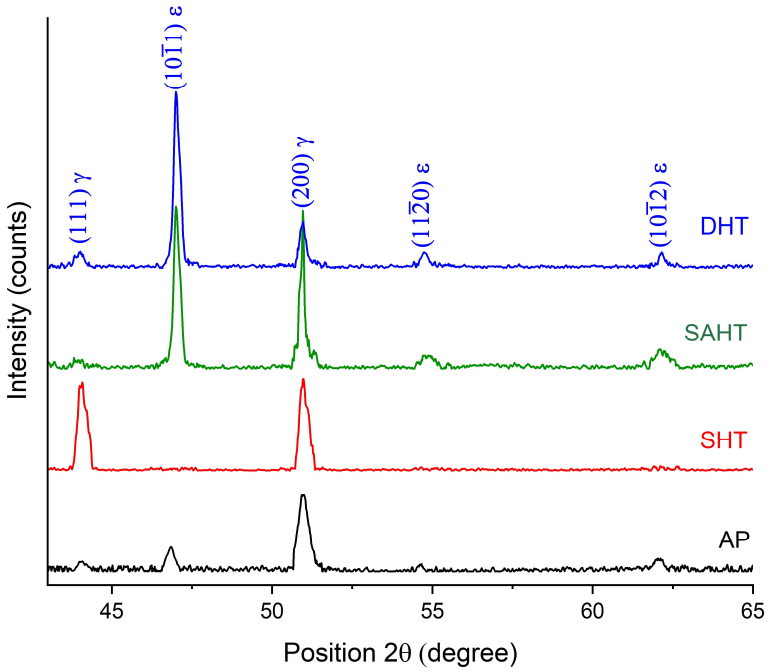


Figure 5.2. Comparison of XRD spectra obtained from the AP, SHT, SAHT and DHT samples.

The EBSD results in Figure 5.3 also reveal that the rapid solidification process produced irregular grains with 31% low-angle grain boundaries (LAGBs) and a small fraction of Σ3 special boundaries. Smaller grains with low aspect ratio are observed near the melt pool core in Figure 5.3a, while columnar grains with a weak <110> // BD and <111> // BD texture exhibit epitaxial growth. Parallel striations inside some grains are confirmed by the pattern quality (PQ) maps in Figure 5.3b, which resembles the bands observed in Figure 1b. Although the results showed a fully γ-phase structure, local strain accumulation due to thermal fluctuations during solidification resulted in faint indications of small orientation changes scattered throughout the microstructure. Parallel strain localization in some subgrains with low KAM angles of up to 3° observed in Figure 5.3c may indicate the

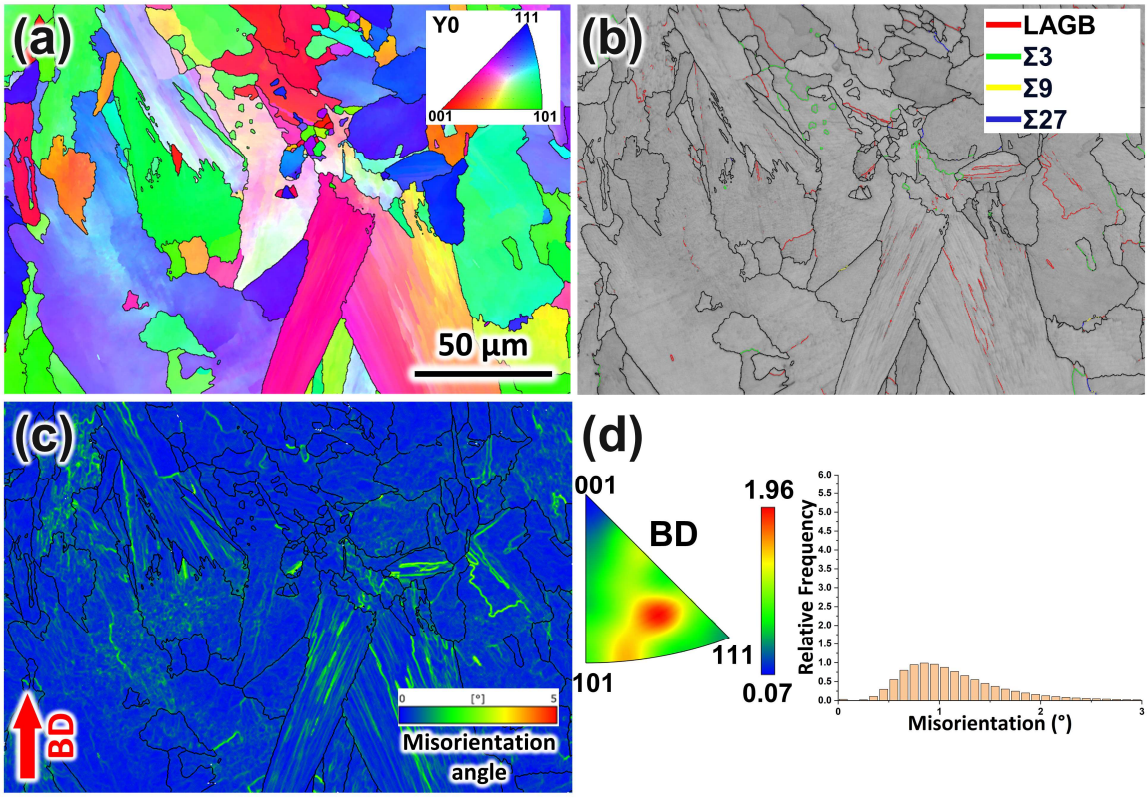


Figure 5.3. EBSD Analysis of an AP sample: (a) Inverse pole figure color map for 100 % fcc structure, (b) band contrast maps with LAGBs and CSL boundaries, (c) Kernel average misorientation map, and (d) corresponding IPF representation and misorientation angle distribution.

presence of ultra-fine ε-hcp strips, but the phase detection was limited by the EBSD step size of 0.2 μm.

On the other hand, the SHT samples in Figure 5.4a and Figure 5.4b show the transformation to a heavily twinned morphology without the previous cellular structure. The melt pools, martensitic laths, and previous sites for chemical segregation vanished and were replaced by equiaxed polygonal grains that contain multiple annealing twins and no precipitates. EBSD analysis in Figure 5.5 shows a polygonal γ-fcc phase structure with twin boundaries at a misorientation axis-angle of <111> 60° that indicates the conditions for Σ3 special grain boundaries (GBs). After SHT, the $(10\bar{1}1)$, $(11\bar{2}0)$, and $(10\bar{1}2)$ ε-phase XRD peaks in Figure 5.2 have also disappeared completely. Additionally, the KAM map in Figure 5.5c shows the disappearance of lamellar patterns that previously formed due to local misorientation concentration inside the FCC grains after printing. Most regions exhibited low KAM values due to internal stress relief, and the results suggest the occurrence of static recrystallization during heat treatment, as evidenced by the uniform grain size of ~34.8 ± 2.7 μm and absence of previously observed LAGBs.

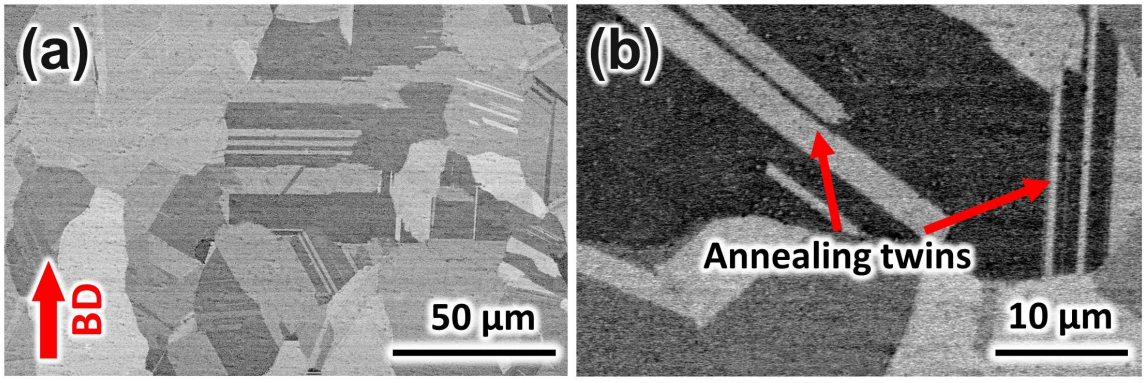


Figure 5.4. Initial microstructure of CoCrMo alloy in low (a) and high (b) magnification: equiaxed microstructure and annealing twins are shown for the solution heat-treated (SHT) sample.

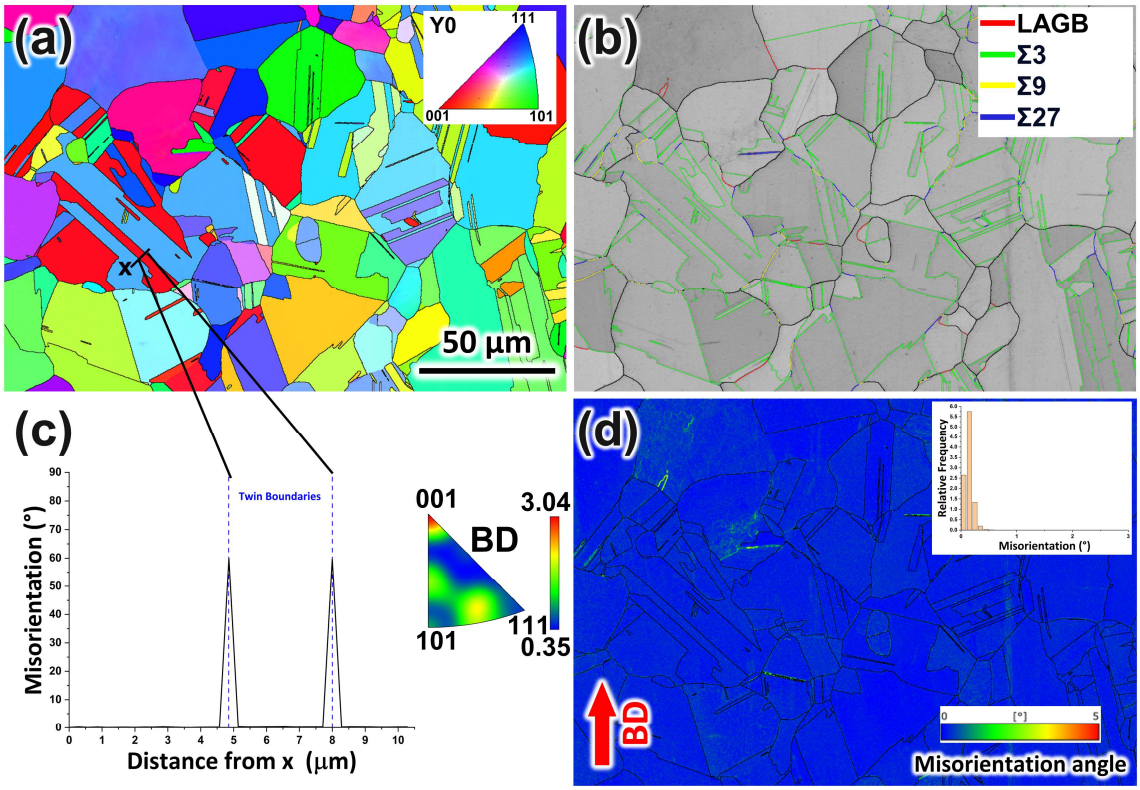


Figure 5.5. EBSD Analysis of an SHT sample: (a) Inverse pole figure color map for 100 % fcc structure, (b) band contrast maps with LAGBs and CSL boundaries, (c) Misorientation distribution along twin boundaries (left) and over-all IPF representation (right), and (d) Kernel average misorientation map with misorientation angle distribution.

5.3.2 Microstructure evolution of CoCrMo alloy upon isothermal aging

The microstructure of AP and SHT samples resulted in different transformation behavior during subsequent aging at 940 °C. The DHT samples, as shown in Figure 5.6a, revealed the partial disintegration of the cellular structure and the disappearance of melt tracks. Parallel ε-phase striations densely populated the overall structure. In contrast to the AP samples where the bands mainly stayed within the grains, transgranular bands can be observed in Figure 5.6b, indicated by the red rectangle. These bands also influenced the decomposition of cell walls, leading to the formation of elongated precipitates along the band direction, as marked by red arrows. Inside the grains, parallel arrays of fine, spherical precipitates can be observed. These precipitates, with an average diameter of 0.4 ± 0.1 µm

and an area fraction of 12.4%, are particularly prominent in the crisscross intersections and thick bands, as indicated by the green arrows. EDS point analysis shows a higher percentage of Mo and C inside the precipitates, also identified as $M_{23}C_6$ carbides. The precipitates along the GBs showed a similar morphology to those in the matrix, but with a larger average diameter of 1.1 ± .2 μm. The initial composition of the alloy also indicated the presence of nitrogen, which inhibits the athermal martensitic transformation and favors the creation of nanoscale Cr_2N precipitates within the γ matrix [26].

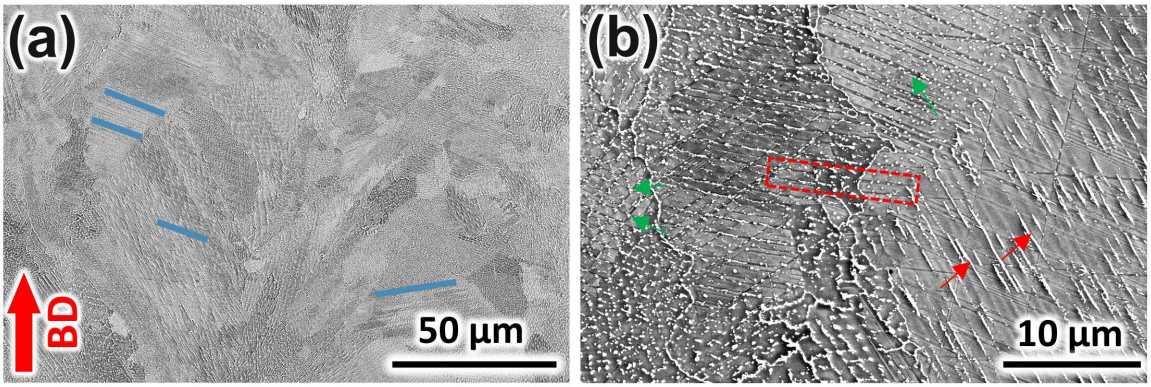


Figure 5.6. Microstructure of CoCrMo alloy after 5 hr. aging heat treatment at 940 °C: (a) trans-granular laths after direct aging (DHT), (b) ordered carbide precipitates after DHT.

The relationship between ε-phase laths and precipitate formation will be discussed later.

The EBSD analysis results in Figure 5.7 indicate a more significant phase transformation in DHT samples compared to SAHT samples, with 73.6 % and 43.8 % ε-phase, respectively. The XRD peak analysis similarly shows that DHT has a higher amount of ε-phase than SAHT, with 71.2% compared to 49.2%, respectively. The ε-phase grains of the DHT samples also display an irregular morphology with an average grain size of 11 ± 6 μm, smaller than the average grain size of 21 ± 15 μm for the γ-phase grains. In addition, ε-phase grains contain a lower percentage of LAGBs (16.2 %) compared to AP samples. Untransformed γ-phase grains exhibit parallel ε-phase strips that coincide with the lath

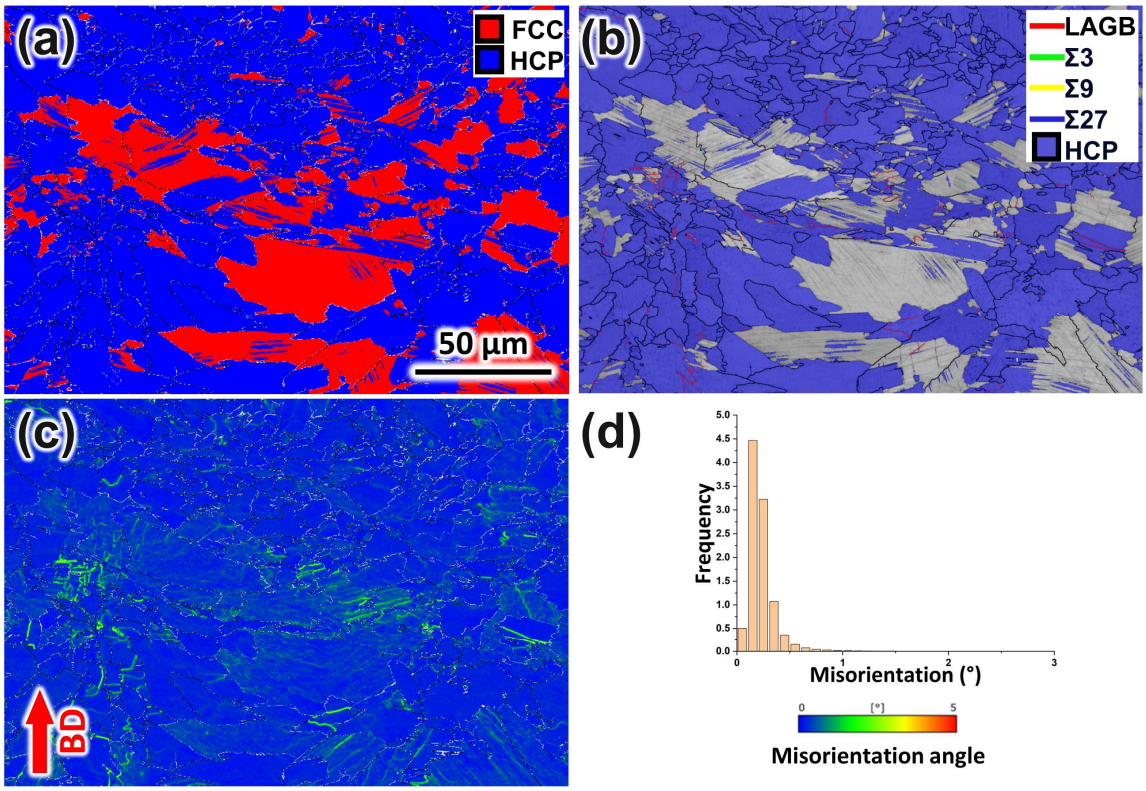


Figure 5.7. EBSD Analysis of the DHT sample: (a) Phase maps showing fcc and hcp structures, (b) pattern quality maps with LAGBs and CSL boundaries, (c) Kernel average misorientation maps, and (d) corresponding misorientation angle distribution.

arrays observed in the PQ map in Figure 5.7b, which suggests that the nucleation of ε-phase begins as fine bands inside γ-phase grains. The KAM maps in Figure 5.7c reveal little to no misorientation in hcp grains and high KAM values that are lamellar and heterogeneously distributed in γ-phase grains. However, low KAM angles of up to 2° are still present in the FCC grains, likely due to the existence of ultra-fine ε-hcp strips that have not yet undergone significant transformation.

For SAHT samples, which started with the SHT microstructure, multiple parallel martensitic bands were observed within the grains, as marked by blue lines in Figure 5.8a. It was notable that a significant number of these bands originated near grain boundaries and grew continuously without crossing the interface. Carbide precipitation has also

reemerged throughout the microstructure, but at a lower rate (5.09 % area fraction) compared to DHT (12.4 %), which was shown in Figure 5.6b. As a result of chemical homogenization, the preferred sites for carbide precipitation changed from cellular walls to grain boundaries. Initially, round precipitates with an average diameter of 1.4 ± 0.6 µm exhibited unrestricted growth, which is marked by red arrows in Figure 5.8b. Continuous aging allowed the precipitates to extend along the GBs and form elongated structures with a high aspect ratio of 2.6 ± 1.2. Both round and elongated precipitates with an average size of 0.6 µm also grew in all directions within the grains. The EBSD results in Figure 5.9 reveal the transformation to a block-type ε-phase originating from the GBs. The fully transformed hcp grains (43.8% phase fraction) had a similar grain size to the surrounding fcc grains (33 ± 14 µm and 31 ± 11 µm, respectively). Figure 5.9b also shows that the special Σ3 boundaries from SHT were preserved in the untransformed FCC grains but disappeared in the newly formed ε-phase grains. The presence of coherent interfaces with lower critical nucleation barriers such as annealing twins [27] allowed for additional sites for ε-phase nucleation, resulting in uniform transformation that extended across GBs and in all directions. Furthermore, The KAM maps in Figure 5.9d demonstrate that evenly

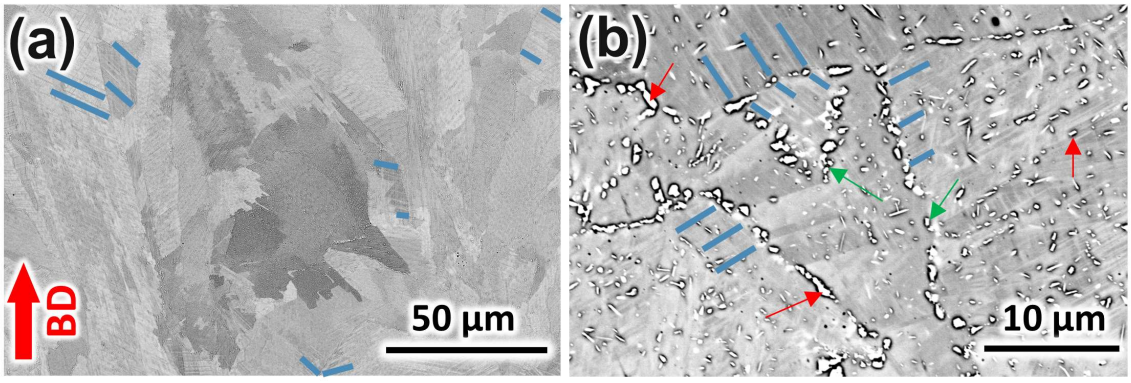


Figure 5.8. Microstructure of CoCrMo alloy after 5 hr. aging heat treatment at 940 °C: (a) lath formation after solution and aging heat treatment (SAHT), and (b) GB carbide precipitation after SAHT.

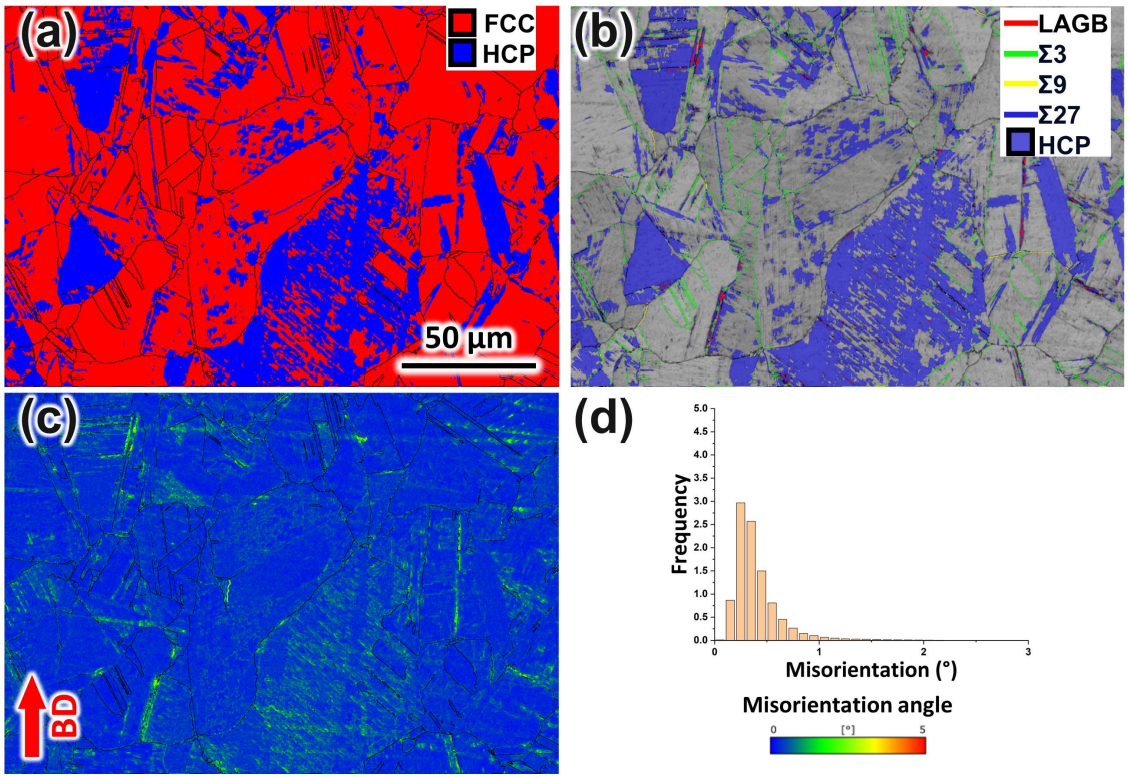


Figure 5.9. EBSD Analysis of the SAHT sample: (a) Phase maps showing fcc and hcp structures, (b) pattern quality maps with LAGBs and CSL boundaries, (c) Kernel average misorientation maps, and (d) corresponding misorientation angle distribution.

distributed low angle misorientations are present on the new ε-phase grains that reemerged after stress relief during SHT, particularly on the γ-ε phase boundaries with incomplete transformation. Locally-distributed stresses were similarly observed in ε-phase structures during the aging treatment of CoCrMo alloy after solution heat treatment [12].

Figure 5.10 compares the characteristic engineering stress-strain curves of prepared tensile samples from each condition. The heat-treated samples exhibited improved tensile strength and ductility compared to the as-built condition, which generally resembles the observed changes in microstructure. For the as-built samples, the tensile strength reached 1162 MPa, the 0.2% offset yield strength was 951 MPa, and the ductility measured at 16.4%. After undergoing solution heat treatment (SHT), the CoCrMo sample exhibited a marked increase in elongation (26.1 %) but maintained the tensile strength to 1151 MPa, although

the yield strength decreased to 745 MPa. In contrast, the DHT specimen showcased the highest tensile strength of 1261 MPa, at the expense of ductility which decreased to 11.9 %. A good balance between improved strength while sustaining sufficient ductility was observed in the SAHT sample, which displayed a tensile strength of 1197 MPa and elongation of 14.7 %.

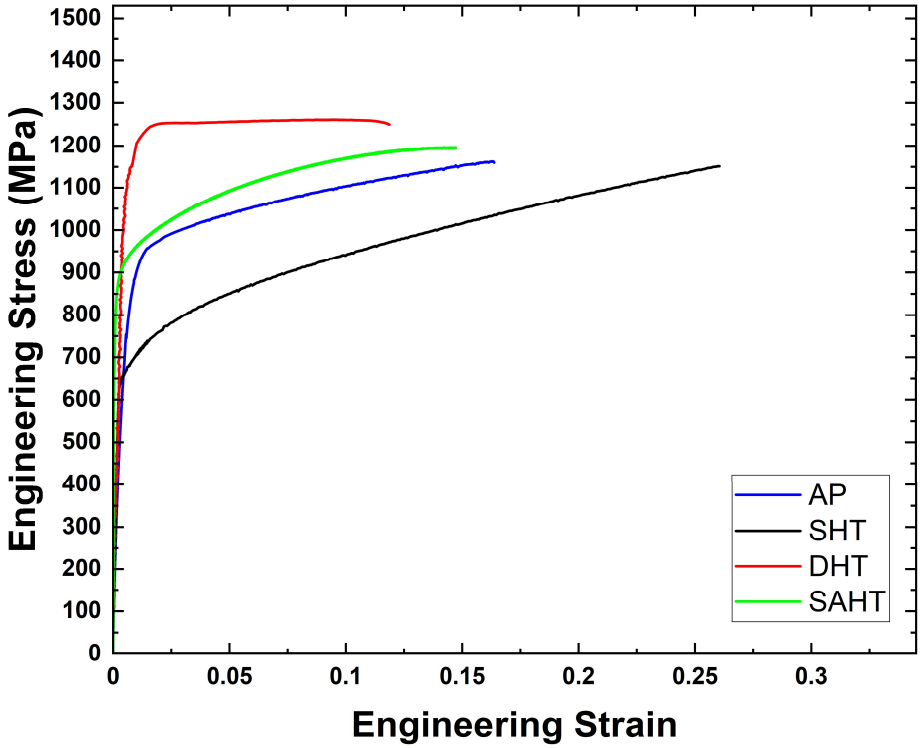


Figure 5.10. Representative engineering stress-strain curves at different conditions.

Figure 5.11 presents a closer look at the progress of carbide precipitation and isothermal transformation after 2 hr., 3 hr., and 4 hr. agi1ng of SAHT samples. The ε-phase percentages were measured as 5.2 %, 23.2 %, and 36.3 %, respectively. As aging progresses, a slight increase in grain size is observed for both the γ-phase and ε-phase. The grain size of the γ-phase changed to 24.2 ± 6 µm, 26.5 ± 9 µm, and 29.1 ± 9 µm for aging times of 2 hr., 3 hr., and 4 hr., respectively. Similarly, the grain size of the ε-phase changed to 7.1 ± 2 µm, 11.7 ± 6 µm, and 15.9 ± 8 µm, respectively. The analysis of phase maps

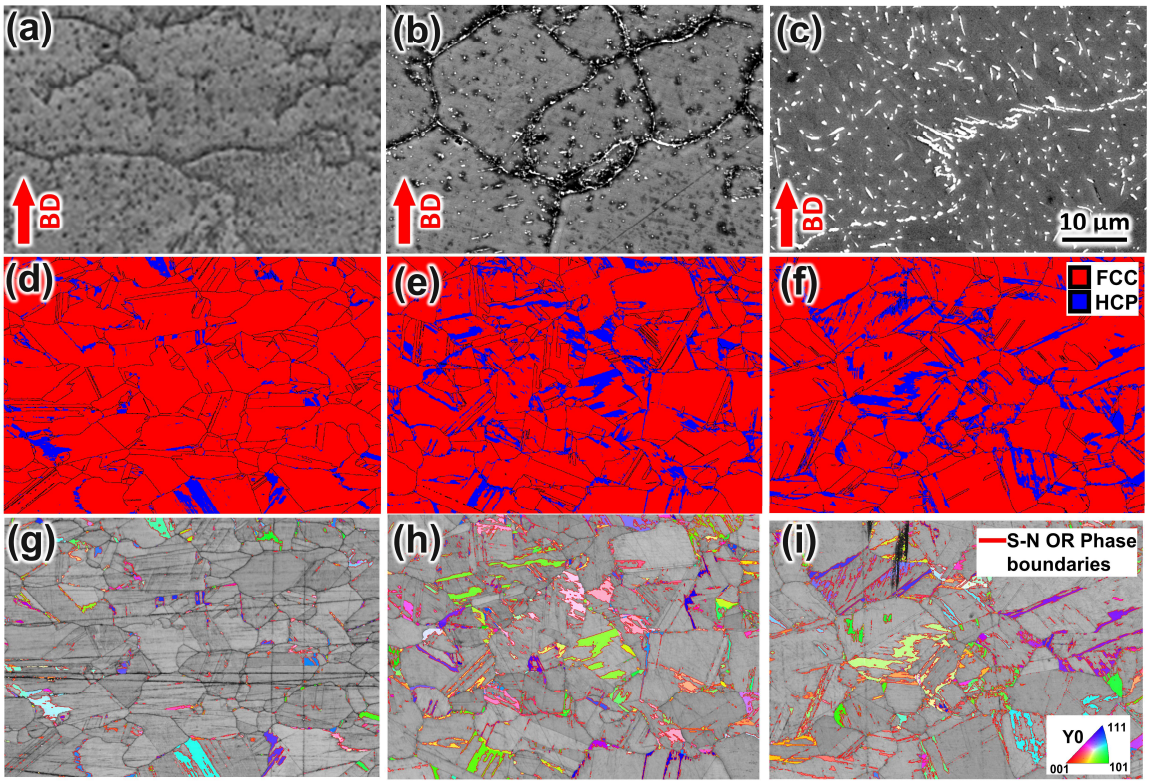


Figure 5.11. Analysis of ε-phase transformation progression over time for SAHT samples, illustrating 2 hr. aging (11a, 11d, 11g), 3 hr. aging (11b, 11e, and 11h), and 4 hr. aging (11c, 11f, 11i). SEM images highlight carbide precipitation (11a-11c), phase maps showcase the isothermal transformation (11d-11f), band contrast maps with IPF color representation of hcp phases, highlighting ε-γ phase-boundaries that satisfy the Shoji-Nishiyama orientation relationship within 5° (11g-11i).

revealed that both uniformly distributed annealing twins and grain boundaries serve as nucleation sites for the γ-ε phase transformation. These nucleation sites are characterized by low-energy coherent interfaces, initiating the transformation by lateral growth along the boundaries. However, as the transformation progresses, it extends in all directions inside the γ grains. Similarly, carbide precipitation begins near and inside grain boundaries but gradually spreads throughout the entire structure. Over time, thicker precipitates with a high aspect ratio develop along the grain boundaries. The isothermal transformation of ε-phase structures as striations inside γ grains occurs periodically along $\{111\}_\gamma$ habit planes

[28] . As a result, the phase boundaries °exhibit the Shoji-Nishiyama orientation relationship (S-N OR) [8,29] with a lattice correlation of:

$$(111)_{\gamma\text{-fcc}} \,||\, (0001)_{\varepsilon\text{-hcp}}$$

$$[11\bar{2}]_{\gamma\text{-fcc}} \,||\, [1\bar{1}00]_{\varepsilon\text{-hcp}} \text{ or } [1\bar{1}0]_{\gamma\text{-fcc}} \,||\, [11\bar{2}0]_{\varepsilon\text{-hcp}}$$

The IPF map of ε phase was superimposed to the band contrast maps at different aging times (2 hr., 3 hr., and 4 hr.) in Figure 5.11g-5.11i, highlighting γ-ε phase boundaries that satisfy the S-N OR in red. It is observed that all ε-phase structures adhere to the S-N OR within a deviation of 5°, indicating a consistent transformation mechanism at low-energy twin interfaces and grain boundaries. As the transformation progresses, a random distribution of orientations and gradual growth can be observed, with most ε-phase bands inside a previous γ grain showing a preference for a single orientation. Interestingly, when ε-phase bands develop on opposite sides of a grain boundary, they tend to have different orientations. The growth direction occurs away from the boundary and merges with transformed twins until the γ grain is entirely converted. The orientation distribution allows the retention of the original γ grain boundaries even after the isothermal transformation took place. This also shows that the carbide formation along the grain boundaries had a considerable influence to the ε-phase growth mechanism.

5.4 Discussion

5.4.1 Comparison of the as-printed and solution heat-treated microstructures

In order to establish a correlation between the resulting microstructure, precipitate formation, and phase distribution after aging of the CoCrMo alloys, it is important to first examine the differences in the initial conditions of the as-printed (AP) and solution heat-treated (SHT) samples. Since L-PBF components are subject to cyclic thermal stresses

during printing, high residual stresses are accumulated as incremental layers are added over time in AP samples. Accordingly, a high density of low angle misorientations were observed in the KAM maps. The observed cellular network can thus be associated with dislocation tangles [30], with the cellular boundaries allowing for the concentration of solute elements like C, Mo, and Si. In addition, the repeated exposure to steep thermal gradients and fast solidification rates can lead to intrinsic heat treatment and trigger the formation of precipitates [1]. Figure 5.1c shows that the cell walls contain carbides enriched with Mo and C, which can alter the ε-phase transformation mechanism. The localized reduction in carbon content, which affects the stability of the γ-phase, is a key factor in turning carbide precipitation along grain boundaries into nucleation sites for isothermal ε-phase transformation.

At high quench rates and with sufficient isothermal aging treatments below the critical temperature (T_c) of around 970 °C [13], the γ_{fcc}-ε_{hcp} martensitic transformation occurs in CoCrMo alloys. This transformation manifests as parallel striations of the ε-phase at specific orientations relative to the parent γ grain. Since the fcc and hcp stacking sequences have comparable lattice arrangements, the transition from γ to ε can be readily achieved by gliding of a/6 <112> Shockley partial dislocations on alternate close-packed {111} planes [31,32]. This transformation is amplified by the solidification structure of AP samples, since the accumulated thermal strains can also generate high amounts of vacancies and fractions of stacking faults around lattice dislocations [33]. The reaction and dissociation of perfect dislocations led to the emergence of multiple arrays of parallel bands highlighted in the SEM, PQ, and KAM maps of the AP samples. Although the phase maps predominantly displayed a γ-phase structure, the emergence of Shockley partial

dislocations from lattice dissociation led to the creation of ultrafine dendritic ε-phase embryos within the γ grains. These embryonic structures originate under non-equilibrium solidification conditions, resulting in an increased density of internal defects like dislocations and stacking faults. Alongside localized alloy segregation and carbide precipitation, these defects serve as potent nucleation sites that facilitate subsequent phase transformations during the aging heat treatment process. The KAM maps show lamellar subgrain boundaries that indicate ε-phase boundary strain regions and XRD results recorded a considerable ε-phase percentage (15.6 %). Similar observations regarding the role of pre-existing strain on phase transformations were confirmed in nitrogen-doped CoCrMo alloys [11]. Unlike the lamellar structures observed in unstrained samples, the cold-rolled specimens underwent phase decomposition, evolving into ε, Cr_2N, and σ phases after heat treatment. SEM images in this study already detected the presence of striations that coincide with the cellular structure in the AP samples, while high-resolution analyses by other researchers have also observed ultrafine ε-phase bands with a thickness of approximately 9 nm inside γ grains [30,34].

After solid solution heat treatment (SHT), the solutes within the material became uniformly distributed as cellular substructures disappeared. A solution heat treatment step above the fcc-hcp transformation temperature is usually first performed to recover the ductility, release the internal stresses, redistribute the alloying elements, dissolve the precipitates, and achieve a homogenous structure. The previously observed low-angle grain boundaries (LAGBs) have been replaced by a considerable amount of Σ3 annealing twin boundaries, resulting in the development of equiaxed, polygonal grains with evenly distributed local misorientations. While cast CoCrMo alloys expect the development of around ~12 % ε-

phase formation upon quenching of solution heat-treated samples [13], the SHT sample did not detect any ε-phase bands in the PQ and SEM Maps. This absence can be attributed to the presence of nitrogen as it inhibits athermal ε-martensite formation from stacking faults if the composition exceeds 0.10 wt. % [35]. Another reason is the occurrence of static recrystallization triggered by tangled dislocations and the homogenization of carbon, which acts as a stabilizer for the γ-phase. However, Kajima et al. [36] reported complete recrystallization and elimination of anisotropic behavior after a longer exposure duration of 6 hrs. This observation is consistent to the localized dendritic misorientation that remained inside some grains in the KAM map of the SHT sample, despite the overall reduction in residual stresses resulting from cooperative motion of boundary dislocations. Therefore, the SHT sample can utilize a combination of low-energy coherent twin boundaries, which can function as new nucleation sites, and retained strain energy from cyclic reheating, which can serve as the driving force for the required transformation.

5.4.2 Effects of isothermal aging at 940 °C to as-printed samples

Various microstructural features, including low-energy coherent twins, solute clusters, grain boundaries, and ultrafine dendrites, can serve as ε-phase embryos under specific heat treatment conditions. The subsequent growth is controlled by the local dislocations and the systematic arrangement of Shockley partials, as the transformation takes place by faulting along the fcc's most densely packed planes [37,38]. The nucleated ε-phase also displays the Shoji-Nishiyama orientation relationship [29] with the surrounding γ-phase grains and manifests as dense parallel bands that can eventually thicken and form complete grains.

The difference in ε-phase formation and distribution between DHT and SAHT samples is evident from EBSD analysis (73.6 % and 43.8 % ε-phase, respectively) and XRD

calculations (71.2% compared to 49.2% ε-phase, respectively). For DHT samples, the microstructure is densely populated with thick ε-phase bands, which strongly influenced the distribution of the decomposed cell structures. Figure 5.6b reveals the presence of transgranular and criss-cross bands, showing the extent of isothermal transformation. The green arrows in the figure indicate regions with high concentrations of Mo and C from EDS maps (not shown here), which suggests that thick ε-phase bands and criss-cross junctions are preferred carbide nucleation sites. The intersection of the newly formed ε-phase regions along intrinsic faults with the preexisting stacking faults triggers the development of partial arrays of vacancies if a sufficient driving force is available. These regions containing high vacancy planes can accommodate the lattice mismatch between the faulted region and possible precipitates [39]. The presence of ordered precipitates aligned inside ε-phase bands can be explained by this phenomenon.

The isothermal transformation process starts within γ-fcc grains along parallel bands and ultra-fine ε-phase embryos, as shown from the nucleation sites observed in the KAM map of Figure 5.7c and as originally observed in the as-built microstructure in Figure 5.1b. The slight inherent initial texture due to printing can provide an explanation for the development of transgranular bands, as similarly oriented γ grains develop continuous striations during transformation. As the aging process continues, adjacent lamellae experience thermally activated growth at the expense of stacking faults. This progression occurs inside the grains until the transformation to the more stable ε-phase is complete [40]. The growth of the ε-hcp phase from the metastable γ-phase is limited by the movement of Shockley partial dislocations and can be accelerated by increasing the temperature and prolonging the duration of the aging process [37]. However, Putaux [28]

noted that Shockley partials along grain boundaries that satisfy the transformation condition are limited by the nucleation rate of correlated dislocations. Lateral growth will be challenging since the elastic energy associated with thickening is not favorable and the stacking fault sequence should be preserved. Moreover, the alternating Shockley partials in layered ε-phase substructures result in zero overall deformation and lower elastic energy. Therefore, the thickening of ε-phase bands in the martensitic transformation alone cannot fully account for the observed mechanism in the EBSD maps. These maps reveal a more extensive and heterogeneous transformation, with newly formed grains being smaller than the original γ grains. Most of the ε-phase grains, which demonstrate minimal internal misorientation, lack the striations observed within the untransformed γ-phase grains. This indicates the occurrence of another transformation mechanism, which is termed massive transformation accompanied by recrystallization.

Similar to the analysis in Figure 5.11g-5.11i, a comparison of the orientation relationships between phase boundaries in DHT and SAHT samples are shown in Figure 5.12. The analysis revealed various types of ε-phase morphology in the DHT samples. These include large ε-hcp grains surrounded by γ-fcc grains without any specific orientation relationship (OR), compact ε-hcp grains with a smaller grain size and no local misorientation, and parallel arrays of ε-phase within untransformed γ-fcc grains exhibiting the S-N OR. Researchers have observed massive transformation as an alternative martensitic transformation at temperatures exceeding 800 °C [6,14,30]. However, it is important to note that only the initial nucleation boundary exhibits a low-energy interface with the S-N OR, while the selective growth of grains generates surfaces that lack crystallographic coherency with the surrounding γ-phase. As a result, most of the newly formed ε-hcp grains

in Figure 5.12a do not exhibit the S-N OR with the surrounding γ grains. A comparison is drawn using two highlighted grains displaying the transformation start and finish conditions. While some ε-phase bands within the γ grain that exhibit S-N OR can be observed at the start of transformation, the surrounding ε-phase grains consume the original γ grain boundaries and form new phase boundaries that do not obey S-N OR. Consequently, these ε-phase grains can readily merge over time, leading to uneven grain growth and a diverse grain size distribution at the end of transformation. The orientation distribution within a single γ grain (labeled c and highlighted with red in Figure 5.12a) was also outlined using pole figures in Figure 5.12c. The mean orientation of the γ phase is (270.2°, 21.3°, and 71.8°), with an average deviation of 4.4°. Considering this as the parent orientation, the theoretical orientations necessary for the transformed ε-phase to obey the S-N OR were predicted and shown in red in Figure 5.12c. The corresponding (0001) and $(11\bar{2}0)$ projections of the recorded ε-phase measurements were then compared to the idealized orientations. Only a portion of the ε-phase orientations are found to cluster closely around the projected S-N predictions. Furthermore, in this study, a slightly elevated aging temperature was employed, facilitating the consumption of newly transformed ε-hcp grains by smaller grains. This process led to the formation of recrystallized structures with random orientation and minimal local misorientation, utilizing the cumulative strain regions generated during the printing process. Figure 5.12a also displays multiple ε-γ phase boundaries that do not exhibit a specific OR, highlighting the extensive growth after DHT.

Massive transformation capitalizes on the localized reduction of carbon content due to precipitate formation along heavily dislocated cell walls. The short-range diffusion process destabilizes the γ-phase and triggers the preferred and uninterrupted linear growth of the ε-

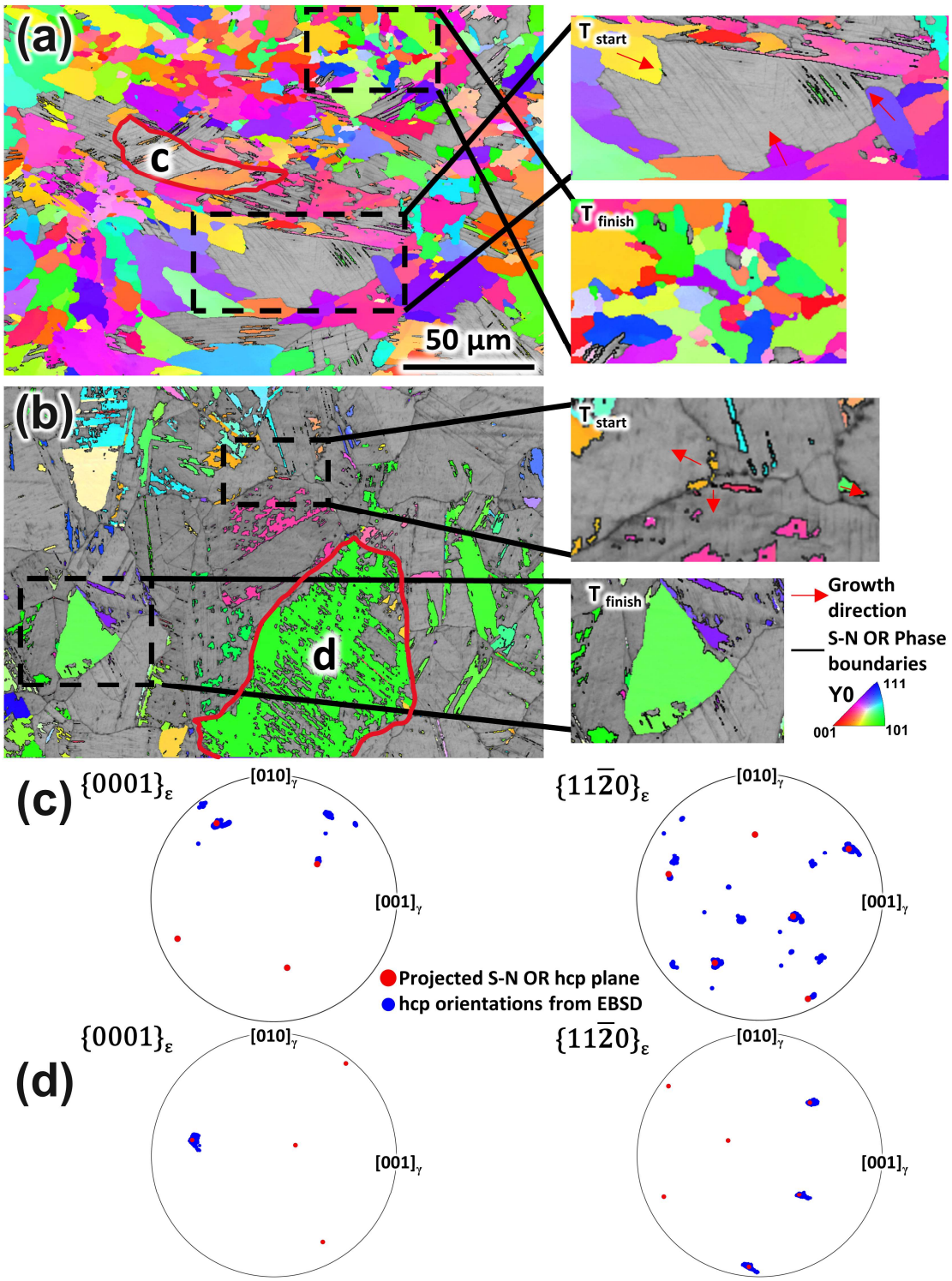


Figure 5.12. Transformation analysis: Figures 12a and 12b show band contrast maps with IPF color representation of hcp phases, highlighting ε-γ phase-boundaries that satisfy the Shoji-Nishiyama orientation relationship within 5° for DHT and SAHT, respectively. Grains that portray the start and end of γ-ε transformation are magnified, along with the growth direction of ε-phase. Pole figure projections of hcp grains for DHT and SAHT are illustrated in Figures 12c and 12d, comparing ε-phase orientations to the projected hcp planes satisfying the Shoji-Nishiyama orientation relationship based on the mean fcc orientation.

phase across the boundaries between grains [14]. However, some regions in the cellular

structure do not have sufficient segregation for the mechanism to be energetically favored, which results to non-uniform transformation and growth. Overall, a heterogeneous ε-phase structure was formed during DHT as a result of a combined transformation mechanism involving both martensitic and massive modes.

5.4.3 Effects of isothermal aging at 940 °C to solution heat-treated samples

In contrast, the SHT samples exhibited a more gradual ε-phase transformation. The morphology of the previous γ grains were retained, and regions with incomplete transformation show that grain boundaries and annealing twins served as preferred sites for nucleation during the isothermal transformation. The ε-phase transformation spreads inside the grain in all directions, without consuming the previous γ grain boundaries. The chemical homogenization during SHT resulted in a shift of preferential carbide nucleation sites from inside the grains and partially disintegrated cellular structures to the grain boundaries. This change, coupled with stress relief and the elimination of dislocations and stacking faults, significantly modifies the transformation dynamics observed after SAHT. The microstructures depicted in Figure 5.8a and Figure 5.8b illustrate that most ε-phase bands originated from grain boundaries, which served as preferential sites for carbide precipitation. The polygonal grain boundaries acted as carbon sinks and preferred nucleation sites for martensite bands that extend into the grains, which is evident in the microstructure. Moreover, the presence of carbide precipitates at the interfaces creates solute drag, which hinders interface migration during the transformation [12]. As a result, both phases exhibit similar grain sizes and grain boundary morphologies after aging, facilitating a uniform transformation albeit at a slower pace.

While DHT samples can instigate autocatalytic martensite nucleation events from inside grains through the intercellular network that is saturated with solutes, SAHT samples are limited to grain boundaries and low-energy twin boundaries. Bollman's model of intersecting faults [41] also suggests that the growth of ε-phase layers can be affected by the size of the grain, as the presence of grain boundaries can hinder local transformation. In order to continue the transformation process, faults that meet the three possible orientations along the local stress field must be found. Despite the presence of multiple ε-phase bands surrounding the central region in Figure 5.8b, there are no visible martensite striations indicating ε-phase transformation inside the grain. Figure 5.9b also displays untransformed γ-phase regions where Σ3 CSL boundaries are retained within the grains, even though the transformed regions have utilized the special boundaries for nucleation. This suggests that regions lacking nucleation sites along boundaries would require more time to undergo transformation, as the boundaries impede the progress of martensite nucleation. Nevertheless, carbide nucleation continues to a lesser extent with aging, as evidenced by the presence of discontinuous precipitates randomly distributed within the untransformed γ-phase grains. The localized reduction in carbon around these precipitates then promotes further transformation in multiple directions, enabling the complete transformation of γ-phase grains with their previous boundaries intact.

Similar to the analysis in the DHT sample, the orientation distribution within a single γ grain (labeled d and highlighted with red in Figure 5.12b) was also examined using pole figures in Figure 5.12d. The mean orientation of the γ phase is (330.9°, 41.1°, and 34.0°), with a lower average deviation of 1.7° compared to the DHT sample. The corresponding (0001) and $(11\bar{2}0)$ projections of the recorded ε-phase measurements were again compared

to the idealized S-N OR reflections. Despite a slight scatter, which can be caused by the huge sample size, the observed orientations fall close to the predicted S-N OR. A majority of regions within a transformed grain exhibit the same orientation, enabling the preservation of the initial average grain size and reducing internal misorientations. The reduced density of stacking faults and dislocations after SHT has hindered the ε-phase transformation that occured during SAHT, as some potential growth sites for ε-phase embryos created during the printing step have already been consumed for the formation of new, equiaxed γ grains. The KAM maps obtained after DHT are consistent with this observation, showing a higher degree of transformation with fully developed ε-phase grains and practically no internal misorientation after transformation. Studies on the kinetics of γ-ε transformation [40] have also found that solution-treated specimens undergo a longer incubation time and a more sluggish growth due to a reduction in the available sites for ε-phase nucleation. Additionally, the measured lattice strains show a gradual decrease in solution-treated samples, whereas there is minimal change observed in the as-printed samples after the initial stages of aging.

Figure 5.13 summarizes the transformation mechanisms observed in different conditions. While cast and wrought alloys exhibit low residual ε-phase percentage inside equiaxed grains with dendritic morphology [13,42], the non-equilibrium conditions in AM structure develop multiple parallel ε-phase striations, carbide precipitates in cell walls, and dendritic embryos from local strain. Applying SHT promotes an equiaxed single-phase fcc microstructure featuring annealing twins. The absence of athermal ε-phase bands typically found in cast alloys is linked to nitrogen inhibition. Aging at slightly elevated temperatures utilizes distinct nucleation sites for phase transformations. DHT grows ε-phase along

ordered carbide precipitates, expanding ε-phase bands, and decomposed cell structures. Heterogenous growth is promoted by alloy segregation and localized strains. On the other hand, carbide precipitation along grain boundaries and the low-energy annealing twins act as nucleation sites for the SAHT sample.

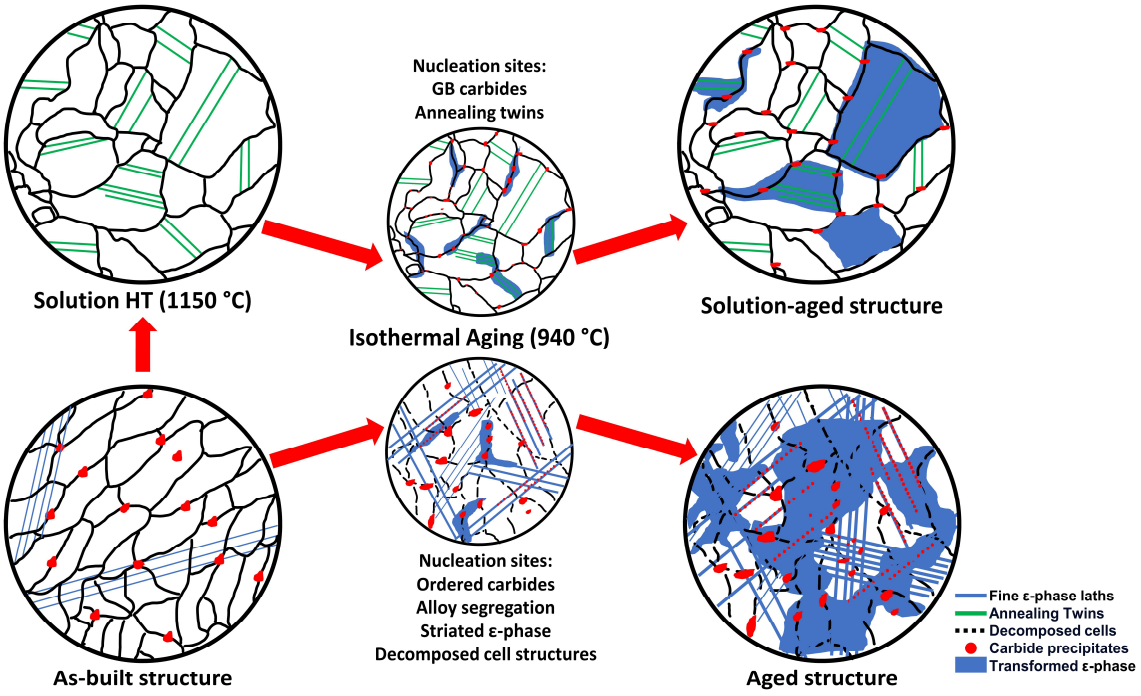


Figure 5.13. Illustration of transformation mechanisms observed in AM CoCrMo alloy.

Prolonged aging promotes noticeable differences in the developed microstructure. The DHT specimen exhibited irregular grain growth and precipitate formation. In this sample, 61.7% of ε-γ phase boundaries conform to the S-N orientation relationship (OR), thereby attributing a minimum of 38.3% of the transformation boundaries to massive transformation. Conversely, SAHT samples maintained the shape of prior fcc grains and promoted a homogenous distribution of precipitates. Most (90.2 %) of the ε-γ phase boundaries adhere to the S-N OR, indicative of the prevalent isothermal transformation.

5.5 Conclusions

This study examined the γ-ε phase transition and carbide precipitation mechanisms during the aging heat treatment of both as-printed and solution-treated CoCrMo samples fabricated using L-PBF. The conclusions drawn from the observations are as follows:

- The initial microstructures of as-printed and solution-treated samples significantly influenced the transformation morphology after aging heat treatment. As-printed samples exhibited a highly dislocated cellular structure with uniformly distributed $M_{23}C_6$ carbides and multiple parallel ultrafine ε-phase bands. In contrast, solution heat-treated samples leveraged a blend of low-energy coherent twin boundaries as new nucleation sites and retained strain energy from cyclic reheating as the driving force for the necessary transformation.

- EBSD analysis and XRD calculations confirmed a higher ε-phase fraction in DHT samples compared to SAHT samples. DHT samples were densely populated with transgranular ε-phase bands, partially dissolved cell walls, and ordered carbide precipitates resulting from the combined effects of isothermal transformation, massive transformation, and recrystallization. Conversely, SAHT samples exhibited a more gradual isothermal transformation originating along grain boundaries and coherent interfaces, preserving the initial average grain size and reducing internal misorientations.

- EBSD analysis underscored the significance of the initial AM texture, which can lead to transgranular bands and adjacent ε-phase grains with similar orientations. These can readily merge over time, leading to uneven grain growth and a diverse grain size distribution after transformation. SAHT samples displayed a consistent

orientation inside transformed grains, enabling the retention of previous γ grain boundaries.

- The preferred sites for carbide precipitation shifted from cellular walls in DHT samples to grain boundaries and coherent interfaces in SAHT samples. The isothermal transformation is heavily influenced by the formation of carbon sinks. Elongated precipitates can promote solute drag and hinder interface migration during the transformation.

5.6 Chapter 5 References

[1] Z. Liu, D. Zhao, P. Wang, M. Yan, C. Yang, Z. Chen, J. Lu, Z. Lu, Additive manufacturing of metals: Microstructure evolution and multistage control, J. Mater. Sci. Technol. 100 (2022) 224–236. https://doi.org/10.1016/j.jmst.2021.06.011.

[2] A. du Plessis, S.M.J. Razavi, M. Benedetti, S. Murchio, M. Leary, M. Watson, D. Bhate, F. Berto, Properties and applications of additively manufactured metallic cellular materials: A review, Prog. Mater. Sci. 125 (2022) 100918. https://doi.org/10.1016/j.pmatsci.2021.100918.

[3] M. Godec, S. Zaefferer, B. Podgornik, M. Šinko, E. Tchernychova, Quantitative multiscale correlative microstructure analysis of additive manufacturing of stainless steel 316L processed by selective laser melting, Mater. Charact. 160 (2020) 110074. https://doi.org/10.1016/j.matchar.2019.110074.

[4] S. Gribbin, S. Ghorbanpour, N.C. Ferreri, J. Bicknell, I. Tsukrov, M. Knezevic, Role of grain structure, grain boundaries, crystallographic texture, precipitates, and porosity on fatigue behavior of Inconel 718 at room and elevated temperatures, Mater. Charact. 149 (2019) 184–197. https://doi.org/10.1016/j.matchar.2019.01.028.

[5] B. Konieczny, A. Szczesio-Wlodarczyk, J. Sokolowski, K. Bociong, Challenges of Co–Cr Alloy Additive Manufacturing Methods in Dentistry—The Current State of Knowledge (Systematic Review), Materials 13 (2020) 3524. https://doi.org/10.3390/ma13163524.

[6] S. Kurosu, H. Matsumoto, A. Chiba, Isothermal Phase Transformation in Biomedical Co-29Cr-6Mo Alloy without Addition of Carbon or Nitrogen, Metall. Mater. Trans. A 41 (2010) 2613–2625. https://doi.org/10.1007/s11661-010-0273-8.

[7] X. Dong, Y. Zhou, Y. Qu, M. Wu, Q. Sun, H. Shi, H. Peng, Y. Zhang, S. Xu, N. Li, J. Yan, Recrystallization behavior and grain boundary character evolution in Co-Cr alloy from selective laser melting to heat treatment, Mater. Charact. 185 (2022) 111716. https://doi.org/10.1016/j.matchar.2021.111716.

[8] K. Yamanaka, M. Mori, Y. Koizumi, A. Chiba, Local strain evolution due to athermal γ→ε martensitic transformation in biomedical CoCrMo alloys, J. Mech.

Behav. Biomed. Mater. 32 (2014) 52–61. https://doi.org/10.1016/j.jmbbm.2013.12.019.
[9] M. Mori, K. Yamanaka, A. Chiba, Phase decomposition in biomedical Co–29Cr–6Mo–0.2N alloy during isothermal heat treatment at 1073K, J. Alloys Compd. 590 (2014) 411–416. https://doi.org/10.1016/j.jallcom.2013.12.126.
[10] L.H.M. Antunes, J.J. Hoyos, T.C. Andrade, P.W.C. Sarvezuk, L. Wu, J.A. Ávila, J.P. Oliveira, N. Schell, A.L. Jardini, J. Žilková, P.F. da Silva Farina, H.F.G. Abreu, M. Béreš, Deformation-induced martensitic transformation in Co-28Cr-6Mo alloy produced by laser powder bed fusion: Comparison surface vs. bulk, Addit. Manuf. 46 (2021) 102100. https://doi.org/10.1016/j.addma.2021.102100.
[11] M. Mori, K. Yamanaka, A. Chiba, Effect of cold rolling on phase decomposition in biomedical Co–29Cr–6Mo–0.2N alloy during isothermal heat treatment at 1073K, J. Alloys Compd. 612 (2014) 273–279. https://doi.org/10.1016/j.jallcom.2014.05.175.
[12] M. Roudnická, J. Kubásek, L. Pantělejev, O. Molnárová, J. Bigas, J. Drahokoupil, D. Paloušek, D. Vojtěch, Heat treatment of laser powder-bed-fused Co–28Cr–6Mo alloy to remove its microstructural instability by massive FCC→HCP transformation, Addit. Manuf. 47 (2021) 102265. https://doi.org/10.1016/j.addma.2021.102265.
[13] H.F. López, A.J. Saldivar-Garcia, Martensitic Transformation in a Cast CoCrMo-C Alloy, Metall. Mater. Trans. A 39 (2008) 8–18. https://doi.org/10.1007/s11661-007-9370-8.
[14] B.T. Donkor, J. Song, Y. Fu, M. Kattoura, S.R. Mannava, M.A. Steiner, V.K. Vasudevan, Accelerated γ-face-centered cubic to ε-hexagonal close packed massive transformation in a laser powder bed fusion additively manufactured Co-29Cr-5Mo alloy, Scr. Mater. 179 (2020) 65–69. https://doi.org/10.1016/j.scriptamat.2020.01.012.
[15] K. Nyamuchiwa, Y. Tian, K. Chadha, L. Jiang, T. Dorin, C. Aranas Jr, Precipitation Behaviour at the Interface of an Additively Manufactured M789–N709 Hybrid Alloy, Acta Metall. Sin. Engl. Lett. (2023). https://doi.org/10.1007/s40195-023-01558-z.
[16] Z.H. Liu, D.Q. Zhang, S.L. Sing, C.K. Chua, L.E. Loh, Interfacial characterization of SLM parts in multi-material processing: Metallurgical diffusion between 316L stainless steel and C18400 copper alloy, Mater. Charact. 94 (2014) 116–125. https://doi.org/10.1016/j.matchar.2014.05.001.
[17] V. Utyaganova, A. Filippov, S. Tarasov, N. Shamarin, D. Gurianov, A. Vorontsov, A. Chumaevskii, S. Fortuna, N. Savchenko, V. Rubtsov, E. Kolubaev, Characterization of AA7075/AA5356 gradient transition zone in an electron beam wire-feed additive manufactured sample, Mater. Charact. 172 (2021) 110867. https://doi.org/10.1016/j.matchar.2020.110867.
[18] B. Vamsi Krishna, W. Xue, S. Bose, A. Bandyopadhyay, Functionally graded Co–Cr–Mo coating on Ti–6Al–4V alloy structures, Acta Biomater. 4 (2008) 697–706. https://doi.org/10.1016/j.actbio.2007.10.005.
[19] C. Zhong, J. Liu, T. Zhao, T. Schopphoven, J. Fu, A. Gasser, J.H. Schleifenbaum, Laser Metal Deposition of Ti6Al4V—A Brief Review, Appl. Sci. 10 (2020) 764. https://doi.org/10.3390/app10030764.

[20] J. Pasco, Y. Tian, K. Chadha, L. Jiang, T. Dorin, C. Aranas Jr, Unusual interface phase transformation during continuous additive manufacturing of maraging steel and Co–30Cr–7Mo alloy, Mater. Sci. Eng. A 881 (2023) 145336. https://doi.org/10.1016/j.msea.2023.145336.
[21] M. Zhang, Y. Yang, C. Song, Y. Bai, Z. Xiao, An investigation into the aging behavior of CoCrMo alloys fabricated by selective laser melting, J. Alloys Compd. 750 (2018) 878–886. https://doi.org/10.1016/j.jallcom.2018.04.054.
[22] A. de J. Saldívar García, A. Maní Medrano, A. Salinas Rodríguez, Effect of solution treatments on the FCC/HCP isothermal martensitic transformation in Co-27Cr-5Mo-0.05C aged at 800°C, Scr. Mater. 40 (1999) 717–722. https://doi.org/10.1016/S1359-6462(98)00489-8.
[23] C. Balagna, S. Spriano, M.G. Faga, Characterization of Co–Cr–Mo alloys after a thermal treatment for high wear resistance, Mater. Sci. Eng. C 32 (2012) 1868–1877. https://doi.org/10.1016/j.msec.2012.05.003.
[24] M. Sage, C. Guillaud, Méthode d'analyse quantitative des variétés allotropiques du cobalt par les rayons X, Rev. Métallurgie 47 (1950) 139–145. https://doi.org/10.1051/metal/195047020139.
[25] Z. Wang, S.Y. Tang, S. Scudino, Yu.P. Ivanov, R.T. Qu, D. Wang, C. Yang, W.W. Zhang, A.L. Greer, J. Eckert, K.G. Prashanth, Additive manufacturing of a martensitic Co–Cr–Mo alloy: Towards circumventing the strength–ductility trade-off, Addit. Manuf. 37 (2021) 101725. https://doi.org/10.1016/j.addma.2020.101725.
[26] K. Yamanaka, M. Mori, A. Chiba, Nanoarchitectured Co–Cr–Mo orthopedic implant alloys: Nitrogen-enhanced nanostructural evolution and its effect on phase stability, Acta Biomater. 9 (2013) 6259–6267. https://doi.org/10.1016/j.actbio.2012.12.013.
[27] D. Veeraraghavan, P. Wang, V.K. Vasudevan, Nucleation kinetics of the α→γM massive transformation in a Ti-47.5 at.% Al alloy, Acta Mater. 51 (2003) 1721–1741. https://doi.org/10.1016/S1359-6454(02)00572-4.
[28] J.-L. Putaux, J.-P. Chevalier, HREM study of self-accommodated thermal ε-martensite in an Fe-Mn-Si-Cr-Ni shape memory alloy, Acta Mater. 44 (1996) 1701–1716. https://doi.org/10.1016/1359-6454(95)00268-5.
[29] M.E. Fine, M. Meshii, C.M. Wayman, Z. Nishiyama, eds., MATERIALS SCIENCE AND TECHNOLOGY, in: Martensitic Transform., Academic Press, 1978: p. ii. https://doi.org/10.1016/B978-0-12-519850-9.50001-6.
[30] M. Roudnická, O. Molnárová, J. Drahokoupil, J. Kubásek, J. Bigas, V. Šreibr, D. Paloušek, D. Vojtěch, Microstructural instability of L-PBF Co-28Cr-6Mo alloy at elevated temperatures, Addit. Manuf. 44 (2021) 102025. https://doi.org/10.1016/j.addma.2021.102025.
[31] G. Barucca, E. Santecchia, G. Majni, E. Girardin, E. Bassoli, L. Denti, A. Gatto, L. Iuliano, T. Moskalewicz, P. Mengucci, Structural characterization of biomedical Co–Cr–Mo components produced by direct metal laser sintering, Mater. Sci. Eng. C 48 (2015) 263–269. https://doi.org/10.1016/j.msec.2014.12.009.
[32] S. Mahajan, M.L. Green, D. Brasen, A model for the FCC→HCP transformation, its applications, and experimental evidence, Metall. Trans. A 8 (1977) 283–293. https://doi.org/10.1007/BF02661642.

[33] P. Huang, H.F. López, Strain induced ε-martensite in a Co–Cr–Mo alloy: grain size effects, Mater. Lett. 39 (1999) 244–248. https://doi.org/10.1016/S0167-577X(99)00021-X.
[34] K.K. Bawane, D. Srinivasan, D. Banerjee, Microstructural Evolution and Mechanical Properties of Direct Metal Laser-Sintered (DMLS) CoCrMo After Heat Treatment, Metall. Mater. Trans. Phys. Metall. Mater. Sci. 49 (2018) 3793–3811. https://doi.org/10.1007/s11661-018-4771-4.
[35] K. Yamanaka, M. Mori, A. Chiba, Effects of nitrogen addition on microstructure and mechanical behavior of biomedical Co–Cr–Mo alloys, J. Mech. Behav. Biomed. Mater. 29 (2014) 417–426. https://doi.org/10.1016/j.jmbbm.2013.10.006.
[36] Y. Kajima, A. Takaichi, N. Kittikundecha, T. Nakamoto, T. Kimura, N. Nomura, A. Kawasaki, T. Hanawa, H. Takahashi, N. Wakabayashi, Effect of heat-treatment temperature on microstructures and mechanical properties of Co–Cr–Mo alloys fabricated by selective laser melting, Mater. Sci. Eng. A 726 (2018) 21–31. https://doi.org/10.1016/j.msea.2018.04.048.
[37] N.C. Dahn, D. Morphy, K. Rajan, Kinetics of the martensitic f.c.c.→ h.c.p. transformation in CoCrMo alloy powders, Acta Metall. 32 (1984) 1317–1322. https://doi.org/10.1016/0001-6160(84)90077-4.
[38] G.B. Olson, M. Cohen, A general mechanism of martensitic nucleation: Part I. General concepts and the FCC → HCP transformation, Metall. Trans. A 7 (1976) 1897–1904. https://doi.org/10.1007/BF02659822.
[39] J.B. Vander Sande, J.R. Coke, J. Wulff, A transmission electron microscopy study of the mechanisms of strengthening in heat-treated CoCrMo-C alloys, Metall. Trans. A 7 (1976) 389–397. https://doi.org/10.1007/BF02642835.
[40] L.H.M. Antunes, M. Béreš, J.J. Hoyos, L. Novotný, H.F.G. de Abreu, P.F. da Silva Farina, Kinetics of FCC to HCP Transformation During Aging Heat Treatment of Co–28Cr–6Mo Alloy Fabricated by Laser-Powder Bed Fusion, Metall. Mater. Trans. A (2023). https://doi.org/10.1007/s11661-023-07016-w.
[41] W. Bollmann, On the phase transformation of cobalt, Acta Metall. 9 (1961) 972–975. https://doi.org/10.1016/0001-6160(61)90125-0.
[42] M. Roudnicka, J. Bigas, O. Molnarova, D. Palousek, D. Vojtech, Different Response of Cast and 3D-Printed CoCrMo Alloy to Heat Treatment: A Thorough Microstructure Characterization, Metals 11 (2021) 687. https://doi.org/10.3390/met11050687.

Chapter 6: Variant selection in maraging steel

Background

The unique variant selection and austenite reversion mechanisms observed in the MMAM component after heat treatment warranted a deeper investigation of the martensite transformation mechanisms for maraging steel. This chapter determines if these mechanisms can still be observed after heat treatment of maraging steel samples printed on their own. The variant selection phenomenon for this material has rarely been observed after printing because of a valid reason: normally, after printing, this steel quickly cools down and turns into martensite directly, without forming any austenite. Reliable parent construction software such as MTEX are currently available, but the certainty of the orientation relationship in simulations regardless of the transformation conditions remains a point of contention. To overcome this limitation, over-aging was conducted at 490 °C for 10 hours to trigger the reversion of austenite and investigate the resulting two-phase structure. This procedure led to observations in parent-child orientation relationships that have been seen for the first time in this study: during austenite reversion, the austenite orientation remarkably follows the morphological patterns of preceding melt pools and columns prior to the disappearance of cell structures. The local element segregation induced by rapid solidification contributes to the resulting texture of the reverted austenite, which can then be related to the variant selection mechanisms observed in the previous chapters. Other heat treatments have also been analyzed for comparison, applying parent grain reconstruction to single phase samples.

This section has been published: Pasco, J., He, Y., Keshavarzkermani, A., Aranas, C. (2024). Texture Preference and Variant Analysis of Martensite Formation in Laser Powder Bed Fusion. In: TMS 2024 153rd Annual Meeting & Exhibition Supplemental Proceedings. TMS 2024. The Minerals, Metals & Materials Series. Springer, Cham.

Abstract

In Laser Powder Bed Fusion (L-PBF) of maraging steel, oscillating thermal cycles inherent to additive manufacturing (AM) revert the melt pool to its parent phase repeatedly and creates sharp lath transformation morphologies. Investigating the influence of parent texture and solute distribution, this study delves into the variant formation during fcc-γ austenite to bct-α' martensitic transformation, especially under prolonged aging. Results indicate columnar prior austenite grains in as-built samples, which undergo refinement after direct aging and adopt an equiaxed morphology after annealing. In contrast, overaged specimens revealed that austenite reversion starts at cellular boundaries that have disintegrated over time due to chemical diffusion. The austenite grain formation remarkably mirrors the preceding melt pool patterns. Furthermore, certain reverted austenite grains displayed limited child orientation selection, such as a columnar grain that did not manifest any of the six possible c $(\bar{1}11)$ variants. Future studies will uncover mechanisms dictating selection during austenite reversion.

6.1 Introduction

In the domain of L-PBF applied to maraging steels, a captivating interplay of phase transformation dynamics occur during the sequential layer printing due to cellular solute segregation and the overlapping solidification morphology. Within the melt pool, distinct regions showcase varying martensite lath structures after AM and after subsequent heat treatment. Typically in martensitic systems, an orientation relationship (OR) is established between the parent austenite grain and a set of resulting product orientations, termed

variants, irrespective of whether the transformation pathway involved displacive or diffusional processes [1]. Each variant possesses identical odds of forming from a prior grain and the resulting configuration dilutes the parent texture for energy minimization. Prominent ORs such as the Kurdjumov-Sachs (K-S) relationship characterized by the $\{111\}_\gamma \parallel \{110\}_\alpha$ and $<1\bar{1}0>_\gamma \parallel <1\bar{1}1>_\alpha$ parallelism conditions, corresponding to 24 variants, and the Nishiyama-Wassermann (N-W) relationship, defined by $\{111\}_\gamma \parallel \{110\}_\alpha$ and $<\bar{2}11>_\gamma \parallel <1\bar{1}0>_\alpha$, which results to 12 possible variants [2], are often reproduced in research examining fcc-bcc transformation pairs.

However, variable heating during AM reverts the melt pool to the parent phase multiple times and creates sharp lath transformation morphologies. The mechanism entails complex solidification textures and might not preserve all potential martensitic variants. This study explores the influence of parent grain texture and solute distribution on the fcc-γ austenite to bct-α' martensitic transformation in as-built, aged, and annealed maraging steel. The apparent variant selection during austenite reversion after long aging conditions were also investigated. Given that most as-built and heat-treated microstructures predominantly exhibit a fully transformed martensitic matrix, we employed reconstruction algorithms for parent grain analysis, simulating the prior austenite structure using recognized ORs as a basis. Interestingly, the over-aged sample exhibits reverted austenite structures and therefore permits a fresh perspective on examining phase transformation phenomena. Martensite clusters that surround adjacent austenite regions with uniform orientation were compared with predicted variants of the aforementioned ORs to establish the selection of product orientations during austenite reversion. This research presents two possible

pathways for probing phase transformation in AM components while avoiding the challenges of simulating rapid thermal cycles thermodynamically.

6.2 Experimental Procedure

The maraging steel component containing 18 % Ni and 9.5 % Co was fabricated using gas-astomized powders sourced from voestalpine Additive Manufacturing Center Ltd. (vAMC) utilizing the EOS M290 printer. Table 1 presents the Inductively Coupled Plasma - Optical Emission Spectroscopy (ICP-OES) analysis results of the employed powders which have sizes between 15 and 70 μm. During printing, the following printing parameters were preserved: laser power of approximately 290 W, laser speed at 1.1 cm/s, layer thickness close to 50 μm, hatch distance near 0.1 mm, and a zigzag hatching style with a 50° rotation in every successive layer.

Table 6.1. Composition of the investigated maraging steel (in wt %).

Ni	Co	Mo	C	Si	Mn	Ti	Fe
17.9	9.4	4.8	0.03	0.15	0.15	1.3	Bal.

The as-fabricated samples underwent varied heat treatment schedules to induce distinct lath morphologies and cellular decomposition scenarios. For HT1, direct aging was performed at 490 °C for 3 hours, based on dilatometric analyses that pinpointed the precipitation temperature between 450-580 °C [3]. HT2 involved annealing at 940 °C for 2 hours to partially decompose the AM structure, exceeding the recognized austenite finish temperature of 820 °C. Over-aging for HT3 was conducted at 490 °C for 10 hours to trigger the reversion of austenite and investigate the resulting two-phase structure. All treatments were carried out within a sealed tube furnace, adhering to a constant argon pressure of 10^{-5} bar, heating rate of 2 °C/s and water quenching to room temperature. Samples from each

condition underwent orientation analysis using a ThermoFisher Scios 2 SEM geared with an EBSD detector. For the conditions involving consistent bct phase structures (as-built, HT1, and HT2), multiple modified functions involving the MATLAB-based MTEX parentGrainReconstructor algorithm [1] were programmed to establish the prior austenite grains (PAGs) for variant analysis. On the other hand, austenite reversion in HT3 was investigated using pole figures by projecting all $\{100\}_{\alpha}$ bct orientations into the $\{111\}_{\gamma}$ austenite plane and comparing them to predicted orientations of K-S and N-W variants.

6.3 Results and Discussion

The initial microstructure after LPBF depicted in Figure 6.1a shows a mixture of thick and fine fragmented laths aligned with the underlying melt pool morphology. Due to the fluctuating thermal conditions experienced by the powder bed during solidification, the hierarchical packet-block-lath martensite structures observed in as-quenched maraging steels did not manifest in the EBSD orientation maps. What emerged instead were elongated grains with similar orientations but are isolated by incomplete growth, hinting at parallel lath structures that could have fully formed under stable solidification conditions. After direct aging, the HT1 sample in Figure 6.1b reveals pronounced disintegration of laths while the melt-pool matrix morphology remains intact. A slight grain refinement occurs as the cellular structures produced by additive manufacturing are partially decomposed due to the redistribution of alloying elements. In addition, the aging temperature also triggers the formation of strengthening precipitates (Ni_3Ti, Ni_3Mo and Fe_7Mo_6, etc. [4,5]) with contrasting morphologies that, in turn, also influences the strain distribution during lath reconfiguration. Nevertheless, matrix morphology largely mirrors the as-built sample.

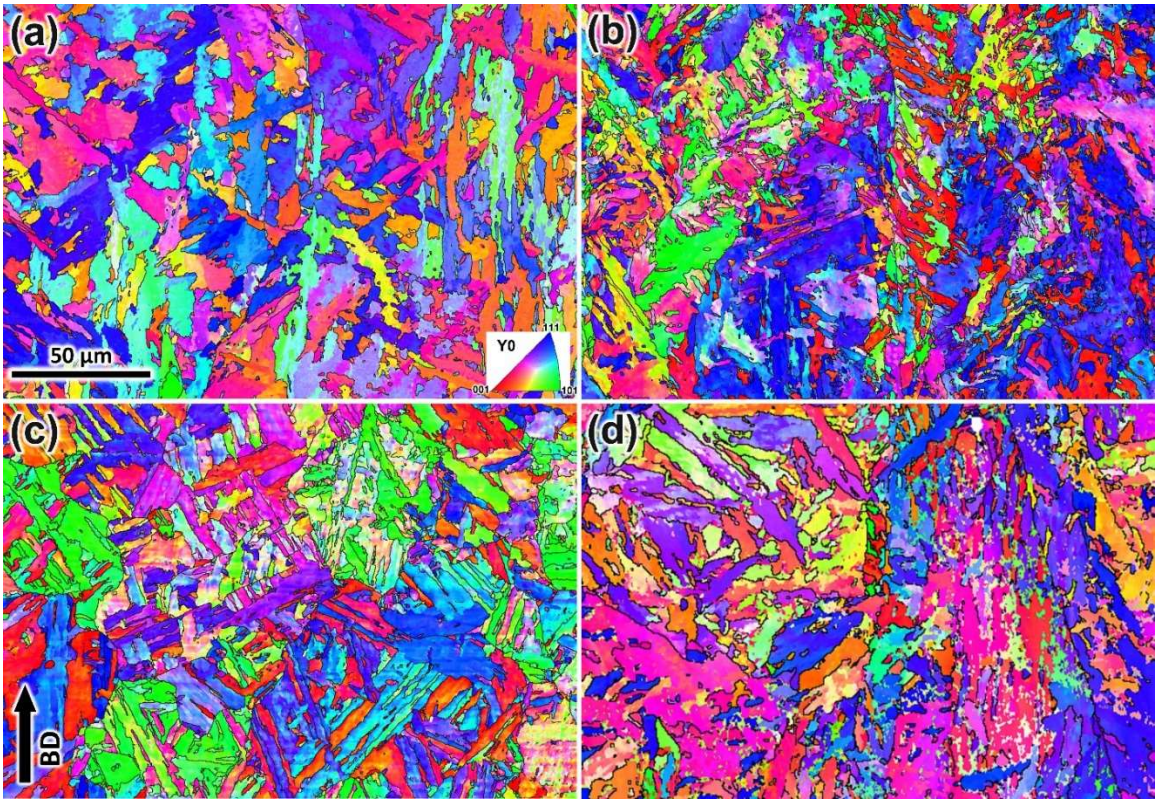


Figure 6.1. Inverse pole figure (IPF) color map of maraging steel subjected to various conditions: (a) as-built, (b) direct aging at 490 °C for 3 hours (HT1), (c) annealing above A_f at 940 °C for 2 hours (HT2), and (d) over-aging at 490 °C for 10 hrs (HT3).

On the other hand, the HT2 sample annealed above A_f as illustrated in Figure 6.1c features a more consistent lath morphology and an equiaxed matrix. Since this heat treatment triggers the partial dissolution of cellular structures, quenching permits the formation of multiple parallel laths with uniform thickness throughout the microstructure. A few isolated martensite islands that have not developed into parallel structures still exist, suggesting that thorough homogenization of these structures might require a longer annealing period or a solution heat treatment above 1100 °C [3]. The final condition displayed in Figure 6.1d shows the orientation properties of the HT3 sample after over-aging for 10 hours at 490° C. Among the conditions evaluated, only HT3 exhibited austenite reversion that is typically seen at slightly higher temperatures (530-670 °C [6]). Extended aging enabled chemical diffusion, cellular structure disintegration, grain growth,

and phase transformation. The segregation of austenite-stabilizing elements led to the emergence of austenite islands that persist at ambient temperature after quenching. Thicker laths can also be observed at HT3 compared to those at HT1, which was only exposed for 3 hours.

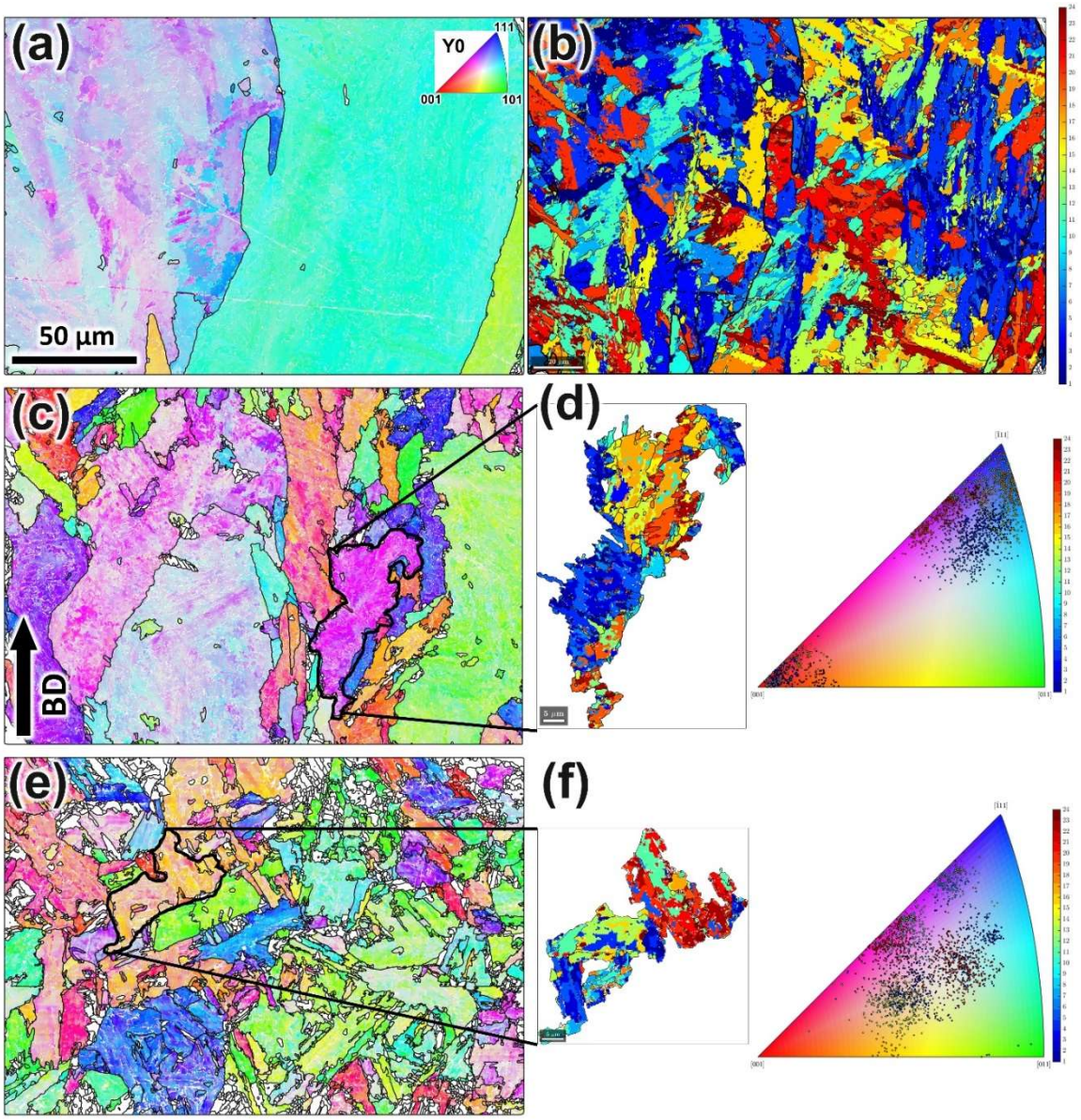


Figure 6.2. Parent grain reconstruction and analysis of fully martensitic structures: IPF color map of reconstructed prior austenite grains for (a) as-built, (c) HT1, and (e) HT2 conditions. Figure 2b shows the variant distribution color map in the as-built sample, referencing the 24 variants from K-S OR. For HT1 and HT2, representative grain-scale variant distribution maps are showcased in Figures 2d and 2f, respectively, with the variant color map (left) and variant orientation distribution superimposed in the IPF map (right).

Since the as-built, HT1 and HT2 conditions completely transformed to single-phase bct martensite, the ORtools library in MTEX was employed to reconstruct the PAGs and analyze the variant distribution. The prior parent orientation is inferred from several distinct, neighboring child grains that pinpoint a single parent grain through all possible configurations of the designated orientation relationship, which is the K-S OR for all cases in Figure 6.2. The algorithm uses Voronoi decomposition to classify the most appropriate parent orientations based on a voting system gathered from all adjacent child grains. Suboptimal matches are discarded, and orientations with high confidence are iteratively nucleated to rebuild the entire microstructure [1]. The results in Figure 6.2a, 2c, and 2e reveal significant differences between the austenite morphology prior to transformation under various conditions.

For the as-built sample in Figure 6.2a, the PAGs that decomposed to different variants appear columnar and aligned with the building direction (BD). The variant color distribution in Figure 6.2b also indicates multiple variants of the same type that nucleated in the same orientation but had their growth interrupted due to the rapid heating and cooling cycles during the printing process. After undergoing direct aging in HT1 as seen Figure 6.2c, the columnar structure of PAGs aligned with the BD was still maintained, but a non-uniform austenite grain size distribution has developed. Some regions have also not resolved to a common parent orientation that fits the K-S OR. Factors such as cellular decomposition and chemical redistribution reduce the overall predominant texture from printing, although analysis of variant distribution at the granular level in Figure 6.2d still shows clustering of child orientations along {100} // BD and {111} // BD. A more homogenous PAG distribution is evident in the HT2 sample shown in Figure 6.2e,

confirming the dissolution of the melt morphology after printing. Although regions with no parent solutions based on K-S OR have increased, the detection of grains with randomly oriented variants shown in Figure 6.2f confirms the efficacy of the short annealing time in producing PAGs that transform into complete martensite packets.

Some challenges arise during parent austenite reconstruction of maraging steels. The high crystallographic symmetry inherently produces 24 potential variants, implying multiple possible parent orientations from a singular orientation. The presence of annealing twins also leads to six indistinguishable variants within the same (111) habit plane. Adjacent laths also have low relative misorientation that complicates granular categorization [7]. The certainty of the orientation relationship regardless of the transformation conditions is also a point of contention.

However, the analysis undertaken for HT3 in Figure 6.3 and Figure 6.4 successfully circumvents these challenges. Here, regions with similarly oriented reverted austenite were used as basis in identifying the surrounding martensite grains that are expected to exhibit the K-S OR, along with predicting the orientation of possible variants. The phase map in Figure 6.3a reveals that austenite reversion starts at the melt pool and cell boundaries that have disintegrated over time due to chemical diffusion. Besides having higher concentrations of austenite-stabilizing elements, the presence of dislocation walls in cell boundaries [8] can provide the necessary driving force for the austenite reversion kinetics. As documented for the first time in this study, Figure 6.3b also shows that the formation of austenite grains during reversion *remarkably mirrors the morphological patterns of preceding melt pools and columns*. Although the cellular structures have partially disintegrated, they play a crucial role in the phase and orientation distribution during

austenite reversion, adding a critical dimension to the understanding of the transformation process.

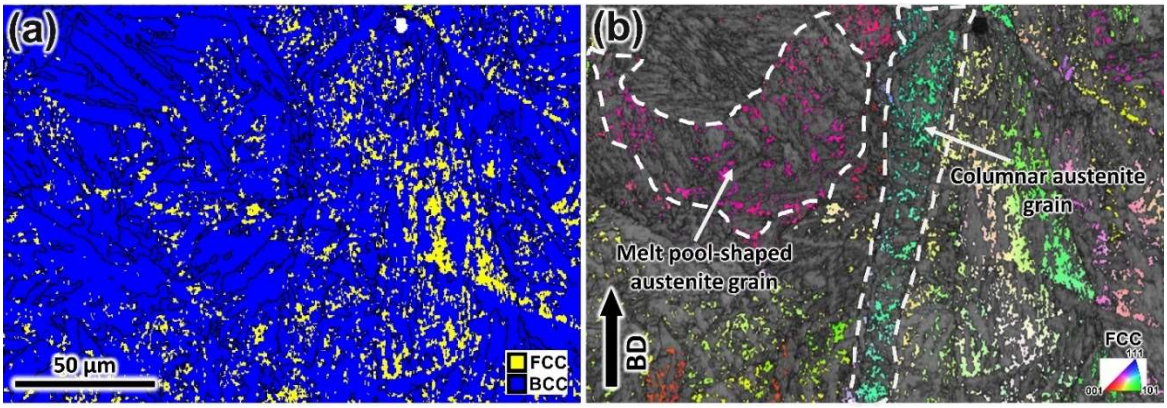


Figure 6.3. EBSD analysis of HT3: phase map showing fcc and bcc regions, and (b) band contrast map overlain with the reverted austenite (fcc) IPF color map.

Taking the highlighted austenite regions with consistent orientation in Figure 6.3b, variant analysis was conducted with the surrounding martensite laths. Figure 6.4a illustrates the $\{100\}_\gamma$ austenite orientations within the melt-pool shaped grain, revealing a mean orientation of $\varphi_1 = 57°$ $\phi_2 = 42°$ and $\varphi_3 = 18°$ and a notably low average deviation of 3°. On the other hand, the $\{100\}_\gamma$ orientations inside columnar austenite grain are captured in Figure 6.4b, showing a mean orientation of $\varphi_1 = 246°$ $\phi_2 = 21°$ and $\varphi_3 = 45°$ with an average deviation of 4°. Figure 6.4c and 6.4d portray the $\{100\}_\alpha$ orientations of the surrounding martensite laths shown in gray that are inside the outlined melt pool and column regions, respectively. To analyze the distribution of martensite orientations, the experimental results were compared to the predicted variants of the relevant orientation relationships, as shown in Figure 6.4e and 6.4f. Both the projected K-S and N-W OR variants (calculated from the average γ orientation) are represented: blue circles for K-S and red triangles for N-W. These are overlaid onto the gray-shaded $\{100\}_\alpha$ orientations of the included martensite laths projected onto the $(111)_\gamma$ plane. For clarity in visualization, the $[1\bar{1}0]$ and $[\bar{1}\bar{1}2]$ planes of the average austenite orientation were aligned with the x- and y-axes, showcasing the

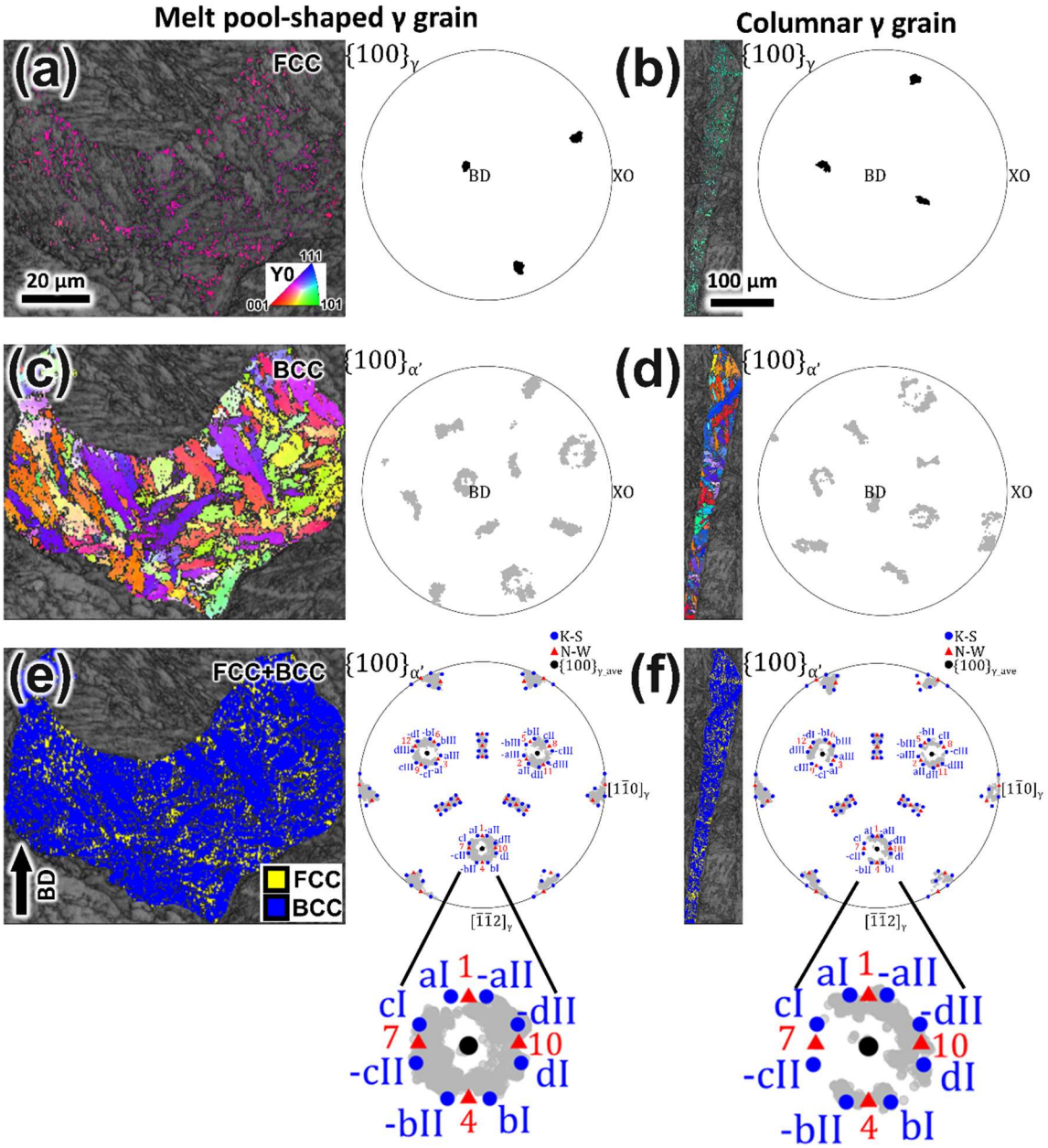


Figure 6.4. Pole figure analysis of melt pool-shaped and columnar shaped austenite grain: (a-b) band contrast overlaid with IPF color map of fcc phase (left) with pole figures of {100}γ projected along the BD (right), (c-d) band contrast overlaid with IPF color map of bcc phase (left) with pole figures of {100}α projected along the BD (right), (e-f) band contrast overlain with the phase map (left) with comparison of {100}α to the predicted K-S and N-W variants along the {111}γ plane. (a), (c), and (e) refer to the melt pool-shaped austenite grain while (b), (d) and (f) refer to the columnar austenite grain.

variant distribution around the three Bain circles and the mean austenite orientation [2].

Furthermore, the predicted K–S variants in Figure 6.4e and 6.4f are also denoted using the

Bishop–Hill [9] naming system, where the labels are designated according to all possible variations of the closely-packed $\{111\}_\gamma$ planes.

The pole figure in Figure 6.4e shows that the surrounding martensite laths successfully aligned with all 24 possible K-S variants and 12 N-W variants inside the melt pool-shaped austenite grain. However, certain orientations like a1, bIII, and -bIII have lower densities compared to the rest of the predicted variants. In contrast, Figure 6.4f delineates the absence of several geometrically anticipated variants in the columnar grain: specifically for K-S OR (-aI, aIII, -cI, cI, -cII, cII, cIII, and -cIII) and for N-W OR (v2, v3, v7, v8, and v9). Notably, none of the six possible variants expected from the c $(\overline{1}11)$ austenite plane parallelism condition appeared in the surrounding martensite laths. This grain displayed a distinct variant selection despite not applying any deformation. Upcoming research will reveal the underlying mechanisms governing the selection criteria during austenite reversion.

6.4 Conclusions

Different PAGs morphologies from fully transformed conditions emphasize the influence of the starting melt structure. The printing pattern produces columnar austenite grains aligned with the BD, with multiple variants experiencing interrupted growth despite nucleating in the same orientation. Direct aging shows non-uniform PAG size distribution, while a more homogenous PAG distribution is achieved after annealing above A_f.

The extended aging features a complex interplay between chemical diffusion, cellular structure disintegration, precipitate formation, grain growth, and phase transformation. Thicker laths and reverted austenite are developed while dislocation walls along cell boundaries can provide the energy requirement for the transformation.

As newly established in this research, the formation of austenite grains during reversion closely resembles the morphological patterns of preceding melt pools and columns. Despite partial disintegration of cellular structures, they critically influence phase and orientation during austenite reversion.

The lack of several expected variants can occur during austenite reversion depending on the morphology of the adjacent austenite grains.

6.5 Chapter 6 References

[1] F. Niessen, T. Nyyssönen, A.A. Gazder, R. Hielscher, Parent grain reconstruction from partially or fully transformed microstructures in MTEX, J Appl Cryst. 55 (2022) 180–194. https://doi.org/10.1107/S1600576721011560.

[2] Y. He, J.J. Jonas, S. Godet, P.J. Jacques, Crystallographic features of theγ-to-α transformation in a Nb-added transformation-induced plasticity steel, Metall Mater Trans A. 37 (2006) 2641–2653. https://doi.org/10.1007/BF02586099.

[3] L.G. de Carvalho, M.S. Andrade, R.L. Plaut, F.M. Souza, A.F. Padilha, A dilatometric study of the phase transformations in 300 and 350 maraging steels during continuous heating rates, Mat. Res. 16 (2013) 740–744. https://doi.org/10.1590/S1516-14392013005000069.

[4] Y. Tian, R. Palad, C. Aranas, Microstructural evolution and mechanical properties of a newly designed steel fabricated by laser powder bed fusion, Additive Manufacturing. 36 (2020) 101495. https://doi.org/10.1016/j.addma.2020.101495.

[5] X. Mei, Y. Yan, H. Fu, X. Gao, S. Huang, L. Qiao, Effect of aging temperature on microstructure evolution and strengthening behavior of L-PBF 18Ni(300) maraging steel, Additive Manufacturing. 58 (2022) 103071. https://doi.org/10.1016/j.addma.2022.103071.

[6] F.F. Conde, J.D. Escobar, J.P. Oliveira, M. Béreš, A.L. Jardini, W.W. Bose, J.A. Avila, Effect of thermal cycling and aging stages on the microstructure and bending strength of a selective laser melted 300-grade maraging steel, Materials Science and Engineering: A. 758 (2019) 192–201. https://doi.org/10.1016/j.msea.2019.03.129.

[7] R. Hielscher, T. Nyyssönen, F. Niessen, A.A. Gazder, The variant graph approach to improved parent grain reconstruction, Materialia. 22 (2022) 101399. https://doi.org/10.1016/j.mtla.2022.101399.

[8] J. Pasco, Y. Tian, K. Chadha, L. Jiang, T. Dorin, C. Aranas Jr, Unusual interface phase transformation during continuous additive manufacturing of maraging steel and Co–30Cr–7Mo alloy, Materials Science and Engineering: A. 881 (2023) 145336. https://doi.org/10.1016/j.msea.2023.145336.

[9] J.F.W. Bishop, R. Hill, XLVI. A theory of the plastic distortion of a polycrystalline aggregate under combined stresses., The London, Edinburgh, and Dublin Philosophical Magazine and Journal of Science. 42 (1951) 414–427. https://doi.org/10.1080/14786445108561065.

Chapter 7: Conclusions

The continuous printing and effective heat treatment of a maraging steel-CoCrMo alloy multi-material component was studied in detail. For this purpose, comprehensive characterization and material property testing of the interface after printing and after multiple heat treatment conditions were performed. The analysis was extended to CoCrMo and maraging steel individually since they exhibited unique transformation mechanisms and texture evolution outside conventional heat treatment conditions.

Designing an effective heat treatment schedule for the MMAM component presents two key challenges: firstly, ensuring that alloy migration, intermetallic precipitation, and phase distribution along the transition zones do not weaken or compromise the structural integrity; and secondly, achieving the desired internal structure, dislocation distribution, texture, mechanical properties, and phase transformations in each base alloy. The first challenge is tackled in Chapters 3 and 4, with the objective of identifying the interfacial characteristics in the transition zones and developing an approriate heat treatment strategy to satisfy the mechanical property requirements of the target component applications. The second challenge is answered in Chapters 5 and 6, with the objective of determining the governing phase transformation behaviors and precipitate formation in CoCrMo alloys during heat treatment in Chapter 5 and determining the texture evolution in maraging steels during heat treatment in Chapter 6. These analyses led to the following conclusions:

- The interface of the as-printed samples exhibits discontinuous martensite transformation of fully fcc phase columnar grains influenced by the combined effects of growth orientation, solute segregation, local stress accumulation, and

cellular growth. Future work could investigate the difference in corrosive and wear properties across the interface of the multi-material structure.

- Nano-indentation hardness measurements suggest successful precipitation strengthening and stress relief in the CoCrMo alloy region. Mechanical tests show that its tensile strength remained stable at approximately 1185 MPa before and after heat treatment, with elongation improving from roughly 14.7% to 27.1%. The observed increase in strength and ductility, especially evident at the fracture points after tensile testing, reflects the strong bonding strength between the CoCrMo alloy and maraging steel components.

- After solidification and heat treatment, grain-scale martensite variant selection is observed in the austenite-martensite boundaries of the multi-material component. This is attributed to the presence of residual stress and recoil pressure, which intensify at the melt's center. However, this effect is mitigated near the boundaries of the melt pool, where convective flow is more intense. Future work could investigate the individual effects of printing parameters to the distribution of martensite orientation after phase transformation.

- Exposing the multi-material component to 1150 °C for 2 hours, then to 940 °C for 5 hours, followed by 490 °C for 6 hours, generated the smoothest end-to-end composition, texture, and hardness variation among all tested heat treatment schedules. The superior tensile strength observed is the result of synergistic strengthening effects from the precipitation of intermetallic compounds in maraging steel and a pronounced γ-ε transformation in CoCrMo alloy.

- Homogenous solute distribution, which is achieved during solution treatment of the multi-material component, prevents austenite reversion and overshadows the effects of precipitation-induced alloy depletion during austenite reversion.
- The initial microstructures of as-printed and solution-treated CoCrMo alloy samples dictated the transformation morphology after aging heat treatment. As-printed samples exhibited a highly dislocated cellular structure with uniformly distributed $M_{23}C_6$ carbides and multiple parallel ultrafine ε-phase bands. In contrast, solution heat-treated samples displayed a blend of low-energy coherent twin boundaries as new nucleation sites and retained strain energy from cyclic reheating as the driving force for phase transformation. Future work could investigate the variation in wear properties at different treatment conditions.
- During heat treatment of as-printed maraging steels, the formation of austenite islands during reversion closely resembles the morphological patterns of prior cellular and melt pool boundaries. Despite partial disintegration of cellular structures, they critically influence phase and orientation during austenite reversion. The extended aging features a complex interplay between chemical diffusion, cellular structure disintegration, precipitate formation, grain growth, and phase transformation. Thicker laths and reverted austenite are developed while dislocation walls along cell boundaries can provide the energy requirement for austenite reversion.

Curriculum Vitae

Full Name: Jubert M. Pasco

Education

- PhD Candidate, Mechanical Engineering, University of New Brunswick, Fredericton, Canada (2020-2024)
- Bachelor of Science in Metallurgical Engineering, University of the Philippines, Diliman, Quezon City, Philippines (2012-2017)

Awards

- New Brunswick Innovation Fund (NBIF), 2021
- Best Presenter Award, Canadian Materials Science Conference, 2021
- Mitacs Accelerate Award, 2022

Publications

[1] J. Pasco, A. Keshavarzkermani, K. Nyamuchiwa, L. Jiang, T. Dorin, C. Aranas Jr, Heat treatment effects and variant selection in multi-material laser powder bed fusion of FeNi- and CoCr-based alloys, Virtual and Physical Prototyping 19 (2024) e2372629. https://doi.org/10.1080/17452759.2024.2372629.

[2] J. Pasco, Y. Tian, K. Chadha, L. Jiang, T. Dorin, C. Aranas Jr, Unusual interface phase transformation during continuous additive manufacturing of maraging steel and Co–30Cr–7Mo alloy, Materials Science and Engineering: A 881 (2023) 145336. https://doi.org/10.1016/j.msea.2023.145336.

[3] J. Pasco, L. Jiang, T. Dorin, A. Keshavarzkermani, Y. He, C. Aranas, Phase transformation in additively manufactured Co-Cr-Mo alloy after solution and aging heat treatment, Materials Characterization 207 (2024) 113467. https://doi.org/10.1016/j.matchar.2023.113467.

[4] J. Pasco, Z. Lei, C. Aranas, Additive Manufacturing in Off-Site Construction: Review and Future Directions, Buildings 12 (2022) 53. https://doi.org/10.3390/buildings12010053.

[5] J. Pasco, Y. Tian, K. Chadha, C. Aranas, Heat Treatment of Multi-Material Additively Manufactured Maraging Steel and Stellite Alloy, in: Proceedings of the 61st Conference of Metallurgists, COM 2022, Springer International Publishing, Cham, 2023: pp. 25–28. https://doi.org/10.1007/978-3-031-17425-4_5.

[6] J. Pasco, T. McCarthy, J. Parlee, N.A. Nazri, S. Padmajan, S. Rodrigues, C. Aranas, Constitutive modeling of modified-H13 steel, MRS Communications (2022). https://doi.org/10.1557/s43579-022-00182-9.

[7] J. Pasco, Y. Tian, K. Chadha, C. Aranas, Heat Treatment of Multi-Material Additively Manufactured Maraging Steel and Co-Cr-Mo Alloy, Defect and Diffusion Forum 421 (2022) 9–14. https://doi.org/10.4028/p-q60291.

[8] J. Pasco, Y. He, A. Keshavarzkermani, C. Aranas, Texture Preference and Variant Analysis of Martensite Formation in Laser Powder Bed Fusion, in: TMS 2024 153rd Annual Meeting & Exhibition Supplemental Proceedings, Springer Nature Switzerland, Cham, 2024: pp. 1808–1816. https://doi.org/10.1007/978-3-031-50349-8_156.

[9] C. Aranas, K. Nyamuchiwa, K. Chadha, J. Pasco, T. McCarthy, Themomechanical Response of an Additively Manufactured Hybrid Alloy by Means of Powder Bed Fusion, Key Engineering Materials 964 (2023) 117–122. https://doi.org/10.4028/p-299lzX.

[10] C. Aranas, J. Pasco, T. McCarthy, Material constitutive modelling of Fe-based, Ni-based and high-entropy alloys: Development of Simu-Mat 1.0, MRS Communications 12 (2022) 585–591. https://doi.org/10.1557/s43579-022-00201-9.

[11] C. Aranas, F. Siciliano, S.F. Rodrigues, J. Pasco, E.J.P. Miranda, J.J. Jonas, Thermomechanical and thermodynamic behavior of deformed austenite in four different steel grades, Journal of Materials Research and Technology 11 (2021) 1911–1916. https://doi.org/10.1016/j.jmrt.2021.02.034.

[12] K. Chadha, Y. Tian, J. Pasco, C. Aranas, Dual-metal laser powder bed fusion of iron- and cobalt-based alloys, Materials Characterization 178 (2021) 111285. https://doi.org/10.1016/j.matchar.2021.111285.

[13] J.C. Ferreira, F.R. de Sousa Machado, C. Aranas, F. Siciliano, J. Pasco, G.S. Reis, E.J. Pedrosa de Miranda, A.E. Macêdo Paiva, S.F. Rodrigues, Physical Simulation Based on Dynamic Transformation Under Hot Plate Rolling of a Nb-Microalloyed Steel, Frontiers in Materials 8 (2021). https://www.frontiersin.org/article/10.3389/fmats.2021.716967 (accessed May 9, 2022).

[14] J. Lewis, J. Pasco, T. McCarthy, K. Chadha, M. Harding, C. Aranas Jr, High strain rate and high temperature mechanical response of additively manufactured alloy 625, Journal of Manufacturing Processes 81 (2022) 922–944. https://doi.org/10.1016/j.jmapro.2022.07.047.

[15] A. Sankar, M. Mallaiah, T. McCarthy, J. Pasco, M. Harding, C. Aranas, High-Strain Rate and High-Temperature Properties of Additively Manufactured Nickel-Based Alloy 718, in: TMS 2024 153rd Annual Meeting & Exhibition Supplemental Proceedings, Springer Nature Switzerland, Cham, 2024: pp. 224–234. https://doi.org/10.1007/978-3-031-50349-8_21.

[16] K. Nyamuchiwa, J. Pasco, T. McCarthy, A. Keshavarzkermani, T. Wang, C. Aranas, Analysis of dynamic recrystallization through austenite grain reconstruction of additively manufactured martensitic M789 steel, Materials Science and Engineering: A 897 (2024) 146345. https://doi.org/10.1016/j.msea.2024.146345.

[17] H. Bongao, J. Pasco, T. McCarthy, K. Nyamuchiwa, C. Aranas, Softening Mechanisms in Additively Manufactured 420 Stainless Steel at Elevated Temperatures, in: TMS 2024 153rd Annual Meeting & Exhibition Supplemental Proceedings, Springer Nature Switzerland, Cham, 2024: pp. 244–253. https://doi.org/10.1007/978-3-031-50349-8_23.

[18] H. Bongao, M. M, P.A. de Yro, J. Pasco, T. McCarthy, K. Nyamuchiwa, C. Aranas, High-temperature mechanical properties of additively manufactured 420 stainless steel, Mater. Res. Express 11 (2024) 056501. https://doi.org/10.1088/2053-1591/ad425d.

Conference Presentations

- Jubert Pasco, ASEAN Conference on Additive Manufacturing (ACAM 2021), Dual-metal laser powder bed fusion of Fe- and Co-based alloys, Online.
- Jubert Pasco, Canadian Materials Science Conference (CMSC 2021), Dual-metal laser powder bed fusion of Fe- and Co-based alloys, Online.
- Jubert Pasco, NSERC Holistic Innovation in Additive Manufacturing in Additive Manufacturing, (NSERC HI-AM 2022), Heat Treatment of Multi-material Additively Manufactured Maraging Steel and Co-Cr-Mo Alloy, Montreal, Quebec, Canada.
- Jubert Pasco, Conference of Metallurgist (COM 2022), Heat Treatment of Multi-material Additively Manufactured Maraging Steel and Co-Cr-Mo Alloy, Montreal, Quebec, Canada.